

# Exotic eutectic microstructures

A THESIS  
SUBMITTED FOR THE DEGREE OF  
**Doctor of Philosophy**  
IN THE  
**Faculty of Engineering**

BY  
**Aramanda Shanmukha Kiran**



Materials Engineering  
Indian Institute of Science  
Bangalore – 560 012 (INDIA)

June 2021

DEDICATED TO

*All my gurus (parents/tutors/mentors)*

*“Philosophy is written in this grand book, the universe, which stands continually open to our gaze. But the book cannot be understood unless one first learns to comprehend the language and read the letters in which it is composed.”*

*—Galileo Galilei*

# Acknowledgements

Although this Ph.D. thesis has my name as an author, going alone in the course of my Ph.D. is an impossible task, and, therefore, it is an effort of several people and opportunities.

First and foremost, I choose to express my sincere gratitude to my thesis advisors, **Dr. Abhik Choudhury** and **Dr. Kamanio Chattopadhyay**, for their insightful guidance and support. I gratefully acknowledge **Dr. Abhik Choudhury**, who has been quite splendid in supervising me.

I would also like to acknowledge the support of the following people/services affiliated with the institute: I would like to express my heartfelt gratitude to the Department of Materials Engineering's prior chairman, **Prof. Abinandanan**, and current chairman, **Prof. Satyam Suwas**, for enabling me to use different departmental facilities to conduct this research. In this regard, I like to thank **Dr. Padaikathan** for allowing me to access DSC, optical, and polishing facilities; **Prof. A Paul** for their polishing facilities usage; **Prof. Dipankar Banerjee** for allowing me to access vibromet, precise polishing machine, etching facilities; **Dr. R. Ravi** for allowing me to access EPMA; **Mr. Chandan** for his help in EPMA, SEM. Furthermore, I would like to thank members and staff (**Mr. Govindaswamy**, **Ms. Archana**, **Ms. Deepika**) of AFMM, IISc; additional thanks to **Prof. Satyam Suwas** for providing access to Helios and **Dr. Surendra Kumar Makineni** for providing access to Scios and for fruitful conversations on ion milling processes. I want to thank the office staff, **Mr. Satish**, **Ms. Rama Peter**, **Ms. M. Venkatalakshmi**, and **Mr. C. Sridharan**, who assisted me in various things. I acknowledge the financial support by the institute (GARB, IISc) for attending conferences during my Ph.D.

It was a pleasure working with my lab-mates and various colleagues in the department. In this regard, perhaps most importantly, I want to thank **Mr. Salapaka Sai Kiran**, (Project Associate) for his valuable help during my experiments in the lab. I would like to gratefully thank **Ms. Sireesha** for introducing me the realm of tellurides and her valuable advices/help

## Acknowledgements

during my stay at IISc. I would like to say thanks to **Mr. Sumeeth Khanna** for his help in computational tools and **Mr. Ravi kumar singh** for his help in computing the thermal profile of the directional solidification apparatus. I would like to thank **Dr. Prafull pandey** for his assistance during my early Ph.D. days when I didn't have access to microscopy facilities and for giving a large number of alloys for conducting test experiments in the directional solidification apparatus. I would like to thank **Dr. Mahander Pratap Singh** for his help at various places like EDM, Helios, AFMM, RSP lab. I want like to thank **Mr. Ujjval Bansal**, **Mr. Dipanjan Kumar** for their help in TEM. I would like to thank **Mr. Yazar**, **Mr. Gyan Shankar**, **Mr. Nitish Bibhanshu** for their discussions and help in EBSD related things. I would like to thank **Mr. Jyotheender** for his discussions regarding grain boundary analysis and TSL-OIM software aspects. I would like to thank **Mr. Vikram Raja** for the discussions and help in x-ray pole figures and x-ray tomography. I would like to thank **Dr. N. Esakkiraja** for discussions regarding EPMA. I would like to thank **Dr. Syed Idrees Afzal Jalali** for his help in EDM. I would like to thank **Mr. Wadood** (dual-degree student), **Ms. Srija**, **Mr. Vinayak** (interns) who worked with me in the course of my Ph.D. I would like to thank **Mr. Jayanth**, prior project assistant for his help during initial studies. I would like to thank **Mr. Sandeep Vura** for his fruitful discussions on crystal growth and characterization aspects. I would like to thank my seniors, juniors and friends in the department, who helped in different places, specially I acknowledge **Dr. Sanjay Kashyap**, **Dr. Arka Lahari**, **Dr. Balachandra badak**, **Dr. Fiyanshu kaka**, **Dr. Varun Baheti**, **Dr. Khushbu Dash**, **Dr. Abhishek Sharma**, **Dr. Manu**, **Dr. Venkata vamsi K**, **Dr. Bhaskar M**, **Dr. Shriparna Mukherjee**, **Dr. Deepali**, **Dr. Girish**, **Dr. Sourabh Mohan Das**, **Mr. Sarvesh Kumar**, **Mr. Anupam**, **Mr. Muni Kumar**, **Ms. Dharita Chandravanshi**.

I would also like to thank **Prof. Michel Rappaz**, **Prof. Silvère Akamatsu**, **Prof. Mathis Plapp** and **Prof. Sabine Bottin-Rousseau** for insightful discussions about eutectics.

I would like to acknowledge the support of the following people/services in establishing directional solidification apparatus: I would like to thank some of the vendors who helped me in providing things on time **Mr. Suresh** (delta automations), **Mr. Ananth** (furnaces), **Mr. Vasanth** (vacuum systems), **Mr. Naveen** (Manufacturing), **Mr. Naresh soni** (Mahajan chemicals), **Mr. Muniramappa** (Manufacturing), **Mr. Srinivas** (cooling systems), **Mr. Sadiq** (cooling systems), **Lokesh Kumara** (electrical works), **Mr. Nagaraj** and **Mr. Ma-**

## Acknowledgements

hesh (Scientific silica, quartz tubes), **Mr. Rakshith and Mr. Sachin** (Green automations). I would like to thank **Mr. Babu**, Department of Materials Engineering for giving suggestions during the design of the directed solidification apparatus. I would like to thank **Mr. Hari Krishna Thota**, ISRO, for his help in providing plating on copper rods.

I acknowledge the financial support for the project (DSTO-1679) by the Department of Science and Technology, India.

Even with all the academic demands met at IISc, one still craves a social life, especially while pursuing a Ph.D. In this regard, I'd want to express my gratitude to a few of my friends, without whom my existence would have been rather monotonous. I had great camaraderie and fun with **Surendra verma, Adithya, Deva, Divya, Bhanu, Ravi babu, and AU summer interns-2016**.

I want to convey my eternal gratitude to my parents, **A V K Prasad, Madhu Valli**, and sister **Deepthi**. Your unconditional love and support is unexpressible.

# Synopsis

Solidification of eutectic systems delivers compelling examples of microstructure formation, which makes the phenomena intriguing to many engineers and scientists. Therefore, eutectic solidification is extensively studied experimentally, theoretically, and numerically. However, some exotic eutectic microstructures are still not understood, particularly the systems that exhibit anisotropy. Anisotropy refers to direction-dependent microstructural dynamics. The main objective of this dissertation is to investigate the exotic microstructure formation during eutectic solidification by emphasizing the influence of anisotropy in stabilizing a particular microstructure. As directional solidification is a convenient method (imposes the temperature gradient, solidification velocity accurately and independently) to study microstructure formation, the first part of the work was directed towards the development of a directional solidification setup. Subsequently, we investigated microstructure formation in three different exotic eutectic systems. Details about each of the systems are as follows:

## **Exotic broken-lamellar structures in the Sn-Zn eutectic system:**

This chapter deals with the formation of two-phase microstructures of the Sn-Zn eutectic alloy, with endeavors to bring new inferences in reference to both well-established theories (Jackson-Hunt) and up-to-date considerations on the effects of anisotropy. The volume percentage of the (Zn)-phase in the eutectic is less than 10%, so one would expect it to form rods in the matrix of (Sn)-phase; instead, thin lamellae are observed as shown in Fig. 1. Further, the interphase boundaries in the solid keep a well-defined orientation during growth, i.e., they are parallel to the basal planes  $\{0001\}$  of the Zn-rich phase and either one of the planes in  $\{100\}$  or  $\{101\}$  family of the Sn-rich phase in steady-state microstructures, and those planes are schematically shown in Fig. 1. We claim that the rod-lamellar transition and well-defined lamellar orientation arise due to the anisotropy in the interfacial free energy of the solid-solid interfaces. Additionally, in

support of this hypothesis, we conduct various experiments for confirming the evidence of solid-solid interface anisotropy. Finally, we report two crystallographic orientational relationships that are observed between a body-centered tetragonal A5 structure (space group is I4<sub>1</sub>/amd) and a hexagonal A3 structure (space group is P6<sub>3</sub>/mmc) in steady-state microstructures.

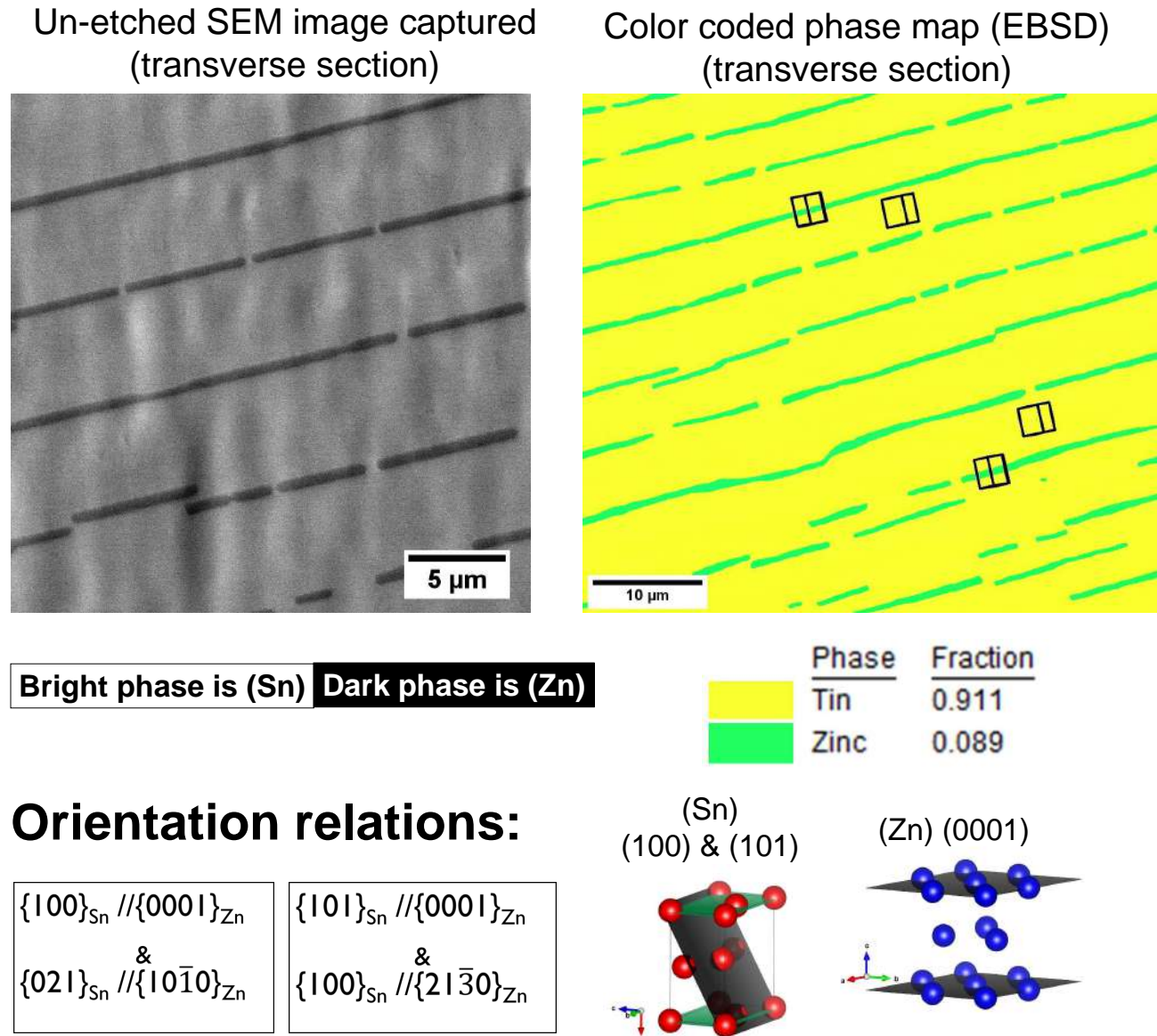


Figure 1: Formation of broken-lamellar morphology in Sn-Zn eutectic system.

## Synopsis

### Exotic two-phase eutectic colonies in Sn-Te system:

Recently, we have discovered the evolution of complex microstructures (refer to Fig. 2) due to the addition of ternary impurities to the Sn-Te eutectic system that consists of the Te-rich solid-solution, and an intermetallic SnTe phase. This chapter investigates the origin of such a microstructure that arises due to a two-phase growth instability induced by impurity addition. The binary eutectics (Sn-Te) and ternary eutectics (Sn-Te-X, where X stems for Ag, Cu, In, Ge, or Sb) are directionally solidified at different interfacial velocities in order to study morphological evolution. The investigation involves metallographic observations (using a scanning electron microscope) of samples grown at various velocities, compositional distribution analysis using electron probe micro-analyzer, crystallographic orientation analysis using electron backscatter diffraction, and peered into site-specific microstructural locations using a dual-beam microscope, i.e., electron and ion beam. The binary Sn-Te eutectic exhibits a rod-like or an interconnected string of rods morphology (refer to Fig. 2), while the addition of a third component leads to a diffusive instability (similar to a Mullins-Sekerka instability) that results in the formation of two-phase colonies. The onset of instability formation depends on both the growth velocity and concentration of the third component. The colonies have a complex internal structure that displays a 3-fold symmetry (refer to Fig. 2) reminiscent of the trigonal symmetry of the tellurium crystal, arising possibly due to strong anisotropy in the solid-liquid interfacial energy or the kinetics of growth. Additionally, the microstructures shown in Fig. 2 reveal that the internal eutectic morphology of the colony due to the addition of Ag, Cu, In, Ge is different from that observed for the addition of Sb. The Sb added samples exhibit the formation of lamellae, while a rod-like feature could be observed for all other impurities. The crystallographic analysis done in the chapter provides crystallographic orientation relationships between a trigonal structure (space group is  $P3_121$ ) and a NaCl-type cubic structure (space group is  $Fm\bar{3}m$ ) which are shown in Fig. 2. Moreover, we have made the crystal-orientation analysis not only for characterization purposes but also as a support for the effect of the anisotropy, where we find that the eutectic phases grow in a branched manner from the central colony axes, with a three-fold symmetry as shown in the schematic of Fig. 2, where we find that the SnTe crystals grow approximately normal to the  $\{001\}$  planes which is the same set of directions as in the binary eutectic. The complex patterns exhibit a structural hierarchy that provides opportunities for designing novel materials, especially in thermoelectric materials design.

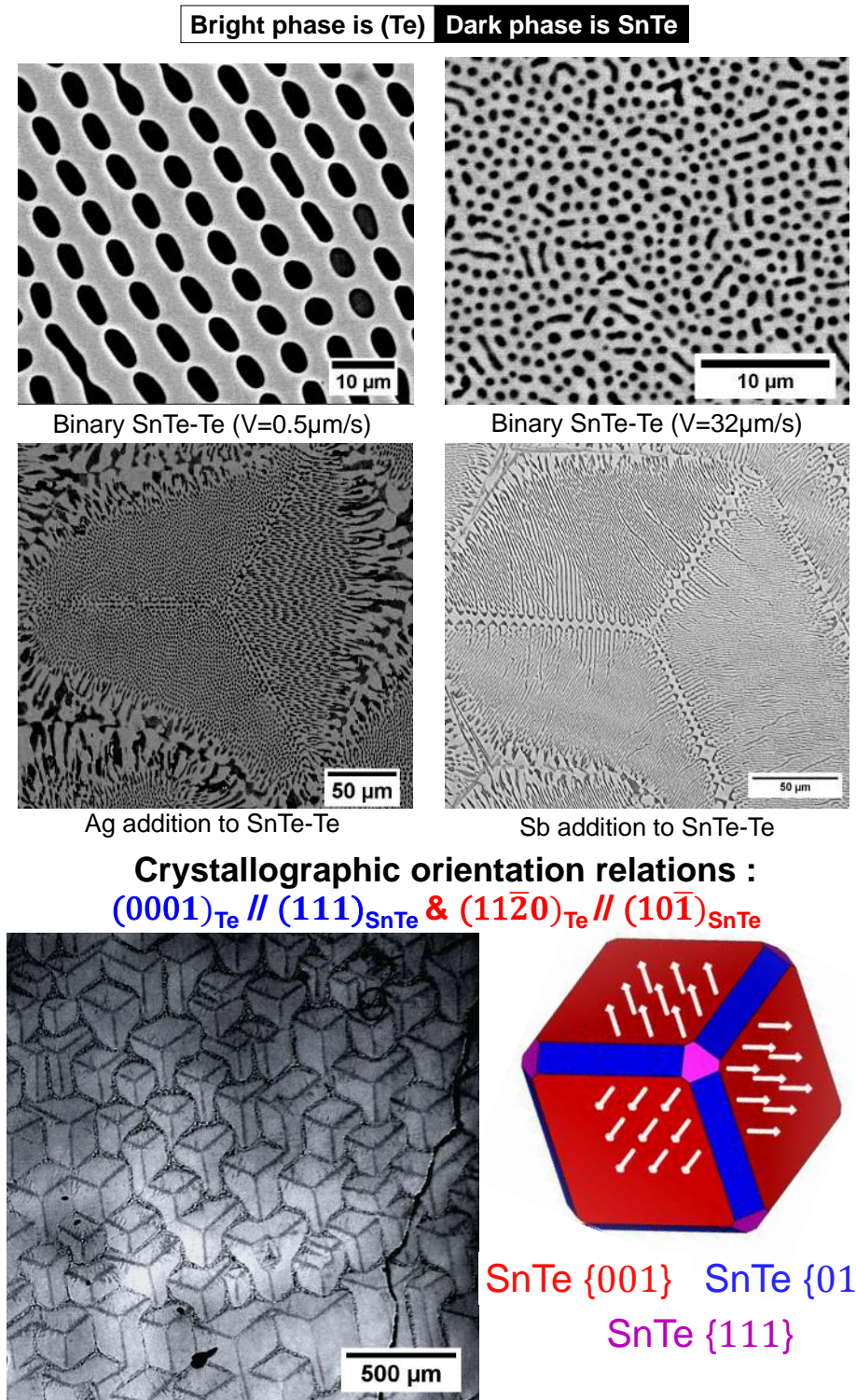


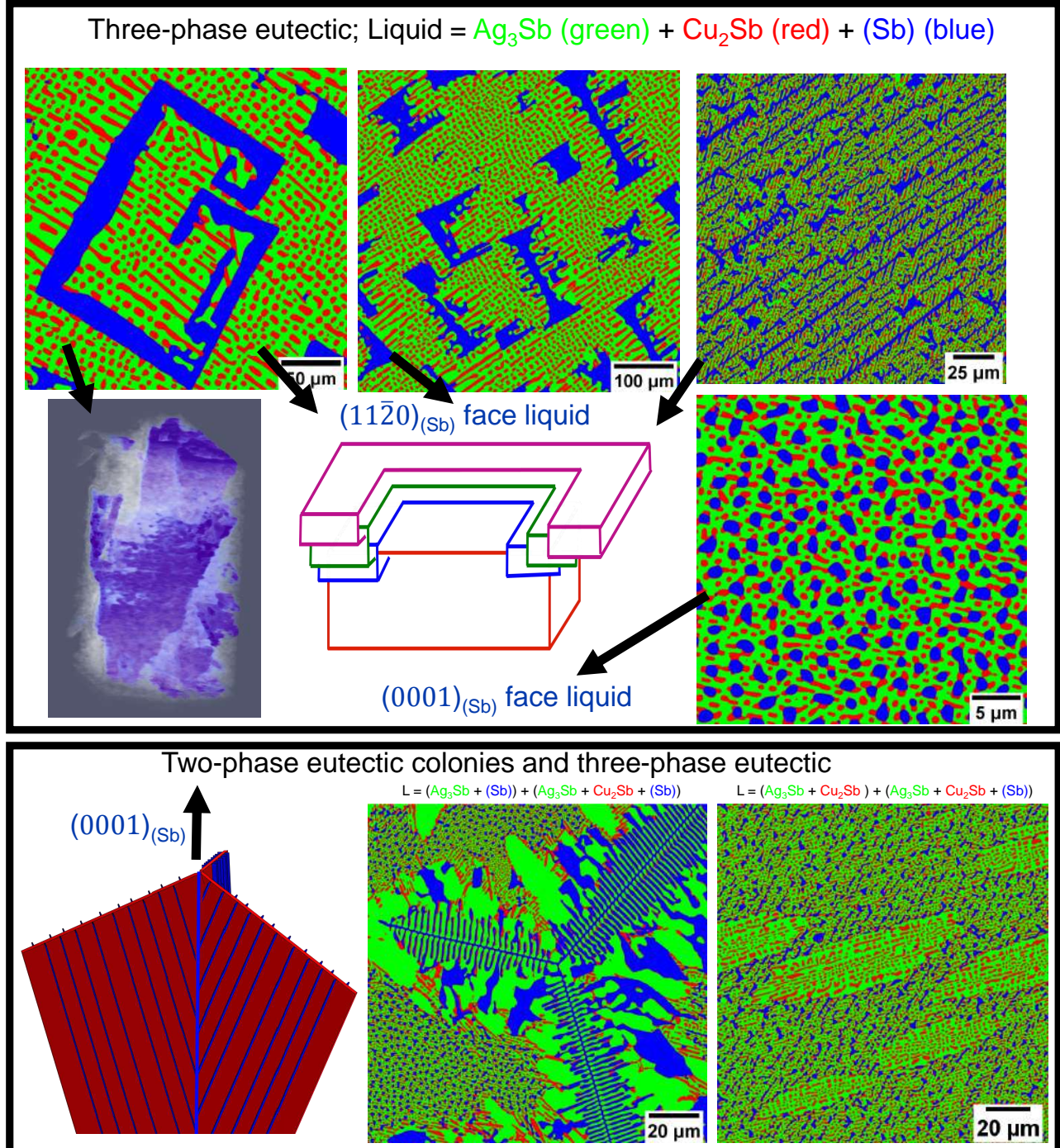
Figure 2: Exotic colony formation in Sn-Te eutectic system.

## Synopsis

### **Exotic three-phase microstructures in the ternary Ag-Cu-Sb eutectic system:**

In this chapter, we have investigated the formation of three-phase microstructures of the Ag-Cu-Sb eutectic system that contains two intermetallic compounds, i.e., silver antimonide- $\text{Ag}_3\text{Sb}$  (dyscrasite), copper antimonide- $\text{Cu}_2\text{Sb}$  (cuprostibite), and an antimony rich solid-solution (Sb). A vast range of microstructures in this system arise due to the possibilities of both invariant reactions giving rise to three-phase eutectic growth as well univariant reactions that are amenable to diffusive instabilities giving rise to microstructures involving two-phase colonies along with three-phase eutectic morphologies. The wide variety of microstructures observed in the system are shown in Fig. 3. The combination of interfaces influenced by anisotropy in either the solid-solid and solid-liquid interfaces leads to the formation of exotic patterns. This chapter investigates the origin of such three-phase microstructures along with two-phase growth instabilities that arise in the vicinity of three-phase eutectic composition. The different ternary compositions are directionally solidified at various velocities and the solidified samples are morphologically and crystallographically characterized using a combination of scanning and transmission electron microscopes along with high energy X-ray tomography in order to understand the microstructure evolution. The invariant three-phase eutectic reactions give rise to hollow, dog bone and fibrous (Sb) crystals along with lamellar/rod type morphologies of the  $\text{Cu}_2\text{Sb}$  phase while the  $\text{Ag}_3\text{Sb}$  has a continuous morphology. The different microstructures have an underlying crystallographic basis and emerge as a result of different orientation relationships between the crystals as well as distinct growth mechanisms that are influenced by the crystal orientation with the imposed temperature gradient. Among the compositions that give rise to two-phase colonies, a particularly interesting structure emerges in the  $\text{Ag}_3\text{Sb}$ -(Sb) two-phase colonies that exhibit a complex 3-fold fish skeleton structure reminiscent of the rhombohedral (Sb) crystals. Similarly, the  $\text{Ag}_3\text{Sb}$ - $\text{Cu}_2\text{Sb}$  colonies exhibit a complex plate morphology influenced by the anisotropic nature of the  $\text{Ag}_3\text{Sb}$ - $\text{Cu}_2\text{Sb}$  interface.

## Synopsis



Solid-Solid interfaces of  $\text{Ag}_3\text{Sb}$  and  $\text{Cu}_2\text{Sb}$  are anisotropic

Figure 3: Exotic three-phase microstructures in the ternary Ag-Cu-Sb eutectic system.

# Contents

Acknowledgements	i
Synopsis	iv
Contents	x
List of Figures	xiv
List of Tables	xxviii
<b>1 Introduction</b>	<b>1</b>
1.1 Eutectic equilibrium and microstructure . . . . .	3
1.2 Formation of eutectic microstructures . . . . .	3
1.2.1 Formation of eutectic microstructures in binary systems . . . . .	4
1.2.1.1 Binary eutectic with non-faceted interfaces . . . . .	4
1.2.1.2 Binary eutectic with faceted interfaces . . . . .	12
1.2.2 Morphological instability of single phase . . . . .	13
1.2.3 Formation of eutectic microstructures in multi-component systems . . . . .	16
1.2.3.1 Two-phase growth in ternary systems . . . . .	18
1.2.3.2 Three-phase growth in ternary systems . . . . .	21
1.3 Factors influencing eutectic microstructures . . . . .	24
1.3.1 Processing variables . . . . .	24
1.3.1.1 Sample size . . . . .	24
1.3.1.2 Temperature gradient . . . . .	24
1.3.1.3 Velocity . . . . .	24
1.3.2 Volume percentage of phases . . . . .	26

## CONTENTS

1.3.2.1	In two-phase eutectics . . . . .	26
1.3.2.2	In three-phase eutectics . . . . .	26
1.3.3	Presence of anisotropy . . . . .	29
1.3.3.1	Anisotropy in the solid-solid interfacial energy . . . . .	29
1.3.3.2	Anisotropy in solid-liquid interfacial energy or growth kinetics .	31
1.4	Selection of exotic systems . . . . .	32
<b>2</b>	<b>Development of directional solidification apparatus</b>	<b>34</b>
2.1	Bridgman-based apparatus . . . . .	35
2.2	Development of apparatus . . . . .	36
2.2.1	Basic design of Furnace . . . . .	36
2.2.1.1	Usuage of Ni-electroplated copper rod . . . . .	39
2.2.1.2	Sample holder . . . . .	39
2.2.1.3	Modelling using OpenFoam and its experimental validation . .	39
2.2.2	Selection of crucible . . . . .	44
2.2.3	Design for linear motion . . . . .	47
2.3	Alloy making . . . . .	47
2.4	Protocol employed for solidification . . . . .	51
<b>3</b>	<b>Material characterization techniques</b>	<b>52</b>
3.1	Sample preparation for scanning electron microscope (SEM) and image capturing	52
3.2	Image analysis of SEM images . . . . .	53
3.3	Composition analysis . . . . .	53
3.4	Ion milling . . . . .	55
3.5	EBSM and its analysis . . . . .	55
3.6	TEM . . . . .	55
3.7	X-ray diffraction . . . . .	56
3.8	X-ray tomography . . . . .	56
<b>4</b>	<b>Exotic broken-lamellar structures in the Sn-Zn eutectic system</b>	<b>57</b>
4.1	Sn-Zn phase diagram . . . . .	57
4.2	Results and discussions . . . . .	59
4.2.1	Morphology aspects . . . . .	59
4.2.2	Crystallographic orientation aspects . . . . .	72

## CONTENTS

4.2.3 Evidence of anisotropy . . . . .	77
4.2.4 Similarities with Bi-Zn eutectic . . . . .	85
4.3 Summary . . . . .	85
<b>5 Exotic two-phase eutectic colonies in Sn-Te system</b>	<b>87</b>
5.1 Binary Sn-Te eutectic . . . . .	87
5.2 Results and discussions . . . . .	89
5.2.1 Microstructure evolution in binary Sn-Te eutectic . . . . .	89
5.2.1.1 Morphology and length scale selection . . . . .	89
5.2.1.2 Crystallographic orientation relations in binary Sn-Te eutectic .	97
5.2.2 Microstructure evolution of Sn-Te eutectic in the presence of impurities .	100
5.2.2.1 Composition distribution of elements . . . . .	102
5.2.2.2 Ag addition to Sn-Te eutectic . . . . .	107
5.2.2.3 Sb addition to Sn-Te eutectic . . . . .	114
5.3 Summary . . . . .	120
<b>6 Exotic three-phase microstructures in the ternary Ag-Cu-Sb eutectic system</b>	<b>122</b>
6.1 Results and discussions . . . . .	122
6.1.1 Phase selection . . . . .	122
6.1.2 Morphological selection . . . . .	125
6.1.2.1 Ternary eutectic composition . . . . .	125
6.1.2.2 Ternary off-eutectic composition-Ag <sub>35</sub> Cu <sub>25</sub> Sb <sub>40</sub> ) . . . . .	127
6.1.2.3 Discussions . . . . .	128
6.1.3 Crystallographic orientation selection . . . . .	136
6.1.4 Two-phase colonies with three phase eutectic . . . . .	141
6.1.4.1 Ag <sub>3</sub> Sb-(Sb) eutectic colonies . . . . .	141
6.1.4.2 Ag <sub>3</sub> Sb-Cu <sub>2</sub> Sb eutectic colonies . . . . .	146
6.1.4.3 Cu <sub>2</sub> Sb-(Sb) two-phase structures . . . . .	150
6.2 Summary . . . . .	152
<b>7 Conclusions and future prospects</b>	<b>154</b>
7.1 Conclusions . . . . .	154
7.2 Future prospects . . . . .	157

## **CONTENTS**

<b>List of Publications and Conferences</b>	<b>159</b>
<b>References</b>	<b>161</b>

## List of Figures

1	Formation of broken-lamellar morphology in Sn-Zn eutectic system. . . . .	v
2	Exotic colony formation in Sn-Te eutectic system. . . . .	vii
3	Exotic three-phase microstructures in the ternary Ag-Cu-Sb eutectic system. . .	ix
1.1	(a) The morphology of cyclohexane-camphene eutectic. The morphology of the solid-liquid interface exhibits a complex structure where one of the phases is faceted. (b) The morphology of the Azobenzene-benzil eutectic consists of two faceted phases (adopted from [1]). The growth direction is from bottom to top. . . . .	5
1.2	A typical binary eutectic phase diagram is shown in (a), where the dashed lines show local equilibrium conditions, while, the dotted lines are used to show the undercooling requirement for diffusion and interface energy. (b) shows schematic of eutectic interface with diffusion pathways of the components and force balance at the trijunction. . . . .	6
1.3	The average undercooling with eutectic spacing for a particular velocity and regions corresponding to stable and unstable as per Jackson and Hunt theory [2].	10
1.4	(a) Schematic to illustrate the instability for $\lambda < \lambda_m$ that causes the disappearance of lamella in the center. (b) The experimental shows the lamella narrowing and falling below the average interface position until other lamellae cover it. (c) Schematic to show the depressed region that arises for $\lambda_M < \lambda$ . (d), (e) are experimental images taken in sequence to show the formation of the new lamella, where (d) exhibit the formation of pocket in the center of the broader phase, and eventually with time, (d) changes to (e) where we can observe the formation of the new lamella. The images (b), (d), (e) corresponds to carbon tetrabromide - hexachloroethane eutectic and are adopted from [1]. The growth direction is from bottom to top. . . . .	11

## LIST OF FIGURES

## LIST OF FIGURES

1.11 Typical three-phase transverse section microstructures (growth direction is perpendicular to the plane of view), (a) is a microstructure of ternary eutectic in Ag-Al-Cu system (adopted from [7]), (b) is a microstructure of ternary eutectic in Al-Nb-Ni system (adopted from [8]). . . . . .	23
1.12 Variations in Ag-Al-Cu eutectic microstructure due to change in velocity (adopted from [7]). The image corresponds to the transverse section where the growth direction is perpendicular to the plane of view. . . . . .	25
1.13 Different eutectic microstructures (growth direction is perpendicular to the plane of view) for different compositions in the aluminum-copper system that are adopted from [9] (phase diagram is shown in (f)), where (a) is Al-19.5 wt.% Cu alloy that exhibits $\text{Al}_2\text{Cu}$ rods in (Al) matrix, (b) is Al-24.0 wt.% Cu alloy that exhibits coexistence of $\text{Al}_2\text{Cu}$ rods and lamellae in (Al) matrix, (c) is Al-33.2 wt.% Cu alloy that exhibits lamellar morphology of $\text{Al}_2\text{Cu}$ and (Al), (d) is Al-41.0 wt.% Cu alloy that exhibits coexistence of (Al) rods and lamellae in $\text{Al}_2\text{Cu}$ matrix, (e) is Al-42.3 wt.% Cu alloy that exhibits (Al) rods in $\text{Al}_2\text{Cu}$ matrix.	27
1.14 The rod-lamellar transition obtained using phase-field simulation (adopted from [10]). Growth direction is perpendicular to the plane of view. . . . . .	28
1.15 Three-phase morphologies are obtained by changing the volume percentages, where the volume percent of the green phase remains the same. The volume percent of red, blue, and green phases are 31, 33, 36 in (a); 21, 33, 46 in (b), and 12, 33, 55 respectively (adopted from [11]). Growth direction is perpendicular to the plane of view. . . . . .	28
1.16 Morphologies of carbon tetrabromide-hexachloroethane eutectic, (a) shows that lamellar growth is not perpendicular to the solid-liquid interface, while (b) shows two eutectic grains in which one contains locked low energy solid-solid interfaces that are highlighted with an arrow (adopted from [1]). The growth direction is from bottom to top. . . . . .	30
1.17 Morphology of $\text{MgZn}_2$ -Zn eutectic that exhibit spiral morphology (adopted from [1]). The image corresponds to the transverse section where the growth direction is perpendicular to the plane of view. . . . . .	32

## LIST OF FIGURES

2.1 Schematic of the modified Bridgman apparatus is shown in (a), while plot in (b) display the axial temperature distribution with distance from the hot-zone, for different temperatures of the hot zone; where the origin of distance axis is at the center of the hot zone and the distance is measured until the center of the chill zone. Please note that the schematic in (a) is not on the same scale as in (b). The axial lengths of the hot zone, gradient zone, and chill zone are 100, 10, 80 mm, respectively, while the inner diameters are 30, 20 mm for hot and chill zones, whereas the gradient zone has 18 mm inner diameter. . . . .	37
2.2 Schematic of the modified Bridgman apparatus with hollow Ni-electroplated copper rod addition is shown in (a), while plots in (b) display the axial temperature distribution with distance from the hot-zone, for different temperatures of the hot zone; where the origin of distance axis is at the center of the hot zone and the distance is measured until the center of the chill zone. Please note that the schematic in (a) is not on the same scale as in (b). The axial lengths of the hot zone, gradient zone, and chill zone are 100, 10, 80 mm, respectively, while the inner diameters are 20 mm for hot and chill zones, whereas the gradient zone has an 18 mm inner diameter. . . . .	38
2.3 (a), (b) are the schematics that show two different sample holders. In the case of (b), the sample is placed in a holder which has water circulation that is maintained at the same temperature as in the chill zone, as shown in Fig 2.3(b). The actual sample holder with water cooling provision is shown in (c). . . . .	40
2.4 Thermal modeling using OpenFOAM software, where (a) is directional solidification setup 2D view, (b) is thermal profile, and (c) is axial temperature profile in liquid. . . . .	41
2.5 Temperature profile inside the furnace without quartz crucible. . . . .	42
2.6 SEM images captured in longitudinal sections (upper) and transverse sections (lower) at velocities 1.0 and 2.0 $\mu\text{m}/\text{s}$ . . . . .	44
2.7 SEM images (b), (a) were captured in longitudinal sections from transient regions to the regions with an imposed velocity of 1.2 and 1.4 $\mu\text{m}/\text{s}$ . Corresponding high magnification images are shown in (c), (d). . . . .	45
2.8 Quartz crucible having constriction which serves as a natural grain selector. . . . .	46

## LIST OF FIGURES

2.9 Quartz sample made for spiral growth, where (a) is having uniform pitch, while (b) is having variable pitch between each consecutive turn. . . . .	46
2.10 The screw driven linear drive that consists of gearbox and stepper motor. (a) is actual one while (b) is a schematic. . . . .	48
2.11 The actual apparatus made in the lab. . . . .	49
2.12 Image of vacuum unit that consists of rotary and diffusion pump. . . . .	49
2.13 Image of induction furnace that consists of a coil which is used to make alloys. . . . .	50
 3.1 (a) Schematic of sample setup to show how milling was done at grazing incidence angle close to zero to the surface(but not perpendicular to sample surface). Image (b) is to illustrate that an obstacle to the ion beam coming at grazing incidence angle close to zero can cause band-like features in the sample. Image (c) has been captured while removing irregularities formed in the image (b) by removing few layers of material. It is shown here to illustrate how ion-beam coming at a grazing incidence angle removes the material (top to bottom). . . . .	54
 4.1 Sn-Zn binary phase diagram [12]. . . . .	58
4.2 Scanning electron micrographs of the Sn-Zn eutectic alloy solidified at $2.5\mu\text{m}/\text{s}$ , where (a) is longitudinal section (growth direction is from bottom to top), while (b) is transverse section, growth direction is towards the reader. . . . .	59
4.3 Transverse section SEM images of directionally solidified Sn-Zn eutectic alloy at different velocities. . . . .	60
4.4 Transverse section images of the unetched Sn-Zn alloy solidified at $0.6 \mu\text{m}/\text{s}$ , low magnification image in (a) and high magnification image in (b), where bright part is Sn rich phase and dark part is Zn rich phase. . . . .	61
4.5 (a) Variation of average spacing with velocity and (b) Average undercooling with eutectic spacing. . . . .	62
4.6 Images captured using a SEM, which are taken at equally spaced transverse sections along the growth direction, following the same eutectic grain of the sample solidified at $50 \mu\text{m}/\text{s}$ . (a) is 20 mm from the bottom, (b) is 30 mm from the bottom, (c) is 40 mm from the bottom, (d) is 50 mm from the bottom, (e) is 60 mm from the bottom. . . . .	64
4.7 Variation of average length of lamellar fragment with time of solidification. . . . .	65

## LIST OF FIGURES

## LIST OF FIGURES

## LIST OF FIGURES

4.17 (a) Modified quartz tube showing bends that are intended to cause a change in the orientation of the solid-liquid interface as depicted in (b). A small constriction is given at the lower end so as to cause the solidification of a single grain into the straight section of the quartz tube. . . . .	78
4.18 Collage of SEM images revealing the change in the microstructure as the solidification proceeds across the quartz bend shown in (a), starting from b1 to f1 through c1, d1, e1 respectively and the corresponding high-magnification images are shown in b2, c2, d2, e2, f2, f3. . . . .	79
4.19 Crystallographic orientations of the eutectic phases obtained using EBSD at different locations on the longitudinal section (which are highlighted as a, b, c, d, and e on the SEM image) of the sample near the bend in the quartz tube. While Sn maintains its orientation, nucleation of Zn is evident. . . . .	80
4.20 (a) Depicts a directionally solidified sample with two grains that is utilized as a seed; one of the grains is aligned straight with respect to the cylindrical axes, while the second has a slight tilt. (b) The angle of the cutting plane that dissects the sample at an angle of 10°with respect to the growth direction. (c) The cut sample is placed such that planes along which the sample is sectioned are aligned with the quartz tube. This, therefore, mimics the situation where the original sample is now rotated with respect to the growth direction. . . . .	81
4.21 (a) Microstructure of the directionally solidified sample that is solidified using a seed. The horizontal discontinuity in the microstructure demarcates the location from which the resolidification begins. (b) Pole plots for the Grain-2 in (a) derived from EBSD show that the crystallographic orientations of re-solidified grains match that of the original seed. . . . .	82
4.22 Morphology and crystallography of Bi-Zn eutectic system showing close relation to Sn-Zn eutectic system. . . . .	84
5.1 Sn-Te binary phase diagram [14]. . . . .	88
5.2 Scanning electron micrographs of binary Sn-Te eutectic ( Te-15at%Sn) solidified at $0.5\mu m/s$ . . . . .	90
5.3 Morphology of the quenched solid-liquid interface of binary Sn-Te eutectic showing a planar growth front. . . . .	91

## LIST OF FIGURES

5.4	Transverse section SEM images of directionally solidified binary Sn-Te eutectic at different velocities along with their 2-point spatial self-correlations of the SnTe phase, shows that the morphology of the Sn-Te eutectic is predominantly rod. However, the trace of the rod-centroids gives an impression of several strings of rods with weak alignment between them in samples solidified with $V=0.5, 1.0, 2.0, 4.0 \mu\text{m}/\text{s}$ . With increasing velocities, rod distribution becomes random. The colorbar depicts the probability of occurrence of self-correlation vectors. . . . .	94
5.5	Plot depicting the variation of average eutectic spacing with velocity in (a), while (b) is the variation of average undercooling with eutectic spacing computed at higher ( $32.0 \mu\text{m}/\text{s}$ ) and lower velocity ( $0.5 \mu\text{m}/\text{s}$ ) for both rod and lamellar morphology. . . . .	96
5.6	Pole figures of SnTe and (Te) obtained from EBSD data of binary eutectic solidified at $0.5 \mu\text{m}/\text{s}$ exhibiting orientation relationships, i.e., $(111)_{\text{SnTe}} // (0001)_{(\text{Te})}$ and $(10\bar{1})_{\text{SnTe}} // (11\bar{2}0)_{(\text{Te})}$ as highlighted in (b) and (c). Schematic of sample orientation in EBSD setup is shown in (d). Corresponding planes are highlighted in SnTe and (Te) crystals of (e) using VESTA [13]. . . . .	97
5.7	Stereographic projection of Te phase along $(0001)$ plane and SnTe phase along $(111)$ plane. $\{001\}$ , $\{011\}$ , $\{111\}$ families of SnTe are highlighted along with $\{0\bar{1}11\}$ , $\{1\bar{1}02\}$ , $\{11\bar{2}0\}$ , $\{2\bar{2}01\}$ families of Te. . . . .	98
5.8	Inverse pole figures of samples having different morphologies (both are transverse sections). For both morphologies, (Te) maps to greenish yellow color and SnTe maps to red color, which reveal that both have same crystallographic orientation.	99
5.9	Formation of eutectic cells in the presence of an impurity in the Sn-Te eutectic system. . . . .	100
5.10	Morphology of the eutectic colonies in presence of different impurities . . . . .	101
5.11	Composition distribution maps obtained for each of the element using electron probe microanalyzer shows segregation of impurities in the inter-colony regions.	106
5.12	Liquidus Projection of Ternary Phase Diagrams. . . . .	108
5.13	Typical colony microstructure observed due to addition of Ag as an impurity, where transverse section shows inherent three-fold symmetry in the internal morphology and longitudinal section shows tilted growth of eutectic in <b>a</b> , <b>b</b> directions as highlighted in the image where tilt angle is close to $54^\circ$ from the central axis.	109

## LIST OF FIGURES

- 5.14 Microstructures captured from transverse sections of samples solidified with different percentage of Ag (increases from top to down) at different velocities (increases from left to right). . . . . 110
- 5.15 Plot showing the morphology observed for three different percentages of Ag at different velocities thereby revealing the critical velocity beyond which the instability occurs. . . . . 111
- 5.16 Pole figures of SnTe and (Te) obtained from EBSD data of eutectic colony obtained due to Ag addition (SEM image is shown in (e)) for the sample solidified at  $21.0\mu\text{m}/\text{s}$  with sample orientation as shown in schematic (d) are plotted in (a), (b), (c). Orientation relationships are the same as the relations observed in the case of binary eutectic, i.e.,  $(111)_{\text{SnTe}} // (0001)_{(\text{Te})}$  and  $(10\bar{1})_{\text{SnTe}} // (11\bar{2}0)_{(\text{Te})}$ . Crystallographic planes in connection to morphology of the colony shown in (e) are highlighted using VESTA [13] in crystal schematic (f). . . . . 113
- 5.17 Morphology of the quenched solid-liquid interface of the colony, while the schematic shows the shape of the colonies across the solid-liquid interface. . . . . 114
- 5.18 Internal structure of the colony captured using SEM when the sample is tilted at an angle  $52^\circ$  (refer schematic (d)). Image (a) is captured when the colony was cut at an angle  $54^\circ$  as highlighted in the inset schematic. Image (b), (c) are captured after dissecting one of the three parts of the colony close to the central longitudinal axis as highlighted in their respective inset schematics to show eutectic emerging from the central longitudinal section with rod morphology. 115
- 5.19 Typical colony microstructure observed due to addition of Sb as an impurity, where (a) is low magnification and (b) is high magnification transverse section images showing inherent three-fold symmetry in the internal morphology, while the eutectic structure is modified to a lamellar type. . . . . 116
- 5.20 Morphology of eutectic structure in the presence of Ag/Sb as an impurity below critical velocity. Ag addition results in mixture of rod/labyrinth structures while Sb addition results in mixture of rod and well-aligned lamellar structures. . . . . 117
- 5.21 Morphology of colony structure in presence of Ag/Sb as an impurity, where the (Te) phase is removed. Images show lamellar structure for Sb-addition whereas rod-structure for Ag-addition. . . . . 117

## LIST OF FIGURES

- 5.22 Pole figures of SnTe and (Te) obtained from EBSD data of eutectic colony obtained due to Sb addition (SEM image is shown in (e)) for the sample solidified at  $15.0\mu\text{m/s}$  with sample orientation as shown in schematic (d) are plotted in (a), (b), (c). Orientation relationships are same as the relations observed in the case of binary eutectic and Ag added colonies, i.e.,  $(111)_{\text{SnTe}} // (0001)_{(\text{Te})}$  and  $(10\bar{1})_{\text{SnTe}} // (11\bar{2}0)_{(\text{Te})}$ . Crystallographic planes in connection to the morphology of the colony shown in (e) are highlighted using VESTA [13] in crystal schematic (f). . . . . 118
- 5.23 Internal structure of the colony captured using SEM when the sample is tilted at an angle  $52^\circ$  (refer schematic (d)). Image (a) is captured when the colony was cut at an angle  $54^\circ$  as highlighted in the inset schematic. Image (b), (c) are captured after dissecting one of the three parts of the colony close to the central longitudinal axis as highlighted in their respective inset schematics to show eutectic emerging from the central longitudinal section with lamellar morphology. 119
- 6.1 Schematic of a liquidus projection, and the microstructure involving two-phase eutectic colonies along with a three-phase eutectic reaction in the final liquid and an invariant three-phase eutectic. . . . . 123
- 6.2 ((a), (b), (c) are the selected area electron diffraction (SAED) pattern from silver antimonide- $\text{Ag}_3\text{Sb}$ , copper antimonide- $\text{Cu}_2\text{Sb}$ , and antimony rich solid-solution (Sb) taken in such a way that the zone axis matches with the direction of the imposed temperature gradient obtained from site-specific TEM lamella prepared from a region near the blocky (Sb) phase that consists of all three phases. Results correspond to the eutectic alloy solidified at  $0.5 \mu\text{m/s}$ . . . . . 123
- 6.3 (a) is the x-ray diffractogram corresponding to the eutectic sample (solidified at  $0.5 \mu\text{m/s}$ ) obtained by conducting x-ray diffraction on the transverse section (section perpendicular to imposed temperature gradient) as shown in the schematic (b). The inset of (a) has x-ray pole figures corresponding to the  $\text{Ag}_3\text{Sb}$  and (Sb) diffraction peaks.SAED pattern shown in Fig. 6.2 corresponds to the same sample.124

## LIST OF FIGURES

- 6.4 (a)-(e) are the SEM images captured in the transverse section of directionally solidified ternary Ag-Cu-Sb eutectic (at.-%: Ag<sub>42.4</sub>Cu<sub>21.6</sub>Sb<sub>36</sub>) alloys obtained at different velocities i.e., 0.5, 1.0, 8.0, 16.0, 32.0  $\mu\text{m}/\text{s}$  respectively. Images reveal that with decreasing solidification velocity, the (Sb) transforms from a fibrous to bulky structure, whereas Cu<sub>2</sub>Sb is predominantly a mixture of rod/broken-lamellar type morphology. . . . . 126
- 6.5 (a) is Secondary electron image, while (b) is Backscatter electron image from same location. The contrast of the (Sb) phase (bright or dark) depends on the width of the pit. Size of pit influences the BSE signal from (Sb) phase. Hence some of the (Sb) regions appear dark while others appear bright. . . . . 127
- 6.6 (a)-(e) are the SEM images captured in the transverse section of directionally solidified alloys of Ag<sub>35</sub>Cu<sub>25</sub>Sb<sub>40</sub> (at.-%) composition obtained at different velocities, i.e., 0.5, 1.0, 8.0, 16.0, 32.0  $\mu\text{m}/\text{s}$  respectively. Images show that the (Sb) phase exhibits dog bone type morphology at higher velocities and bulky structure at 0.5  $\mu\text{m}/\text{s}$ , whereas Cu<sub>2</sub>Sb phase exhibits predominantly rod/broken-lamellar type morphologies. . . . . 129
- 6.7 Average eutectic spacing variation with velocity. . . . . 131
- 6.8 (a) is the collage of (Sb) phase during evolution obtained using an x-ray tomography dataset, whereas (b), (c) are three-phase microstructures captured using SEM in the transverse and longitudinal sections, respectively. Images correspond to the sample solidified at the velocity of 0.5  $\mu\text{m}/\text{s}$ . Images reveal the formation of hollow space inside the blocky phase morphology, which gradually widens as it evolves. . . . . 133
- 6.9 (a)-(d) are the schematics to elucidate the mechanism at different stages during the growth of the (Sb) phase. . . . . 134
- 6.10 Pole figures obtained from EBSD data of different microstructures. EBSD is performed on transverse sections with A1, A2 directions as shown in the corresponding morphology. Planes lying in the center of the pole figure correspond to the planes facing the liquid. The solid-solid interface trace between Ag<sub>3</sub>Sb and Cu<sub>2</sub>Sb is highlighted on the morphology as well as the pole figures. . . . . 138

## LIST OF FIGURES

- 6.11 (a) is low magnification SEM image captured in transverse section of  $\text{Ag}_{47}\text{Cu}_{15}\text{Sb}_{38}$  (at.%) alloy solidified at  $V = 32.0 \mu\text{m}/\text{s}$  which shows two-phase and three-phase structures. (b)-(e) are the images captured in transverse sections of the alloy solidified at different velocities, i.e.,  $32.0, 20.0, 2.0, 1.0 \mu\text{m}/\text{s}$ , respectively. Colonies exhibit complex internal morphology with inherent three-fold symmetry. . . . . 143
- 6.12 (a) is a longitudinal section of the colony. (b) is a schematic of the Sb-rich phase in the colony. (c) is (Sb) crystal schematic with planes  $((11\bar{2}0), (1\bar{1}02), (\bar{1}104))$  highlighted using VESTA [13]. Image (d) is the sectional view of the colony after dissecting as shown in the inset schematic, which is captured when the sample is tilted as shown in the schematic (e) at an angle  $52^\circ$  and  $38^\circ$  with respective to transverse and longitudinal sections, respectively. . . . . 144
- 6.13 Pole figures of  $\text{Ag}_3\text{Sb}$  phase and (Sb) phase plotted using EBSD data for the two-phase eutectic colony solidified at  $32.0 \mu\text{m}/\text{s}$  with the corresponding image as shown in (h) where growth direction is out of view. The three vanes have plate morphology in the colony corresponding to  $\{11\bar{2}0\}_{(\text{Sb})}$ , which are highlighted in the pole figure as well as in crystal schematics (j) using VESTA [13]. The  $(1\bar{1}02)_{(\text{Sb})}, (\bar{1}104)_{(\text{Sb})}$  poles lie at an angle  $36.9^\circ, 56.4^\circ$  from the central axis respectively, and are perpendicular to  $(11\bar{2}0)_{(\text{Sb})}$ . . . . . 145
- 6.14 (a) and (b) are the SEM images captured in the longitudinal and transverse section of  $\text{Ag}_{43.4}\text{Cu}_{21.6}\text{Sb}_{35}$  (at.%) alloy directionally solidified at  $64.0 \mu\text{m}/\text{s}$ , while (c)-(f) are transverse section images obtained at different velocities, i.e.,  $16.0, 8.0, 4.0, 1.0 \mu\text{m}/\text{s}$  respectively. Samples solidified at  $4.0, 1.0 \mu\text{m}/\text{s}$  do not exhibit the formation of two-phase colonies, while the samples solidified at  $64.0, 16.0, 8.0 \mu\text{m}/\text{s}$  show two-phase colonies and three-phase eutectic. Two-phase colonies exhibit plate-type morphology. . . . . 147
- 6.15 (i), (ii), (iii) are the pole figures of  $\text{Ag}_3\text{Sb}$ ,  $\text{Cu}_2\text{Sb}$ , and Sb-rich phases obtained from  $\text{Ag}_{43.4}\text{Cu}_{21.6}\text{Sb}_{35}$  (at.%) alloy directionally solidified at  $1.0 \mu\text{m}/\text{s}$ , where EBSD is performed on transverse sections with A1, A2 directions as shown in the corresponding morphology (iv). Orientation relations are one of the  $\{001\}_{\text{Ag}_3\text{Sb}}||$  one of the  $\{100\}_{\text{Cu}_2\text{Sb}}||$  one of  $\{11\bar{2}0\}_{(\text{Sb})}$ , and  $(100)_{\text{Ag}_3\text{Sb}}|| (001)_{\text{Cu}_2\text{Sb}}||(0001)_{(\text{Sb})}$ . . . . . 148

## LIST OF FIGURES

- 6.16 (a), (b) are the pole figures of  $\text{Ag}_3\text{Sb}$ , while (c), (d), and (e) are the pole figures of  $\text{Cu}_2\text{Sb}$  obtained from two-phase eutectic colony solidified at  $64.0 \mu\text{m/s}$  consisting of plate morphology as shown in (f). EBSD is performed on transverse section with A1, A2 axis as shown in (f). Orientation relationships obtained are one of the  $\{001\}_{\text{Ag}_3\text{Sb}}||$  one of the  $\{100\}_{\text{Cu}_2\text{Sb}}$ , and  $(120)_{\text{Ag}_3\text{Sb}}|| (001)_{\text{Cu}_2\text{Sb}}$ . The solid-solid interface traces are highlighted on the corresponding pole figures, and crystal schematics (g) and (h) using VESTA [13]. . . . . 149
- 6.17 (a), (b), (c) are the SEM images taken in the transverse section of  $\text{Ag}_{23}\text{Cu}_{27}\text{Sb}_{50}$  (at.%) alloy directionally solidified at  $0.5, 16.0, 32.0 \mu\text{m/s}$  velocities respectively. The morphology observed in the sample solidified at  $0.5 \mu\text{m/s}$  is similar to the ternary eutectic having the bulky structure of (Sb), while at higher solidification velocities ( $16.0, 32.0 \mu\text{m/s}$ ), two phases exhibit uncoupled growth behavior. . . . . 150
- 6.18 EBSD is conducted for both the  $\text{Cu}_2\text{Sb}$  plate and (Sb) dendritic phases, observed in the  $\text{Ag}_{23}\text{Cu}_{27}\text{Sb}_{50}$  alloy solidified at  $32.0 \mu\text{m/s}$  on transverse sections with A1, A2 directions as shown in the respective images. (a) consists of  $\text{Cu}_2\text{Sb}$  pole figures corresponding to plate morphology, while (b) consists of (Sb) pole figures corresponding to its dendritic morphology. The solid traces are highlighted on the corresponding pole figures. . . . . 151

# List of Tables

1.1	Crystal structure and group of some exotic phases. . . . .	33
6.1	Crystal structure of the phases present in the system (*hexagonal cell). . . . .	125

# Chapter 1

## Introduction

*"Nature uses only the longest threads to weave her patterns, so each small piece of her fabric reveals the organization of the entire tapestry." —Richard P. Feynman*

Nature consists of incredible patterns [15, 16] that delight our imagination and question our understanding. What drives these patterns to emerge? Almost all the natural processes responsible for pattern formation are complex; investigating pattern formation helps us discover the underlying principles of all similar patterns occurring in nature. In the spirit of exploring complex pattern formation, we study one such intriguing physical phenomenon of liquid transformation into solid (solidification) that generates fascinating patterns (microstructures<sup>1</sup>)[17, 18, 19] in materials, that involves a complicated interplay of many processing/material parameters [20, 21, 22, 23]. Furthermore, the solidification/melting processes are ubiquitous that persists from the formation of the planet and still showing their impact on the natural world (examples are frost formation during winter, the dynamics of floes in oceans, and the dynamics of magmas in volcanos) and the industrial world (in metal casting, crystal growth, metal joining processes (like welding, soldering, brazing), additive manufacturing, chocolate making, glass making, etc.). Thus, solidification is a universal phenomenon responsible for the formation of various materials from a naturally occurring rock to the most advanced automobile. So, investigating the microstructure formation during solidification is an exciting topic not only for understanding the fundamental aspects of pattern formation but also in designing many novel materials by modifying the solidification paths in a controlled manner.

Furthermore, eutectic systems are appealing materials as they produce fascinating solidi-

---

<sup>1</sup>Metallurgical community uses ‘Microstructure,’ henceforth, it is used in the rest of the thesis

fication microstructures [24, 25, 1, 26, 27, 28, 29, 30, 31] that deliver excellent mechanical / functional properties [32, 33, 34, 35, 36, 37, 38, 39, 40, 41]. Therefore, understanding the microstructure development and solidification mechanisms of eutectics has attracted a great deal of interest in materials engineers/scientists to anticipate and optimize the resulting properties. Physicists are also inquisitive in eutectic research because these materials can deliver various self-organizing patterns, making eutectic solidification an excellent model system for analyzing various nonlinear phenomena. Moreover, eutectic solidification paves the route for creating required morphologies with targeted properties and functionalities [42, 43, 44] simply by tuning the appropriate parameters without concerning oneself with the complexities of processing, such as in the fabrication of synthetic composites. Hence it is an experimentally, theoretically, and numerically well-studied solidification phenomenon. However, some of the exotic eutectic microstructures that appear in anisotropic<sup>2</sup> systems remain unexplored.

This leads to the thesis's key objective, which is to investigate the underlying causes for the emergence of such exotic microstructures. In the spirit of examining the formation of exotic eutectic microstructures, the directional solidification technique is employed in order to explore the following three systems, which display diverse eutectic morphologies, i.e.,

- i) Exotic broken-lamellar structures in the Sn-Zn eutectic system;
- ii) Exotic two-phase eutectic colonies in Sn-Te system;
- iii) Exotic three-phase microstructures in the ternary Ag-Cu-Sb eutectic system.

The thesis is organized into seven chapters as follows:

The 1st current chapter contains an introduction and extensive review of the existing literature related to this thesis. The 2nd chapter concentrates on the design and development of directional solidification apparatus, while the 3rd chapter discusses the characterization tools used in the study. The 4th, 5th, and 6th chapters cover the results and discussions on the selected eutectic systems, and the thesis concludes with a summary and future prospects in chapter 7.

We first review the phenomenon-related eutectic solidification, starting with binary systems and extending the ideas to ternary systems. Subsequently, we discuss some critical factors that influence eutectic microstructures and conclude the chapter by discussing some exotic phases that generate fascinating eutectic morphologies.

---

<sup>2</sup>Property being direction-dependent

## 1.1 Eutectic equilibrium and microstructure

In eutectic systems, liquid coexists with two or more solids at the specified temperature(s) and composition(s). The maximum number of solid phases that can be in equilibrium with liquid is determined by the number of components in the system. For an invariant eutectic reaction, the compositions and temperature are fixed, whereas non-invariant eutectic reactions occur for a range of compositions and temperatures. Therefore, complicated situations arise with an increase in the number of components and phases (which are discussed in the subsequent section 1.2.3); hence, in this section, the binary eutectic is being used to elucidate the basic mechanisms of eutectic solidification. For the simple binary case, the liquid and two solid phases (typically called as  $\alpha$ ,  $\beta$ ) coexist at the eutectic composition ( $C_E$ ) and temperature ( $T_E$ ) as illustrated in Fig. 1.2a. Below the eutectic temperature ( $T_E$ ) based on the material and the experimental parameters, the eutectic liquid ( $C_E$ ) transforms into  $\alpha$  and  $\beta$ , i.e.,  $L(C_E) \rightarrow \alpha(C_\alpha) + \beta(C_\beta)$ . In this context, it is essential to comprehend the distinction between eutectic microstructure and eutectic equilibrium. As explained earlier, eutectic equilibrium refers to the coexistence of eutectic liquid with the solid phases; however, eutectic microstructure arises only when synchronous growth of solid phases happens, which is feasible when lateral solute transport in liquid, ahead of the solid phases occur easily. As a result, diffusion is important in determining the microstructural features of eutectics. Eutectic systems do not always produce eutectic microstructures, particularly at higher undercoolings or high Peclet numbers. Furthermore, compositions that are not eutectic (but close to eutectic) can also form eutectic microstructures (refer to Fig. 1.13, which depicts the formation of eutectic microstructures at eutectic and off-eutectic compositions); hence, the region of compositions/temperatures in a phase diagram that delivers eutectic microstructures is referred to as the coupled zone [45].

## 1.2 Formation of eutectic microstructures

Limited investigations are available on eutectic nucleation, and initial transitions [46, 47]; however, eutectic growth is thoroughly researched, and details are presented as follows. The following steps are necessary to attain steady-state growth conditions:

1. Mass diffusion of atoms in liquid (symbiotic exchange of atoms between the solid phases through the liquid medium).
2. Interface kinetics (transported atoms should be attached to the growing solid).

3. Heat conduction (released latent heat has to be taken away from the interface).

These processes occur in sequential order, and the slowest one controls the overall process. Limiting conditions can be mass/heat diffusion or interface kinetics; typically, for metallic systems, interface kinetics is often fast, and diffusion of species governs the eutectic morphology, whereas, in some semiconducting/non-metallic systems, interface kinetics is slow and impacts the solidification microstructures. In [1], Hunt and Jackson classified eutectic phases using a dimensionless entropy of fusion, i.e.,

$$\alpha_i = \xi \Delta S_f^i / R, \quad (1.1)$$

where  $\Delta S_f^i$  is  $i^{th}$  phase entropy of fusion,  $\xi$  is crystallographic parameter, and  $R$  is gas constant. According to them,  $\alpha > 2$  leads to formation of faceted solid-liquid interface (smooth interface), while  $\alpha < 2$  leads to formation of non-faceted solid-liquid interface (rough interface). Solidification of non-faceted/non-faceted phases exhibit regular periodic structures (typically, lamellar/ plate morphology of solid phases, or labyrinthine/curved-lamellar (chevron) morphology of solid phases, or minority phase as rod morphology in the majority phase, refer to Fig. 1.13 and 1.14); however, in systems having one of the phases as faceted can lead to complex or irregular structures (refer to Fig. 1.1a). In a faceted/faceted combination, both phases can grow independent of each other, leading to no regularity in the microstructure (refer to Fig. 1.1b). We start the discussion about each of them in the following sections beginning with non-faceted/non-faceted phases.

## 1.2.1 Formation of eutectic microstructures in binary systems

### 1.2.1.1 Binary eutectic with non-faceted interfaces

The discussion in this section is restricted to binary non-faceted isotropic systems where both the interface kinetics and thermal diffusion are rapid (thermal/kinetic effects are ignored), and thereby conditions correspond to lower velocities (lower Peclet numbers =  $\frac{\lambda V}{2D}$ ,  $V$  is the velocity and  $D$  the solute diffusivity) where growth is controlled by solute diffusion. For the eutectic transformation, liquid (of composition  $C_E$ ) changes into  $\alpha$  (of composition  $C_\alpha$ ) and  $\beta$  (of composition  $C_\beta$ ). For steady-state growth, once the  $\alpha$  phase forms, the extra B component in front of the  $\alpha/L$  interface should laterally diffuse away from A rich  $\alpha$  (diffusion paths are shown in the Figure 1.2b), leading to the formation of the B rich  $\beta$  phase. The process should

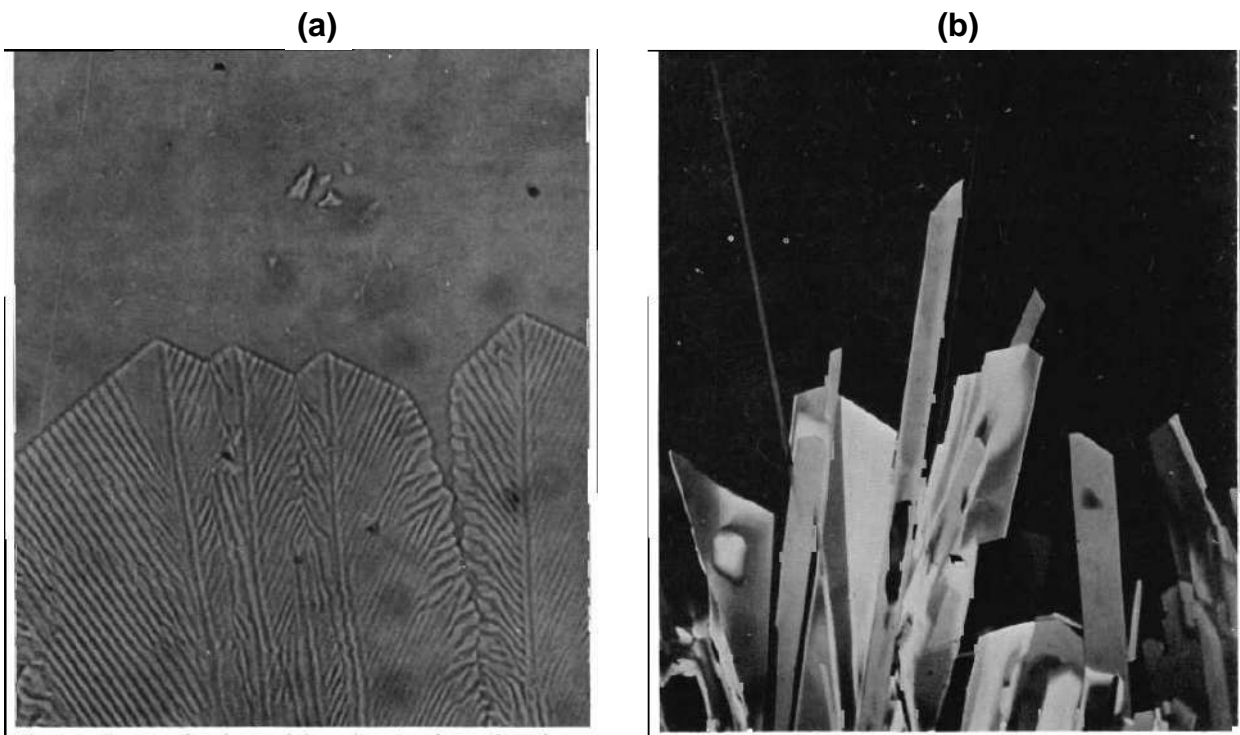
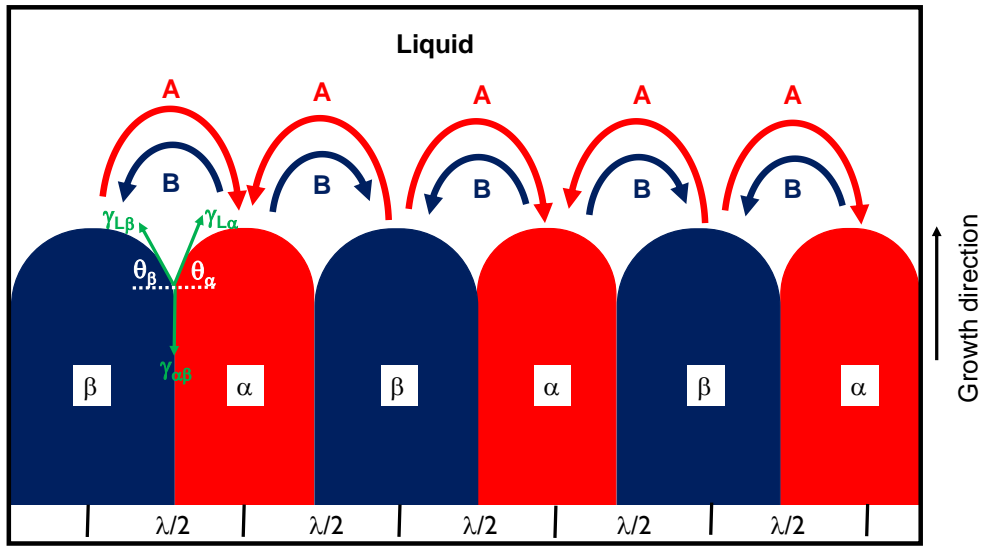
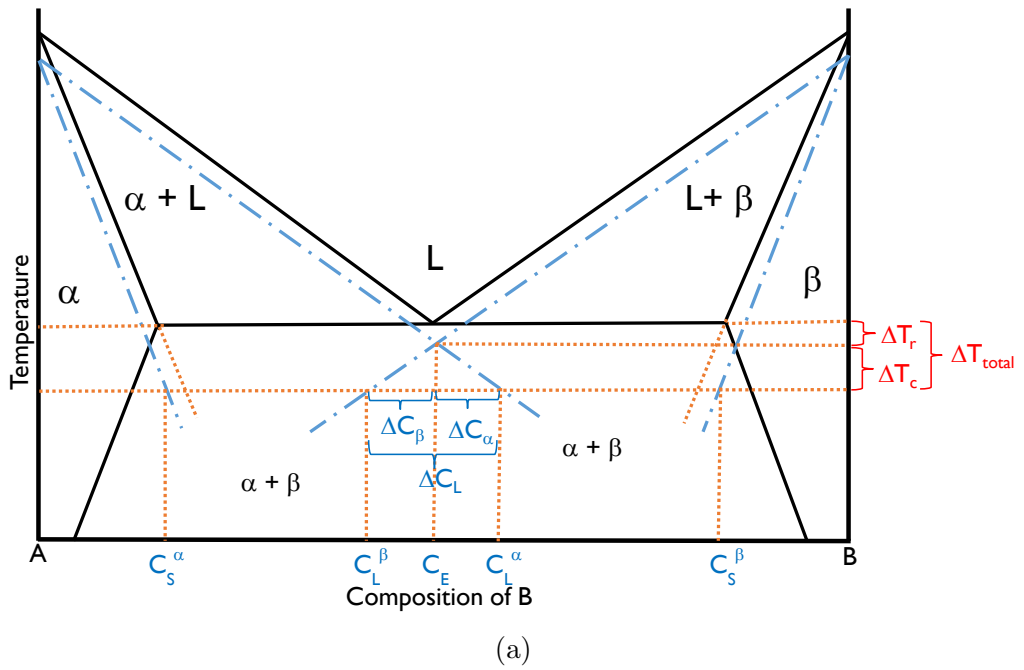


Figure 1.1: (a) The morphology of cyclohexane-camphene eutectic. The morphology of the solid-liquid interface exhibits a complex structure where one of the phases is faceted. (b) The morphology of the Azobenzene-benzil eutectic consists of two faceted phases (adopted from [1]). The growth direction is from bottom to top.



(b)

Figure 1.2: A typical binary eutectic phase diagram is shown in (a), where the dashed lines show local equilibrium conditions, while, the dotted lines are used to show the undercooling requirement for diffusion and interface energy. (b) shows schematic of eutectic interface with diffusion pathways of the components and force balance at the trijunction.

happen vice-versa in a coupled fashion leading to the simultaneous growth of the phases. As a result, lateral coupled diffusion of A and B components with a diffusive boundary layer (half the eutectic spacing) is necessary for eutectic growth. Otherwise, rejected species might form a solutal boundary layer ahead of the solid-liquid interface, causing the eutectic front to destabilize, and examples of uncoupled eutectics can be found in the literature [48].

Further, length scales associated with eutectic phases for growth at lower Peclet numbers are of the order of micrometres (due to diffusion-limited growth); thus, interfacial area per unit volume is substantial, and force balance (mechanical equilibrium) at the trijunctions (where three-phases meet) makes the solid-liquid interfaces curved as illustrated in Fig. 1.2b, which necessitates the following condition for isotropic situations:

$$\gamma_{\alpha\beta} = \gamma_{\alpha L} \sin\theta_\alpha + \gamma_{\beta L} \sin\theta_\beta. \quad (1.2)$$

where,  $\gamma_{\alpha\beta}$  is solid-solid interfacial free energy,  $\gamma_{L\beta}$  is solid-liquid interfacial free energy of  $\beta$ ,  $\gamma_{L\alpha}$  is solid-liquid interfacial free energy of  $\alpha$ ;  $\theta_\alpha$ ,  $\theta_\beta$  are the angles the  $\alpha$ -liquid and the  $\beta$ -liquid tangents make with the horizontal, respectively, as shown in Fig. 1.2b. The curvature alters the equilibrium conditions at the interface, and the modified conditions are illustrated as the dashed lines in the phase diagram shown in Fig. 1.2a. Hence, the following criteria determine the characteristics of the steady-state solution for a regular non-faceted eutectic growth:

- i) mass diffusion of required components in the liquid,
- ii) conservation of mass at the solid-liquid interface (Stefan boundary condition),
- iii) interfaces need to be in local equilibrium as per capillarity induced curvature (Gibbs–Thomson equation), and
- iv) force balance at the trijunctions (Young's equation).

Jackson and Hunt (JH) [2] established a steady-state solution for two different morphologies, i.e., rod and lamellar, with the following assumptions:

- i) The eutectic spacing was assumed to be much lesser than the diffusion length scale in the liquid; (this implies lower Peclet number)
- ii) The diffusion field solution is obtained by assuming a flat and isothermal interface,
- iii) Solid-solid interface is perpendicular to solidification front
- iv) Diffusion in solid phases is ignored,
- v) For the computation of the average undercooling at the solidification interface average interfacial undercooling was considered to be equal for both phases, i.e.,  $\Delta T = \Delta T^\alpha = \Delta T^\beta$ .

In Ref. [2], JH calculated the average interfacial undercooling for each solid phase as the sum of the solutal and curvature undercooling, i.e.,

$$\Delta T^j = \Delta T_r^j + \Delta T_c^j; j = \alpha(\text{or})\beta. \quad (1.3)$$

where,  $\Delta T$  is the total undercooling,  $\Delta T_r$  is the curvature undercooling, and  $\Delta T_c$  is the solutal undercooling.

The curvature undercooling is determined by multiplying the average curvature with the Gibbs-Thomson coefficient as

$$\Delta T_r^j = \Gamma^j \bar{\kappa}_j; j = \alpha(\text{or})\beta. \quad (1.4)$$

where  $\Gamma$  is the Gibbs-Thomson coefficient ( $\gamma/\Delta S$ ),  $\gamma$  is the solid-liquid interfacial energy,  $\Delta S$  is entropy of fusion,  $\kappa$  is the curvature of the interface. The solutal undercooling is determined by multiplying average liquid composition ahead of the solid-liquid interface with liquidus slope as

$$\Delta T_c^j = |m^j| \bar{\Delta C}_j; j = \alpha(\text{or})\beta. \quad (1.5)$$

where  $m$  is liquidus slope,  $\bar{\Delta C}$  is average liquid composition obtained by solving steady-state diffusion equation. By adding both the contributions, JH provided a relationship between undercooling and eutectic scaling for a given velocity for both morphologies, i.e., lamellar (L) and rod morphology (R) as

$$\Delta T = K_1 V \lambda + K_2 / \lambda. \quad (1.6)$$

where  $K_1$  and  $K_2$  are constants which depends on the morphology and the material parameters. For the lamellar morphology,

$$K_1^L = \bar{m} C_o P / f_\alpha f_\beta D \quad (1.7)$$

and

$$K_2^L = 2\bar{m} (\Gamma_\alpha \sin \theta_\alpha / f_\alpha m_\alpha + \Gamma_\beta \sin \theta_\beta / f_\beta m_\beta), \quad (1.8)$$

where  $C_o = (C_\alpha - C_\beta)$  ( i.e  $C_o$  is the composition difference between of the solid phases at the eutectic temperature),  $f_\alpha, f_\beta$  are the volume fractions of the solid-phases,  $1/\bar{m} = (1/m_\alpha + m_\beta)$ ,  $m_\alpha, m_\beta$  are the liquidus slopes of the solid phases.  $\Gamma_\alpha$  and  $\Gamma_\beta$  are the Gibbs-Thomson coefficients of the solid and the liquid phases while the  $\theta_\alpha$  and  $\theta_\beta$  are angles the  $\alpha$ -liquid and the  $\beta$ -liquid

tangents make with the horizontal.

$$P = \sum_{n=1}^{\infty} \frac{1}{(n\pi)^3} \sin^2(n\pi f_\alpha) \quad (1.9)$$

Similarly for rod morphology,

$$K_1^R = \bar{m} C_o M / f_\beta D, \quad (1.10)$$

where

$$M = \sum_{n=1}^{\infty} \frac{1}{(\gamma_n)^3} \frac{J_1^2(\sqrt{f_\alpha} \gamma_n)}{J_0^2(\gamma_n)}, \quad (1.11)$$

where  $\gamma_n$  is the  $n$ -th zero of the first order Bessel function  $J_1$ , while  $J_0$  is the zeroth order Bessel function.

$$K_2^R = K_2^L \sqrt{f_\alpha} \quad (1.12)$$

This allows us to determine the  $\Delta T$  vs. spacing  $\lambda$  relationship for both morphologies.

### Lengthscale selection:

Tiller [49] proposed that the spacing ( $\lambda_m$ ) corresponds to the least amount of undercooling at the interface and suggested that under directional solidification conditions as illustrated in Fig. 1.3, this would be the spacing that would be selected. However, even though the minimal undercooling criterion provides a unique solution, there is no physical reason why a system would have to choose this value. Jackson and Hunt propose physically motivated arguments based on the eutectic front stability and commented based on the shapes of the interface the regime of stable spacings that would be observed in experiments [2]. They demonstrated that the spacings less than minimum undercooling spacing (say  $\lambda_m$ ) are unstable because depression in the interface causes the deletion of a lamella as illustrated in Fig. 1.4a,b, and then local spacing increases. However, for the spacing much greater than  $\lambda_m$  (say beyond  $\lambda_M$ ), a pocket arises in the middle of the broader phase as illustrated in Fig. 1.4c, where a new lamella arises because of instabilities (refer to Fig. 1.4d,f). Thus they concluded that there exists a spacing range  $\lambda_m < \lambda_m < \lambda_M$ , which would be stable for a given velocity. Later, in [50], the authors demonstrated experimentally that the average spacing will always be greater than minimum undercooling spacing  $\lambda_m$ . Moreover, they observed that by decreasing solidification velocity, the minimum value on the undercooling vs. spacing gets shallower, leading to the

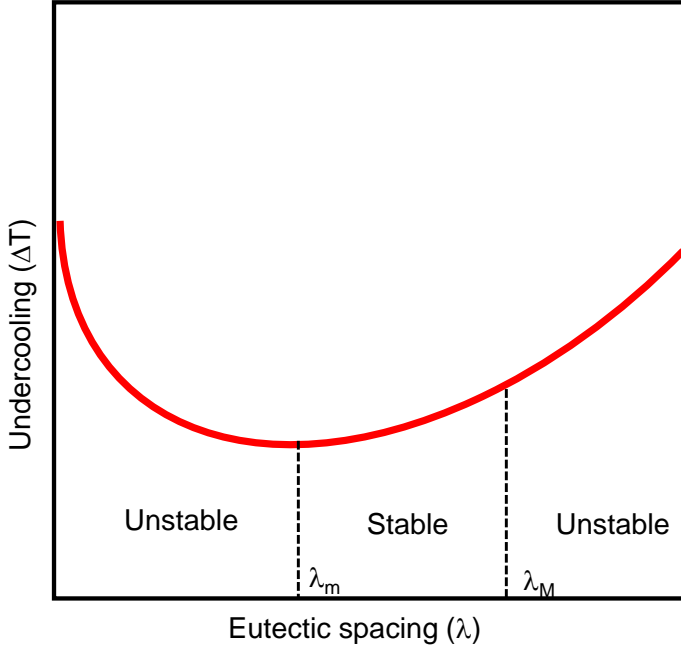


Figure 1.3: The average undercooling with eutectic spacing for a particular velocity and regions corresponding to stable and unstable as per Jackson and Hunt theory [2].

increase in the stability range of spacings. In [51], authors studied rod morphologies and found a rod termination mechanism for the lower limit of spacing and a branching mechanism for the higher limit of spacing, while in [52], authors studied lamellar morphologies and found faster decay of spacing perturbations when the spacing approaches  $\lambda_m$ . Langer [53], performs a stability analysis of a lamellar array to long-wavelength perturbations in spacing and calculated the conditions for stability. Langer [53] concluded that the minimum undercooling spacing ( $\lambda_m$ ) is the marginal stability point where spacings lower than  $\lambda_m$  are unstable to elimination through the Eckhaus instability [54], while spacings larger are prone to oscillatory and other morphological instabilities in thin-film and bulk solidification conditions respectively, thereby limiting the observable spacings in a range around the minimum undercooling spacing. Thus, the minimum undercooling spacing is a physical scale in the eutectic solidification problem, which can be thought about as the spacing where the influence of the capillarity and diffusion are balanced. Further, the minimum undercooling spacing follows the scaling relation ( $\lambda_m$ ) and velocity (V), i.e.,

$$\lambda_m^2 V = \frac{K_2}{K_1}. \quad (1.13)$$

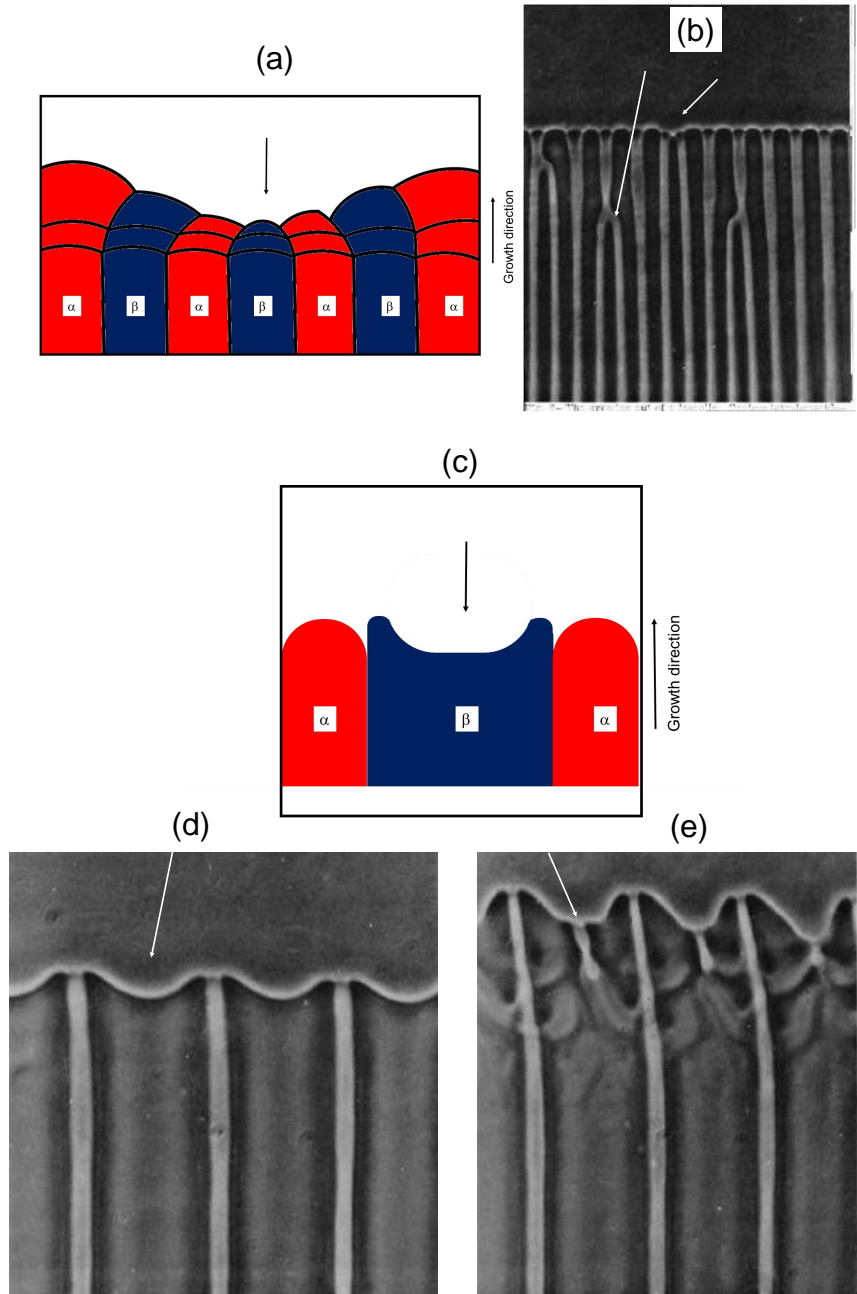


Figure 1.4: (a) Schematic to illustrate the instability for  $\lambda < \lambda_m$  that causes the disappearance of lamella in the center. (b) The experimental shows the lamella narrowing and falling below the average interface position until other lamellae cover it. (c) Schematic to show the depressed region that arises for  $\lambda_M < \lambda$ . (d), (e) are experimental images taken in sequence to show the formation of the new lamella, where (d) exhibit the formation of pocket in the center of the broader phase, and eventually with time, (d) changes to (e) where we can observe the formation of the new lamella. The images (b), (d), (e) corresponds to carbon tetrabromide - hexachloroethane eutectic and are adopted from [1]. The growth direction is from bottom to top.

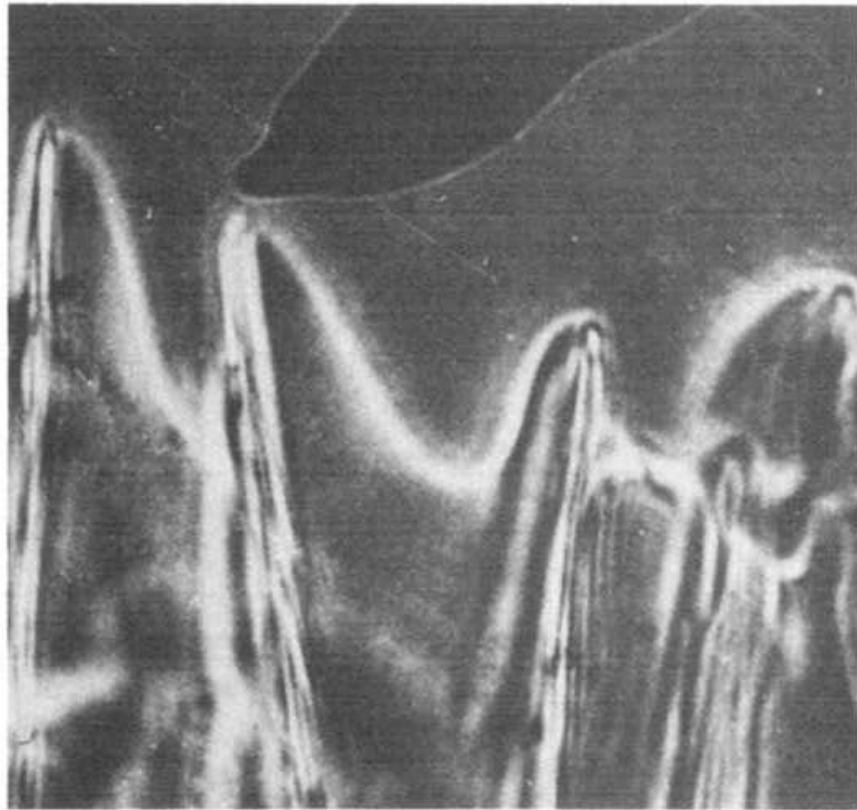


Figure 1.5: The solid-liquid interface of borneol-succinonitrile (faceted/non-faceted), the dark feature is a thermocouple (adopted from [3]). The growth direction is from bottom to top.

Experimentally, however, spacings lower than the minimum undercooling spacing are also observable. Akamatsu et al. [55, 56] experimentally and theoretically using phase-field simulations illustrate that, indeed, there exist stabilizing mechanisms by which spacings even lower than  $\lambda_m$  could become stable to spacing perturbations. For more details about various spacing adjustment mechanisms, refer to [57, 58, 59, 60, 61, 62, 63].

### 1.2.1.2 Binary eutectic with faceted interfaces

When one of the phases is faceted, due to the restricted growth behavior of the faceted phase (due to growth kinetics), the minimum undercooling spacing ( $\lambda_m$ ) becomes larger compared to binary non-faceted eutectics. However, the analysis performed for the non-faceted eutectics (refer to previous section 1.2.1.1) has neglected the kinetic undercooling term that would need to be considered in the case of faceted eutectics in calculating total undercooling. In Ref. [3], Fisher and Kurz presented a model that describes irregular eutectic growth; some of the salient

points are as follows. The two-phase (faceted/non-faceted) eutectic front is non-isothermal. If the two neighboring faceted lamellae deviate as shown in Fig. 1.5, an increase in spacing leads to the development of negative curvature on the non-faceted to compensate for the rise in solutal undercooling. Therefore, the eutectic front becomes non-isothermal as undercooling continuously increases until curvature can compensate for it. This implies that the faceted phase initiates the solidification process due to lower undercooling, further extending into the melt. As illustrated in Fig. 1.5, the non-faceted phase lags but expands along the sides of the faceted flakes at their growing edges. However, this model has been contradicted by McLeod et al. [64], who proposed that non-faceted phase can nucleate heterogeneously and frequently on the faceted flakes. Thus, according to McLeod et al. [64], the polycrystallinity [65, 66, 67] of the non-faceted phase in irregular eutectics could be clarified by using the re-nucleation phenomenon.

Before commencing the discussion on the multi-component eutectic solidification, it is worth revisiting the concepts related to the formation of morphological instabilities in the case of single-phase. Therefore, in the following section, we briefly present the relevant concepts and then start discussing multi-component systems.

### 1.2.2 Morphological instability of single phase

Consider a liquid of binary alloy (with solute composition as  $C_o$ ) as shown in Fig. 1.6c. The first solid that nucleates will be of composition  $kC_o$ . Under directional solidification conditions where a positive thermal gradient( $G$ ) is imposed across the interface and translated with velocity ( $V$ ), the composition of the solid will continuously increase from its initial value of  $kC_o$ , while the rejected solute due to the solidification of a solid leaner in the solute will enrich the liquid leading to the formation of a composition boundary layer. It can be shown that for a planar solidification front that a steady-state composition boundary layer develops at the solidification interface where the composition of the liquid becomes  $C_o/k$  and decreases exponentially to the value of  $C_o$  far from the interface, which is the far-field composition, while the composition of the solid becomes equal to the value of the far-field liquid composition. This is the situation described in Fig. 1.6a. The presence of this composition boundary layer lends to the instability of the planar interface to morphological perturbations. This instability in the system can lead to the formation of cellular or dendritic structures depending on the imposed conditions. In a nutshell, the stability of the interface under directional solidification conditions depends on the

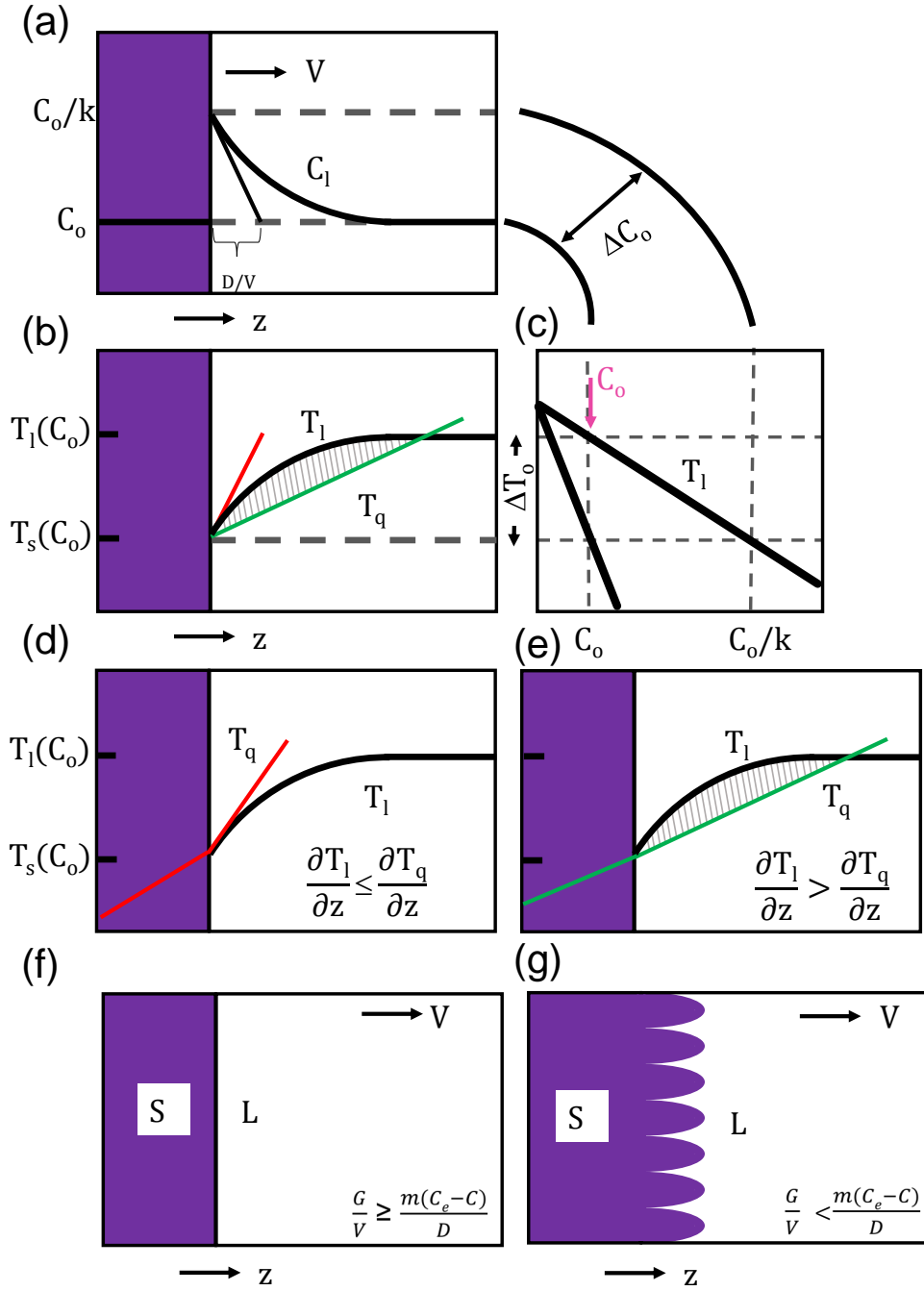


Figure 1.6: Schematics to show the conditions for the formation of instabilities in the case of single-phase solidification. (a) shows the composition profile having diffusion boundary layer ( $D/V$ ), (b) is melting temperature profile corresponding to each composition for two imposed temperature gradients shown by red and green color. The highlighted region corresponds to constitutional supercooling that leads to instabilities. (c) is a part of the phase diagram for the alloy under consideration. (d) shows imposed gradient larger than liquidus temperature leading to the formation of the planar front as shown in (f), while for (e), imposed gradient is smaller than liquidus temperature leading to the formation of instabilities as shown in (g).

balance of the forces destabilizing the interface, which is the imposed velocity (that essentially controls the strength of the concentration gradients in the liquid at the solidification interface) and the forces stabilizing the interface that are the capillarity and the positive thermal gradient. This can be qualitatively understood through the following argumentation. Depending upon the magnitudes of the thermal gradient and the velocity, two situations can arise, as shown in Fig. 1.6d, e. If the imposed gradient is less than the gradient of the melting point of the compositions ahead of the solidification interface, a layer of liquid around the interface will have a temperature lower than its melting point leading to constitutional supercooling. An approximate measure of the stability of the interface can be ascertained based upon this observation and is known as the constitutional supercooling limit, which essentially states that the presence of undercooled liquid ahead of the solidification front makes the interface unstable to morphological perturbations. Therefore, the critical gradient  $G$  ( $\frac{dT_q}{dz}$ ) to avoid constitutional supercooling is  $G \geq \frac{dT_l}{dz}$ . This concept was proposed by Tiller et al. [68], where the undercooled regime forms based on  $\frac{G}{V}$  ratio as

$$\frac{G}{V} \geq \frac{m\Delta C_o}{D}, \quad (1.14)$$

where  $m$  is liquidus slope,  $D$  is diffusivity,  $\Delta C_o$  is the difference between equilibrium composition and far-field composition. While this analysis leads to an understanding of the instability, it is only approximate as this does not consider the influence of capillarity. A more complete analysis is proposed by Mullins and Sekerka [69] who have performed a linear stability analysis by considering infinitesimal sinusoidal perturbations of the interface and demonstrated that a constitutionally supercooled interface is stable for extremely long wavelengths due to the solute's large diffusion distances and for extremely short wavelengths due to capillarity, but unstable for all wavelengths in between. The stability of the solidification front depends on three different length scales, i.e., diffusive ( $l_d$ ), capillary ( $d_o$ ), and thermal ( $l_T$ ), which can be expressed as

$$l_d = \frac{D}{V}, \quad (1.15)$$

$$l_T = \frac{m\Delta C_o}{G}, \quad (1.16)$$

$$d_o = \frac{\gamma_{sl}T_m}{mL\Delta C_o}, \quad (1.17)$$

where  $L$  is latent heat of fusion,  $T_m$  is melting temperature,  $\gamma_{sl}$  is solid-liquid interfacial energy and other terms are as defined in the previous discussion. A criterion of stability may be determined using the diffusion and thermal length scales for the case of considerably larger perturbations where capillarity terms do not become prominent. The threshold condition for stability of interface in such cases can be written as

$$l_T \leq l_d, \quad (1.18)$$

$$\text{i.e., } \frac{m\Delta C_o}{G} \leq \frac{D}{V} \quad (1.19)$$

After rearranging the terms, we get the following equation.

$$\frac{G}{V} \geq \frac{m\Delta C_o}{D}, \quad (1.20)$$

which is the same as the constitutional supercooling limit. The elegance of this equation is that left-hand side terms are process parameters, while right-hand side terms are material parameters. However, the Mullins-Sekerka analysis also predicts the entire dispersion curve where the growth rates of all possible perturbations as a function of the wavenumber can be derived which also includes the influence of capillarity. The analytical formulations derived by them are validated using dynamical phase-field simulations [70].

### 1.2.3 Formation of eutectic microstructures in multi-component systems

Solidification microstructures become increasingly complex and interesting in multi-component and multi-phase systems [24, 23, 25]. Ternary systems are useful model alloys for studying multi-component solidification, wherein uni-variant two-phase solidification and invariant three-phase solidification are possible in eutectic systems that provide insights into the microstructures and their distribution as a function of alloy composition and processing conditions. The different phase reactions expected in a simple ternary eutectic system are schematically described in Ref. [4] and are shown in Fig. 1.7, which provide multiple avenues for microstructural engineering. The possible morphologies include combinations of stable front and instabilities that consist of single-phase, two-phase, and three-phase as shown in Fig. 1.7. Further, they examined

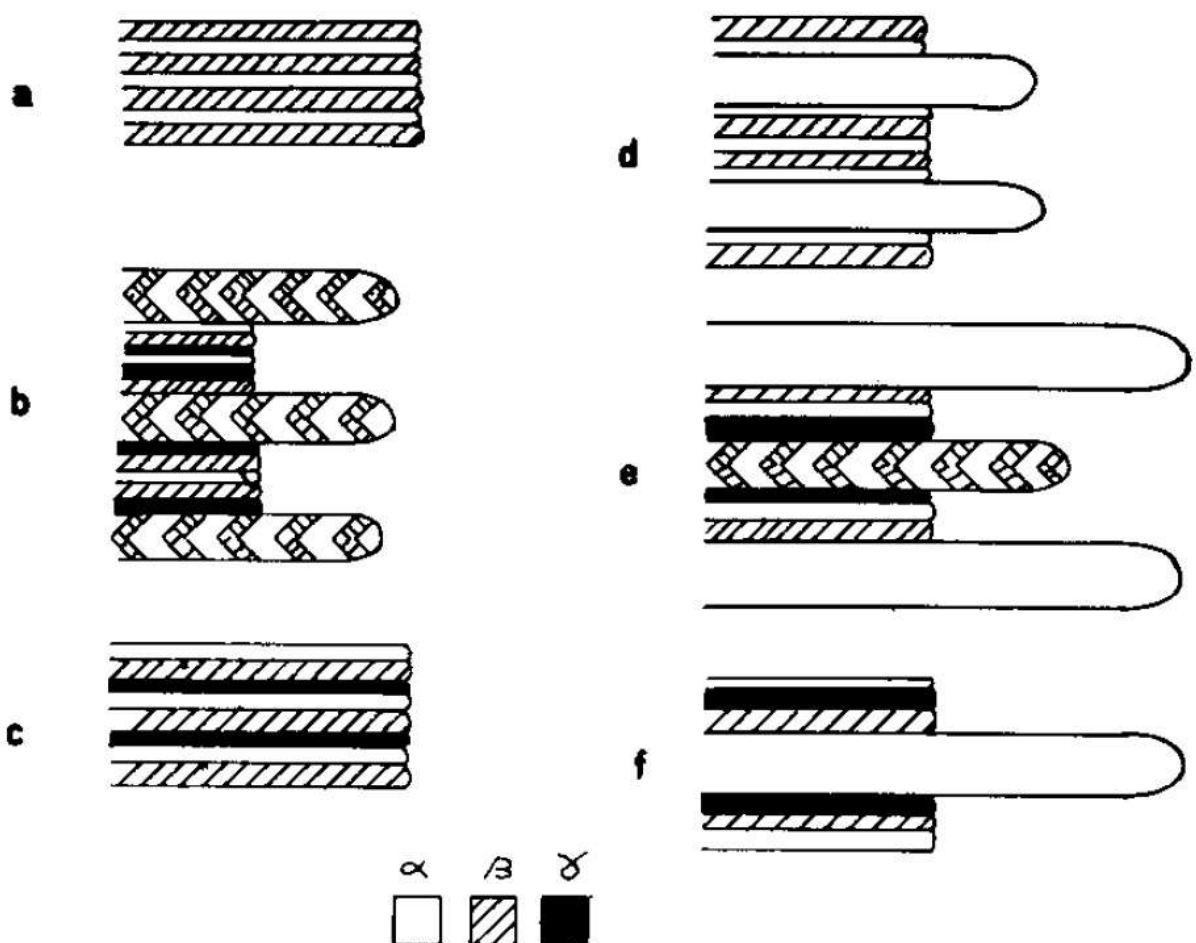


Figure 1.7: Schematic of different reactions, (a)stable two-phase, (b)two-phase cells with ternary eutectic, (c) stable three-phase eutectic, (d) single phase instability with two-phase eutectic, (e) single phase and two-phase instabilities with three-phase eutectic, and single phase instabilities with three-phase eutectic (adopted from [4]). The growth direction is left to right.

these predictions by conducting experiments at various compositions and confirmed the regions of existence in the phase diagram qualitatively [71]. The understanding gained from these investigations will enable alloy and process design in more complex multi-component eutectic systems. To demonstrate the intricacies involved in the ternary systems, we have selected a simple ternary phase diagram that contains three binary eutectics, and it is schematically shown in Fig.1.8. The ternary phase diagram in Fig. 1.8 shows an increase in the degree of freedom (in comparison to the binary phase diagram) by transforming equilibrium points into lines and lines into surfaces. In this simple ternary phase diagram, uni-variant equilibrium binary eutectic lines start from the invariant binary and meet at the invariant ternary eutectic, wherein four-phase (three-solid, one liquid) are in equilibrium. Due to the complexity of the three-dimensional ternary phase diagrams, liquidus projection diagrams and isothermal sections are typically used to predict the equilibrium aspects. The phase diagram shown here for illustration is a simple one; however, in reality, ternary phase diagrams can much more complex and can lead to much complex microstructure formation.

### 1.2.3.1 Two-phase growth in ternary systems

During the solidification of all the compositions on the univariant line, we observe either the formation of a stable/uniform eutectic front or destabilization of the eutectic front depending on the processing/ material parameters. The destabilization of the eutectic front resulting in the formation of eutectic colonies with a scale much larger than that of the eutectic scaling due to the formation of a solutal boundary layer ahead of the solid-liquid interface as a result of solute(s) rejected by the eutectic phases, which is similar to Mullins-Sekerka instability [69] that is discussed in section 1.2.2. Typically the instability occurs beyond a critical velocity (for a fixed temperature gradient and alloy composition) which can be determined using constitutional-supercooling concepts [72]; however, eutectics possess more complexity due to its inherent nonlinear growth dynamics. The formation of such cells is observed experimentally in Ref. [1, 73, 74, 75, 76, 77] and using phase-field simulations in Ref. [31, 78, 79].

M. Plapp and A. Karma [80] conducted a linear stability analysis for a lamellar eutectic front with a third component solutal boundary layer ahead of the solid-liquid interface and found that the formation of eutectic growth front instability is fundamentally very similar to single-phase instability; [69]. Later dynamical phase-field simulations [78] by the same authors confirmed the theory and provided some exciting results in isotropic systems. They demonstrate that the

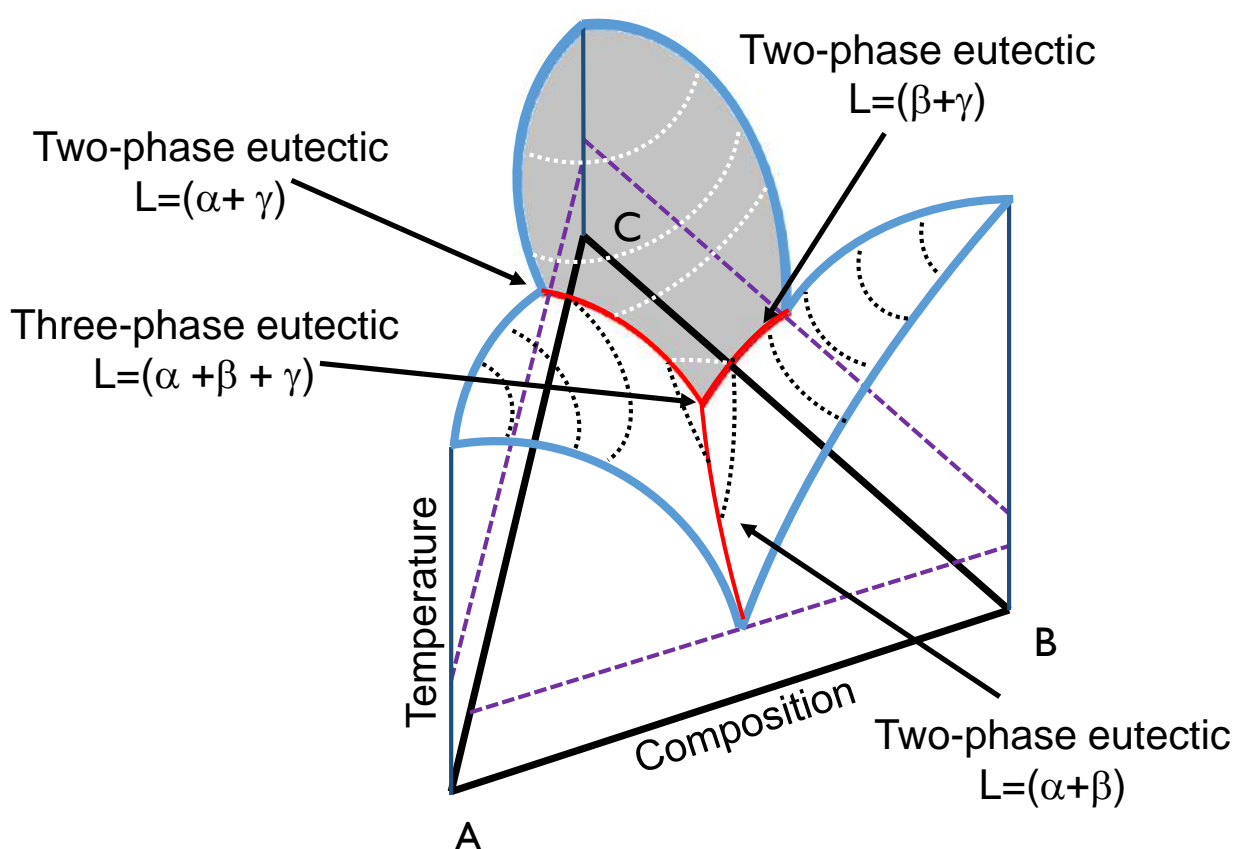


Figure 1.8: Schematic of a simple ternary phase diagram that contains three-binary eutectics.



Figure 1.9: Morphology of eutectic colonies in the camphor-succinonitrile system consists of an unknown impurity (adopted from [1]). The growth direction is from bottom to top.

two-phase colonies in an isotropic system are unstable, that don't have well-defined orientations and length scales that constantly widen and split, like cells in single-phase materials. Further, such colonies typically have cellular shapes with the lamellae, locally growing perpendicular to the solidification envelope. Exotic structures with the two phases spiraling during growth as a colony have also been observed in both experiments and simulations [76, 81, 79]. In Ref. [82], Akamatsu et al. illustrate the tip radius of the spiral eutectic linearly scales with  $V^{-0.5}$  ( $V$  is velocity), which is analogous to a single-phase dendrite.

### 1.2.3.2 Three-phase growth in ternary systems

The three-phase morphologies that arise during the invariant reaction, i.e., liquid transforming into three-solid phases, are examined in this section. Examples of three-phase microstructure formation are elaborated in a literal form in Ref. [6]. These possibilities in three-phase eutectics are based on geometrical arguments (combinations of rod and lamellar morphologies) and are schematically shown in Fig. 1.10 taken from the Ref. [5]. However, in reality, the structures observed are much more complicated, and the physical basis for their formation is not clarified. Using the well-established Jackson and Hunt theory [2] developed for binary systems, Himemiya et al. [83] has derived analytical equations between undercooling with spacing for a given velocity for different morphologies that include lamellar, rod with hexagon, and semi-regular brick. Further, those theoretical concepts are extended in other works [84, 85, 86]. Invariant three-phase growth dynamics has been explored in Ag-Al-Cu [87, 88, 7, 89, 90], Al-Ni-Nb [91, 92, 93, 8], Ag-Cu-Sn [5, 94, 95], Bi-In-Sn [6, 96, 97, 98, 99, 100, 101, 102, 103, 104] systems. Some of the studies involving spacing selection mechanisms for three-phase eutectics are as follows. The effects of process and material conditions on the tilt angle of ternary eutectics during directed solidification were investigated using phase-field simulations in Ref. [105], where authors found that for a given spacing, a high tilt angle is possible in cases where interface energy ratios are high, for lower diffusivities and velocities. Dynamics of spacing adjustment and recovery mechanisms of  $\alpha\beta\alpha\gamma$  three-phase patterns in ternary systems are studied in Ref. [100, 104]. In [104], authors observed complicated  $[\alpha\beta]_m[\alpha\gamma]_n$  patterns, and the patterns that do not have mirror symmetry, i.e.  $\alpha\beta\gamma$ , are also observed during initial transient conditions, which additionally also grow tilted. Lamellar spacing variation and different stability ranges of the initially set microstructure of ternary eutectics are studied in Ref. [106].

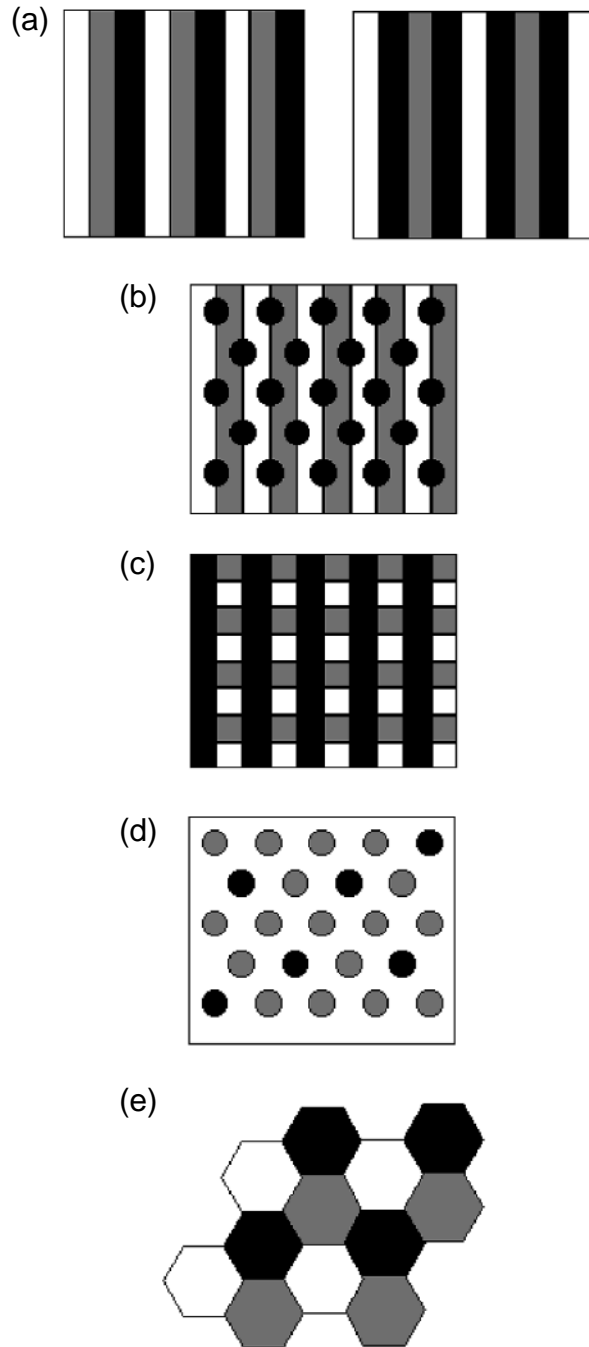


Figure 1.10: The schematics of three-phase morphologies taken from [5] as verbally listed by Ruggerio and Rutter [6], where (a) consists of three phases as lamellar morphology, (b) consists of one phase as rod and two phases as lamellar, (c) consists of two phases as rod and one phase as lamellar, (d) consists of two phases as a rod in a continuous matrix, and (e) consists of three phase as rod morphology. (a) consists of two types of lamellar arrangements. Schematics correspond to the transverse sections.

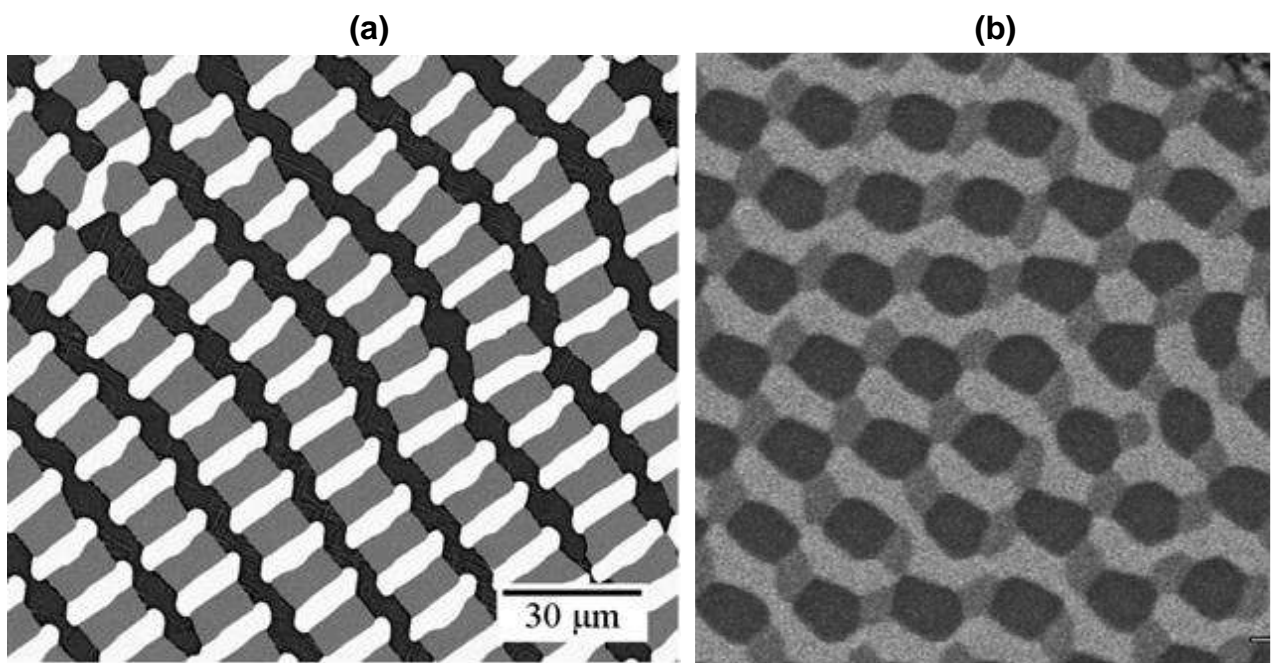


Figure 1.11: Typical three-phase transverse section microstructures (growth direction is perpendicular to the plane of view), (a) is a microstructure of ternary eutectic in Ag-Al-Cu system (adopted from [7]), (b) is a microstructure of ternary eutectic in Al-Nb-Ni system (adopted from [8]).

## 1.3 Factors influencing eutectic microstructures

Some of the factors that influence the eutectic microstructure are discussed in the following subsections.

### 1.3.1 Processing variables

#### 1.3.1.1 Sample size

The sample's size impacts the microstructure [107, 108], especially when the size is close to the length scale range of the phenomena. Akamatsu et al. [63], Serefoglu et al. [109, 110, 111] have shown the influence of sizes (when comparable to that of eutectic spacing) on the eutectic morphology and length scales associated.

#### 1.3.1.2 Temperature gradient

The magnitude and direction of the temperature gradient play a vital role in forming eutectic microstructures. For example, the magnitude of the thermal gradient can be a critical factor in deciding the stability of the solidification front for the case of non-invariant growth (refer section 1.2.2). Similarly, the thermal gradient direction is also essential as it can modify the growth direction, and we adopted this strategy in our quartz bend experiments of section 4.2.3. Further, a transverse gradient in the sample can change the morphology of the labyrinth to lamellar [112]. Furthermore, phase-field simulations reveal the emergence of rod-lamellar transitions in the presence of tilted temperature gradients [113].

#### 1.3.1.3 Velocity

The velocity of the solidification impacts the formation of microstructure in several ways. First of all, the length scale associated with the microstructure is a strong function of the velocity. As discussed in section 1.2.1.1, velocity determines the stability range of eutectic spacing [50]. Moreover, certain eutectic systems exhibit morphological transitions with the change in velocity [114]. One such example that exhibits variations in eutectic microstructure is shown in Fig. 1.12. These are some of the microstructural attributes that get influenced by velocity; however, the scope of microstructural changes achieved with velocity is enormous that varies from system to system, which are not possible to cover in the scope of this thesis.

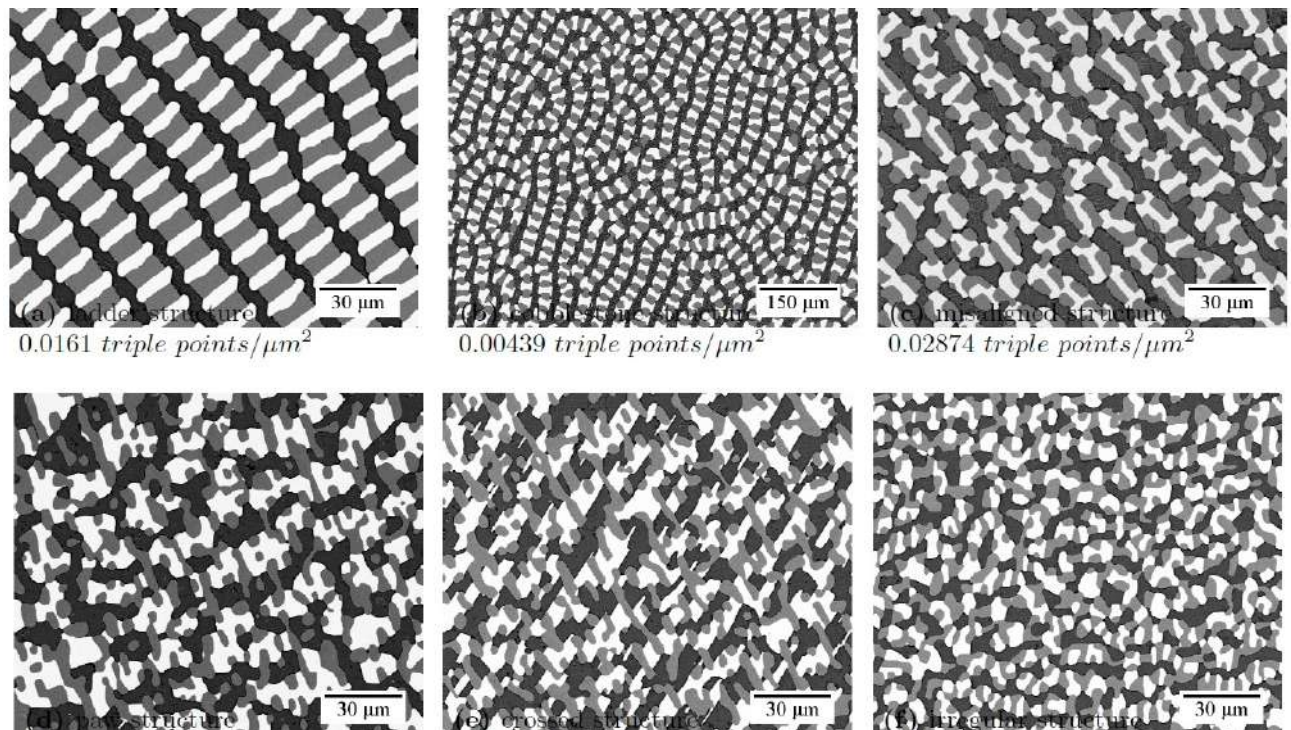


Figure 1.12: Variations in Ag-Al-Cu eutectic microstructure due to change in velocity (adopted from [7]). The image corresponds to the transverse section where the growth direction is perpendicular to the plane of view.

### 1.3.2 Volume percentage of phases

The liquid composition is one of the significant factors in multi-component systems as it influences the volume percentage of the phases during invariant reactions. The volume percentages of the phases that are dynamically selected during the eutectic reaction is one of the critical factors influencing morphological change during eutectic growth. The volume percentages of the phases are usually close to the value obtained by the mass balance between the far-field liquid and solid-phase compositions at the eutectic temperature (accurate only for low solidification velocities, i.e., low Peclet numbers), which depend on the solidification conditions and the mobilities of the elements.

#### 1.3.2.1 In two-phase eutectics

Typically for two-phase evolution in binary eutectics, rod morphologies are observed for lower percentages of the minority phase; in contrast, a lamellar/labyrinthine morphology is observed for near equal volume percentages. Experimental evidence of this is shown by Trivedi et al. [9] in the Al-Cu alloy where various microstructures with change in the far-field compositions are obtained that consist of a rod, lamellar, and mixed growth forms shown in Fig. 1.13. While energetic discussions by Cooksey et al. [115] and others lead to critical values of the volume percentages demarcating the regions of stability of the rod and the lamellar morphologies, this has not been experimentally verified, and examples to the contrary are available, notably from dynamical phase-field simulations. Simulation studies by Plapp et al. [10] and Gránásy et al. [116] reveal that there is no clear unique volume percentage where the rod-lamellar transition occurs and there are volume percentages (for different liquid compositions) where mixed-morphologies may be observed. Fig. 1.14 illustrates the rod-lamellar (and vice versa) transitions with the change of volume percentage in the isotropic system. Furthermore, the rod-lamellar transition is shown to be dependent on the history of the solidification process [10], and thereby, there is no pattern selection in the strong sense as a function of change in the volume fraction of the phases.

#### 1.3.2.2 In three-phase eutectics

For the case of three-phase growth, Choudhury [11] has demonstrated the influence of volume percentage in three-phase structure formation using phase-field simulations for isotropic solid phases, wherein connectivity or coordination among the phases changes as a function of volume

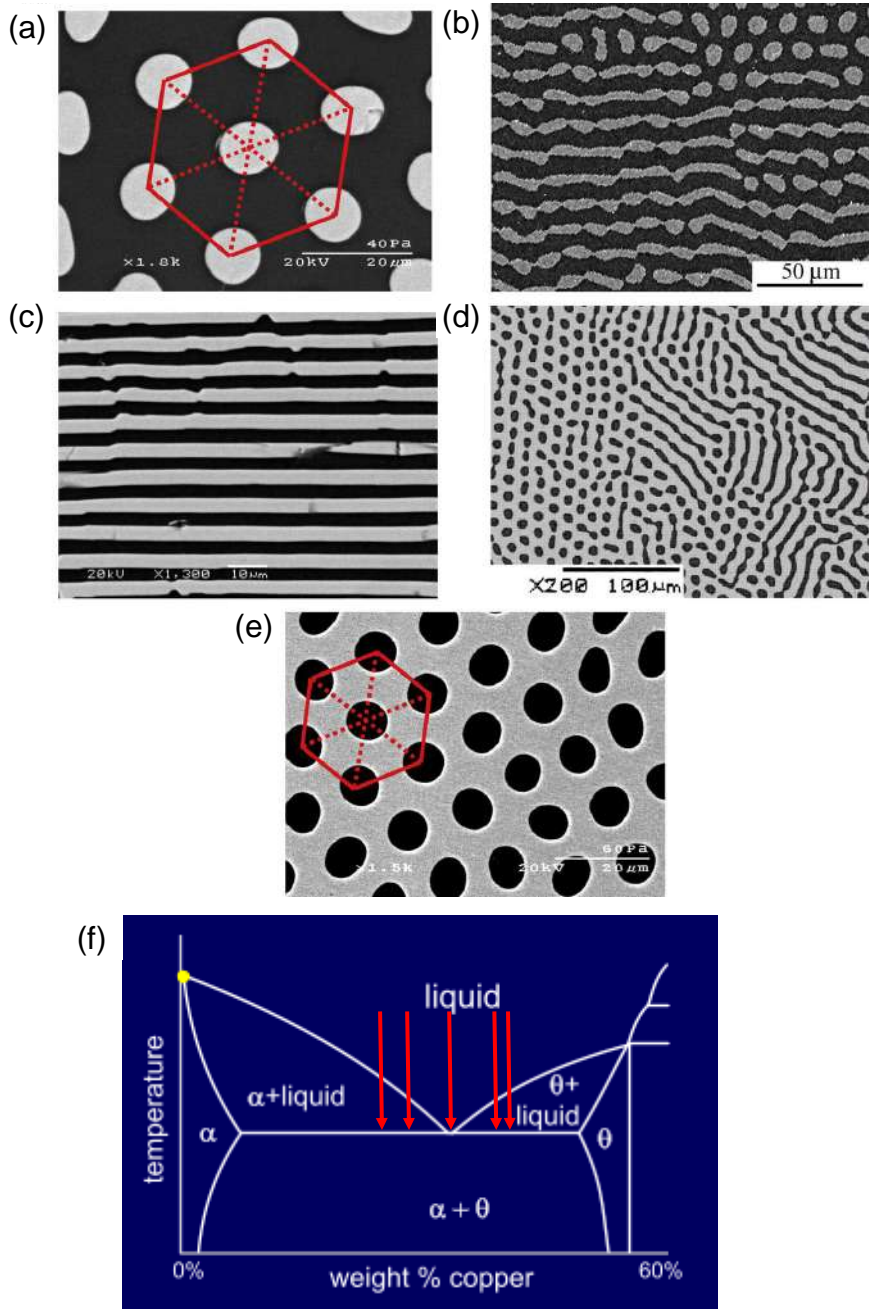


Figure 1.13: Different eutectic microstructures (growth direction is perpendicular to the plane of view) for different compositions in the aluminum-copper system that are adopted from [9] (phase diagram is shown in (f)), where (a) is Al-19.5 wt.% Cu alloy that exhibits  $\text{Al}_2\text{Cu}$  rods in ( $\text{Al}$ ) matrix, (b) is Al-24.0 wt.% Cu alloy that exhibits coexistence of  $\text{Al}_2\text{Cu}$  rods and lamellae in ( $\text{Al}$ ) matrix, (c) is Al-33.2 wt.% Cu alloy that exhibits lamellar morphology of  $\text{Al}_2\text{Cu}$  and ( $\text{Al}$ ), (d) is Al-41.0 wt.% Cu alloy that exhibits coexistence of ( $\text{Al}$ ) rods and lamellae in  $\text{Al}_2\text{Cu}$  matrix, (e) is Al-42.3 wt.% Cu alloy that exhibits ( $\text{Al}$ ) rods in  $\text{Al}_2\text{Cu}$  matrix.

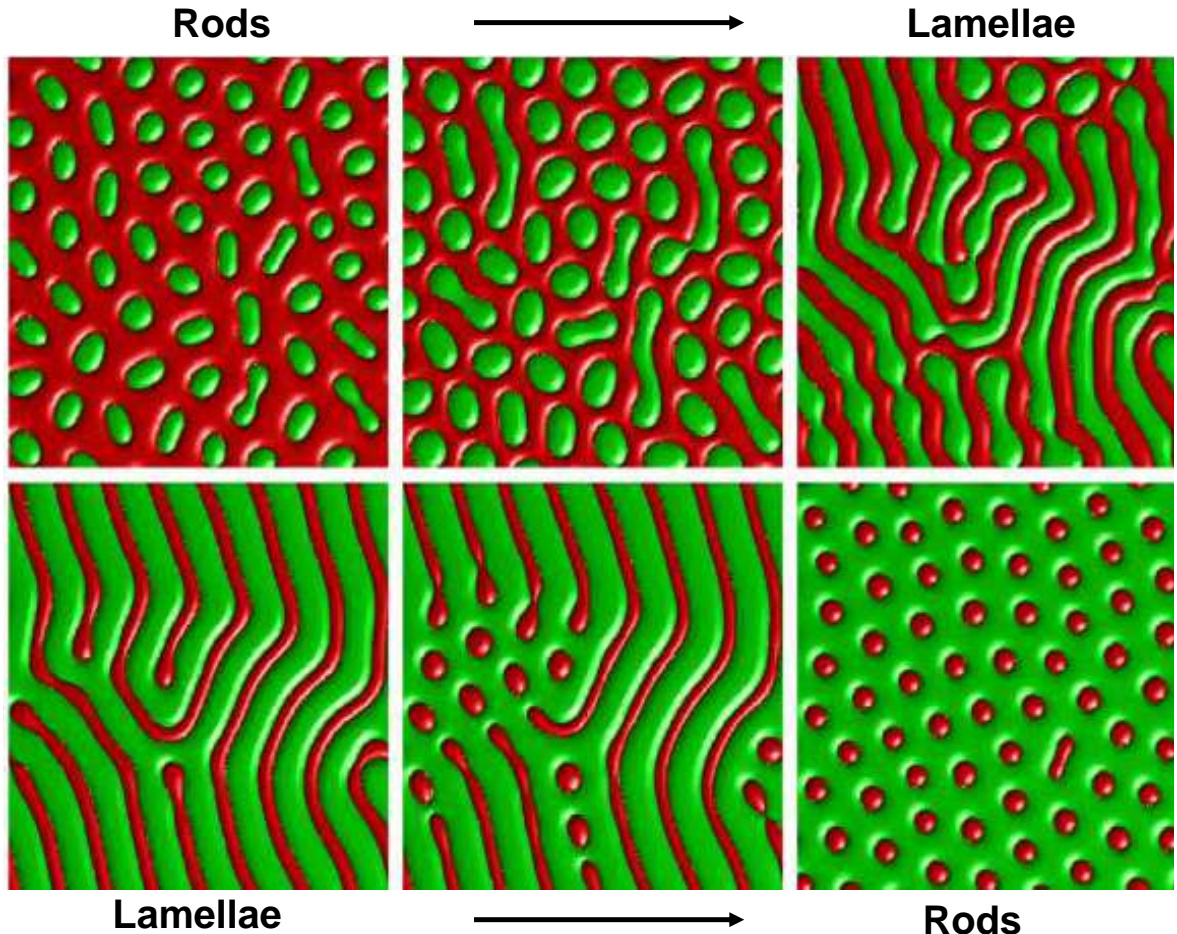


Figure 1.14: The rod-lamellar transition obtained using phase-field simulation (adopted from [10]). Growth direction is perpendicular to the plane of view.

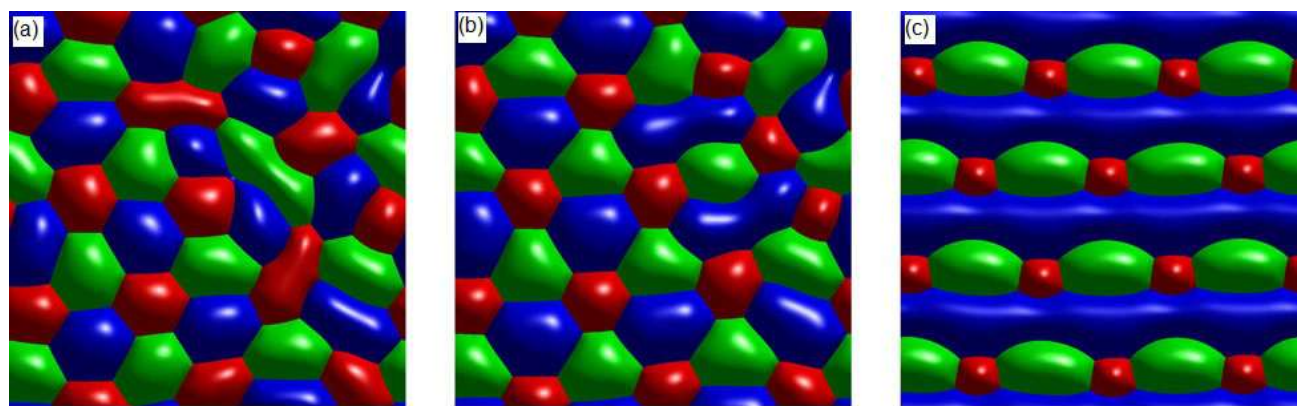


Figure 1.15: Three-phase morphologies are obtained by changing the volume percentages, where the volume percent of the green phase remains the same. The volume percent of red, blue, and green phases are 31, 33, 36 in (a); 21, 33, 46 in (b), and 12, 33, 55 respectively (adopted from [11]). Growth direction is perpendicular to the plane of view.

percentage as shown in Fig. 1.15. In [117], Steinmetz et al. have varied the far-field concentration of the melt in the vicinity of Al-Ag-Cu ternary eutectic point using phase-field simulations and observed the evolution of the different patterns based on the composition.

### 1.3.3 Presence of anisotropy

Typically, crystalline materials possess anisotropy due to their inherent arrangement of atoms. Thus, the crystal's interfacial energy ( $\gamma$ ), one of the critical factors for the solidification process, can vary based on the local crystallographic orientation. Such variations can induce anisotropy either in the solid-liquid interfacial free energy or the solid-solid interfacial free energy. Wulff's plot [118, 119] or  $\gamma$ -plot is a standard way of plotting the changes in  $\gamma$  of the interface for all orientations in polar coordinates. Such plots help us anticipate the equilibrium forms of a crystal with its melt or other crystal. In the following subsections, we discuss the influence of anisotropy in the formation of eutectic microstructures.

#### 1.3.3.1 Anisotropy in the solid-solid interfacial energy

Based on the discussion in the previous section 1.3.2, we notice that a binary system with a low volume percent minority phase chooses a rod-like morphology in the continuous majority phase. However, multiple examples exist where the morphology of the minority phase is biased towards a lamellar structure rather than a rod microstructure, even for substantially low volume percentages of the minority phase. Some of the examples where lamellar (i.e., broken-lamellar) morphology is observed even when the volume percent of the minority phase is less than 10% are Ag-Bi [120, 121, 122, 123, 124, 125], Ag-Pb [124, 126], Ag-Sn [127, 128], Al-Au [129], Al-Sb [130], Al-Sn [131, 126], Bi-Mg [131], Bi-Mn [132], Bi-Zn [122, 125], Cd-Ge [133], In-Zn [126, 134], Sn-Zn [26, 135, 136, 137, 138, 139, 140, 141] and some organic systems [142]. One of the critical factors that can influence the stabilization of the lamellar structure over the rod morphology is the presence of anisotropy in the solid-solid interfacial energy, which is hinted at in Ref. [2, 30], while experimental results illustrating the possible influence of solid-solid interfacial energy anisotropy is provided by Chadwick [26], Jaffrey and Chadwick [136] along with Caroli and co-authors [143].

Fascinating patterns that arise due to solid-solid interfacial free energy anisotropy can be seen in Ref. [1, 143, 144, 145, 146, 147, 148, 149], where locked eutectic grains grow with the direction of growth being different from that of the imposed thermal gradient. Fig. 1.16 shows

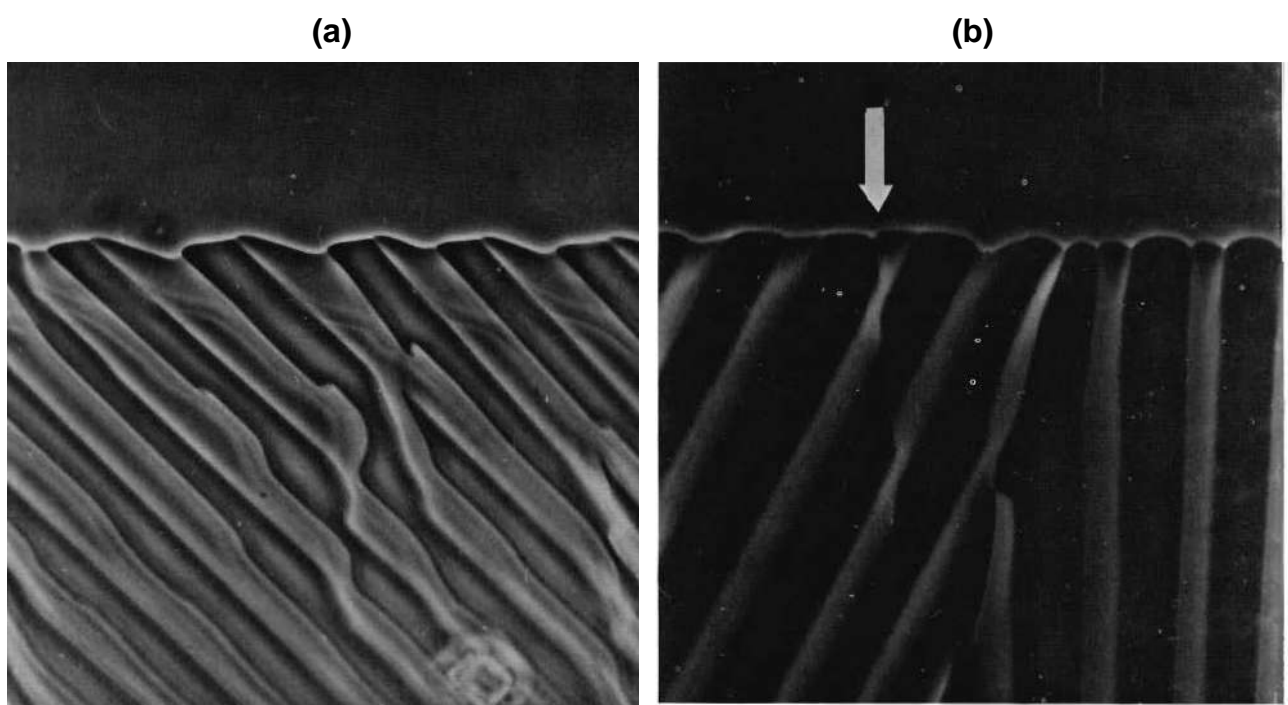


Figure 1.16: Morphologies of carbon tetrabromide-hexachloroethane eutectic, (a) shows that lamellar growth is not perpendicular to the solid-liquid interface, while (b) shows two eutectic grains in which one contains locked low energy solid-solid interfaces that are highlighted with an arrow (adopted from [1]). The growth direction is from bottom to top.

the existence of such locked grains. This is presumably because the solid-solid interface is oriented along a low energy direction in the  $\gamma$ - plot of the solid-solid interface. The investigations in Ref. [145, 146, 147, 148] are compelling as the authors propose a new method of determining the strength of anisotropy by tracing the solid-solid interface using a rotating directional solidification (RDS) apparatus, and thereby, the authors provide evidence for the presence of anisotropy in the solid-solid interfacial energy while also illustrating the influence of anisotropy on morphological evolution. More recently, it has also been shown that such anisotropy can lead to well-aligned lamellar morphologies in contrast to labyrinthine growth forms during bulk solidification using dynamical phase-field simulations [150] as well as in experiments [151]. Similarly, experimental studies by Bottin-Rousseau et al. [152] have shown that coincident low-index lattice planes between the solid phases can lead to special orientations with lower interfacial energies leading to locked lamellar eutectic growth in thin films of (In)-In<sub>2</sub>Bi binary system. Finally, Mohaghegh et al. [99] have studied the effects of interphase boundary anisotropy on the three-phase growth dynamics in  $\beta$ -(In)-In<sub>2</sub>Bi- $\gamma$ -(Sn) ternary eutectic system. Therefore, there is enough evidence to show that anisotropy in the solid-solid interfacial energy can influence the morphological evolution during multi-phase eutectic growth.

### 1.3.3.2 Anisotropy in solid-liquid interfacial energy or growth kinetics

The presence of anisotropy in the solid-liquid interfaces leads to complex or irregular patterns [153, 154, 27, 114, 155, 156] depending on the faceting and growth kinetics. Some of the structures that arise due to solid-liquid anisotropy are shown in Fig. 1.1, 1.5, 1.17. In Ref. [154], the authors show the formation of instabilities in binary eutectic, which consists of faceted and non-faceted phases. The authors propose that forming a solute boundary layer ahead of the non-faceted interface is the reason for the instability. However, in contrast to the impurity boundary layer, the segregated layer in the binary case forms because of the growth restriction of the faceted phase. This leads to a build-up of solute rejected by the non-faceting interface ahead of the solid-liquid interface. The solute build-up provides the necessary constitutional undercooling required for destabilizing the solid-liquid interface, leading to the cellular growth of non-faceted structures coupled with the phase having faceted interfaces. This results in the complex microstructure [154]. Although dynamical phase-field simulations have supported the mechanism of destabilization of a two-phase growth front through impurity additions [78, 80], the same is not true for the destabilization of faceted/non-faceted binary eutectic interface.



Figure 1.17: Morphology of  $\text{MgZn}_2\text{-Zn}$  eutectic that exhibit spiral morphology (adopted from [1]). The image corresponds to the transverse section where the growth direction is perpendicular to the plane of view.

The formation of a boundary layer because of growth restriction imposed by faceting, proposed in Ref.[154] therefore needs to be examined further. Similarly, one can find the formation of a eutectic colony in binary Mg-Zn system [157, 158, 159], that consists of exotic two-phase spirals with hexagonal symmetry as shown in Fig. 1.17.

## 1.4 Selection of exotic systems

The previous discussions reveal that microstructure formation becomes incredibly complex in anisotropic systems and, furthermore, in multi-component systems. Therefore, in the spirit of exploring complex exotic microstructures, we start the investigation from a simple Sn-Zn

binary system eutectic that consists of exotic broken-lamellar structures; thereafter, we investigate the complex structures that arise in the Sn-Te system due to the addition of impurities; subsequently, we investigate the formation of complex three-phase microstructures in Ag-Cu-Sb system that comprises of invariant three-phase eutectic microstructures and combination of two-phase colonies with three-phase eutectic microstructures which exhibit structural hierarchy. Such microstructure combinations involve the scales and the morphology of the colonies, as well as the length scale of the final three-phase eutectic morphology.

Phases	Periodic table group	Crystal structure
Zn, Cd	Group 12	Hexagonal
Si, Ge	Carbon group	Diamond cubic
As, Sb, Bi	Pnictogens	Rhombohedral
Se, Te	Chalcogens	Trigonal

Table 1.1: Crystal structure and group of some exotic phases.

Furthermore, the table 1.1 depicts some of the exotic phases that are anisotropic in terms of solidification. Among all these, the eutectic systems that consist of (Si) or (Ge) phases are well-studied [27, 114, 155, 156], and relatively simple due to cubic symmetry compared to the other phases in the table 1.1. Therefore, we have chosen (Zn), (Te), and (Sb) one from each of the groups and studied microstructure evolution in eutectic systems that consist of these phases. We have chosen eutectic systems such that the selected anisotropic phases form as the minority phase (i.e., Zn is minority phase in the case of Sn-Zn eutectic system), majority phase (i.e., Te is majority phase in the SnTe-Te eutectic system), and decent volume percent phase (i.e., Sb in the Ag-Cu-Sb ternary system, which is neither majority phase nor minority phase). This covers diverse microstructures that arise because of different types of anisotropic phases that constitute different volume percentages in the eutectic growth morphology.

# Chapter 2

## Development of directional solidification apparatus

*"The grand aim of all science is to cover the greatest number of empirical facts by logical deduction from the smallest number of hypotheses or axioms."*

*–Albert Einstein*

Two essential process parameters that need to be controlled during solidification are the temperature gradient across the solid-liquid growth front and the velocity of the front. Typically (in standard alloy castings), the solidification process is unconstrained, and it is not possible to control temperature gradient and velocity independently. Directional solidification is a constrained process in which the temperature gradient, solidification velocity, and crystal orientation can be imposed independently. Therefore, it is a convenient way to investigate the microstructure formation, allowing for a comparative analysis of experimental results with theory and simulation more accurately. Hence the first part of the thesis was directed towards developing a directional solidification configuration. We have chosen a vertical Bridgman-based directional solidification apparatus for investigating eutectic microstructures because of the following reasons. The configuration of the Bridgman apparatus is simple, which makes it capable of rapid manufacture. The modifications in the configuration are relatively easier to implement, and it can attain a wide range of temperatures. Typically, in the vertical Bridgman configuration, the coldest liquid (densest liquid) is at the bottom part near the solid-liquid interface, which does not cause buoyancy-driven natural convection in the liquid ahead of the solid-liquid interface. Further, Marangoni convection (surface-tension driven due to the thermal gradients across the

free surface of the liquid) is not a significant factor in the vertical Bridgman apparatus due to fewer free surfaces of the liquid (unless bubbles form in liquid). Modeling the Bridgman configuration is simpler than the other processes like the Czochralski process. For example, the use of circular pipes as furnace liners makes the analytical and computational models more realistic with justifiable assumptions (isothermality, azimuthal symmetry) and easier geometric specifications. Therefore, it is an elegant scientific research tool for studying various solidification phenomena. A brief review of the Bridgman apparatus is described in the following section, followed by details about the equipment developed in the lab.

## 2.1 Bridgman-based apparatus

P. W. Bridgman (Harvard University) first developed the apparatus with a single zone, from which the crucible is moved outside [160]. Later, Stockbarger (Massachusetts Institute of Technology) developed the design further by adding a second zone kept at a lower temperature [161, 162]. The purpose of the second zone is to overcome the cracking of crystals that he observed during crystal growth. This second zone addition allowed control over the solid-liquid interface position. Further, Wilcox and Fu [163] modeled the influence of adding a gradient zone (insulating) between the two heating zones. This configuration provided better control on the position of the solid-liquid interface in the apparatus. The variety of Bridgman apparatuses is so vast that it would not be feasible to provide all the extensions/ modifications/developments here. However, it is worth mentioning that a horizontal alternative of the Bridgman is commercially important for certain materials. In the horizontal variant, solid-liquid interface curvature and convection are reasonably present; however, stoichiometry control is easier for growing compounds. Another notable member of the Bridgman family is the gradient freeze furnace [164], where growth is achieved by ramping down the temperature (power) in the two zones programmatically, which shifts the melting temperature isotherm upward in the apparatus. Therefore, this configuration does not have moving parts, i.e., both the sample and furnace are stationary. This configuration is further improved by utilizing multiple independently controllable zones [165]. The temperature of the apparatus follows the predefined path (by programming) so that the melting temperature isotherm moves from the seed to the end of the crucible. This method has the capability of controlling interface shape (planar/concave/convex) by designing the temperature profile utilizing multiple independently controlled heaters [166]. The drawback of the

method is that it is physically complex with multiple heaters, thermocouples, and temperature control loops. Many maintenance problems arise in the configuration, particularly the calibration of many thermocouples used in the apparatus. Hence, it is not extensively used, neither in academic research nor in industrial production, because of the high maintenance needed.

In this context, we have decided to use the vertical Bridgman-type apparatus for investigating the microstructural evolution. Nowadays, several companies produce and sell the Bridgman apparatuses in the marketplace, which are too expensive. Moreover, certain improvements/modifications to the apparatus can be incorporated if it is user-made. So we have decided to make our own apparatus with certain modifications/enhancements. In the following section, details about the homemade apparatus are discussed.

## 2.2 Development of apparatus

The three main components of the Bridgman apparatus are i) furnace, ii) crucible, and iii) linear motion arrangement. The details about each of the components is provided in the following sections.

### 2.2.1 Basic design of Furnace

In order to have reasonable control over the thermal gradient, it was decided to build a three-zone furnace that constitutes a hot zone and a chill zone separated by a thin ceramic-based insulation zone forming the adiabatic zone. The required hot zone temperature is obtained using resistance heating, where Kanthal-A is used as the heating element. The chill zone is built using copper pipes that has a continuous circulation of constant temperature water-glycol mixture. The purpose of the insulation zone is to reduce the heat transfer between the hot and chill zones and thereby automatically result in the establishment of a gradient between the hot and cold zones. The schematic of such an apparatus is shown in Fig. 2.1(a). The axial temperature in the setup was measured using a thermocouple that is held stationary while the furnace is made to traverse a given length. This delivers the temperature distribution with distance along the furnace that is plotted in Fig. 2.1(b) for 400 °C set temperature of the hot zone. For such a case, we obtained a maximum temperature gradient of 13.1 °C/mm.

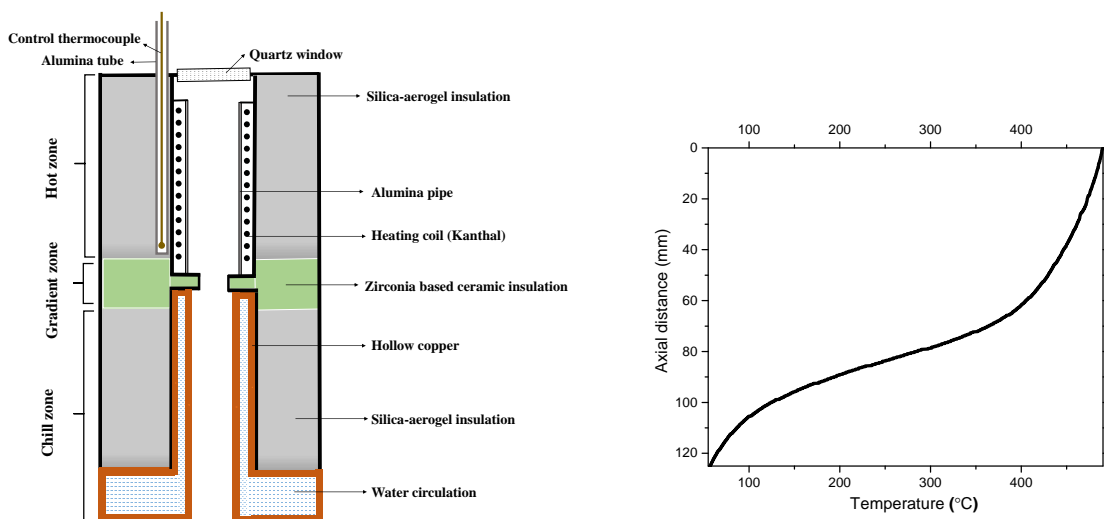


Figure 2.1: Schematic of the modified Bridgman apparatus is shown in (a), while plot in (b) display the axial temperature distribution with distance from the hot-zone, for different temperatures of the hot zone; where the origin of distance axis is at the center of the hot zone and the distance is measured until the center of the chill zone. Please note that the schematic in (a) is not on the same scale as in (b). The axial lengths of the hot zone, gradient zone, and chill zone are 100, 10, 80 mm, respectively, while the inner diameters are 30, 20 mm for hot and chill zones, whereas the gradient zone has 18 mm inner diameter.

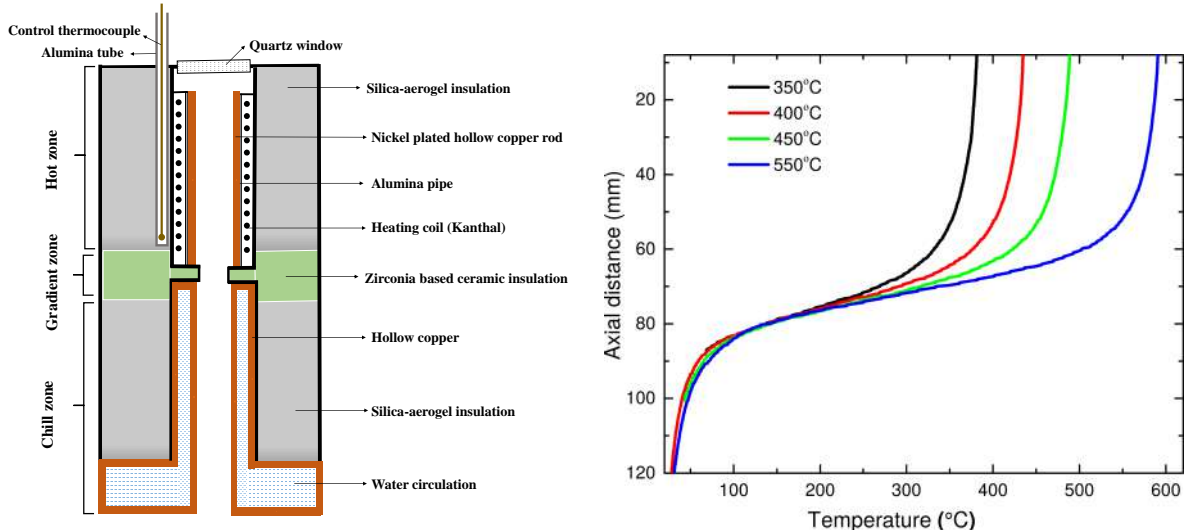


Figure 2.2: Schematic of the modified Bridgman apparatus with hollow Ni-electroplated copper rod addition is shown in (a), while plots in (b) display the axial temperature distribution with distance from the hot-zone, for different temperatures of the hot zone; where the origin of distance axis is at the center of the hot zone and the distance is measured until the center of the chill zone. Please note that the schematic in (a) is not on the same scale as in (b). The axial lengths of the hot zone, gradient zone, and chill zone are 100, 10, 80 mm, respectively, while the inner diameters are 20 mm for hot and chill zones, whereas the gradient zone has an 18 mm inner diameter.

### **2.2.1.1 Usage of Ni-electroplated copper rod**

Additionally, to attain a uniform distribution of temperature in the hot zone and to increase temperature gradient at lower temperatures, a hollow Ni-electroplated copper rod is placed concentrically with the heating elements and held on a groove provided on the adiabatic zone, as shown in Fig. 2.2(a). We have observed the establishment of thermal gradients within the hot zone without the use of the copper rod, which deteriorates the temperature gradient of the apparatus. Therefore, using a highly conductive copper rod helps establish a uniform hot zone and retain high temperatures right up to the adiabatic zone, allowing high-temperature gradients between the hot zone and the chill zone. The axial temperature profiles obtained in the apparatus with the addition of a hollow Ni-electroplated copper rod are shown in Fig. 2.2(b). The temperature profiles reveal the uniformity in the hot zone when compared to the temperature profile (refer to Fig. 2.1(b)) without a hollow Ni-electroplated copper rod. Further, we observe an increase in the maximum temperature gradient with the addition of the hollow Ni-electroplated copper rod. For example, the maximum temperature gradients obtained without and with Ni-electroplated copper rod are 13.1 and 20.5 °C/mm, respectively. The imposed temperature gradient can also be varied by changing the hot and chill zone temperatures (refer to Fig. 2.2(b)).

### **2.2.1.2 Sample holder**

We have designed two types of sample holders as shown in the schematics of Fig. 2.3(a), (b). In the case of the sample holder shown in Fig. 2.3(a), cooling occurs by local equilibration with the surrounding air. In order to enhance the cooling conditions, the sample is placed in a holder which has water circulation that is maintained at the same temperature as in the chill zone, as shown in Fig 2.3(b). The actual sample holder with water cooling provision is shown in Fig. 2.3(c).

### **2.2.1.3 Modelling using OpenFoam and its experimental validation**

The temperature profiles discussed in the previous section, which are measured in the absence of the sample, corresponding essentially to the imposed temperature gradient in the furnace and differs from the value at the liquid-solid interface since the temperature distribution inside the quartz tube containing the sample involves additional heat transfer through the solid and the liquid. While the thermal gradient at the solid-liquid interface may be derived from

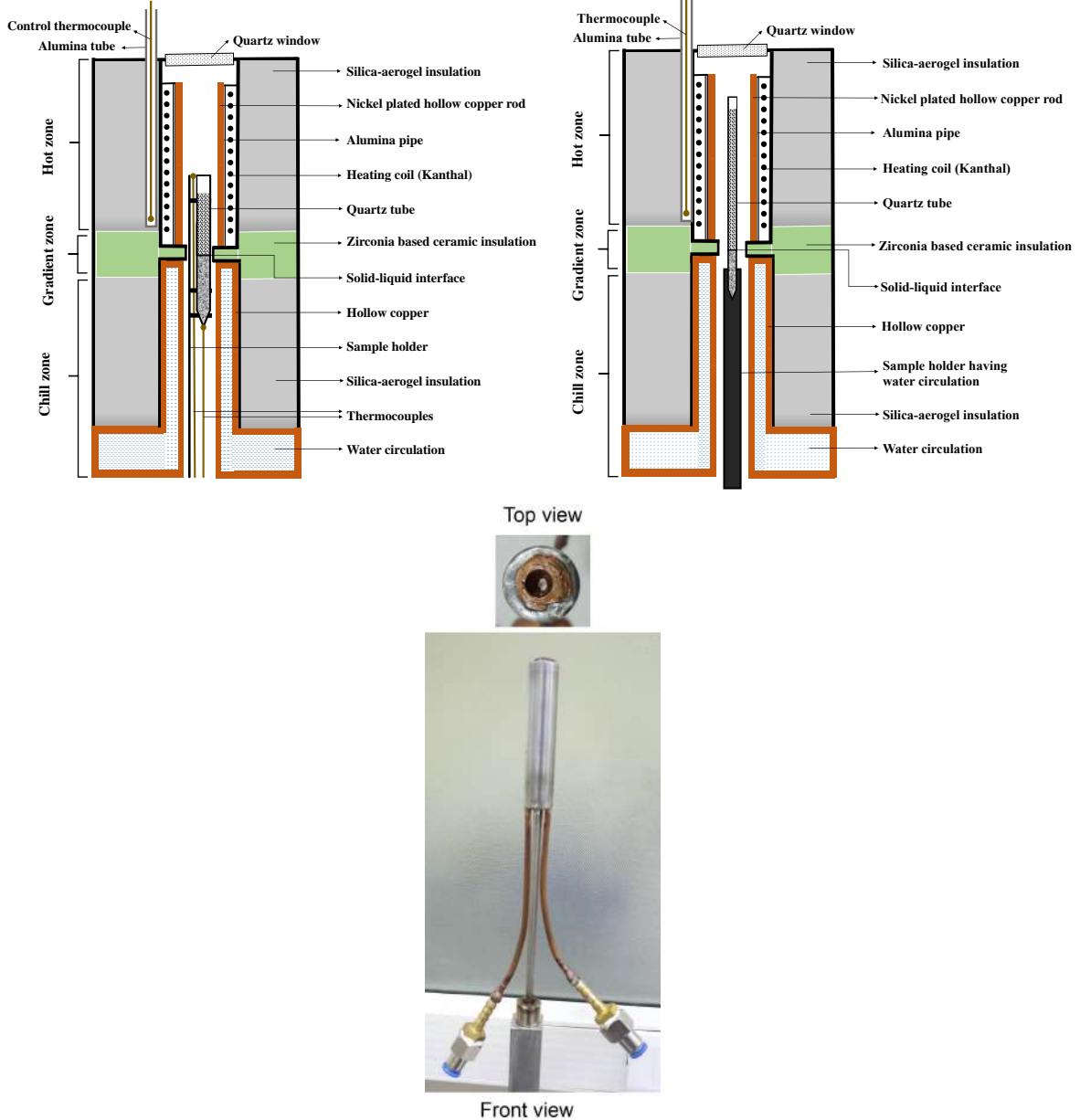


Figure 2.3: (a), (b) are the schematics that show two different sample holders. In the case of (b), the sample is placed in a holder which has water circulation that is maintained at the same temperature as in the chill zone, as shown in Fig 2.3(b). The actual sample holder with water cooling provision is shown in (c).

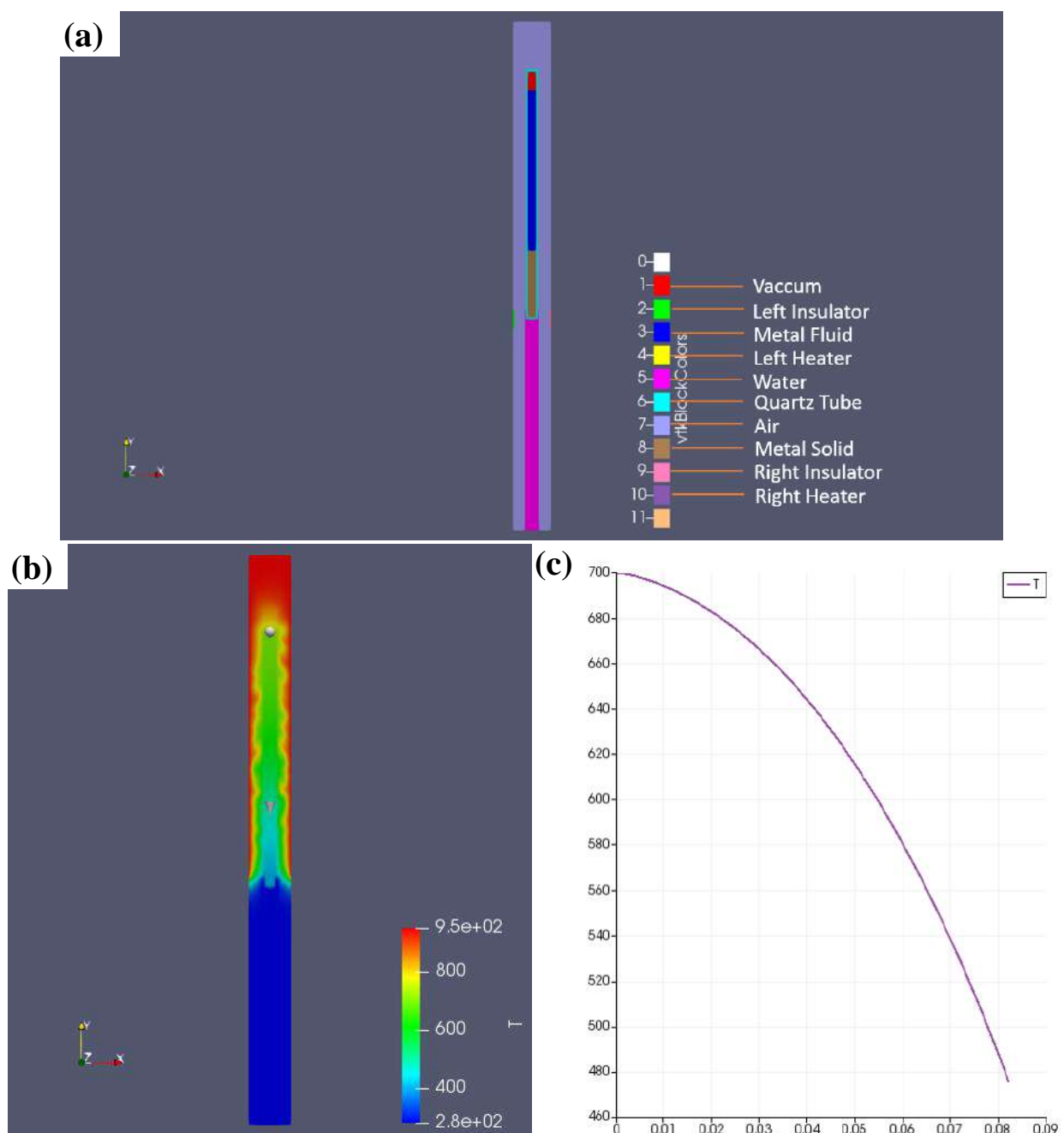


Figure 2.4: Thermal modeling using OpenFOAM software, where (a) is directional solidification setup 2D view, (b) is thermal profile, and (c) is axial temperature profile in liquid.

thermocouples directly placed in the crucible, we have chosen here to estimate the values using mathematical modeling. We have computed the temperature profiles at the solid-liquid interface through a heat-transfer model capturing all the essential modes of heat transfer using the partial differential equation implementation library in the OpenFOAM software [167] that allows us to precisely ascertain the thermal gradients at the solid-liquid interface.

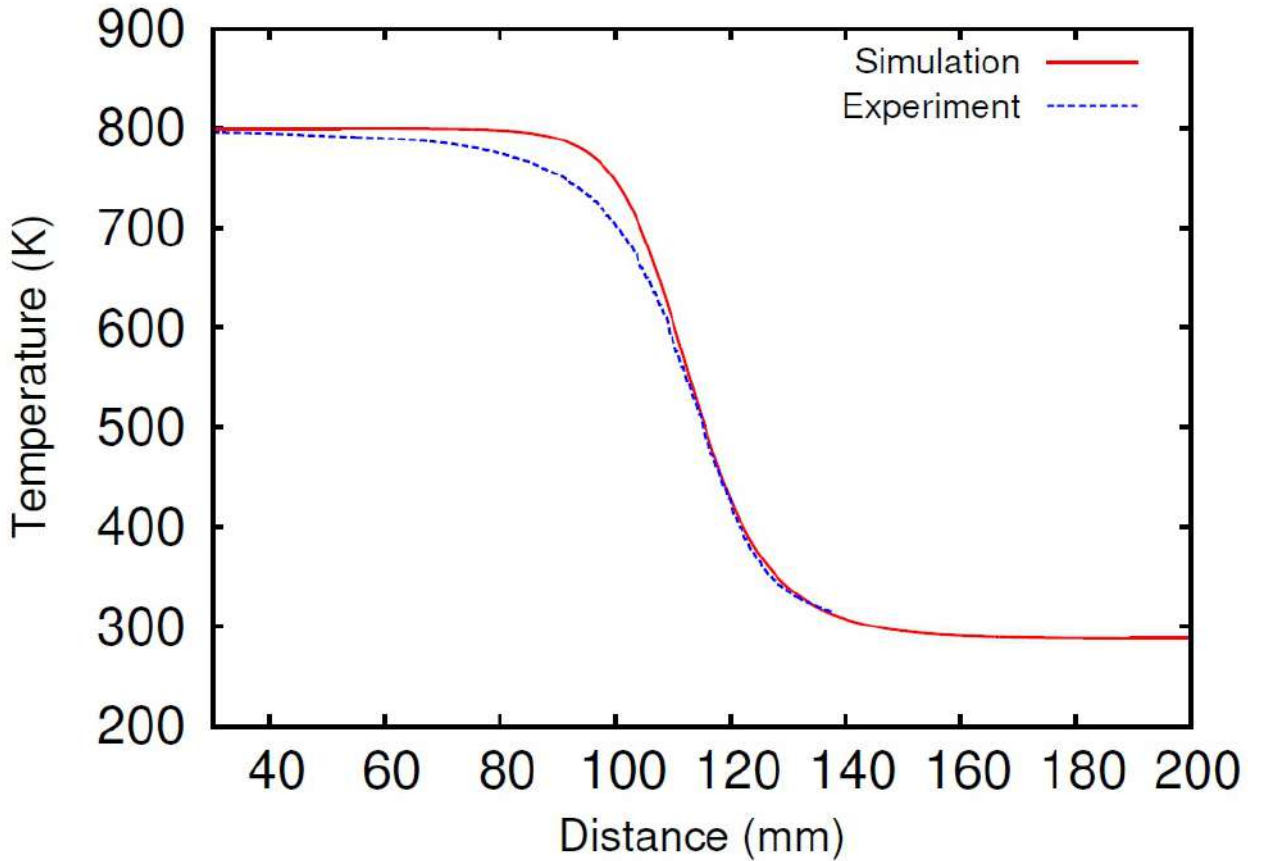


Figure 2.5: Temperature profile inside the furnace without quartz crucible.

Different regions are created with different material properties in this library and are exposed to different boundary conditions. The heaters are modeled using constant heat flux boundary conditions, and the convective heat transfer coefficients are utilized for modeling the cooling in the sample holder and the chill. This is the reason for the different labels that were present in Fig. 2.4(a). Firstly, the heat transfer coefficients have been calibrated with actual temperature measurements in the furnace without the sample holder and the quartz tube. Fig. 2.5 depicts

the experimentally acquired thermal profile in comparison to the modeled one. The results show that the maximum gradient matches approximately in both cases.

After the calibration of the heat transfer coefficients and utilizing the thermo-physical data available for the solid and the liquid phases, the thermal profiles have been modeled in the presence of a quartz tube crucible containing the solid and the liquid. For this purpose, thermo-physical data of off-eutectic Sn-Zn (Sn-5 % wt. Zn) alloy is used for the model, and subsequently, experiments are conducted using the same alloy to benchmark the model. The position of the equilibrium solid-liquid interface for a stationary furnace has been iteratively estimated as the location that corresponds to the alloy's melting temperature. The temperature profile of the furnace in various zones (solid, liquid) is examined using Paraview (a visualization software) as shown in Fig. 2.4b. The light blue region in Fig. 2.4b corresponds to the temperature in the solid, where you expect the gradients to be small, and thereby the temperature profiles are different from those in the liquid. However, what is plotted in Fig. 2.4(c) is the temperature profile in the liquid ahead of the equilibrated solidification front, from which the thermal gradient at the solidification interface can be estimated. The modeling also considers the convection in the liquid, and while we do not report it, we have found that for the imposed thermal conditions and small geometry of the crucible, the convective currents were very weak. We obtained the temperature gradient from the axial thermal profile (refer to Fig. 2.4(c)) in liquid as approximately 6.0 °C/mm at the solid-liquid interface.

In order to benchmark the modeled gradient in the furnace, the onset of the Mullins-Sekerka instability [69] is utilized where the critical condition for the formation of instability depends on  $G/V \leq m\Delta c/D$ . For a constant temperature gradient ( $G$ ), liquid diffusivity ( $D$ ), and slope of liquidus curve ( $m$ ); the critical velocity for the Mullins-Sekerka instability is fixed for the given composition of the alloy. Therefore, we have determined the critical velocity for the formation of the instability using the computed gradient and thermo-physical data of the alloy given in Ref. [168, 139]. We obtained a critical velocity of  $1.33 \mu\text{m/s}$  for the alloy using the computed gradient. In order to determine the formation of instabilities, experiments are conducted with the off-eutectic Sn-Zn alloy (Sn-5wt.%Zn) at velocities of  $1.0 \mu\text{m/s}$  and  $2.0 \mu\text{m/s}$ , where the velocity is ramped up from  $1.0 \mu\text{m/s}$  to  $2.0 \mu\text{m/s}$  in the same experiment. In Fig. 2.6 we see transient microstructures at the start of the solidification, which involves microstructures formed after the initial quench followed by equilibration. Subsequently, microstructures at  $1.0$  and  $2.0 \mu\text{m/s}$  are shown in Fig. 2.6. We can see the formation of instabilities when the velocity changes

to  $2.0 \mu\text{m/s}$  while the interface is planar at  $1.0 \mu\text{m/s}$ . Experimentally, we can say the critical velocity for the instability formation is between  $1$  and  $2 \mu\text{m/s}$  which agrees with the computed temperature gradient. Further experiments are conducted at velocity  $1.2 \mu\text{m/s}$  and  $1.4 \mu\text{m/s}$ , where again the velocity is ramped up from the lower to the higher value after solidification of a finite distance. We can see the formation instabilities at  $1.4 \mu\text{m/s}$  but not at  $1.2 \mu\text{m/s}$  (refer to Fig. 2.7). Therefore the critical velocity computed based on the thermal modeling is close to experimental values. Using the same model, we computed the temperature profile and obtained the thermal gradient at the solid-liquid interface for the Sn-Te system as  $9 \text{ }^{\circ}\text{C/mm}$ .

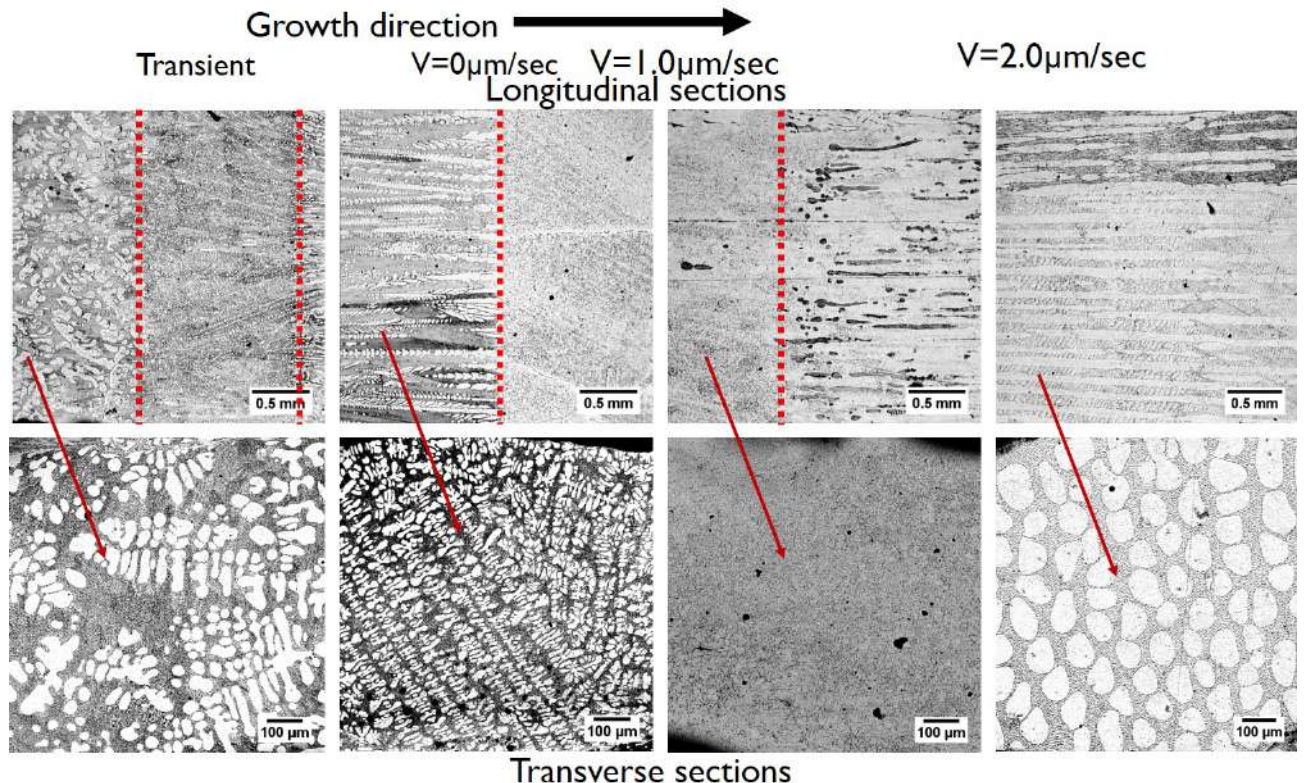


Figure 2.6: SEM images captured in longitudinal sections (upper) and transverse sections (lower) at velocities  $1.0$  and  $2.0 \mu\text{m/s}$ .

## 2.2.2 Selection of crucible

The growing crystal is confined within a crucible, which is one of the characteristics of the Bridgman apparatus. The following factors should be considered when selecting a crucible:

- (i) physical/ chemical interactions between the crucible and the liquid,

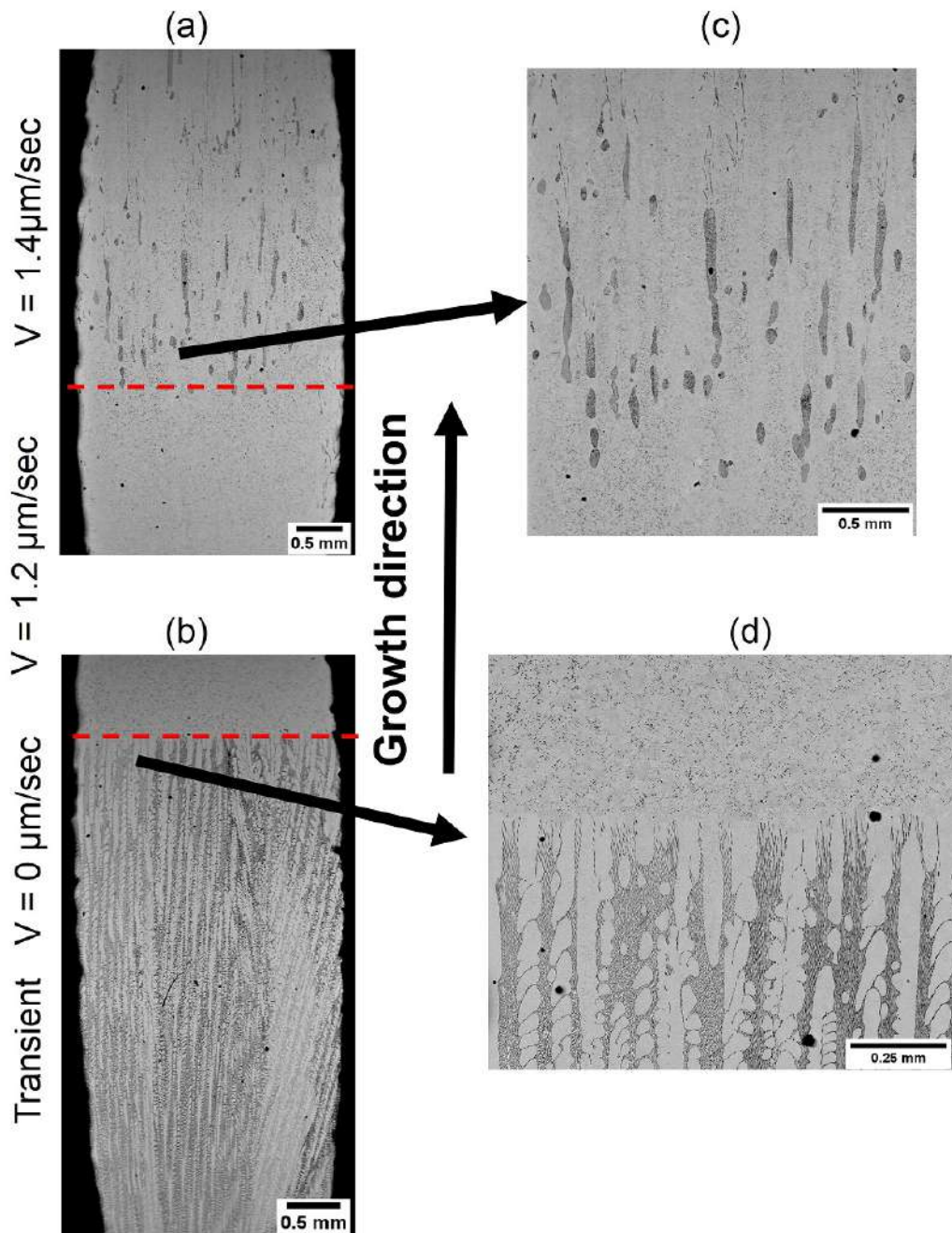


Figure 2.7: SEM images (b), (a) were captured in longitudinal sections from transient regions to the regions with an imposed velocity of  $1.2$  and  $1.4 \mu\text{m/s}$ . Corresponding high magnification images are shown in (c), (d).



Figure 2.8: Quartz crucible having constriction which serves as a natural grain selector.

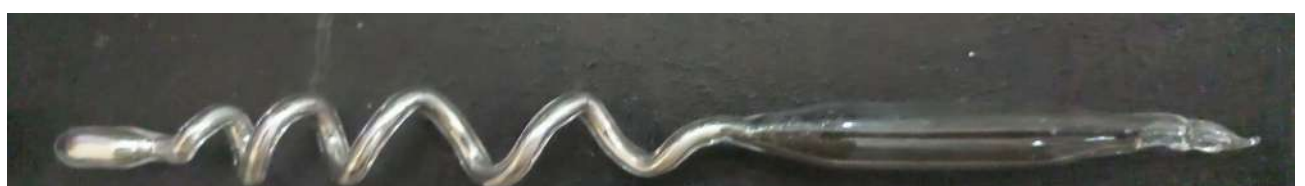


Figure 2.9: Quartz sample made for spiral growth, where (a) is having uniform pitch, while (b) is having variable pitch between each consecutive turn.

(ii) thermal properties of the crucible. An example of a chemical interaction is the reaction between silicon and aluminum/magnesium liquid when they are contained in a quartz crucible.

iii) Another critical parameter that needs to consider before choosing crucible is the "interface effect" [169], which arises due to discontinuity in the thermal conductivity at the solid-liquid interface creating a discontinuity in the thermal gradient, while the crucible thermal gradient remains constant. This leads to local heat transfer close to the interface. This effect can be reduced by selecting appropriate crucible material and geometry such that thermal conductivity in the radial direction is high, whereas thermal conductivity along the crucible length should be low, which provides good coupling between the sample present in the crucible and the furnace. Therefore, we have chosen quartz tubes (low thermal conducting material) with smaller dimensions, i.e., 4mm inner diameter and 6mm outer diameter, that serves all the requirements mentioned above. Further, smaller tubes act as capillary tubes that minimize convective effects in the liquid. Moreover, we have created a constriction before crystal reaching complete crucible diameter, as shown in Fig. 2.8, which serves as a natural grain selector. Further, it is possible to make spiral quartz tubes as shown in Fig. 2.9 which can also be utilized as a natural grain selector. Additionally, spiral tubes help to reveal the strength and form of the anisotropy of the solid-solid interface in three dimensions.

### 2.2.3 Design for linear motion

It's worth noting that the furnace in the Bridgman apparatus can be shifted relative to the stationary crucible containing the sample, which helps to avoid mechanical vibrations, allowing a stable solidification front. Therefore, it was decided to move the furnace instead of the crucible. The speed of the furnace is controlled by a stepper motor and gearbox using a linear drive which can move the furnace in the range of 0.1 - 600  $\mu\text{m}/\text{s}$ . The linear drive movement is independently controlled using software loaded on a data processing computer. The computer also enables data logging of the temperature profiles at various locations along the axial direction of the furnace as a function of time.

## 2.3 Alloy making

Samples of selected compositions were made using high purity elements by melting and stirring them homogeneously using an induction furnace. Solidified alloy ingots were crushed into small

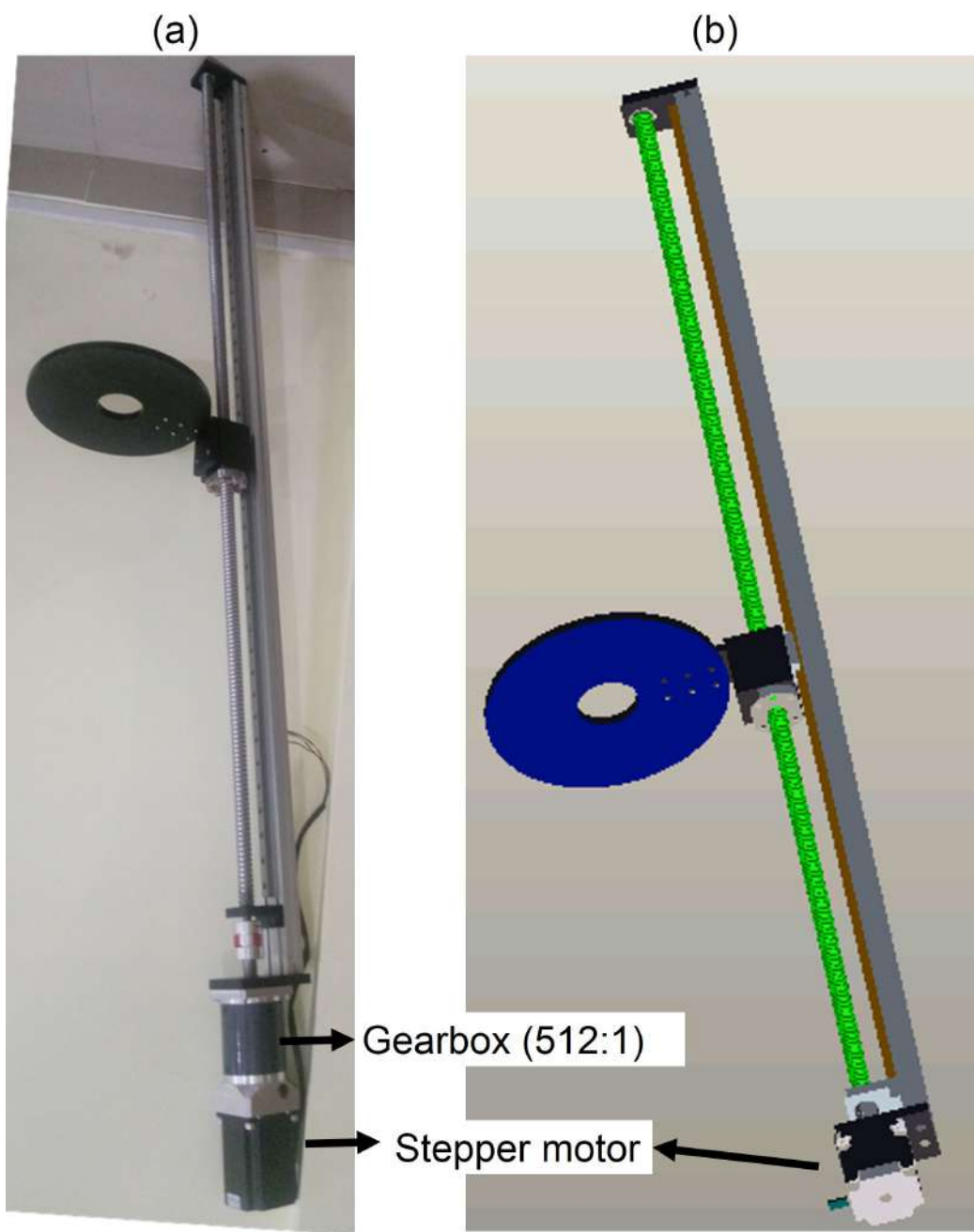


Figure 2.10: The screw driven linear drive that consists of gearbox and stepper motor. (a) is actual one while (b) is a schematic.



Figure 2.11: The actual apparatus made in the lab.

pieces and then filled in small capillary quartz tubes having an inner diameter of 4 mm. The quartz tubes containing the alloy were sealed after creating a  $10^{-5}$  mbar level vacuum inside the tubes using rotary/diffusion pumps shown in Fig. 2.12.



Figure 2.12: Image of vacuum unit that consists of rotary and diffusion pump.



Figure 2.13: Image of induction furnace that consists of a coil which is used to make alloys.

## **2.4 Protocol employed for solidification**

The quartz tube is then placed in the hot zone of the modified Bridgman furnace for around 20 mins such that there is complete melting of the sample and the liquid composition is homogeneous. Thereafter, the water circulation to the sample holder is initiated that leads to a quench of the initial part of the sample, and consequently, the solidification front rises, decelerates, and stabilizes at the melting temperature of the alloy, i.e., the solidification front velocity reaches zero. The system is allowed to equilibrate at this stage until the thermocouple placed at the bottom of the sample reads a constant value. Thereafter, the stepper motor translating the furnace assembly is switched on, which leads to directional solidification with the imposed velocity, where the samples are directionally solidified up to a length of 80 mm.

# Chapter 3

## Material characterization techniques

*"Nothing tends so much to the advancement of knowledge as the application of a new instrument. The native intellectual powers of men in different times are not so much the causes of the different success of their labors, as the peculiar nature of the means and artificial resources in their possession." –Humphry Davy*

### 3.1 Sample preparation for scanning electron microscope (SEM) and image capturing

The directionally solidified Sn-Zn samples are sectioned using a wire electrical discharge machine (WEDM) in transverse and longitudinal directions, while Sn-Te, Ag-Cu-Sb based samples are cut using the surgical blade as these samples are brittle and soft. After that, samples are mounted using epoxy resin, and then traditional polishing techniques are employed to obtain a good surface finish for imaging. A solution of 80% glycerol, 10% nitric acid, and 10% acetic acid is used for the etching (Zn) phase in Sn-Zn samples, whereas for etching the SnTe phase in Sn-Te samples, an etchant solution is prepared by mixing methanol to 33% aqueous KOH and then after cooling it to room temperature, 30% H<sub>2</sub>O<sub>2</sub> is added (methanol:33% aq. KOH:30% H<sub>2</sub>O<sub>2</sub> = 1:4.5:1). The (Sb) phase in the Ag-Cu-Sb system has been etched out just after colloidal silica polishing.

Typical transverse/longitudinal section micrographs of the samples are captured using the FEI (Quanta 200) scanning electron microscope with a tungsten filament and solid-state backscattered electron detector. Before imaging, the samples were kept on a metallic stub using carbon

tape and loaded inside the machine. After attaining the  $\leq 10^{-4}$  Pa level vacuum, accelerating voltages of 25 kV is used for imaging the samples. As the samples are multi-phase materials exhibiting compositional contrast, backscattered electron detectors are used to capture images detailing the morphologies.

## 3.2 Image analysis of SEM images

In the case of two-phase eutectic, the length scale associated with the microstructures is obtained by performing Fast Fourier Transform (FFT) of the transverse section SEM images using Image J software. In the case of the Sn-Te system, short and long-range spatial relationships in the distribution of phases are determined by mapping the microstructure to a reduced vector space using 2-point spatial correlations [170, 171, 172] between the phases in the microstructure. The resulting map consists of all possible vectors and their probabilities of occurrence. Further, in the case of ternary three-phase eutectic, microstructure contains bright, dark, and grayscale phases, which are separated using three-level thresholding[173], and spatial relationships between the distribution of phases are reduced to a vector space using 2-point spatial correlations in order to determine spacing relations.

## 3.3 Composition analysis

In order to determine composition distribution, electron probe microanalyzer (EPMA) based on the physical mechanism of electron stimulated X-ray emission and spectrometry is used. A field-emission microscope, JEOL (JXA-8530F), equipped with dispersive spectroscopy (EDS), and wavelength dispersive spectrometry (WDS) detectors, has been used for obtaining composition distribution. Due to the bulk sizes (more than a few microns) of the samples, atomic number (Z), absorption (A), and fluorescence (F) influence the X-ray intensity; therefore, ZAF corrections were done using respective elemental standards. A gas proportional counter containing P-10 gas (a mixture of 90% argon and 10% methane) is used to determine X-ray counts.

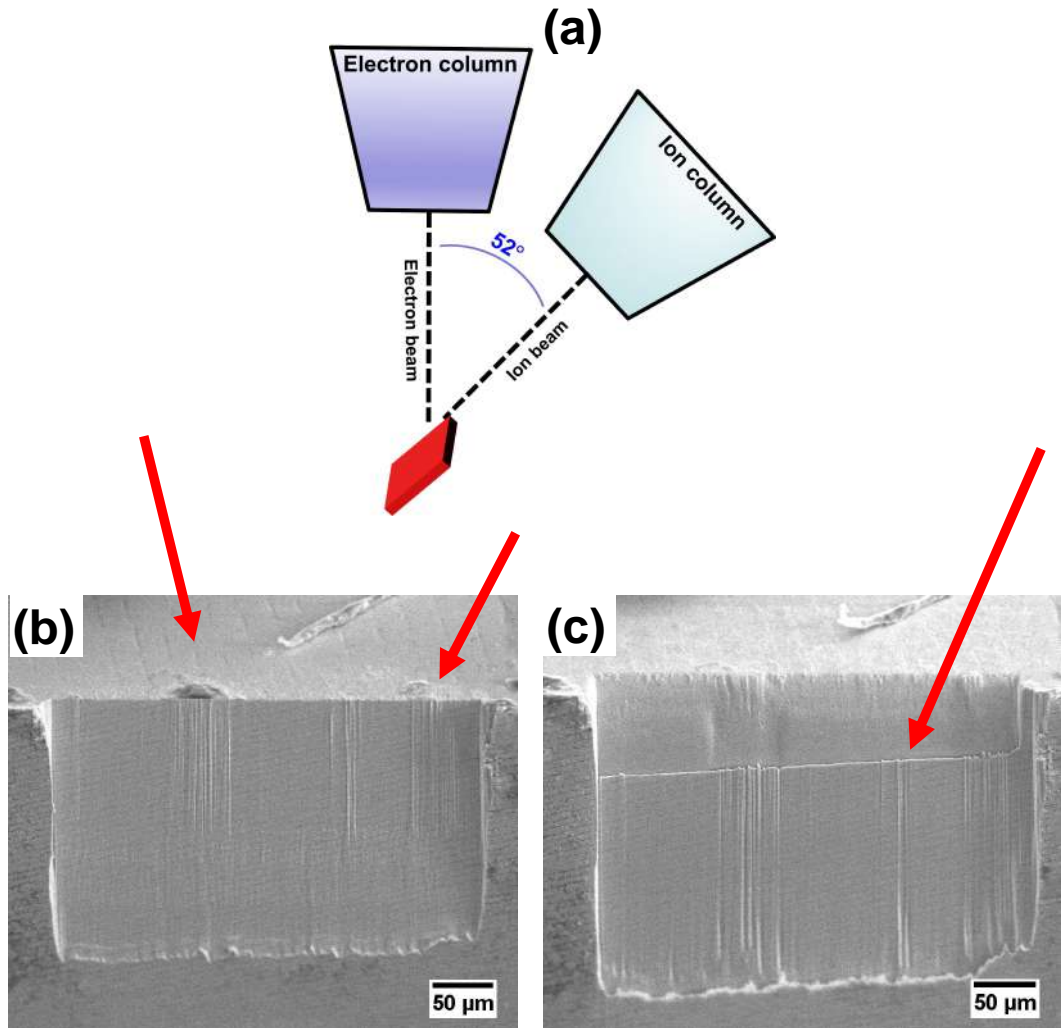


Figure 3.1: (a) Schematic of sample setup to show how milling was done at grazing incidence angle close to zero to the surface (but not perpendicular to sample surface). Image (b) is to illustrate that an obstacle to the ion beam coming at grazing incidence angle close to zero can cause band-like features in the sample. Image (c) has been captured while removing irregularities formed in the image (b) by removing few layers of material. It is shown here to illustrate how ion-beam coming at a grazing incidence angle removes the material (top to bottom).

### 3.4 Ion milling

FEI Helios G4, a dual-beam microscope, is used for ion milling to capture the internal structures as well as in the final preparation of samples for EBSD as a polishing step at zero-grazing incidence angle to the surface as shown in Fig. 3.1. For the case of the Ag-Cu-Sb TEM sample, a site-specific sample is lifted out as lamella such that the zone axis matches with the growth direction for transmission electron microscopy (TEM) characterization utilizing a dual-beam microscope, Scios 2, using a focused ion beam of Ga<sup>+</sup> ions. Initial trenches are made using 9.3nA current, 30kV accelerating voltage, and the final milling was done at 2.3nA current, 30kV accelerating voltage. Low voltage 2kV and 23pA current are used for sample cleanup.

### 3.5 EBSD and its analysis

FEI Helios G4, equipped with an EDAX Digiview camera is used for electron backscatter diffraction (EBSD) experiments. EBSD samples were prepared using conventional metallographic techniques, and the final polishing using Ga<sup>+</sup> ion milling at zero-grazing incidence angle to the surface as shown in Fig. 3.1 for the case of Sn-Zn and Ag-Cu-Sb systems. Ga<sup>+</sup> ion milling is not used for the SnTe-(Te) system prior to EBSD, as milling in the SnTe-(Te) system leads to differential etching between the phases. Post-processing of all the data obtained from the EBSD and plotting the pole figures as well as inverse pole figures was done using commercially available TSL OIM<sup>TM</sup> software.

### 3.6 TEM

The transmission electron microscopy (TEM) analysis was carried out for the Ag-Cu-Sb sample in order to ascertain the crystal structure of the phases present in the system. Sample preparation is as described in section 3.4. T20 TEM microscope with a LaB6 electron source and super twin objective lens system is used to obtain diffraction patterns from each phase at an accelerating voltage of 200kV.

## 3.7 X-ray diffraction

X-ray measurements are conducted using Rigaku X-ray texture goniometer using copper K- $\alpha$  radiation. X-ray pole figures are obtained in Schulz reflection geometry, wherein the Schulz correction formula is used to correct the defocussing error. The data obtained was plotted as pole figures using Matlab (MTEX [174]).

## 3.8 X-ray tomography

X-ray tomography is carried out using X-Radia Zeiss, wherein parameters are optimized for obtaining better contrast by thinning the samples to tiny sizes of the order of  $400\text{-}600\mu\text{m}$  to ensure X-ray transparency. Tomography is carried out at an X-ray voltage of 140kV, with power as 10W, having an exposure time of 5s, with the detector distance as 50.1 mm, source distance as 16.1 mm, and using the filter HE3. Projections are further geometrically magnified using an objective lens (4x). Tomviz, an open-source tomography software, is used for 3D rendering.

# Chapter 4

## Exotic broken-lamellar structures in the Sn-Zn eutectic system

*"Creativity involves breaking out of established patterns in order to look at things in a different way." –Edward de Bono*

The main objective of this chapter is to understand the formation of a broken-lamellar structure in contrast to the rod morphology during solidification of the Sn-Zn eutectic alloy that has a minority phase percent of 9% of the Zn-rich phase. The reason for choosing this system is that none of the previous studies [135, 175, 136, 131, 137, 138, 139, 140, 176, 177, 141] on this system conclusively establish the reason behind the formation of the broken-lamellar morphology. Further, we would like to clarify the existence of crystallographic orientation relationships, given that no unique relationships were observed in earlier studies [136, 137, 178, 179, 180, 168].

### 4.1 Sn-Zn phase diagram

Sn-14.9 at.%Zn (Sn-8.8 wt.%Zn) undergoes an invariant eutectic reaction at 199 °C, during which the liquid transforms into tin-rich solid-solution and zinc-rich solid-solution, where the (Sn) phase crystallizes as the tetragonal A5 structure whose space group is I4<sub>1</sub>/amd (typically called as body-centered tetragonal, BCT), and the (Zn) phase crystallizes as the hexagonal A3 structure whose space group is P6<sub>3</sub>/mmc (traditionally called as hexagonal close-packed, HCP) [168]. Refer Fig. 4.1 for Sn-Zn phase diagram.

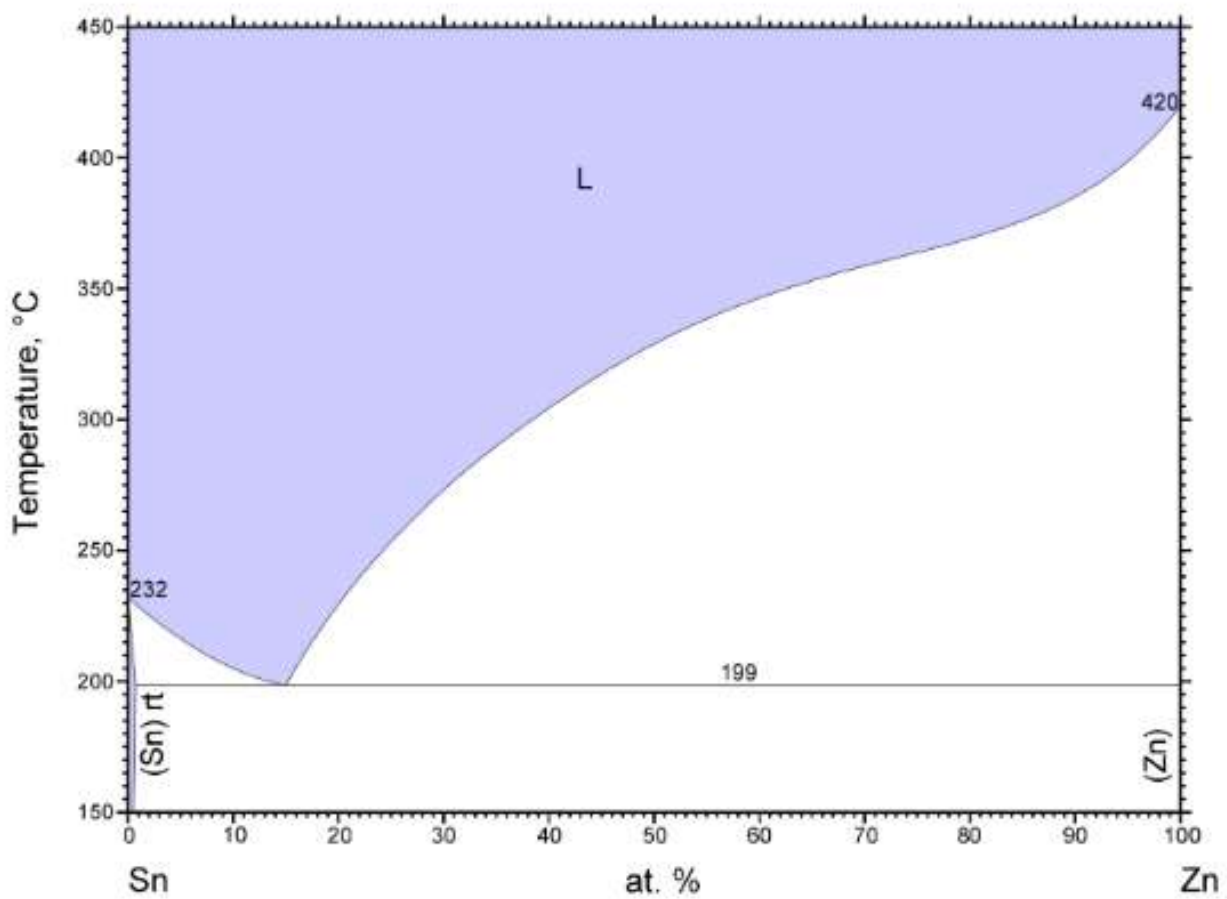


Figure 4.1: Sn-Zn binary phase diagram [12].

## 4.2 Results and discussions

### 4.2.1 Morphology aspects

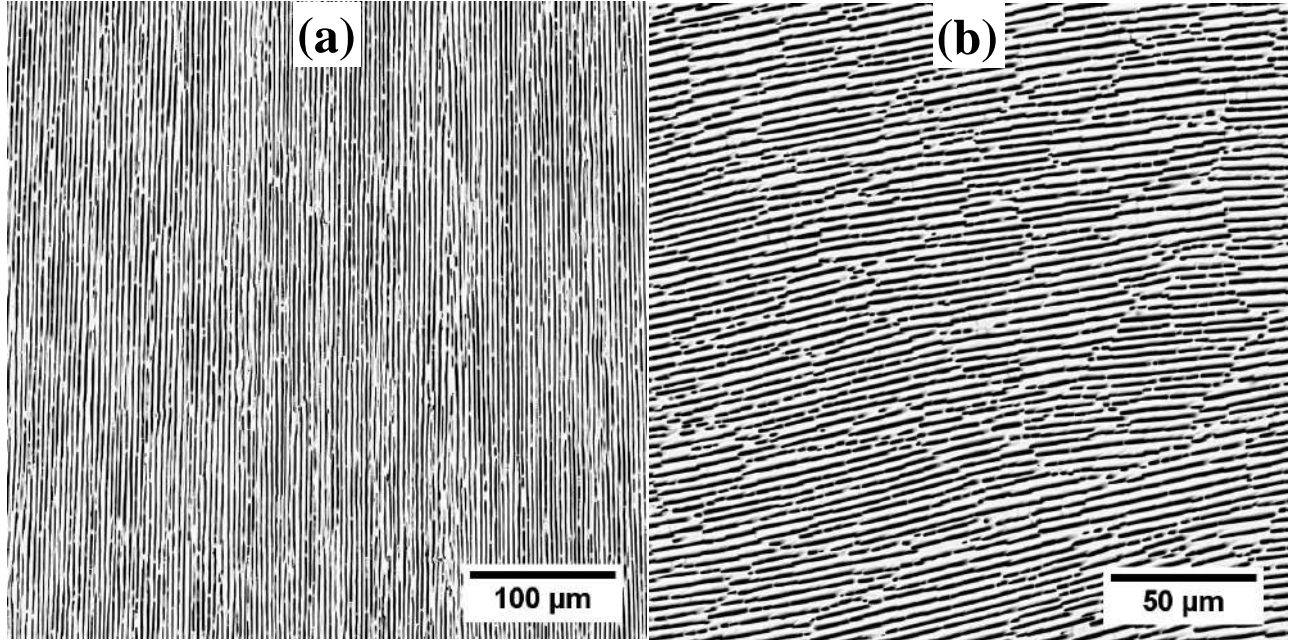


Figure 4.2: Scanning electron micrographs of the Sn-Zn eutectic alloy solidified at  $2.5\mu\text{m}/\text{s}$ , where (a) is longitudinal section (growth direction is from bottom to top), while (b) is transverse section, growth direction is towards the reader.

Fig. 4.2 depicts the microstructure ((a) shows the longitudinal section, (b) shows the transverse section) of the Sn-Zn alloy obtained from the directionally solidified sample at a velocity of  $2.5\mu\text{m}/\text{s}$ . The longitudinal section highlights the alignment of the eutectic phases along the direction of the temperature gradient, while the transverse section shows the “broken” lamellar morphology of the Zn-rich phase. As has been mentioned in the sections 1.3.2, 1.3.3 of the introduction chapter, this is a surprising result, given the small volume fraction of the Zn-rich phase. Further, this structure is quite different from that of the irregular growth structures of eutectic phases [156]. Our observations match with previous studies [135, 136, 137, 138, 139, 140, 141] on this alloy. Fig. 4.3 shows the range of eutectic microstructures of the alloy solidified at different velocities ( $V = 0.6, 1.0, 5.1, 7.5, 10.1, 50.0 \mu\text{m}/\text{s}$ ). Globally, the transverse section images show evidence of a broken-lamellar type of arrangement of the Zn-rich phase at all velocities. Connections of broken-lamellar fragments leading to an increase in average lamella fragment length become more with the decrease in velocity; however, the influence of the imposed thermal

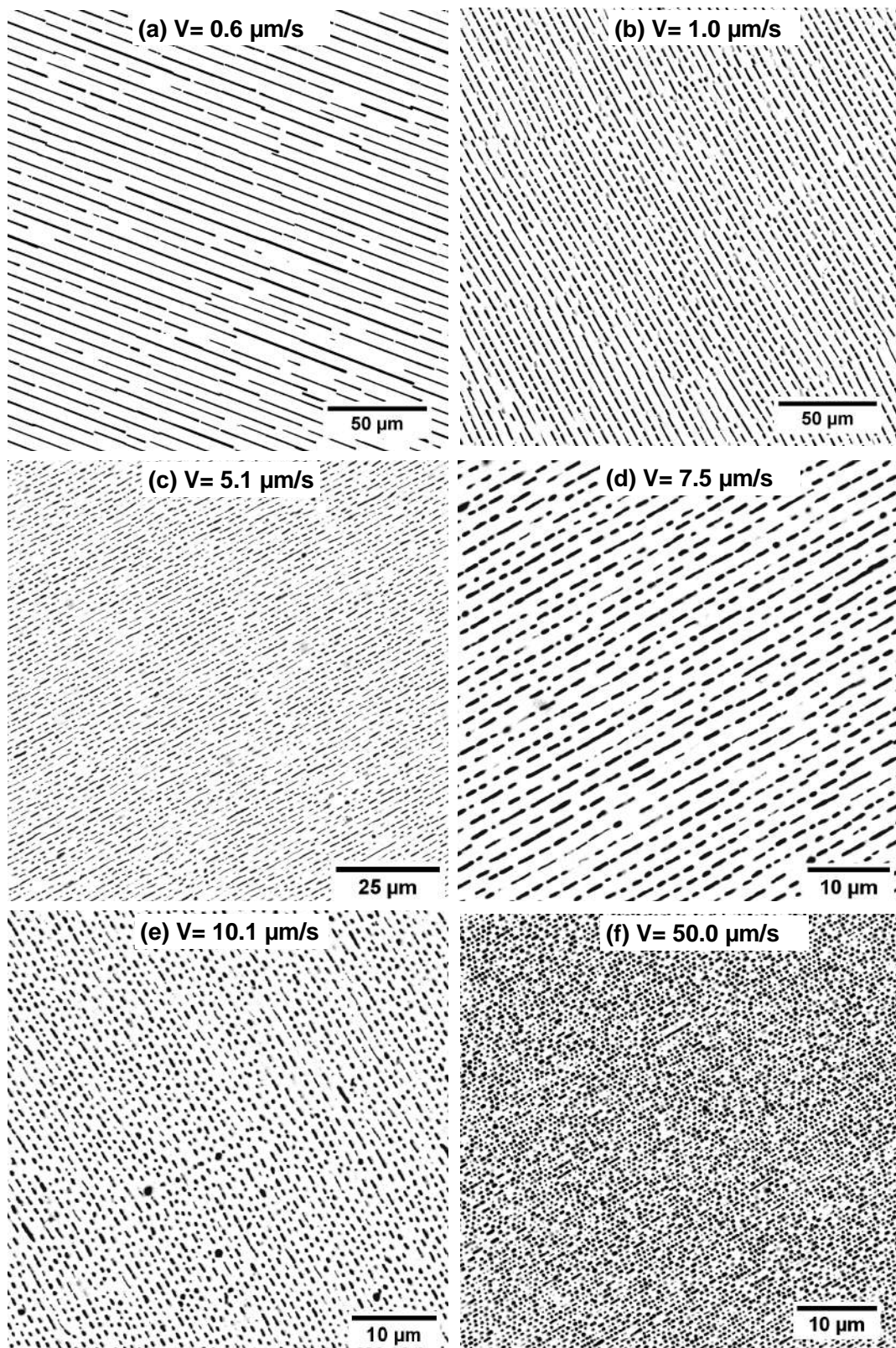


Figure 4.3: Transverse section SEM images of directionally solidified Sn-Zn eutectic alloy at different velocities.

gradients on connections is minor.

Because the SEM images are obtained post-etching, which alters the volume fraction of the phases, we utilize the dual-beam microscope (FEI Helios G4) for imaging subsequent to the polishing of the surface with an ion beam. This retains the information about the spatial distribution of the Zn-rich phases as well as their volume fractions post solidification. High-resolution images captured for the sample solidified at  $0.6 \mu\text{m/s}$  shown in Fig. 4.4, depicts the actual distribution of both the phases and the phase fraction, whereas, in the etched samples, the phase fraction of Zn appears to be higher than actual due to the extent of the pitting reaction that invades the Sn-matrix. Consequently, we have utilized EBSD data for phase quantification, and the derived phase fractions are close to that expected at the eutectic liquid composition as shown in Fig. 4.8b. This confirms that indeed, the liquid composition is at the eutectic during solidification and additionally, the fact that the morphology of the Zn-rich phases appears lamellar in the SEM images is not due to etching of the samples. The lamellar

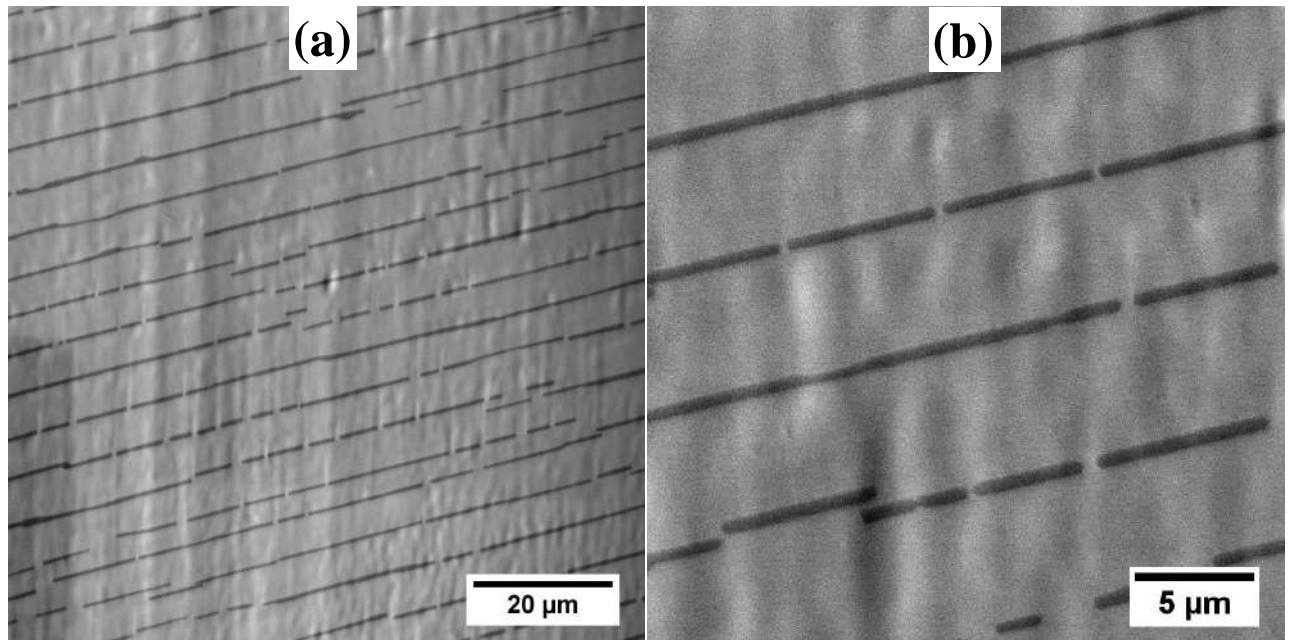


Figure 4.4: Transverse section images of the unetched Sn-Zn alloy solidified at  $0.6 \mu\text{m/s}$ , low magnification image in (a) and high magnification image in (b), where bright part is Sn rich phase and dark part is Zn rich phase.

spacing that is the principal length scale in the microstructure, is not altered with etching as the centroids of the phases remain unchanged. Therefore, we have utilized the SEM images post-etching and evaluated the average spacings using FFT, for each of the thermal gradients and the

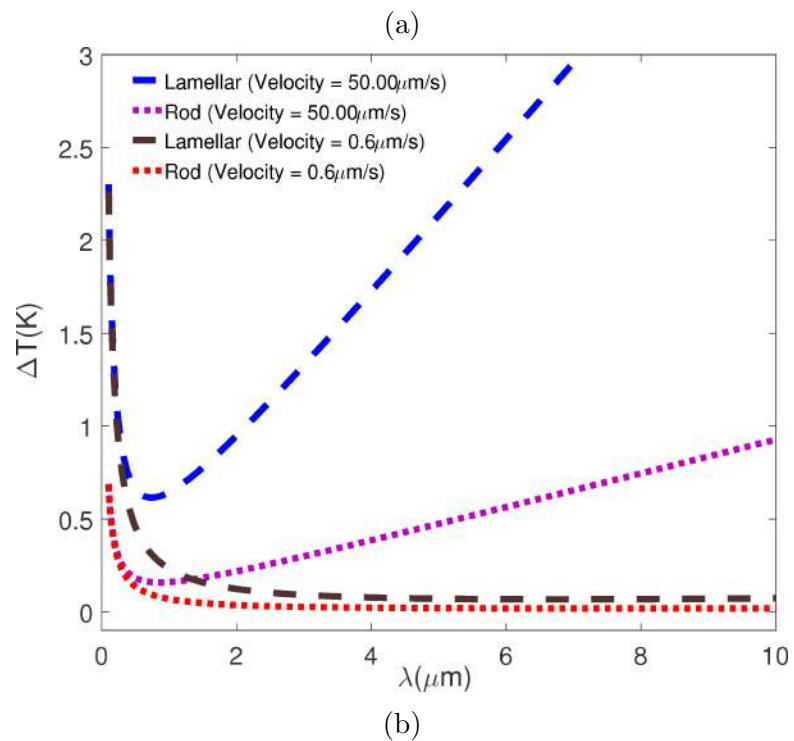
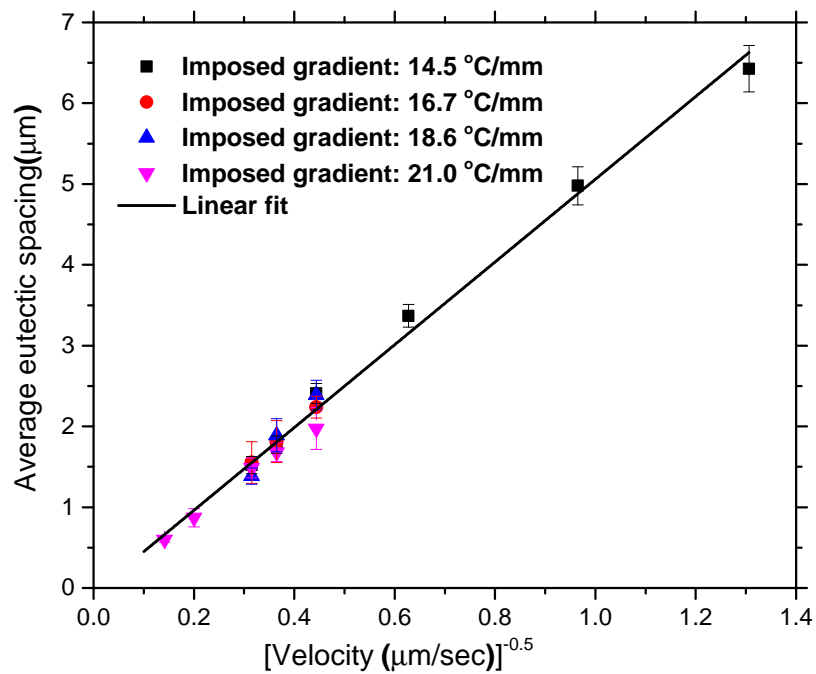


Figure 4.5: (a) Variation of average spacing with velocity and (b) Average undercooling with eutectic spacing.

velocities, and the results are shown in Fig. 4.5a where error bars correspond to the standard deviation of the data obtained over several images. We linearly fit the observed spacings  $\lambda$  against  $V^{-0.5}$  ( $V$  is the velocity), which is also highlighted in Fig. 4.5a, where the slope of the linear fit directly reveals the scaling constant  $\lambda^2 V$  that is approximately  $27.04 \mu\text{m}^3/\text{sec}$  for the Sn-Zn alloy at the eutectic composition.

If we assume that our observed morphology is close to a lamella for most of the imposed conditions, then the corresponding undercooling vs. spacing relation can be calculated using the value of  $\lambda^2 V$  obtained from the experiments. Similarly, we calculated the undercooling vs. spacing relationship for the rod morphology of the alloy (using the equations shown in section 1.2.1.1). The undercooling vs. spacing relations for both the rod and the lamellae morphologies are plotted for the  $50.0 \mu\text{m}/\text{s}$  and the  $0.6 \mu\text{m}/\text{s}$  velocities in Fig. 4.5b. For both velocities, we see that the minimum undercooling for the rod is lower than that of the lamellae, which would suggest going by the arguments in the Jackson-Hunt paper [2] that the rod would be the preferred microstructure. However, this seems contrary to our experimental observations, which seem to suggest that the morphologies are biased more towards lamellae than rods. A possible explanation is already provided by Jackson and Hunt[2] where they propose that anisotropy in the solid-solid interfacial energy may lead to the lamellar morphology possessing a minimum undercooling that is lower than that of the rod microstructure. This is because, for a lamellar morphology, the alignment of the lamellae such that the solid-solid interfaces correspond to the minimum interfacial energy orientations, would lead to a much lower undercooling than the corresponding case of the rod morphology where the solid-solid interface has to perforce possess a larger proportion of orientations that are of higher solid-solid interfacial energy leading to increased undercooling at the growth front. Therefore, it is apparent that lamellar fragment merging events along higher energy orientations would lead to an overall decrease of the growth undercooling with the formation of a more planar interface. Additionally, it would result in a natural biasing of the microstructure that would closely resemble the merging of lamellar fragments along well-defined directions leading to the appearance of a periodic arrangement of broken lamellae. We find experimental evidence of merging of lamellar fragments along well-defined directions in our SEM images as seen in Fig.4.6, where we see an increase in the average length of the broken-lamellar fragment with time, which is shown in Fig. 4.7.

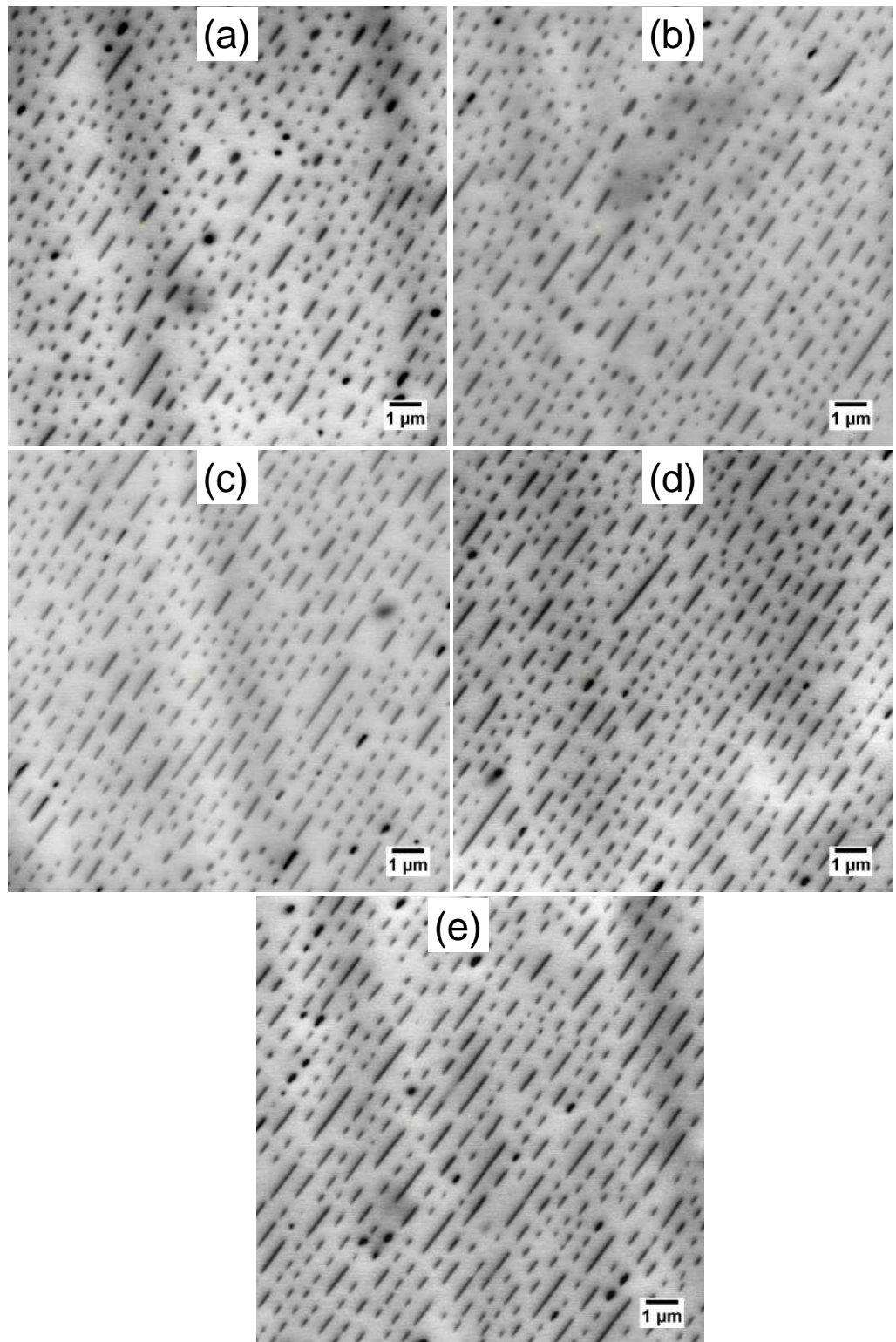


Figure 4.6: Images captured using a SEM, which are taken at equally spaced transverse sections along the growth direction, following the same eutectic grain of the sample solidified at  $50 \mu\text{m/s}$ . (a) is 20 mm from the bottom, (b) is 30 mm from the bottom, (c) is 40 mm from the bottom, (d) is 50 mm from the bottom, (e) is 60 mm from the bottom.

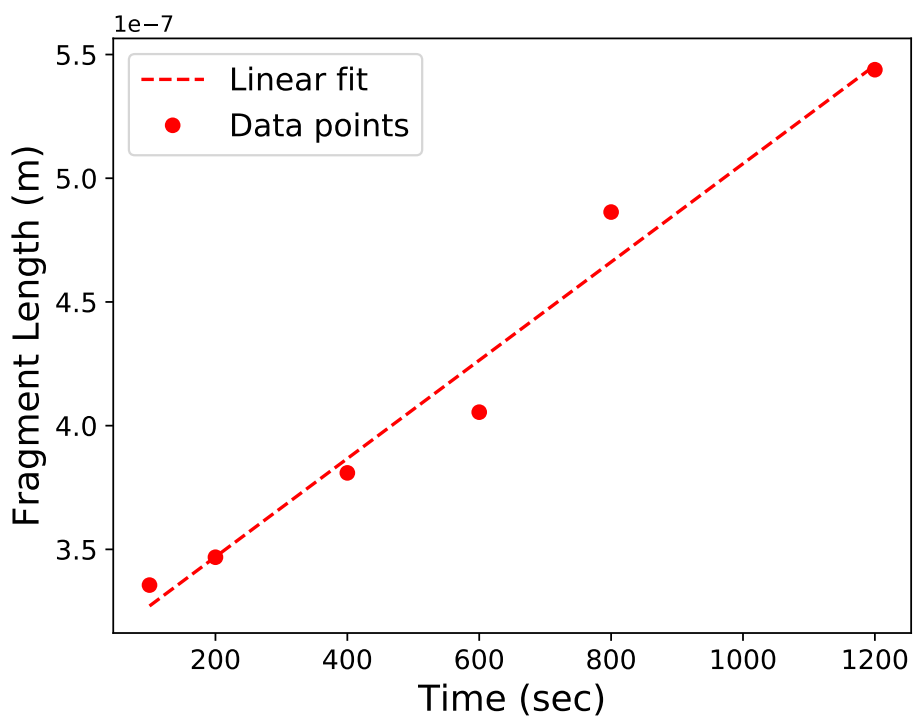


Figure 4.7: Variation of average length of lamellar fragment with time of solidification.

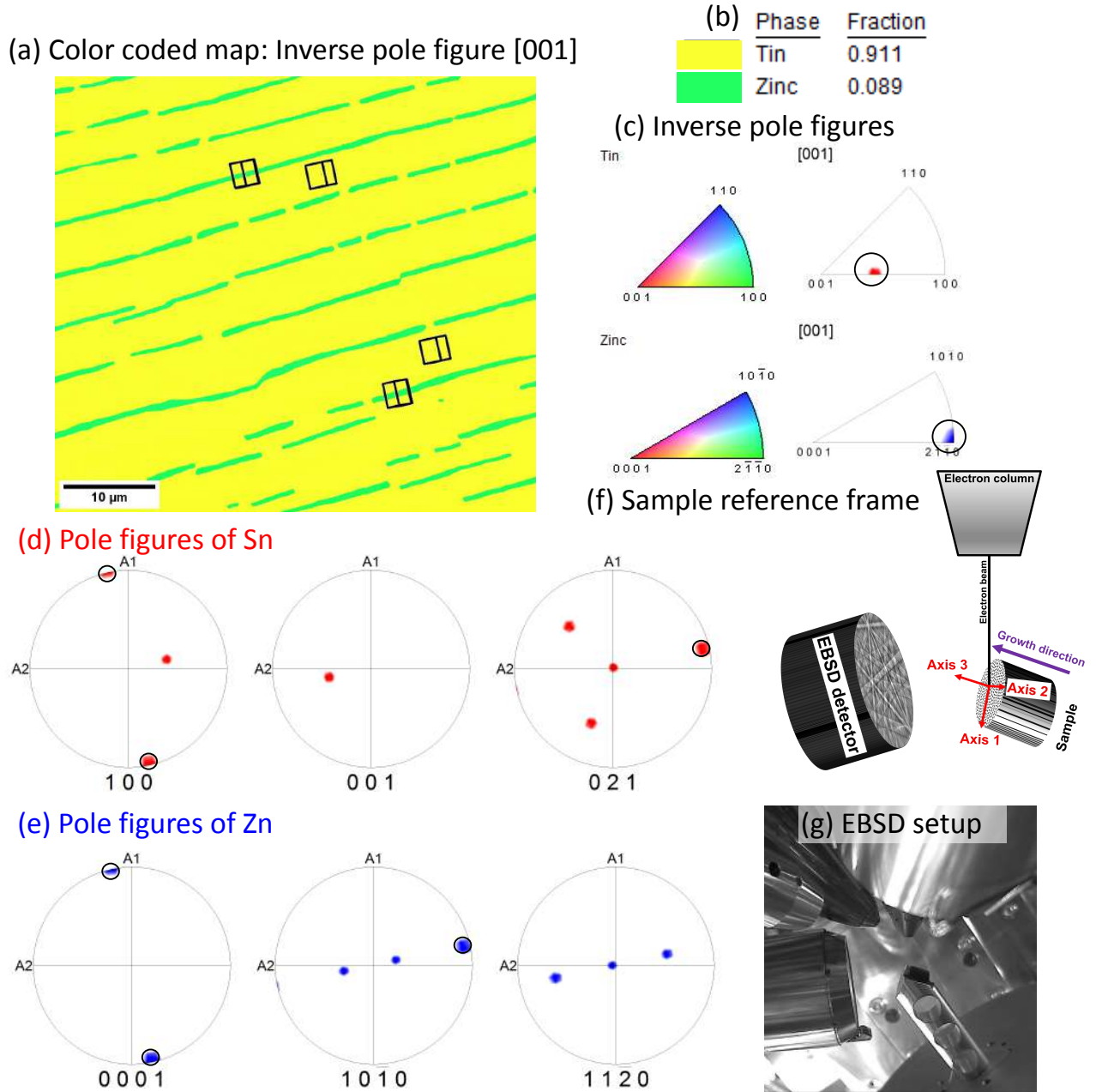


Figure 4.8: (a) is inverse pole figure map of the alloy solidified at  $0.6 \mu\text{m/s}$ . The orientation of the unit cells is depicted in each of the phases that reveal that the basal plane of (Zn) is always parallel to the lamellar interface (given that this transverse section is a true section, i.e., the lamellae plates are oriented exactly perpendicular to the plane of the paper). The orientation relationships that we derive from this experiment is shown in (d) and (e), which is one of the planes in Sn{100} family || Zn{0001} and one of the planes in Sn{021} family || one of the planes in Zn{0110} family.

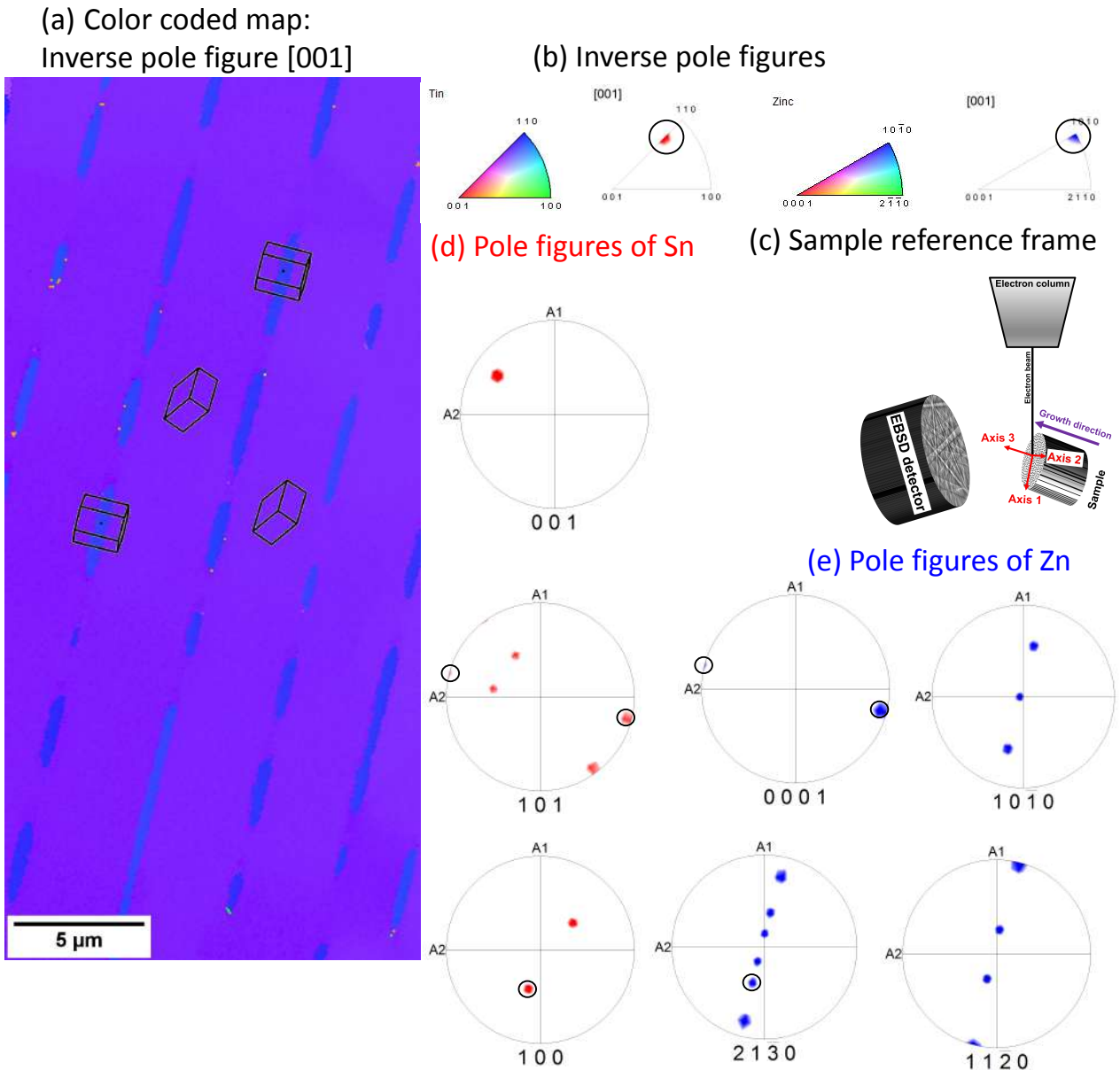


Figure 4.9: (a) is inverse pole figure map of the alloy solidified at  $1.0 \mu\text{m/s}$ . The orientation of the unit cells is depicted in each of the phases that reveal that the basal plane of (Zn) is always parallel to the lamellar interface (given that this transverse section is a true section, i.e., the lamellae plates are oriented exactly perpendicular to the plane of the paper). The orientation relationships that we derive from this experiment is shown in (d) and (e), which is one of the planes in Sn{101} family || Zn{0001} and one of the planes in Sn{100} family || one of the planes in Zn{2130} family.

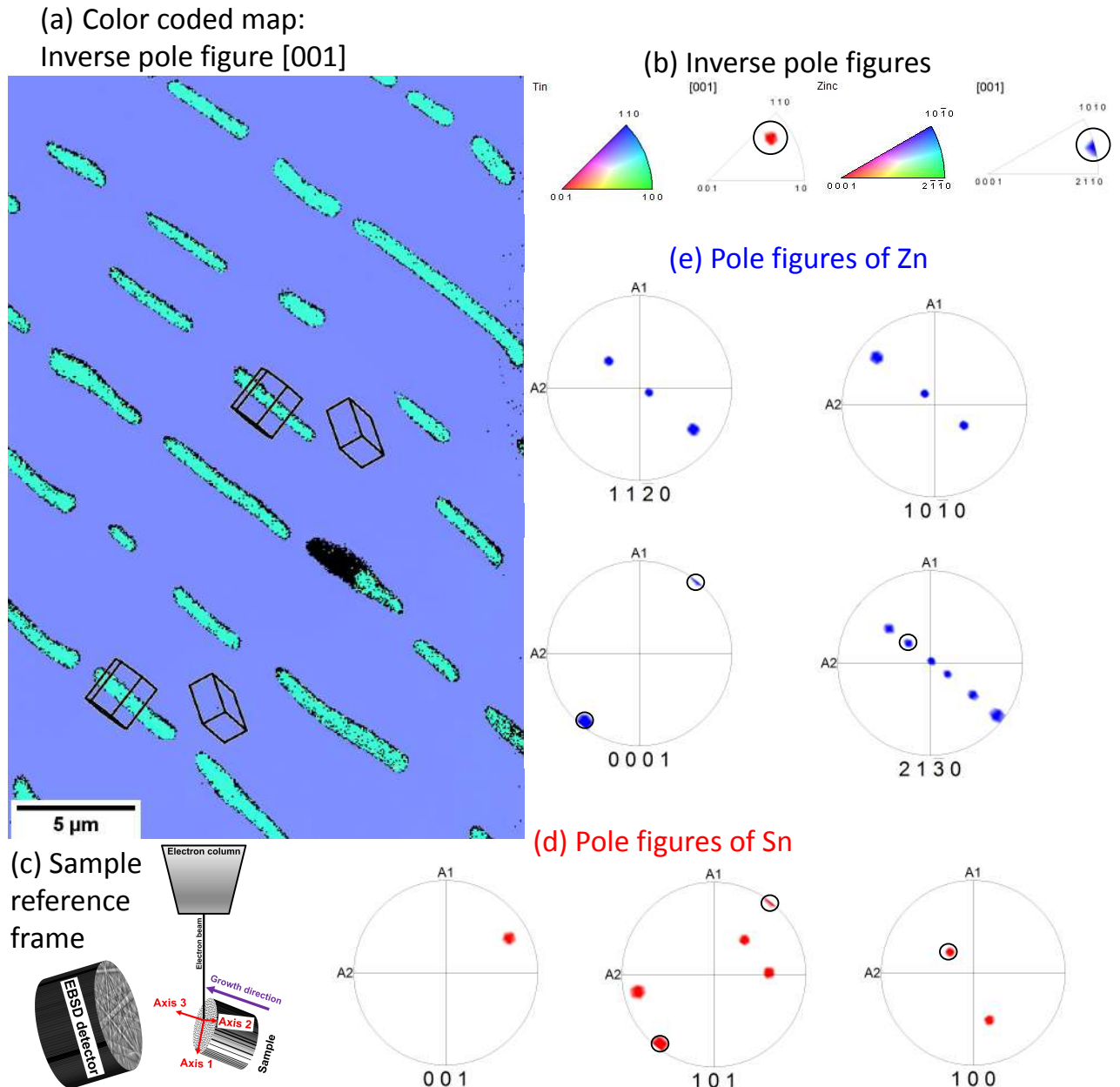
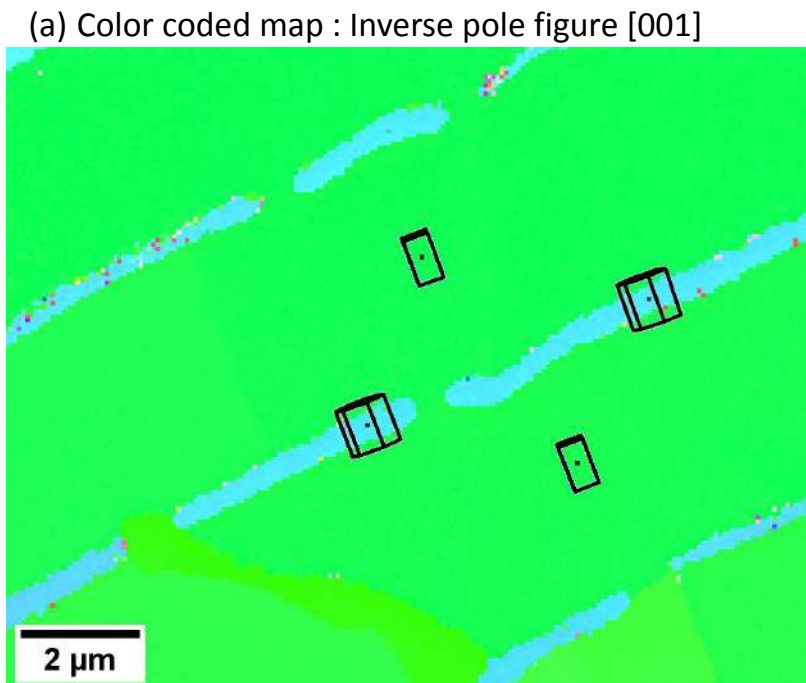
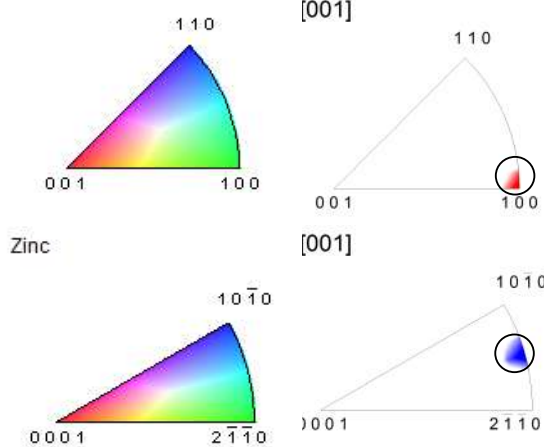


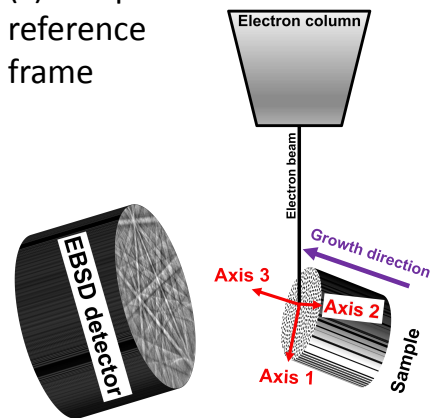
Figure 4.10: (a) is inverse pole figure map of the alloy solidified at  $1.0 \mu\text{m/s}$ . The orientation of the unit cells is depicted in each of the phases that reveal that the basal plane of (Zn) is always parallel to the lamellar interface (given that this transverse section is a true section, i.e., the lamellae plates are oriented exactly perpendicular to the plane of the paper). The orientation relationships that we derive from this experiment is shown in (d) and (e), which is one of the planes in Sn{101} family || Zn{0001} and one of the planes in Sn{100} family || one of the planes in Zn{2130} family.



Tin (b) Inverse pole figures



(c) Sample reference frame



(d) Pole figures of Sn

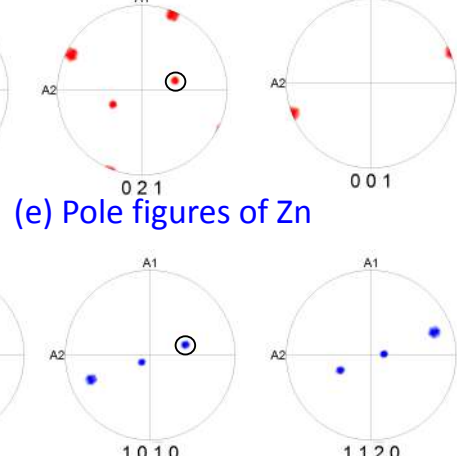


Figure 4.11: (a) is inverse pole figure map of the alloy solidified at  $2.5 \mu\text{m}/\text{s}$ . The orientation of the unit cells is depicted in each of the phases that reveal that the basal plane of (Zn) is always parallel to the lamellar interface (given that this transverse section is a true section, i.e., the lamellae plates are oriented exactly perpendicular to the plane of the paper). The orientation relationships that we derive from this experiment is shown in (d) and (e), which is one of the planes in Sn{100} family || Zn{0001} and one of the planes in Sn{021} family || one of the planes in Zn{0110} family.

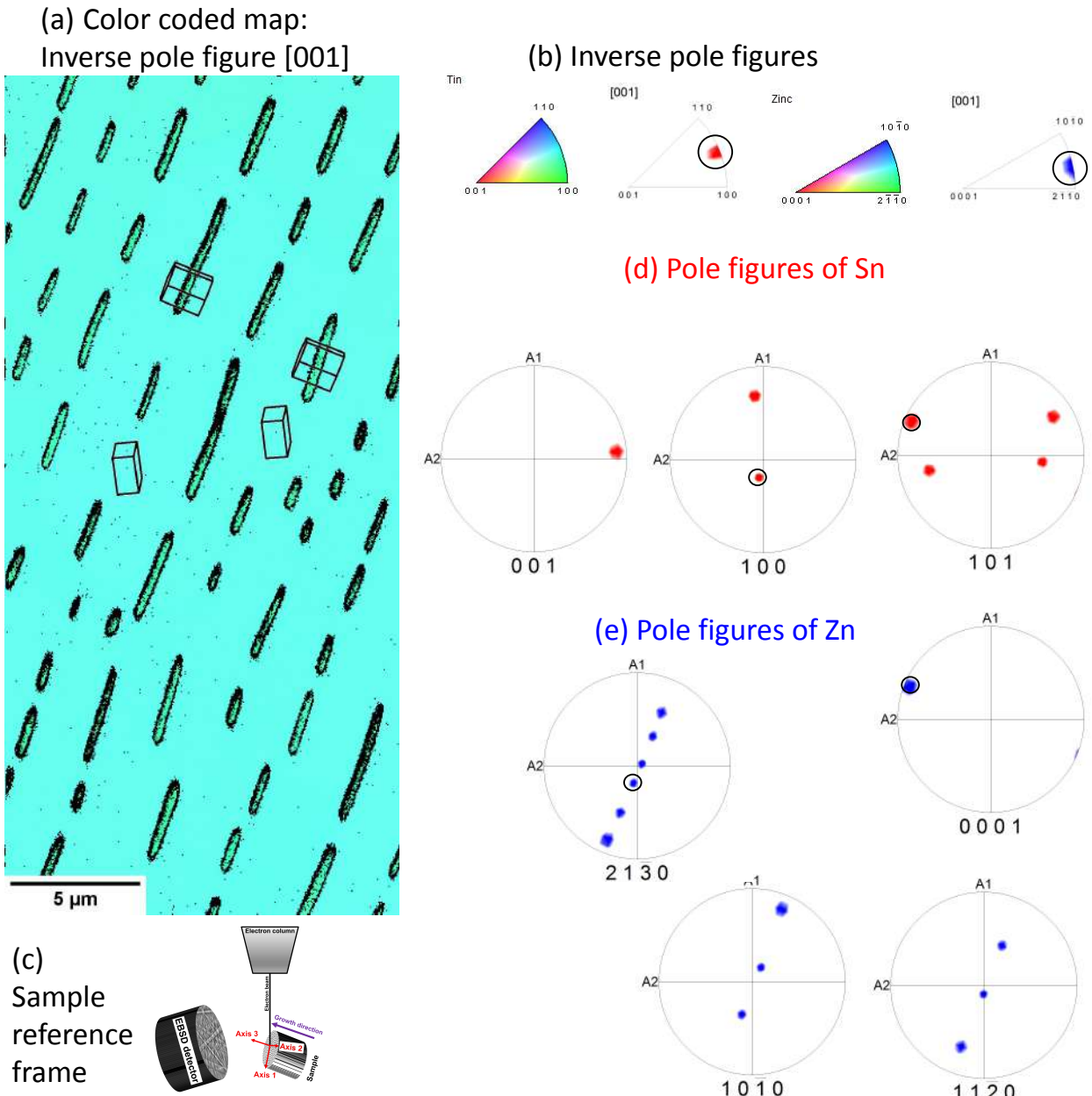
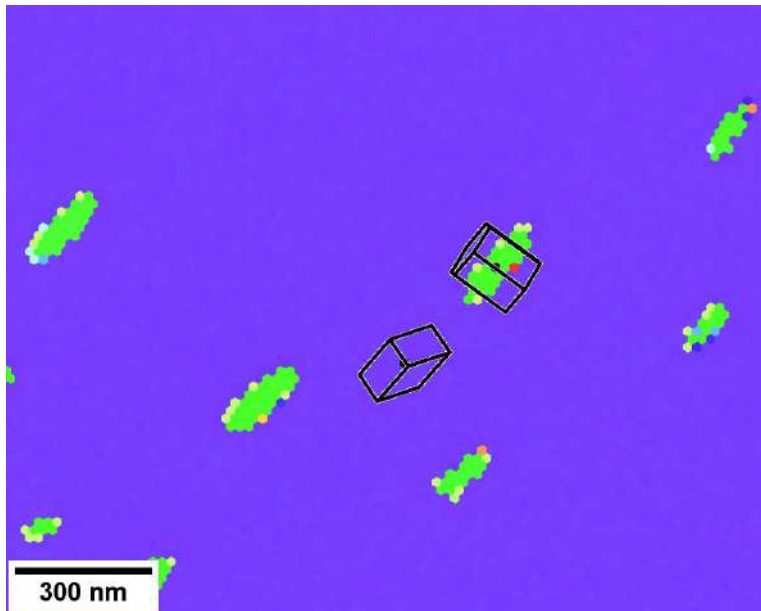
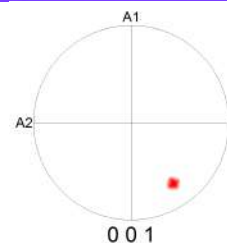
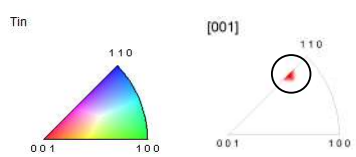


Figure 4.12: (a) is inverse pole figure map of the alloy solidified at  $5.1 \mu\text{m/s}$ . The orientation of the unit cells is depicted in each of the phases that reveal that the basal plane of (Zn) is always parallel to the lamellar interface (given that this transverse section is a true section, i.e., the lamellae plates are oriented exactly perpendicular to the plane of the paper). The orientation relationships that we derive from this experiment is shown in (d) and (e), which is one of the planes in Sn{101} family || Zn{0001} and one of the planes in Sn{100} family || one of the planes in Zn{2130} family.

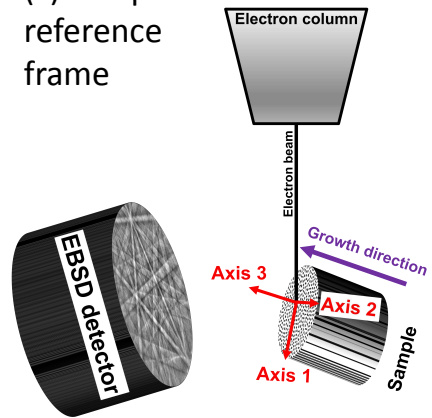
(a) Color coded map : Inverse pole figure [001]



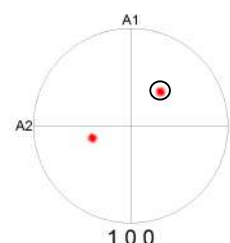
(b) Inverse pole figures



(c) Sample reference frame



(d) Pole figures of Sn



(e) Pole figures of Zn

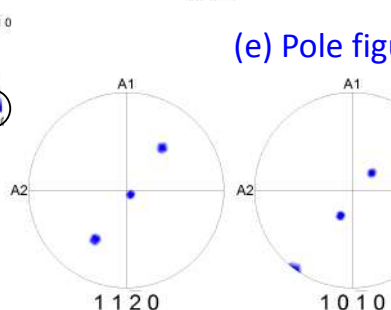
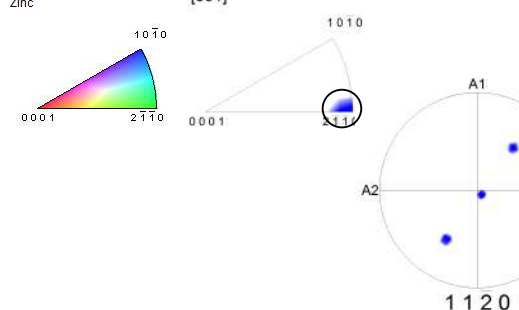


Figure 4.13: (a) is inverse pole figure map of the alloy solidified at  $50.0 \mu\text{m/s}$ . The orientation of the unit cells is depicted in each of the phases that reveal that the basal plane of (Zn) is always parallel to the lamellar interface (given that this transverse section is a true section, i.e., the lamellae plates are oriented exactly perpendicular to the plane of the paper). The orientation relationships that we derive from this experiment is shown in (d) and (e), which is one of the planes in  $\text{Sn}\{101\}$  family ||  $\text{Zn}\{0001\}$  and one of the planes in  $\text{Sn}\{100\}$  family || one of the planes in  $\text{Zn}\{21\bar{3}0\}$  family.

### 4.2.2 Crystallographic orientation aspects

We find crystallographic orientation relationships corresponding to the (Sn) and the (Zn) phases that are reported in literature [178, 136, 179, 180, 168, 137]. However, we do not find a unique relation being reported among the findings from these studies. Chadwick et al. [136, 180] report an orientation relation that suggests that the  $\{\bar{1}01\}$  planes of Sn are parallel to  $\{\bar{1}012\}$  planes of Zn while the  $\langle 120 \rangle$  directions of Sn are parallel to  $\langle 01\bar{1}0 \rangle$  directions of Zn in all of their experiments (irrespective of rod/lamellar morphology). This relation is, however, contradictory to relations reported by Straumanis et al. [178] that are referred to in a separate work[180, 168] who find that the  $\{100\}$  planes of Sn are parallel to  $\{0001\}$  planes of Zn and  $\langle 001 \rangle$  directions of Sn are parallel to  $\langle 01\bar{1}0 \rangle$  directions of Zn. The differences could be due to the technique that the authors employ in order to obtain the orientation relation, wherein Chadwick et al.[180] have used conventional X-ray texture diffractometry whereas Straumanis et al. have obtained the relations based on Laue X-ray reflection method[168]. The problem with these techniques is that X-ray diffraction is not a very sensitive tool for determining crystal orientation relations. In order to clarify the presence/absence of a crystallographic orientation relationship, we have utilized a more sophisticated tool, EBSD, that is currently available. The Kikuchi patterns which are used for determining the crystallographic orientation in EBSD are extremely sensitive to crystal orientation [181, 182] and thereby are more reliable for determining the orientation relationships. EBSD is performed on the transverse sections of the solidified samples and the results obtained are shown in the form of inverse pole figure maps and pole figures (refer to Fig. 4.8, 4.9, 4.10, 4.11, 4.12, and 4.13). We will first mention the principal finding in our thesis, which is that the basal planes of Zn are always parallel to the solid-solid interfaces in the lamellar plate morphology. This points towards the possibility that this is a low-energy orientation for the solid-solid interface and any other orientation is probably energetically unfavorable (detailed description follows). Secondly, we have observed predominantly two orientation relations in our experiments, i.e. one as  $\text{Sn}\{100\} \parallel \text{Zn}\{0001\}$  and  $\text{Sn}\{021\} \parallel \text{Zn}\{0\bar{1}10\}$ ; and other as  $\text{Sn}\{101\} \parallel \text{Zn}\{0001\}$  and  $\text{Sn}\{100\} \parallel \text{Zn}\{21\bar{3}0\}$ , which are depicted in Fig. 4.8, 4.9, 4.10, 4.11, 4.12, and 4.13. We have chosen to report the OR using parallel plane normal vectors in both crystals, which should be geometrically equivalent to the more frequently used method of a combination of plane and a direction, where the direction is in the plane. The combination of planes in each crystal are chosen such that these are perpendicular to each other (one is in the center, and the other is in the great-circle of the stereographic projection, see pole figures in Fig. 4.8, 4.9, 4.10,

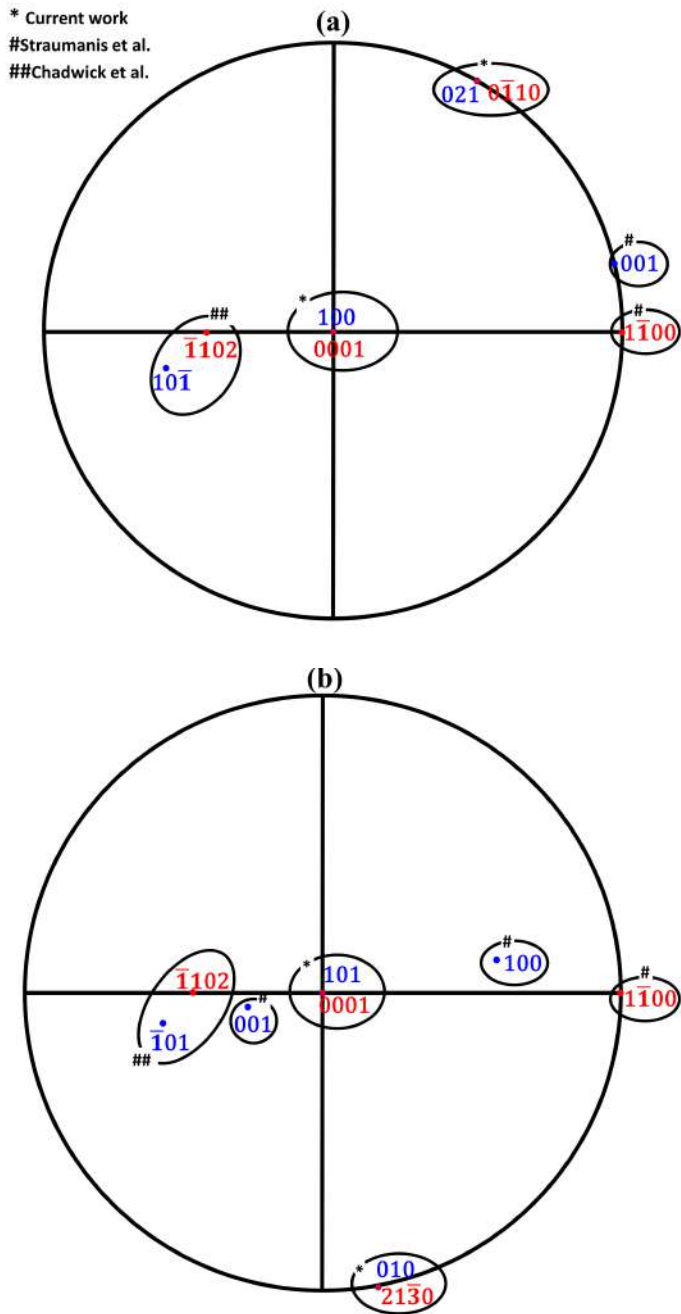


Figure 4.14: (a) Superimposed stereographic projection obtained upon matching the basal planes  $\{0001\}$  of Zn with  $\{100\}$  of Sn, and rotating around these normal vectors to match the second set of planes  $(0\bar{1}10)$  of Zn with  $(021)$  of Sn. (b) Superimposed stereographic projection obtained upon matching the basal planes  $\{0001\}$  of Zn with  $(101)$  of Sn, and rotating around these normal vectors to match the second set of planes  $(21\bar{3}0)$  of Zn with  $(010)$  of Sn. This sets the orientation of the unit-cells/crystals.

[4.11](#), [4.12](#), and [4.13](#). We have verified geometrically by comparing the resultant orientations of the unit-cells that would result with each of the OR mentioned in the previous citations. We find that these are indeed different and are highlighted in the stereographic projections plotted for our results, as shown in Fig. [4.14](#). For instance, the OR from Straumanis et al. [178] has one set of parallel planes, the same as in one of our OR, i.e. ( $\{100\}$  of Sn ||  $\{0001\}$  of Zn). The set of directions from Straumanis et al. [178] that are indexed as  $[h,k,i,0]$  are also the normal vectors of the planes with the same  $\{h,k,i,0\}$  and therefore, we have plotted the poles of the normal vectors of the planes corresponding to the index of the parallel directions. This is highlighted as in Fig.[4.14a](#) where we do not find a match between the said directions  $\{001\}$  of (Sn) and  $\{0\bar{1}10\}$  of (Zn) that are encircled. Therefore, the resultant orientation of the crystals with respect to each other is different from what is reported by Straumanis et al.[178]. Further, the relations reported by Chadwick et al. [180] are entirely different from that of our results. This is highlighted in Fig.[4.14a](#), where the poles corresponding to the suggested parallel planes by Chadwick et al. [180] clearly do not superimpose when we impose the OR that we find in our work as the crystallographic relation between the Sn and Zn crystals. The mismatch with the ORs is also true for the second orientation relation that we find in our work, as shown in Fig.[4.14b](#).

While our relations are therefore different from that reported in the literature, however, we do not claim that this is an exhaustive set, and there could be other possibilities that might have nucleated but are outgrown by crystals with different orientations. Here, we concur with the findings of Jaffrey and Chadwick [136] that it is possibly Sn that nucleates first followed by Zn. We hypothesize that among the orientations of Zn that form, the ones that lead to lower interfacial energy along with a favorable growth direction with respect to the imposed thermal gradient survive and are the ones that are observed at the end of the directional solidification experiment. This fact can be appreciated by comparing the SEM and EBSD images during the initial transient and those occurring later during the solidification (refer Fig. [4.15](#)). Here, we see that while multiple variants of Zn grow along with Sn during the initial transient, a selection of a single variant occurs as solidification progresses that is highlighted in the inverse pole figure of the microstructure occurring later during solidification. The basal planes of (Zn), as well as the (100) and (101) planes of (Sn), are the closest packed planes in comparison to the other planes (refer Fig. [4.16](#)), and this might lead to the formation of a low energy solid-solid interface between the (Sn) and (Zn) crystals. The growth competition among the variants

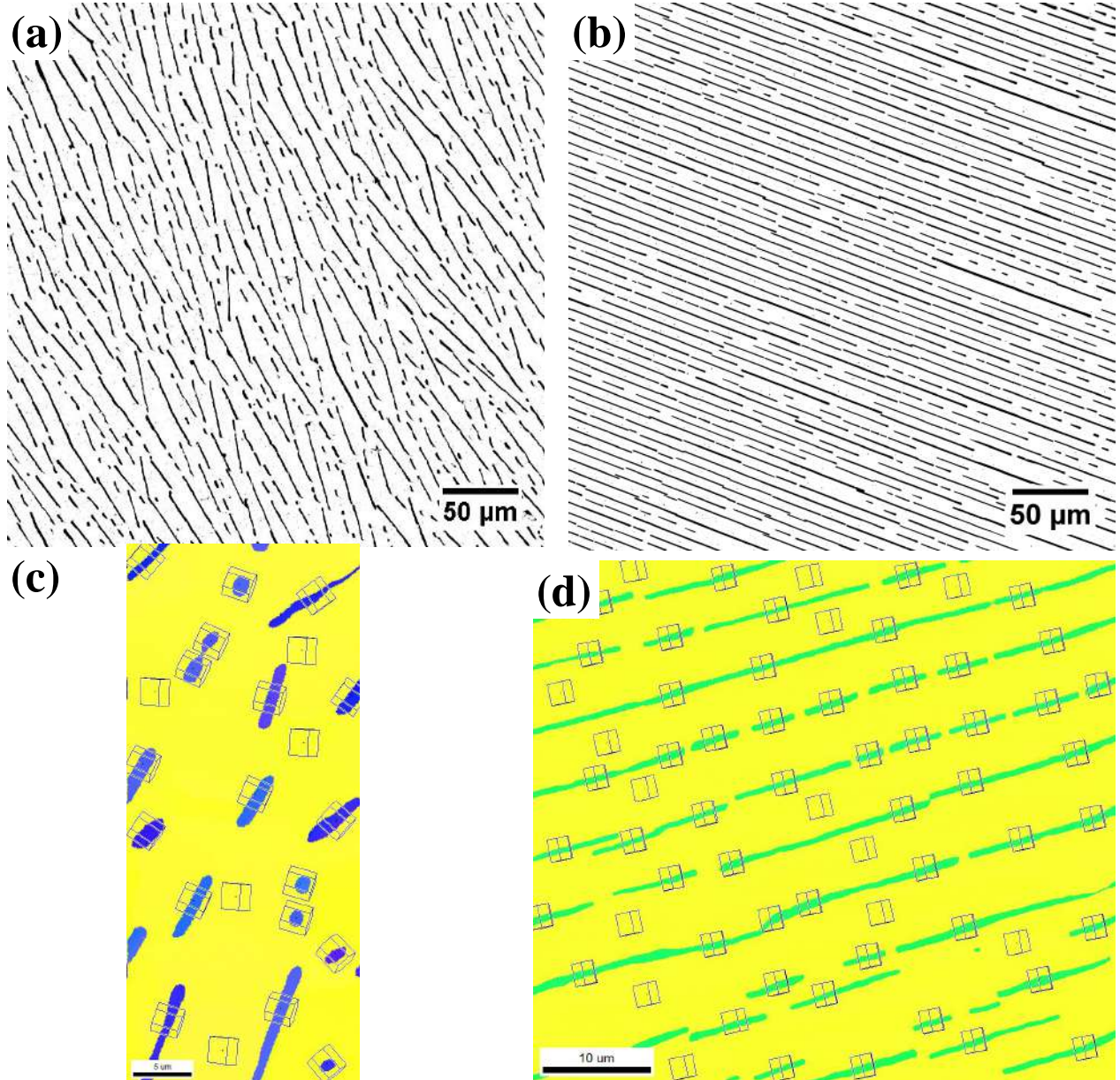


Figure 4.15: Comparison of the SEM images during the initial transient in (a) and later during the solidification in (b). The inverse pole figures in (c) corresponding to the SEM image in (a) reveals the presence of multiple variants of Zn growing along with Sn, while later during the solidification, a single orientation of Zn survives as highlighted in (d). The solidification is carried out at  $0.6\mu\text{m}/\text{s}$ .

that might nucleate must undoubtedly depend on the solid-solid interfacial energy, and this is certainly an interesting topic for future research. However, the common thing we find in all our experiments is that the basal planes  $\{0001\}$  of (Zn) and either  $\{100\}$  or  $\{101\}$  planes of (Sn) are always parallel to the lamellar interface. The results reported by Straumanis et al. [178] also has the (Zn) basal planes and (100) planes of (Sn) parallel to the lamellar interface [180]. In the EBSD results of all our experiments on transverse sections (refer to inverse pole figures

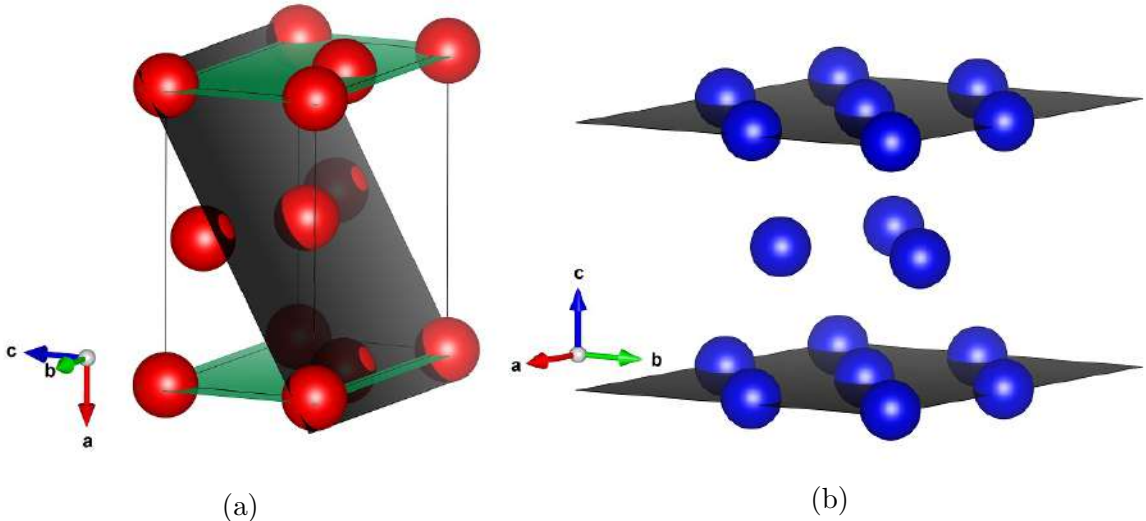


Figure 4.16: (a) Unit cell of (Sn) where  $\{100\}$  and  $\{101\}$  planes are highlighted, while (b) Unit cell of (Zn) where  $\{0001\}$  planes are highlighted using VESTA [13]. Highlighted planes corresponds to close packed planes.

and their maps in Fig. 4.8, 4.9, 4.10, 4.11, 4.12, and 4.13), we do not observe a preferential growth direction to suggest the presence of any interfacial energy anisotropy of the solid-liquid interface. What we do expect, however, is that since the basal plane of Zn is always parallel to the lamellar interface and because of which it seems that Zn decides the orientation of the solid-solid interface, the solid-solid interfacial energy is likely anisotropic, where the orientation for which the lamellar interface becomes parallel to the Zn basal planes, also corresponds to a low energy direction in the  $\gamma-$  plot of the solid-solid interfacial energy. In the following, we present experimental evidence of anisotropy in the solid-solid interfacial energy.

### 4.2.3 Evidence of anisotropy

Experimental evidence of anisotropy may be derived by imposing changes in the growth directions and seeing the relative change in the solid-solid interface orientations. One of the ways of causing a change in the growth direction is by modification of the thermal and solutal gradients in the crucible so as to have biased growth in specific directions. Some of the ways of achieving this are by changing the geometry of the crucible, such as introducing hoops or bends [136, 183]. In the following, we choose a geometry (see Fig.4.17) of the crucible(quartz tube) that would lead to the introduction of lateral thermal and solutal gradients in the crucible that is intended to influence a change in the growth direction of the crystals. This is because, as the crystals approach a bend, the liquid that is closer to the acute end(the edge of the quartz tube that makes an acute inner angle with the horizontal)of the bend, will get hotter with respect to the obtuse end(the edge of the quartz tube that makes an obtuse angle with the inner horizontal) of the quartz tube because of geometric confinement of the released latent heat. This will introduce a lateral thermal gradient over and above the thermal gradient that is imposed in the growth direction leading to a change in the orientation of the resultant thermal gradient. Similarly, the solutal gradients will also get affected as solute rejection in the confined space next to the acute bend compared to the relatively free-liquid ahead of the obtuse bend will lead to a change in the direction of the solutal fluxes. Isotropic crystals would typically be influenced by the change in the thermal and solutal gradients, and there would be associated changes in the growth direction of the crystals as shown in Fig.4.17(b), however, this is not true in the presence of anisotropy (refer to Fig. 1.16 in section 1.3.3.1). Fig.4.18 shows a collage of SEM images as the Sn and Zn crystals grow into a quartz bend. We see that the Sn and Zn crystals that are present in the straight section of the quartz tube continue to grow in the same direction, as they grow into the bend, without a change in the orientation of the solid-solid interface. However, at the obtuse end of the quartz tube nucleation of new grains is apparent. We performed a crystallographic analysis at different locations of the longitudinal section of the sample near the bend in order to verify this as highlighted in Fig.4.19. We find that while the initial eutectic grain continues to grow in the original direction, new Zn-crystals continuously nucleate at the obtuse end during growth, whereas the Sn-crystal retains its original orientation during growth ahead of the bend. The fact that the original eutectic grain in the straight part of the quartz tube does not change direction, while it moves into the bend, provides apparent evidence that the solid-solid interface is probably corresponding to a low energy orientation in

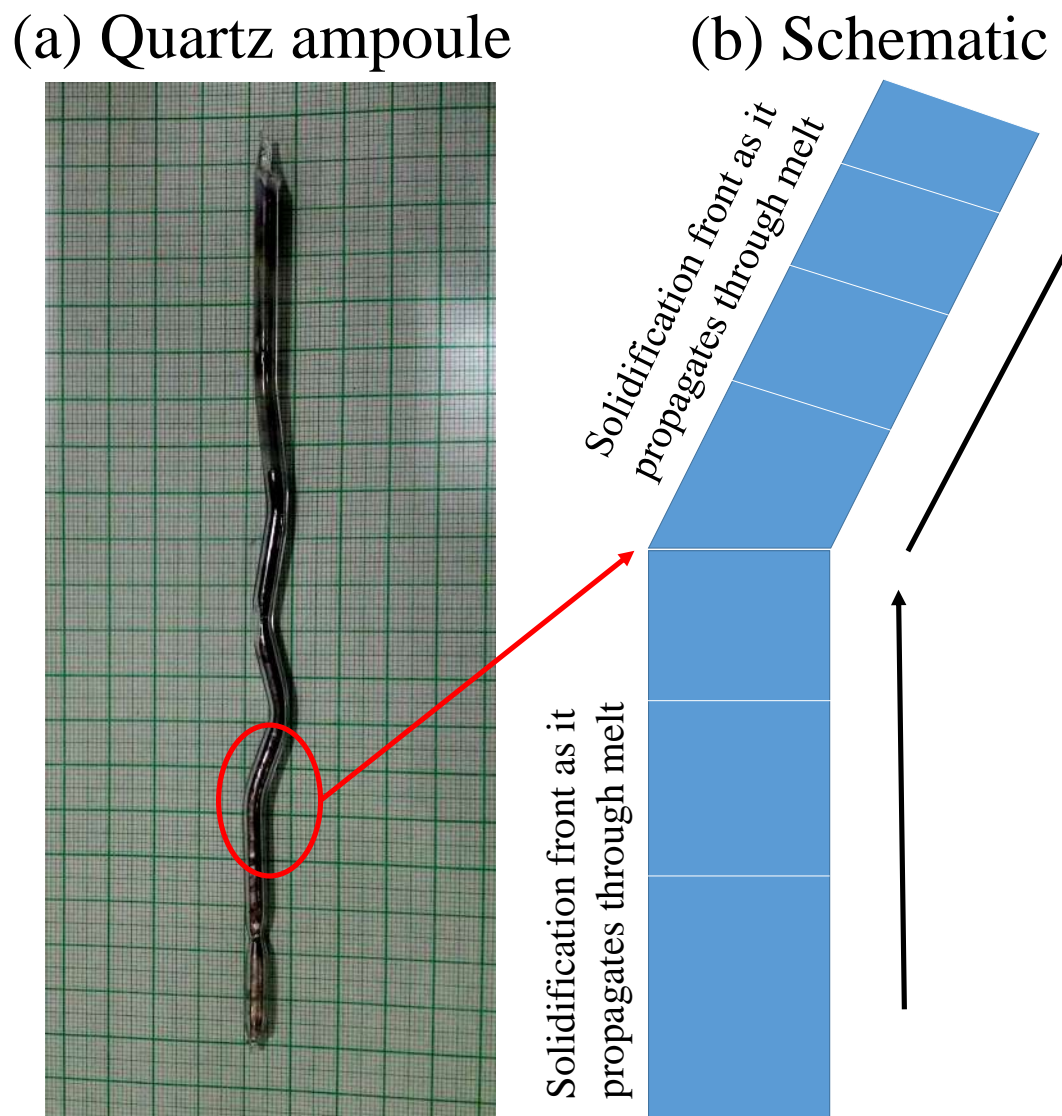


Figure 4.17: (a) Modified quartz tube showing bends that are intended to cause a change in the orientation of the solid-liquid interface as depicted in (b). A small constriction is given at the lower end so as to cause the solidification of a single grain into the straight section of the quartz tube.

the  $\gamma -$  plot of the solid-solid interfacial energy for a given crystallographic relation between the Sn- and the Zn- crystals. This is the same conclusion that Jaffrey and Chadwick [136] reach on performing a similar experiment. In addition, since we did not determine any fixed growth directions from the crystallography the only reason that remains for noticing such invariance in growth directions with the change in heat and mass flow conditions, is possibly because the solid-solid interface is indeed anisotropic.

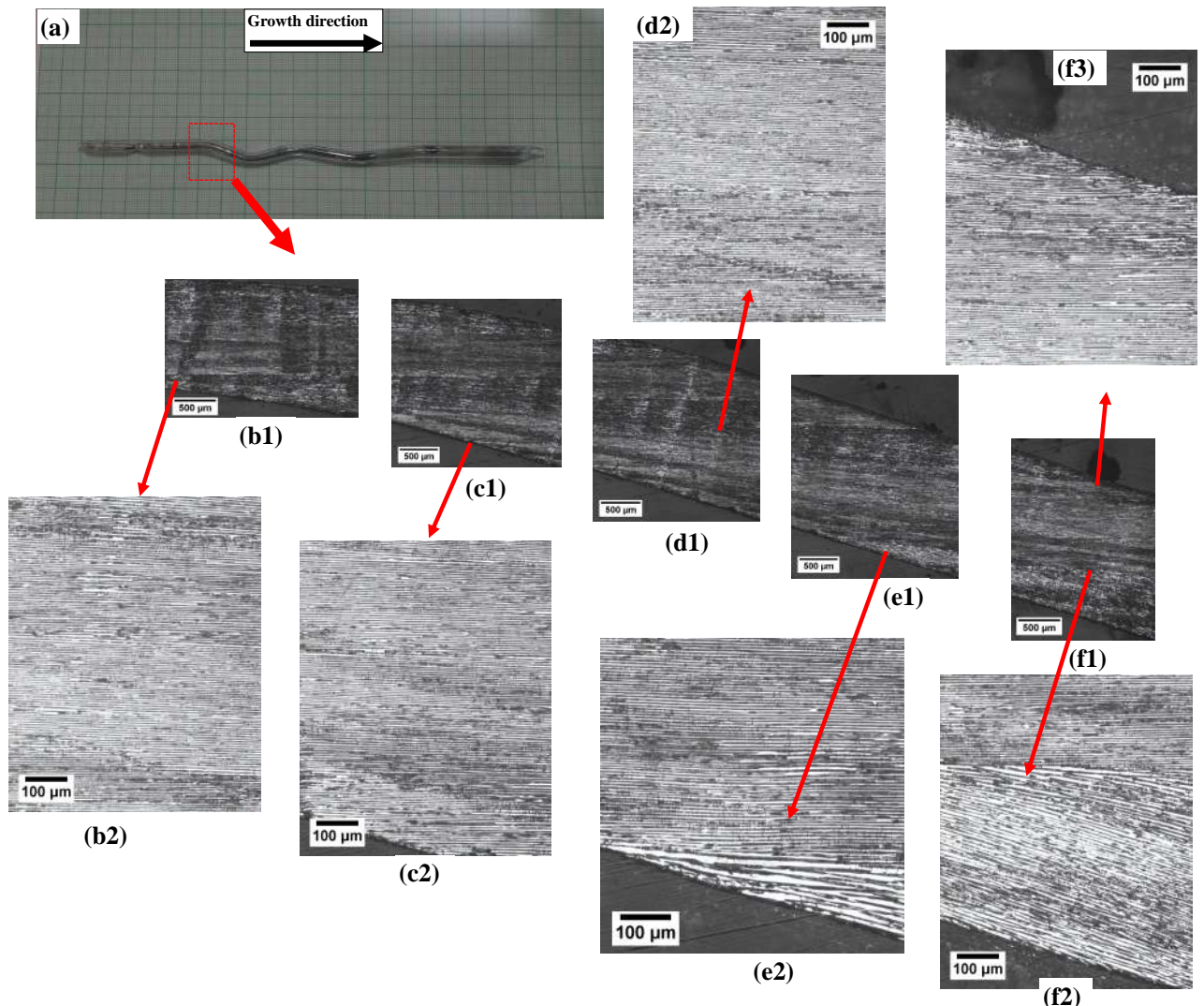


Figure 4.18: Collage of SEM images revealing the change in the microstructure as the solidification proceeds across the quartz bend shown in (a), starting from b1 to f1 through c1, d1, e1 respectively and the corresponding high-magnification images are shown in b2, c2, d2, e2, f2, f3.

In order to provide further evidence for the anisotropy in the solid-solid interfacial energy,

For location of the images, refer previous figure

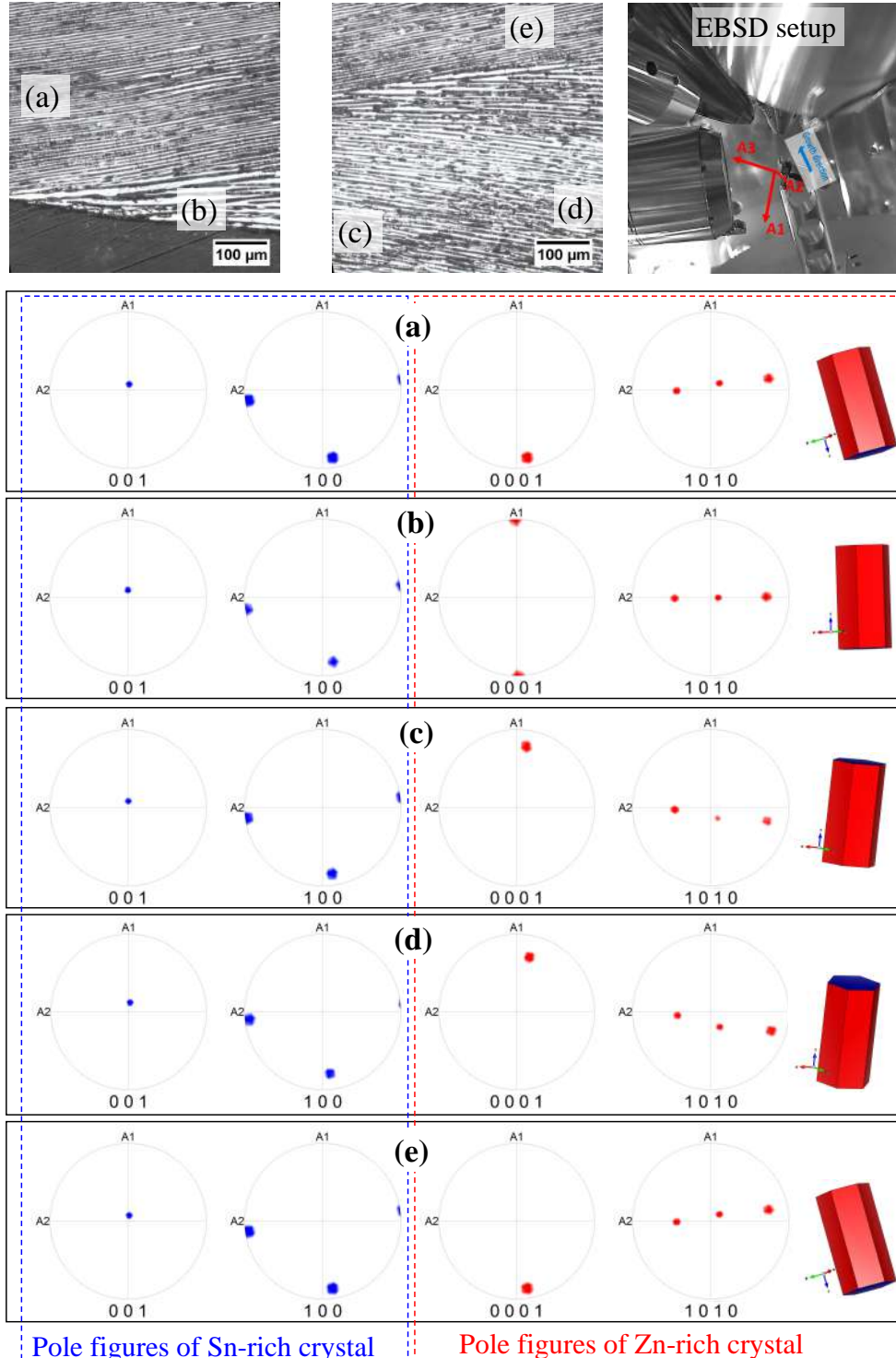


Figure 4.19: Crystallographic orientations of the eutectic phases obtained using EBSD at different locations on the longitudinal section (which are highlighted as a, b, c, d, and e on the SEM image) of the sample near the bend in the quartz tube. While Sn maintains its orientation, nucleation of Zn is evident.

we performed an additional experiment in which we cut a small piece from a directionally solidified sample and utilize this as a seed for another directional solidification experiment. For the latter experiment, however, we impart a physical rotation to the seed with respect to the original growth direction. This is illustrated in Fig.4.20 depicts this procedure where the original sample is cut at an angle with respect to the growth direction, and then the sample is placed in the quartz tube with the sectioning plane normal perpendicular to the crucible axis. This, therefore, imparts a rotation to the original grain with respect to its previous growth direction. Thereafter, we conduct the directional solidification experiment by utilizing the

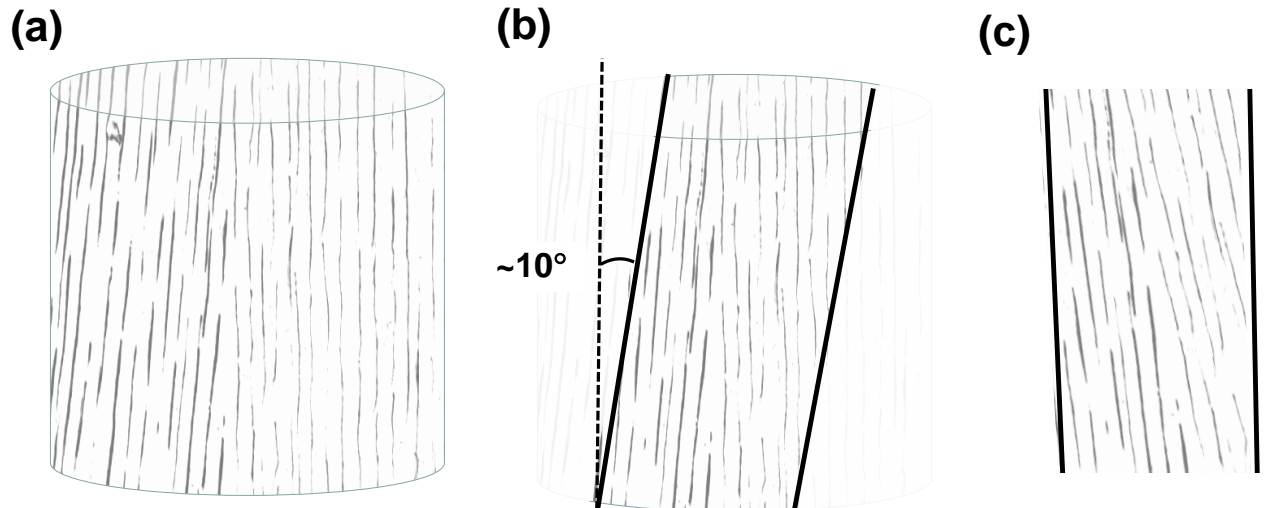


Figure 4.20: (a) Depicts a directionally solidified sample with two grains that is utilized as a seed; one of the grains is aligned straight with respect to the cylindrical axes, while the second has a slight tilt. (b) The angle of the cutting plane that dissects the sample at an angle of  $\sim 10^\circ$  with respect to the growth direction. (c) The cut sample is placed such that planes along which the sample is sectioned are aligned with the quartz tube. This, therefore, mimics the situation where the original sample is now rotated with respect to the growth direction.

rotated seed, and the microstructure is depicted in Fig.4.21(a). Here, we see that the grains upon re-solidification continue to retain the same direction for the solid-solid interface which implies that the growth direction of the crystals is rotated by the same amount as the magnitude of the physical rotation of the seed. We have also verified that the crystals that re-solidify share the same crystallographic orientation of the original seed, as shown in Fig.4.21(b), and thus, there is no renucleation. Thus, it is clear that once the crystal orientations are fixed, the

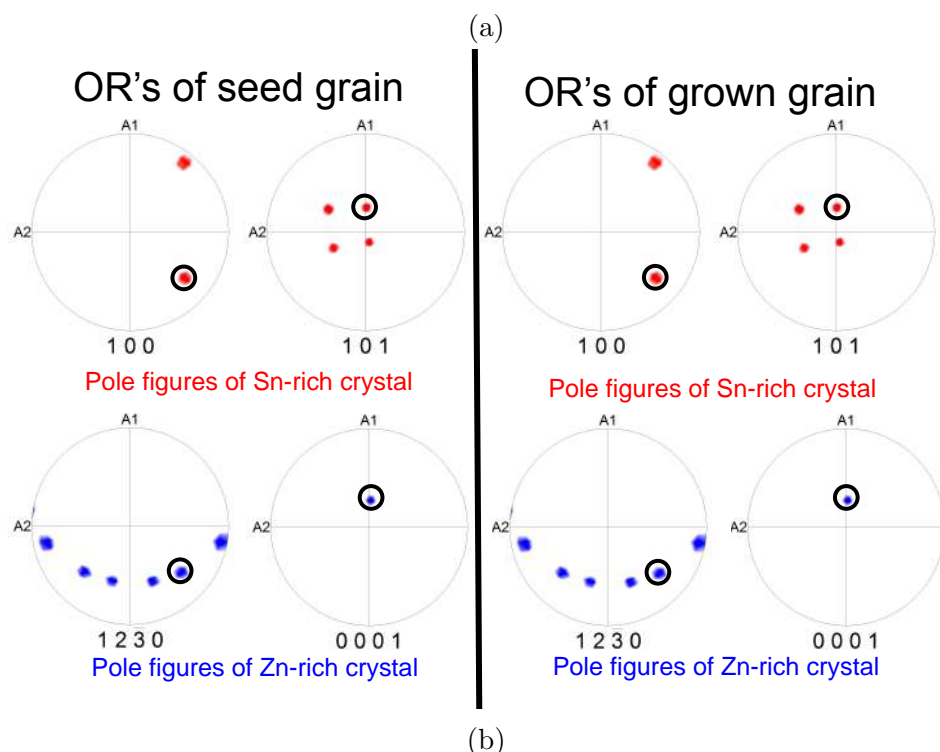
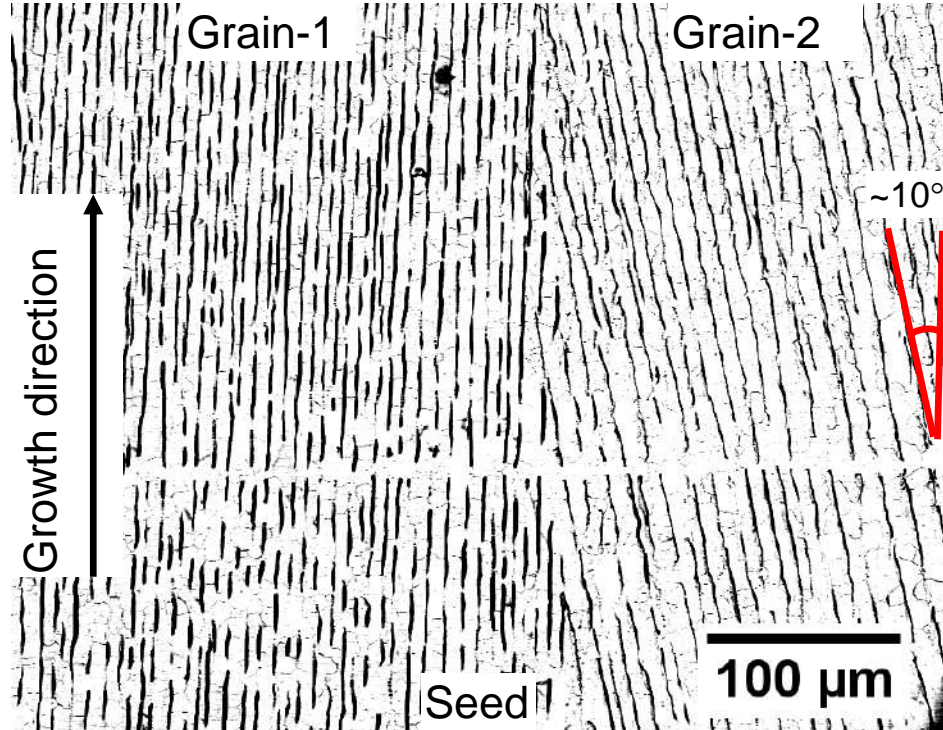
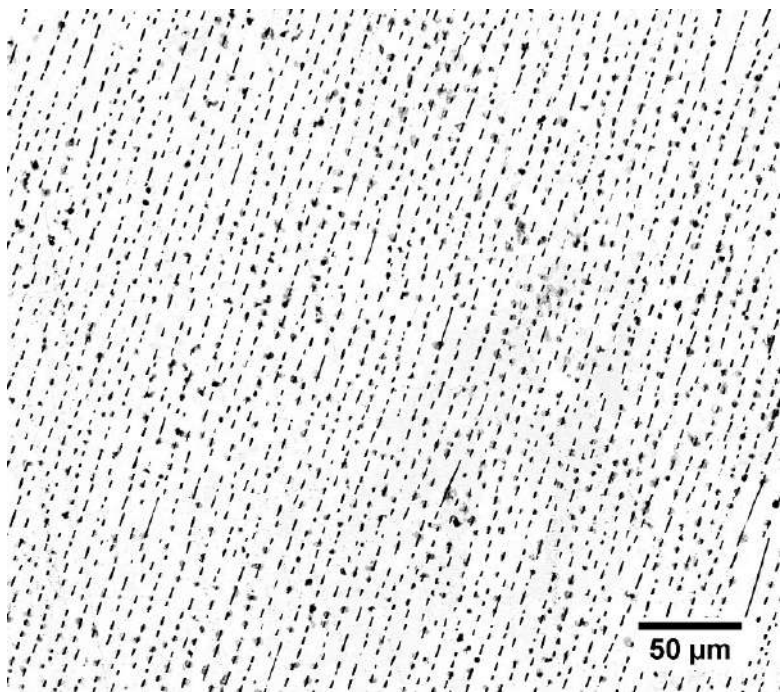


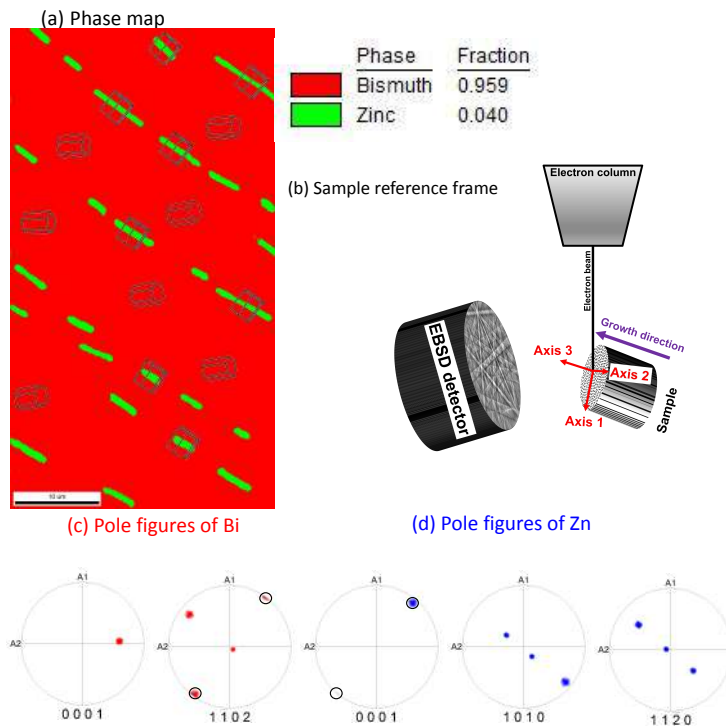
Figure 4.21: (a) Microstructure of the directionally solidified sample that is solidified using a seed. The horizontal discontinuity in the microstructure demarcates the location from which the resolidification begins. (b) Pole plots for the Grain-2 in (a) derived from EBSD show that the crystallographic orientations of re-solidified grains match that of the original seed.

orientation of the lamellar interface gets determined, and therefore, the lamellar orientation in this alloy is a function of the crystallography of the individual phases and not a function of the imposed thermo-solutal conditions as in isotropic crystals. This, therefore, suggests and provides further evidence that the solid-solid interface in the Sn-Zn alloy is anisotropic.

While the crystallographic and experimental characterization indeed points towards the possibility of anisotropy in the solid-solid interfacial energy we presently do not have an estimation of its form. Additionally, because of the aforementioned reasons, that it is predominantly the Zn-crystal that determines the orientation of the solid-solid interface, it seems plausible that the Wulff-plot of the solid-solid interface inherits the symmetry of the Zn crystal. A possible approximation with regards to the symmetry of the  $\gamma$ - plot may be derived from the fact that the principal plane that leads to the anisotropy in the solid-solid interfacial energy is the basal plane of the Zn-rich phase. Out of plane orientations (perpendicular to the direction of solidification) would then certainly have at least a two-fold symmetry while in-plane rotations (in the plane of the lamellar interface) could have a maximum six-fold symmetry. A quantitative determination of the form and strength of the anisotropy maybe ascertained using RDS [147] that can reveal the trace of solid-solid interface as the orientation of the solid-solid interface is changed during solidification keeping all other parameters fixed. This remains the scope for future work. However, our proposed hypothesis that the presence of the solid-solid interfacial energy anisotropy leads to the formation of broken-lamellar morphologies forms the motivation of a theoretical analysis in our group which presents evidence based on dynamical phase-field simulations. Finally, while through our results, we argue that the solid-solid interface is anisotropic, it is kind of surprising that we don't find evidence for the presence of solid-liquid interfacial energy anisotropy, considering that previous studies [184] show that the Zn-liquid interface is anisotropic, particularly because the basal planes of Zn corresponds to a deep minimum in the  $\gamma$ - plot of the solid-liquid interfacial energy. We believe this is because the basal plane in the eutectic morphology is parallel to the solid Sn instead of the liquid, and thereby, we don't observe either faceting of the solid-liquid interface or unique growth directions that would indicate the presence of strong solid-liquid anisotropy. In the configuration where the basal planes are parallel to the lamellar interface, it possible that the  $\{10\bar{1}0\}$  and  $\{11\bar{2}0\}$  face the liquid, and in the microstructures, it is not evident that either of these planes show any faceting. Therefore, while it is true that the presence of solid-liquid interfacial energy anisotropy in an appropriate form could also lead to the formation of lamellar-like structures,



(a) Transverse section image of Bi-Zn eutectic solidified at 1.0  $\mu\text{m}/\text{s}$ .



(b) Phase map and pole figures of Bi-Zn eutectic solidified at 1.0  $\mu\text{m}/\text{s}$ .

Figure 4.22: Morphology and crystallography of Bi-Zn eutectic system showing close relation to Sn-Zn eutectic system.

however, since we do not find evidence of strong anisotropy in the solid-liquid interfaces, the formation of these structures can most certainly be attributed to the presence of anisotropy in the solid-solid interfacial energy.

#### 4.2.4 Similarities with Bi-Zn eutectic

This type of broken-lamellar morphologies is not just limited to the Sn-Zn system, the Bi-Zn eutectic system, which has an even lower fraction of the Zn-rich phase, also exhibits a broken-lamellar morphology with the basal planes of Zn being parallel to the lamellar interface as shown in Fig.4.22. Apparently then, it is the orientation of the Zn crystal that determines the orientation of the solid-solid interface in such alloys.

### 4.3 Summary

In this chapter, we have investigated two-phase growth in the Sn-Zn alloy, where the minority phase fraction is low. Using directional solidification experiments, we derive that the microstructures during invariant growth in this alloy are predominantly “broken-lamellar”. Additionally, from the etched SEM images, we have measured the spacings between the broken-lamellae units and estimated the eutectic scaling constant as  $\lambda^2 V = 27.04 \mu\text{m}^3/\text{sec}$ . We find that the experimental observations of a broken-lamellar arrangement are not in agreement with theoretical predictions based on a Jackson-Hunt type analysis for isotropic conditions using undercooling vs. spacing relationships of the morphologies. We propose that this deviation is possibly due to the solid-solid interfacial energy being anisotropic that leads to the merger of lamellar fragments along higher interfacial energy orientations. Subsequently, characterization using EBSD of samples obtained from several experiments were conducted, on the basis of which we find two crystallographic relations, i.e., first OR is one of the poles in Sn{100} family || Zn{0001} and one of the poles in Sn{021} family || one of the poles in Zn{0110} family; and other OR is one of the poles in Sn{101} family || Zn{0001} and one of the poles in Sn{100} family || one of the poles in Zn{21̄30} family both of which are different from the ones reported in the literature. While we do not find a unique orientation relationship, we always find that the basal planes {0001} of the Zn-rich phase and either of one of the planes in {100} or {101} family of the Sn-rich phase are parallel to the solid-solid interfaces that form the lamellar morphology. The fact that the orientation of the Zn-crystal always determines the orientation of the lamel-

lar interface points to the possibility that the solid-solid interface is anisotropic. Further, the orientation of the lamellar interface for which it becomes parallel to the basal planes of (Zn) is probably a low-energy orientation in the  $\gamma$ - plot of the solid-solid interfacial energy. While we do not present the actual Wulff-plot of the solid-solid interface, we do show evidence that the solid-solid interface is indeed anisotropic.

# Chapter 5

## Exotic two-phase eutectic colonies in Sn-Te system

*"All truths are easy to understand once they are discovered; the point is to discover them." –Galileo Galilei*

In the previous chapter, we investigated the existence of solid-solid interfacial energy anisotropy, which results in the formation of broken-lamellar structures instead of rod microstructures in the Sn-Zn eutectic system with a very low minority phase fraction. This chapter deals with the formation of two-phase microstructures in binary Sn-Te and ternary Sn-Te-X eutectic alloys, where X stands for Ag, Cu, In, Ge, or Sb.

### 5.1 Binary Sn-Te eutectic

Te-15 at.%Sn undergoes an invariant eutectic reaction at 401 °C during which the liquid transforms into SnTe (intermetallic compound) and tellurium solid solution as shown in the Sn-Te phase diagram of Fig. 5.1). Tellurium crystallizes into a trigonal structure (space group is P3<sub>1</sub>21) whereas SnTe compound crystallizes into a NaCl-type cubic structure (space group is Fm $\bar{3}$ m) [185, 186].

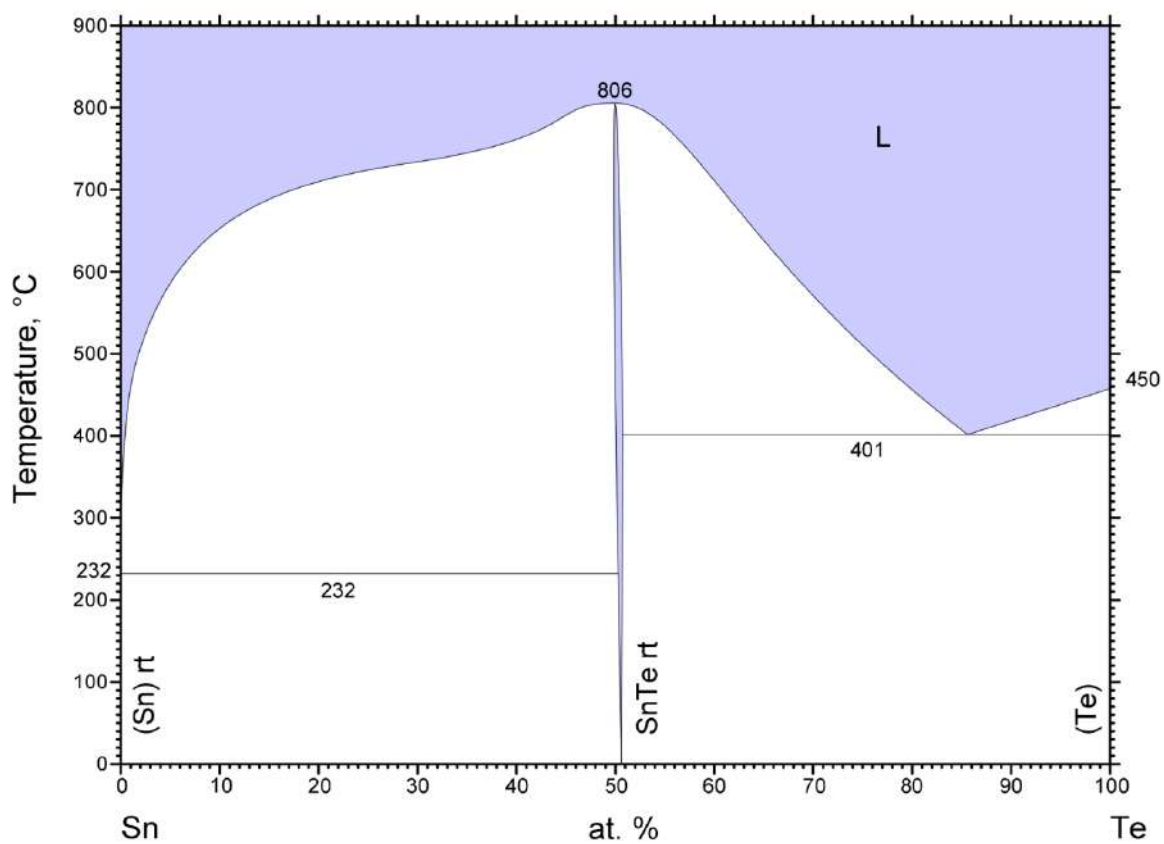


Figure 5.1: Sn-Te binary phase diagram [14].

## 5.2 Results and discussions

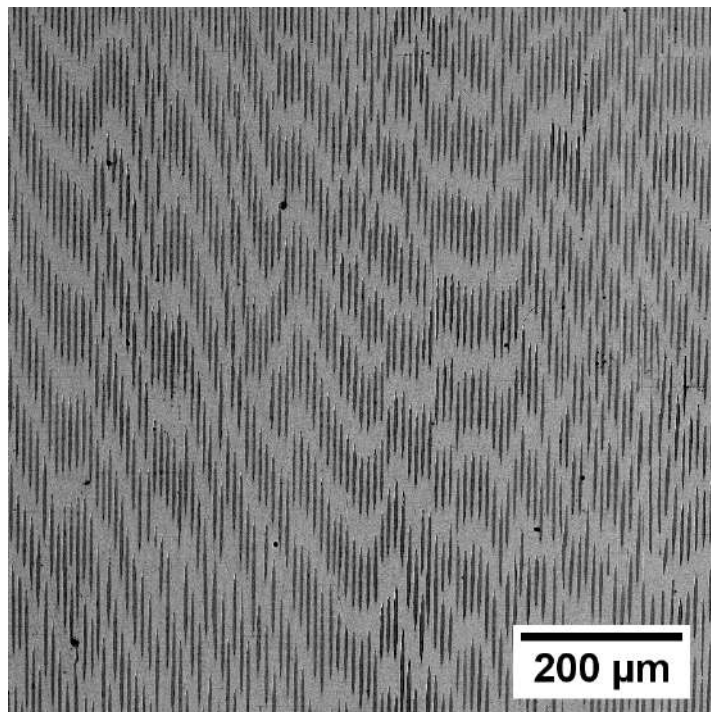
### 5.2.1 Microstructure evolution in binary Sn-Te eutectic

#### 5.2.1.1 Morphology and length scale selection

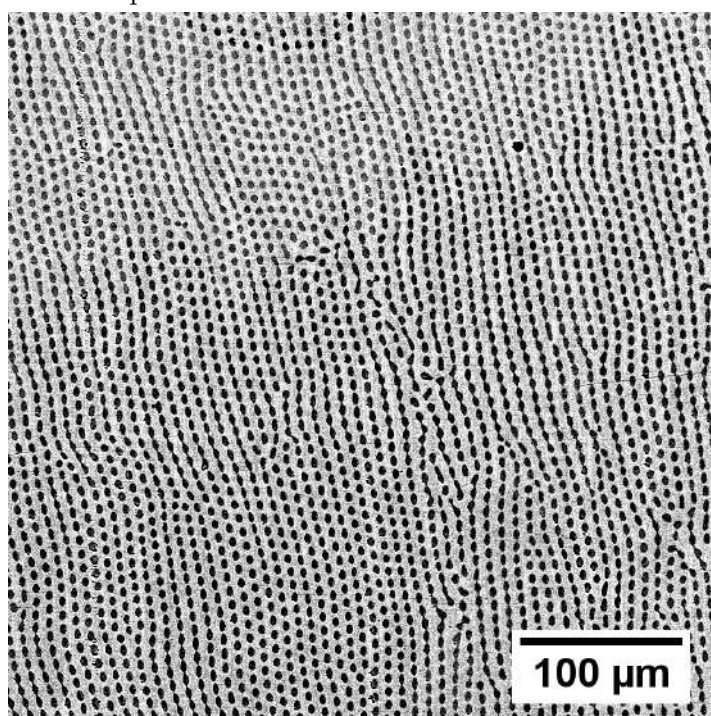
The steady-state microstructure of the eutectic system solidified at an imposed velocity of  $0.5 \mu\text{m/s}$  is shown in Figs. 5.2a and 5.2b. The longitudinal section in Fig. 5.2a shows the growth of eutectic phases along the imposed thermal gradient, whereas the transverse section in Fig. 5.2b reveals a microstructure that resembles strings of rods, where the strings may be perceived by joining the centroids of the nearest neighbor rods. An individual string can be thought to be continuous until there is a change in the nearest neighbor distance between the rods, this results in the termination of the string, and instead, a new string may get initiated. The strings of rods in Fig. 5.2b are not arranged in definite straight lines in contrast to the broken-lamellar structures that have well-defined orientations of the solid-solid interfaces as observed in other eutectic systems [126, 139, 122]. The lack of such strong alignment between the strings of connected rods indicates the absence of strong anisotropy in both the solid-solid and the solid-liquid interfaces, but the possibility of the presence of weak anisotropy in the solid-solid interface exists.

To derive the quenched interface, an additional experiment is performed with an abrupt velocity change for sample growing at  $0.5 \mu\text{m/s}$  that is shown in Fig. 5.3, which gives the trace of the solid-liquid interface during solidification. From the quenched interface, we can say that the solid-liquid interface of this binary system during solidification is planar without having an irregular or faceted morphology.

Microstructures possess short and long-range spatial relationships in the distribution of phases, which becomes explicitly visible when we map the microstructure to a reduced vector space. A way to perform this data reduction is using 2-point spatial correlations [170, 171, 172] between the phases in the microstructure. The resulting map with all possible vectors and their probabilities of occurrence becomes the basis for understanding the different microstructures in this paper. Fig. 5.4 shows the transverse section images of the eutectic samples solidified at different imposed velocities and their corresponding self-correlation images of the SnTe phases (appearing dark in the microstructures). 2-point correlations reveal that rods are arranged in a distorted hexagonal-lattice (as depicted by the pattern of the high-intensity spots near the center of the spatial correlation image) while also highlighting that the trace of the rod centroids



(a) Longitudinal section, growth direction is from bottom to top



(b) Transverse section, growth direction is out of view

Figure 5.2: Scanning electron micrographs of binary Sn-Te eutectic ( Te-15at%Sn) solidified at  $0.5\mu\text{m}/\text{s}$ .

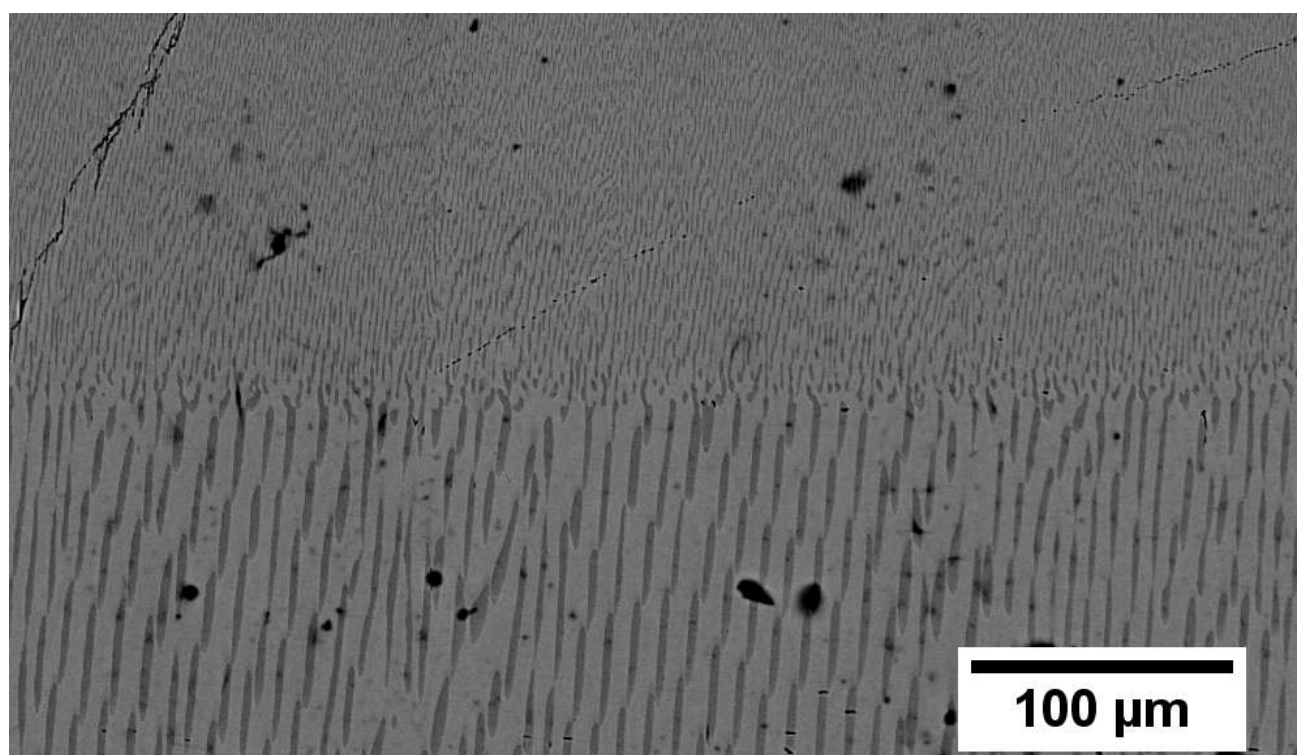
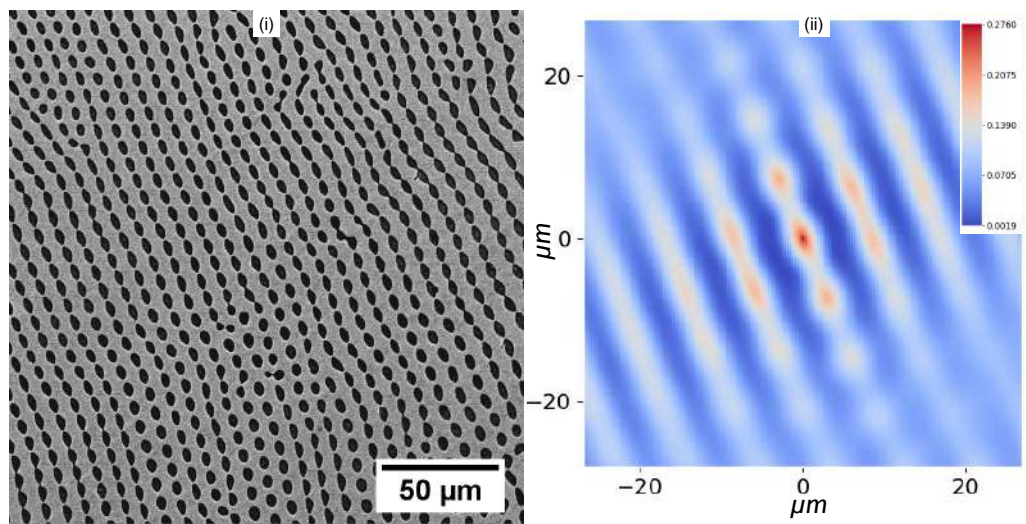
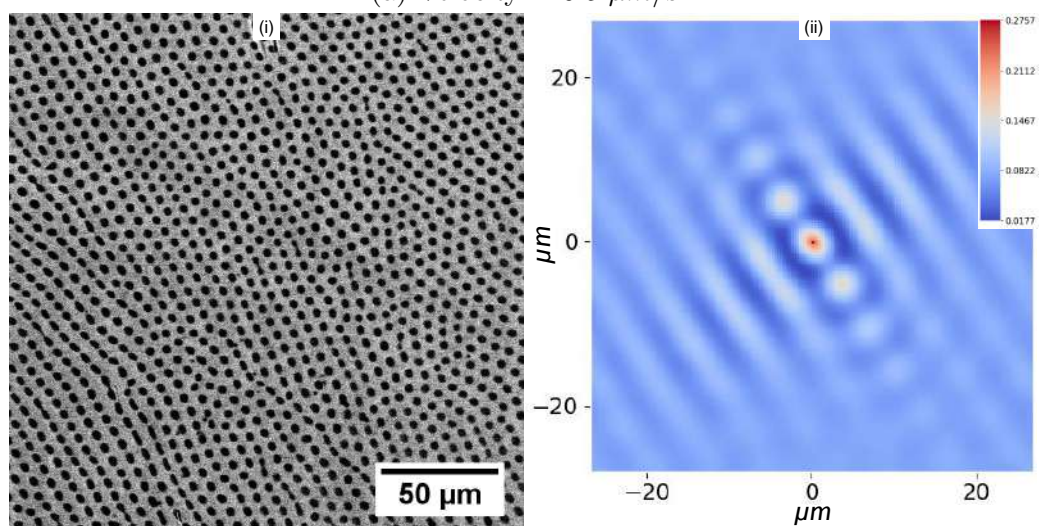


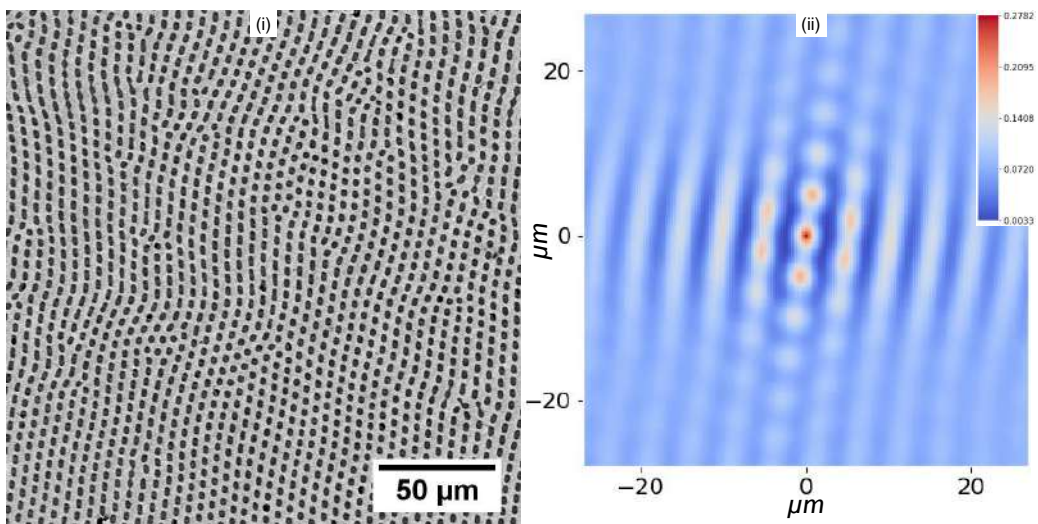
Figure 5.3: Morphology of the quenched solid-liquid interface of binary Sn-Te eutectic showing a planar growth front.



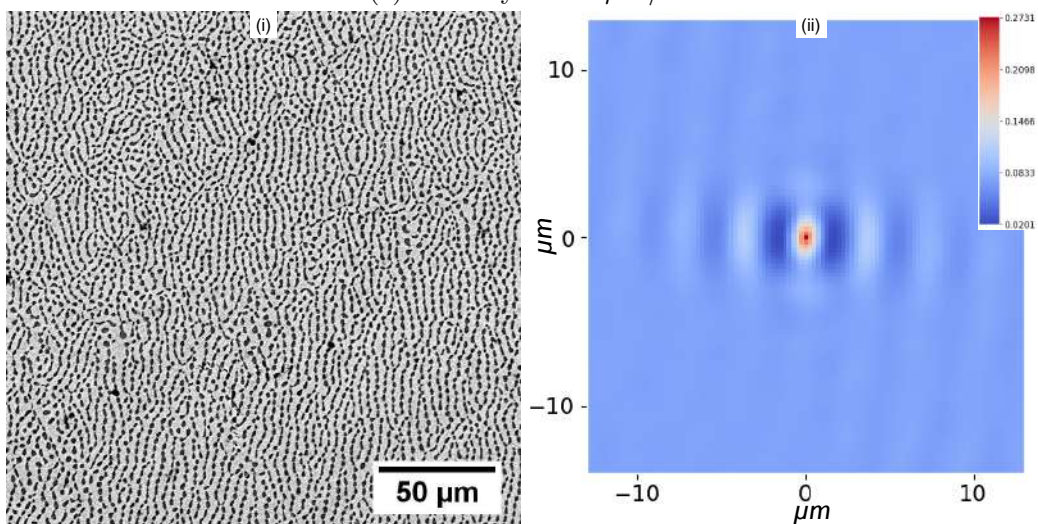
(a) Velocity =  $0.5 \mu\text{m/s}$



(b) Velocity =  $1.0 \mu\text{m/s}$



(c) Velocity =  $2.0 \mu\text{m/s}$



(d) Velocity =  $4.0 \mu\text{m/s}$

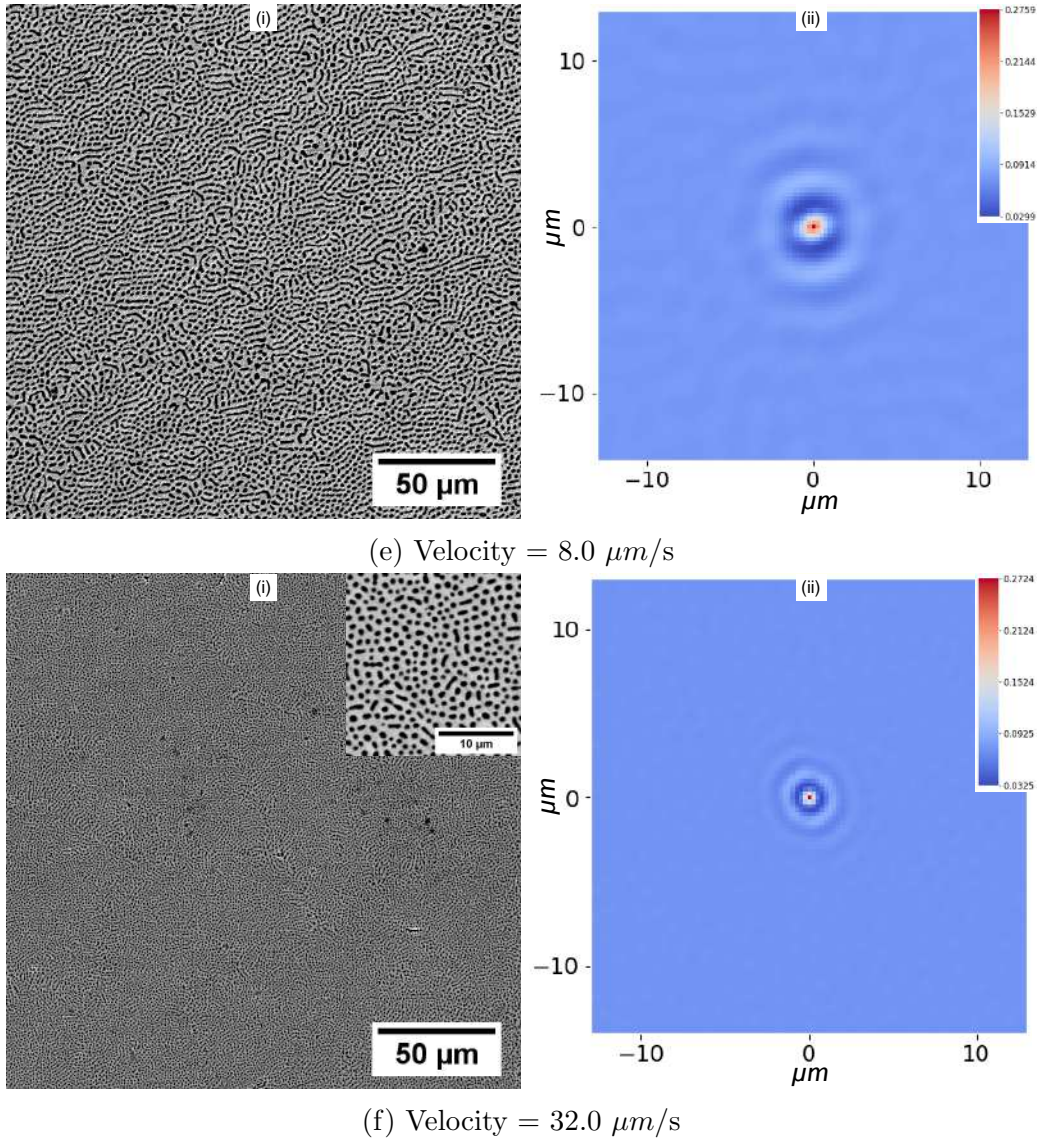
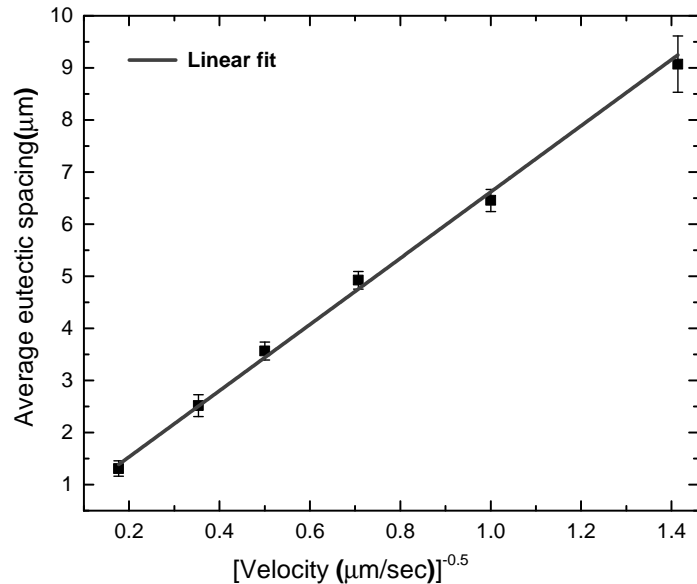
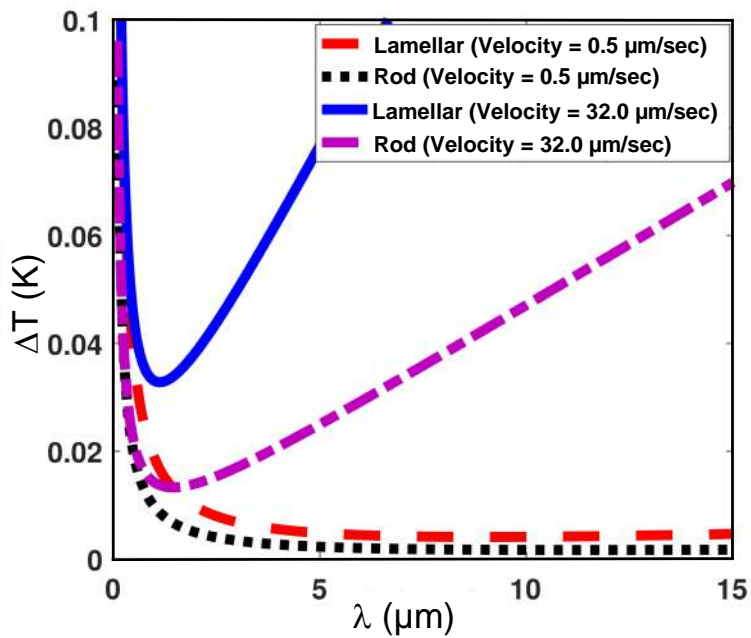


Figure 5.4: Transverse section SEM images of directionally solidified binary Sn-Te eutectic at different velocities along with their 2-point spatial self-correlations of the SnTe phase, shows that the morphology of the Sn-Te eutectic is predominantly rod. However, the trace of the rod-centroids gives an impression of several strings of rods with weak alignment between them in samples solidified with  $V=0.5, 1.0, 2.0, 4.0 \mu\text{m/s}$ . With increasing velocities, rod distribution becomes random. The colorbar depicts the probability of occurrence of self-correlation vectors.

forms strings that exhibit alignment at lower solidification velocities ( $V=0.5, 1.0, 2.0 \mu\text{m}/\text{s}$ ). Such morphologies in a distorted hexagonal lattice have been previously simulated using phase-field simulations by Plapp et al. [187] where such structures arise beyond a critical eutectic spacing for isotropic eutectic systems whose minority phase fraction fall in between 0.2-0.3. For  $V=4.0 \mu\text{m}/\text{s}$ , two of the spots on either side of the central spot in the spatial correlation plot merge, leading to blurring. This leads to the development of a diffuse circular ring in the spatial correlation plot instead of sharper spots in the correlation plots near the center at lower velocities. This indicates that the structure is transitioning towards a random distribution of rods and rod strings. With increase in solidification velocities, the spatial distribution of the rods becomes increasingly random where the alignment between the strings of rods breaks down as well as the individual strings become shorter, that is revealed both in the microstructure as well as in the spatial correlations. We have used transverse section images captured in the SEM for determining the average eutectic spacing by performing FFT (Fast Fourier Transform). The spacing is averaged from several images captured around the middle of the sample. For this eutectic, two different length scales are observed at lower solidification velocities where the transverse section resembles strings formed by the connection of the nearest neighbor rods. The first principal length scale in the FFT corresponds to the inter-rod spacing along the rod strings, and the second is the uniform length scale in between the strings. We have utilized the latter for deriving the spacings at the lower velocities. The morphology tends towards a random distribution of rods at higher velocities (greater than  $8 \mu\text{m}/\text{s}$ ). Here, the strongest FFT peaks become diffuse and closely resemble a circular ring. Therefore, for this situation, we have derived the spacing from the radius of the first diffuse circular intensity spot in the FFT. Fig. 5.5a shows the variation of the average eutectic spacing with velocity. Although the morphologies vary with velocity, the plot of the spacing against the  $V^{-0.5}$  shows a good linear fit, which is most likely because the differences in morphology are due to slight rearrangement of the rods. We have obtained the scaling constant  $\lambda^2 V$  as  $40.32 \mu\text{m}^3/\text{sec}$  from the linear fit of the observed spacing. Using the value of the scaling relation  $\lambda^2 V$  obtained from the experiments combined with the thermodynamic data corresponding to the phase diagram and the liquid diffusivities, one can derive the undercooling vs spacing relationships (using the equations shown in section 1.2.1.1) for the rod and lamellar morphologies. Fig. 5.5b gives the variation of undercooling with spacing for both the morphologies (under different imposed velocities  $0.5 \mu\text{m}/\text{s}$  and  $32.0 \mu\text{m}/\text{s}$  velocities). At a higher velocity (i.e.,  $32.0 \mu\text{m}/\text{s}$ ), the minimum undercooling for the rod



(a)



(b)

Figure 5.5: Plot depicting the variation of average eutectic spacing with velocity in (a), while (b) is the variation of average undercooling with eutectic spacing computed at higher (32.0  $\mu\text{m/s}$ ) and lower velocity (0.5  $\mu\text{m/s}$ ) for both rod and lamellar morphology.

is lower than that of the lamellae and hence by the arguments in the Jackson-Hunt theory [2] the rod microstructure would be the preferred morphology, and we observed the same at that velocity. At lower velocity (i.e.,  $0.5 \mu\text{m}/\text{s}$ ), the minimum undercooling for the rod morphology is comparable to that of the lamellae. The curves corresponding to both the morphologies at lower velocities are so flat, it implies that both morphologies can possibly co-exist (and even give rise to mixed growth forms). We find some evidence of this in our experiments where microstructures for  $V=0.5 \mu\text{m}/\text{s}$  share characteristics of both lamellae (because of the formation of a weakly aligned string of rods) and rods. The essential point from this analysis is that with decreasing velocity, the difference between the minimum undercooling of the two morphologies reduces. Additionally, the minimum undercooling spacing is similar for the different morphologies (rod and lamellae), which is possibly the reason we do not see much variation in the  $\lambda^2V$  values that we derive at the higher and lower velocities for seemingly different experimental microstructures.

### 5.2.1.2 Crystallographic orientation relations in binary Sn-Te eutectic

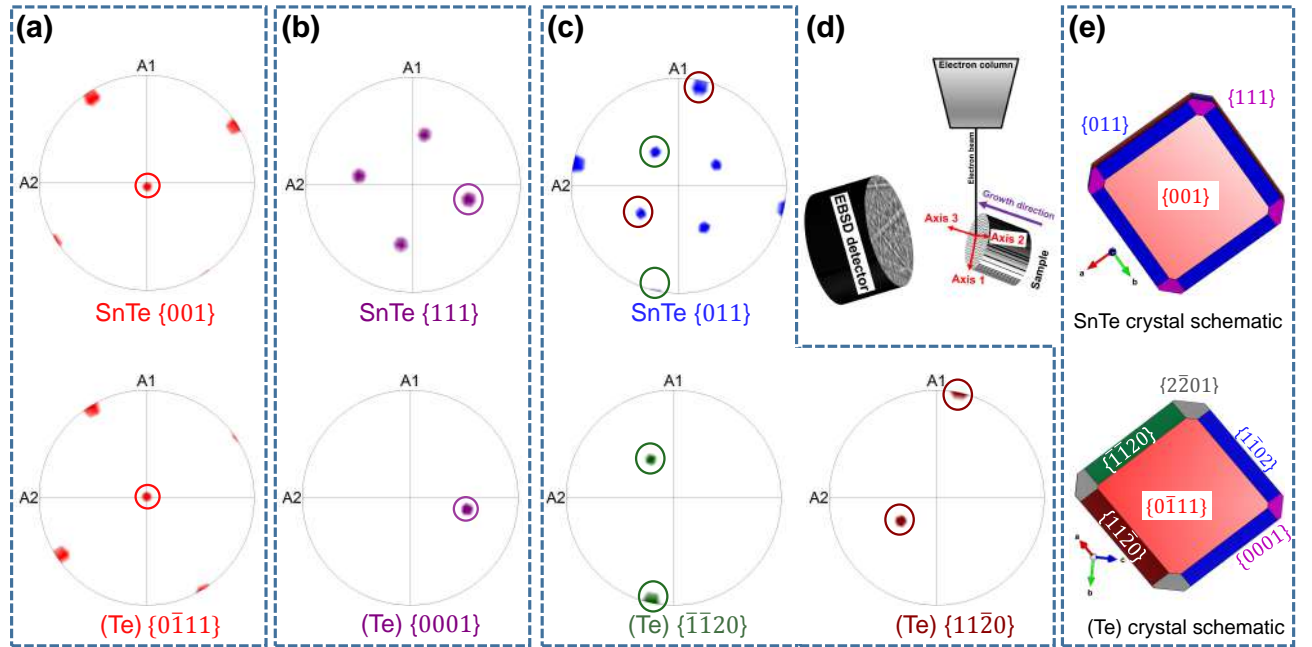


Figure 5.6: Pole figures of SnTe and (Te) obtained from EBSD data of binary eutectic solidified at  $0.5 \mu\text{m}/\text{s}$  exhibiting orientation relationships, i.e.,  $(111)_{\text{SnTe}} // (0001)_{(\text{Te})}$  and  $(10\bar{1})_{\text{SnTe}} // (11\bar{2}0)_{(\text{Te})}$  as highlighted in (b) and (c). Schematic of sample orientation in EBSD setup is shown in (d). Corresponding planes are highlighted in SnTe and (Te) crystals of (e) using VESTA [13].

Electron backscatter diffraction (EBSD) has been utilized to determine the existence of crystallographic orientation relationships between the eutectic phases. We conducted EBSD on the transverse section of the sample solidified at  $0.5 \mu\text{m}/\text{s}$  and the corresponding pole figures of SnTe and (Te) phases are shown in Fig. 5.6. Orientation relations are determined by matching the pole locations of each phase in the same reference frame. Combining the EBSD pole plots we find that the  $(111)$  plane of the SnTe crystal is parallel to the  $(0001)$  plane of (Te) crystal, while the  $(10\bar{1})$  plane of SnTe is parallel to  $(11\bar{2}0)$  plane of (Te), that are highlighted in Fig. 5.6(b),(c). Note that the second set of planes are also directions in the respective planes in the first set. Further, EBSD has been done on samples having different morphology, and

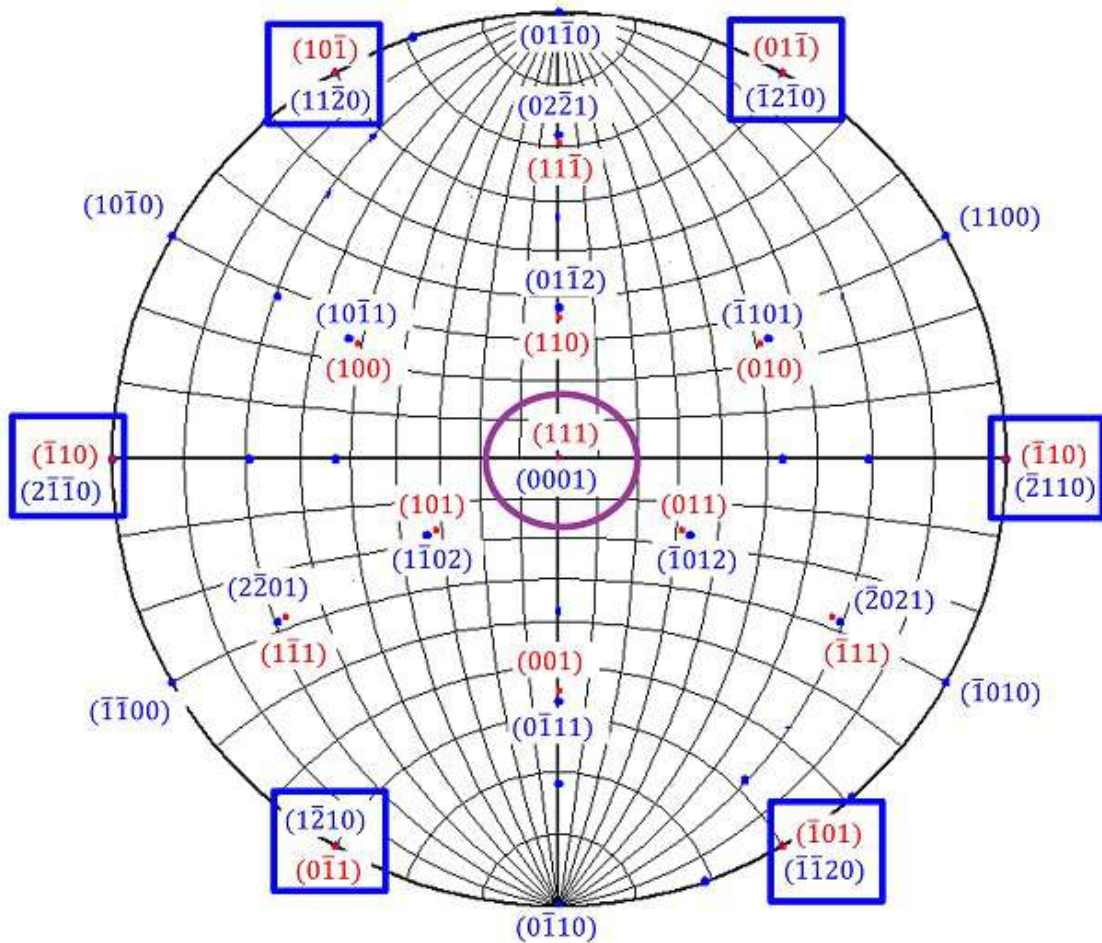


Figure 5.7: Stereographic projection of Te phase along  $(0001)$  plane and SnTe phase along  $(111)$  plane.  $\{001\}$ ,  $\{011\}$ ,  $\{111\}$ families of SnTe are highlighted along with  $\{0\bar{1}11\}$ ,  $\{1\bar{1}02\}$ ,  $\{11\bar{2}0\}$ ,  $\{2\bar{2}01\}$  families of Te.

we found the same orientation relationships in both the samples (refer Fig. 5.8). We find

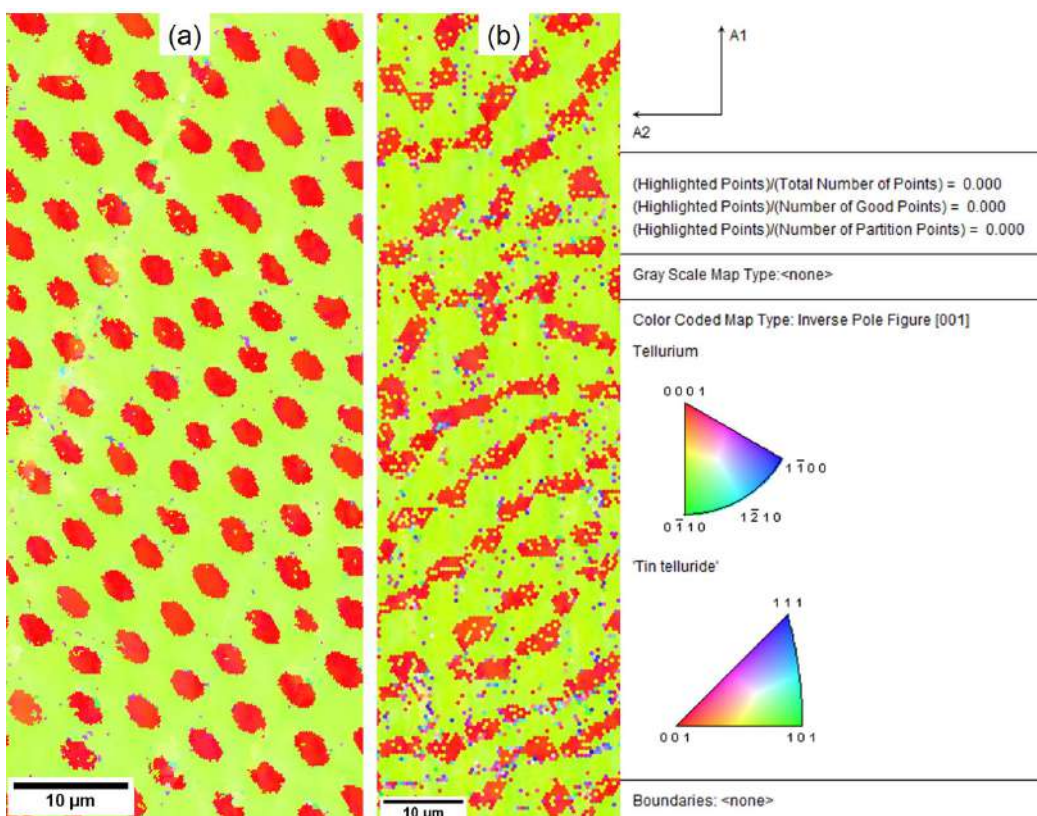


Figure 5.8: Inverse pole figures of samples having different morphologies (both are transverse sections). For both morphologies, (Te) maps to greenish yellow color and SnTe maps to red color, which reveal that both have same crystallographic orientation.

that the same orientation relations are observed in all samples that remain invariant upon the change in solidification velocity. We notice that the crystallographic planes forming the solid-liquid interface are approximately  $\{001\}$  of SnTe and  $\{0\bar{1}11\}$  of (Te) in all binary eutectic growth experiments and is shown in Fig. 5.6(a). Note that the planes  $\{001\}$  of SnTe and  $\{0\bar{1}11\}$  of (Te) are not exactly parallel (refer Fig. 5.7) and therefore the growth relation is only approximate.

### 5.2.2 Microstructure evolution of Sn-Te eutectic in the presence of impurities

In the previous sections, we have established the morphologies that arise during stable invariant two-phase growth in the SnTe-(Te) eutectic system. In this section, we further investigate the formation of colonies and their inherent microstructures. In order to destabilize the stable two-phase eutectic front; we add impurities to the eutectic system, that generally partition into the liquid, causing a boundary layer formation in front of the solid-liquid interface that becomes unstable to perturbations beyond a particular velocity similar to a Mullins-Sekerka instability for single-phase growth. A typical colony microstructure is shown in Fig. 5.9 formed due to the presence of impurities in the Sn-Te system.

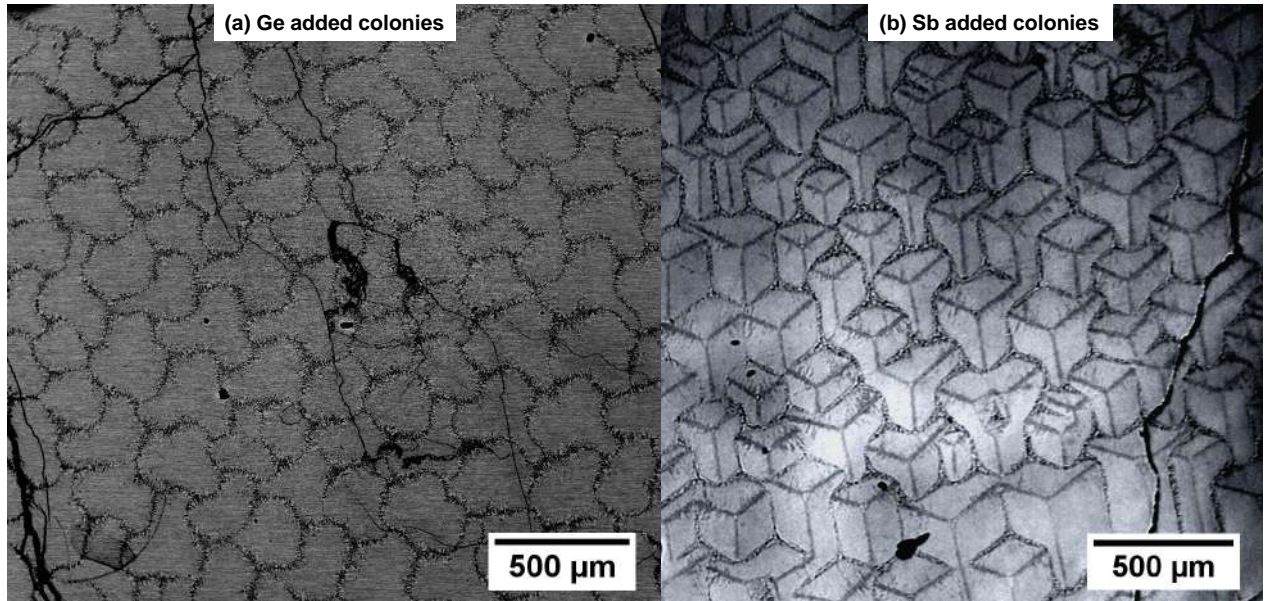


Figure 5.9: Formation of eutectic cells in the presence of an impurity in the Sn-Te eutectic system.

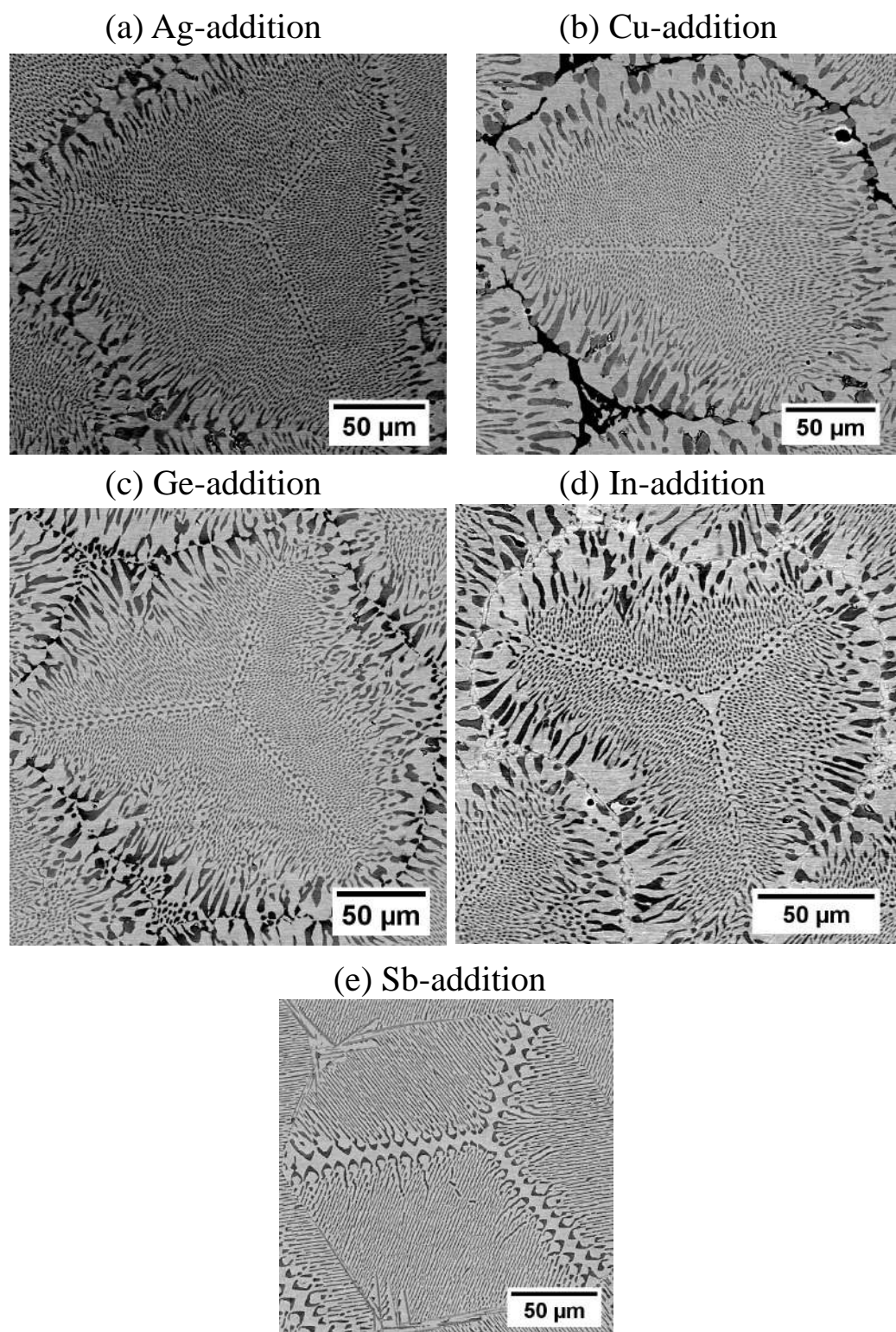
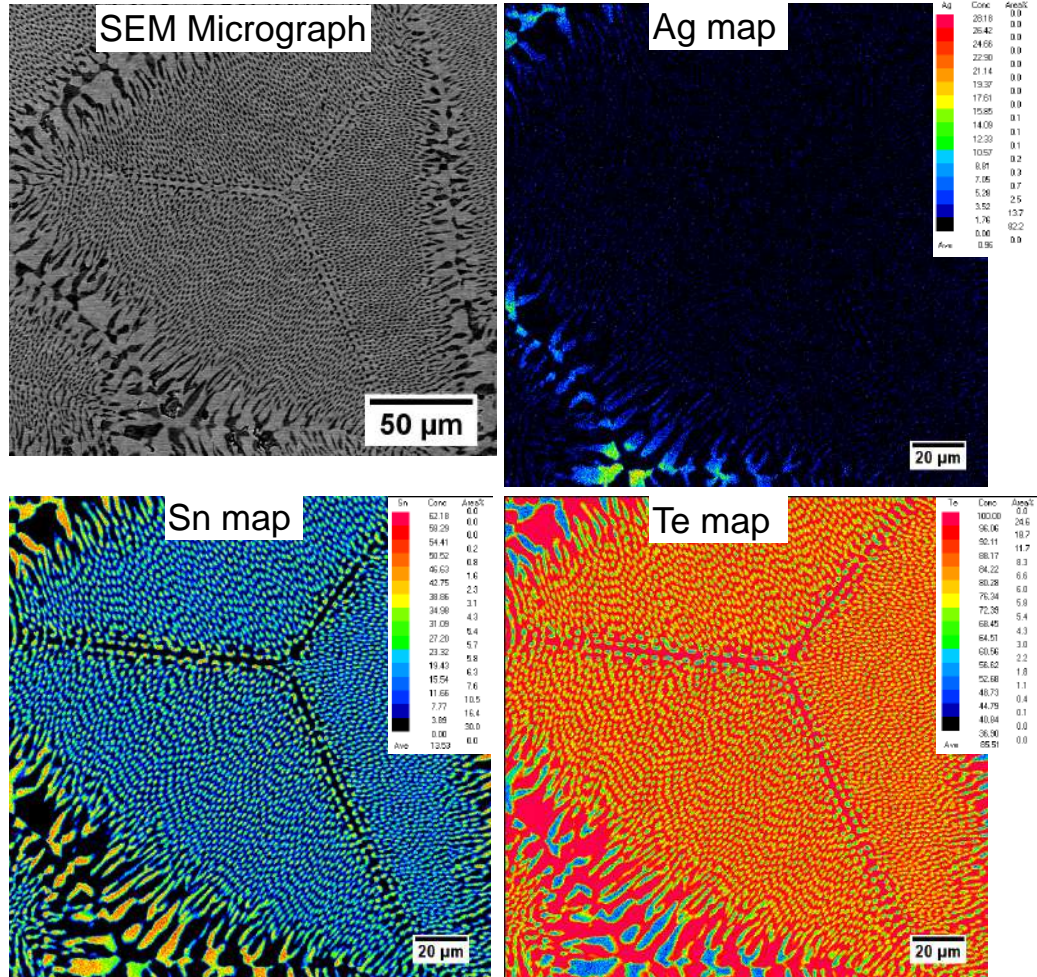


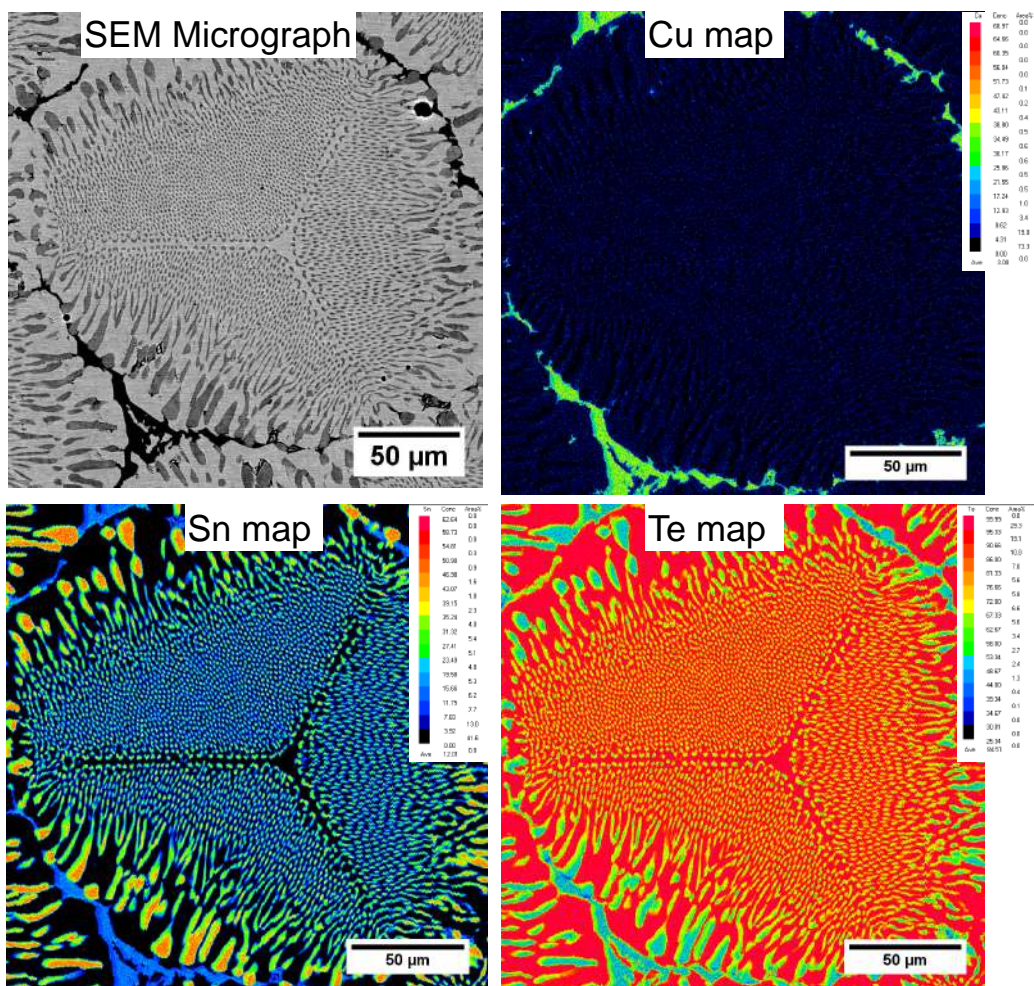
Figure 5.10: Morphology of the eutectic colonies in presence of different impurities

We have conducted experiments with Ag, Cu, Ge, In, Sb as impurity additions and the microstructural features observed are shown in Fig. 5.10. We observed the colony structure with an inherent three-fold symmetry in the internal morphology, while the intrinsic eutectic structure remains rod-like or connected rod-like for Ag, Cu, Ge. However, for Sb-addition, the morphology of the eutectic is lamellar. The colony structures observed in SnTe-(Te) system are very similar to those observed in other eutectic systems such as Al<sub>2</sub>O<sub>3</sub>- ZrO<sub>2</sub> (Y<sub>2</sub>O<sub>3</sub>) [188, 189, 190], MnSb-(Sb,Bi) and MnSb-(Sb,Sn) [191] where the two-phase eutectic front is destabilized because of the addition of a third component.

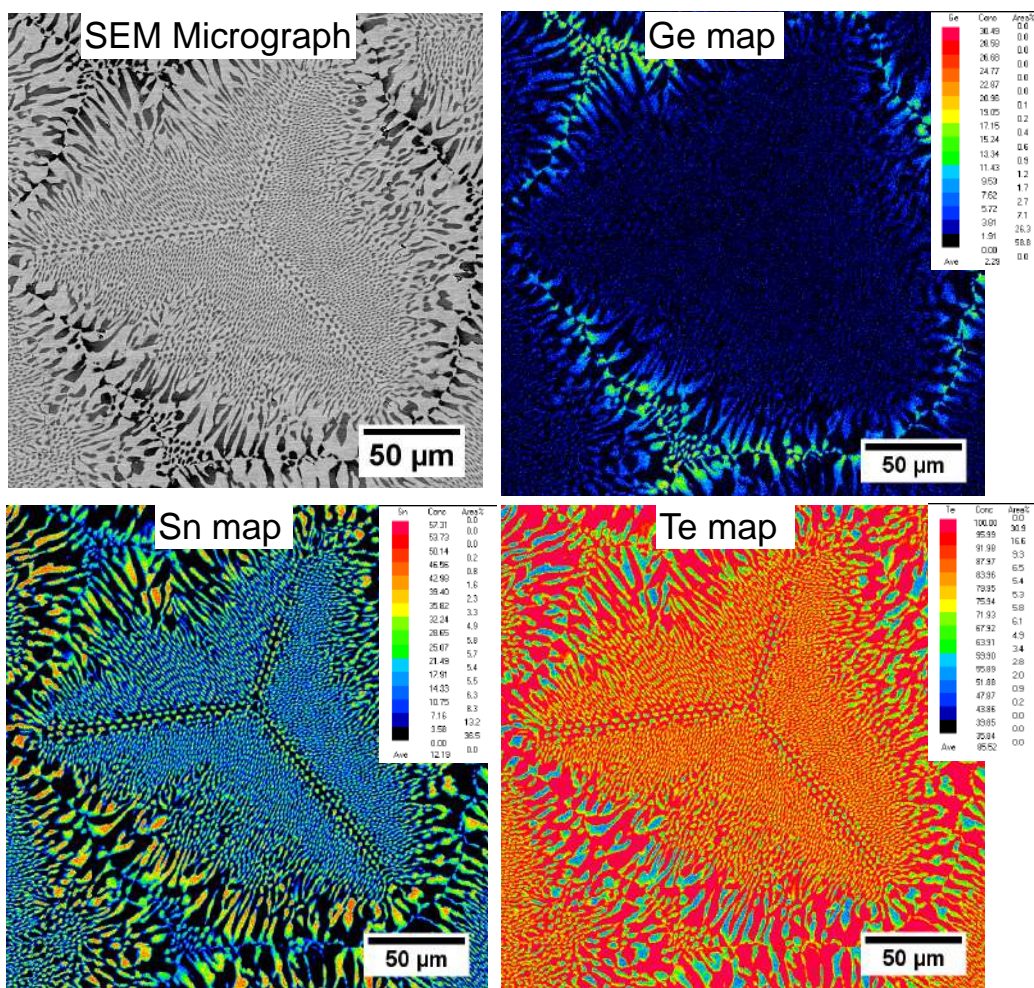
### 5.2.2.1 Composition distribution of elements



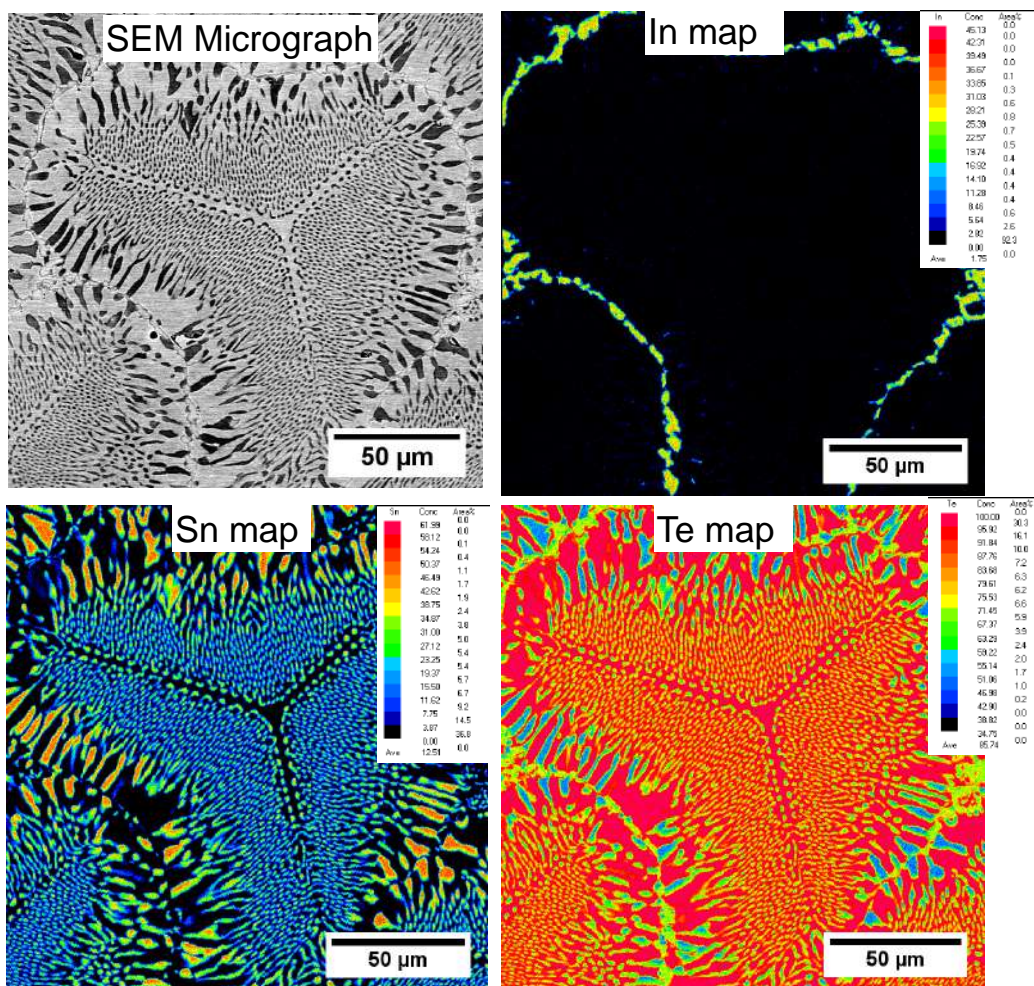
(a) Eutectic colony due to Ag-addition.



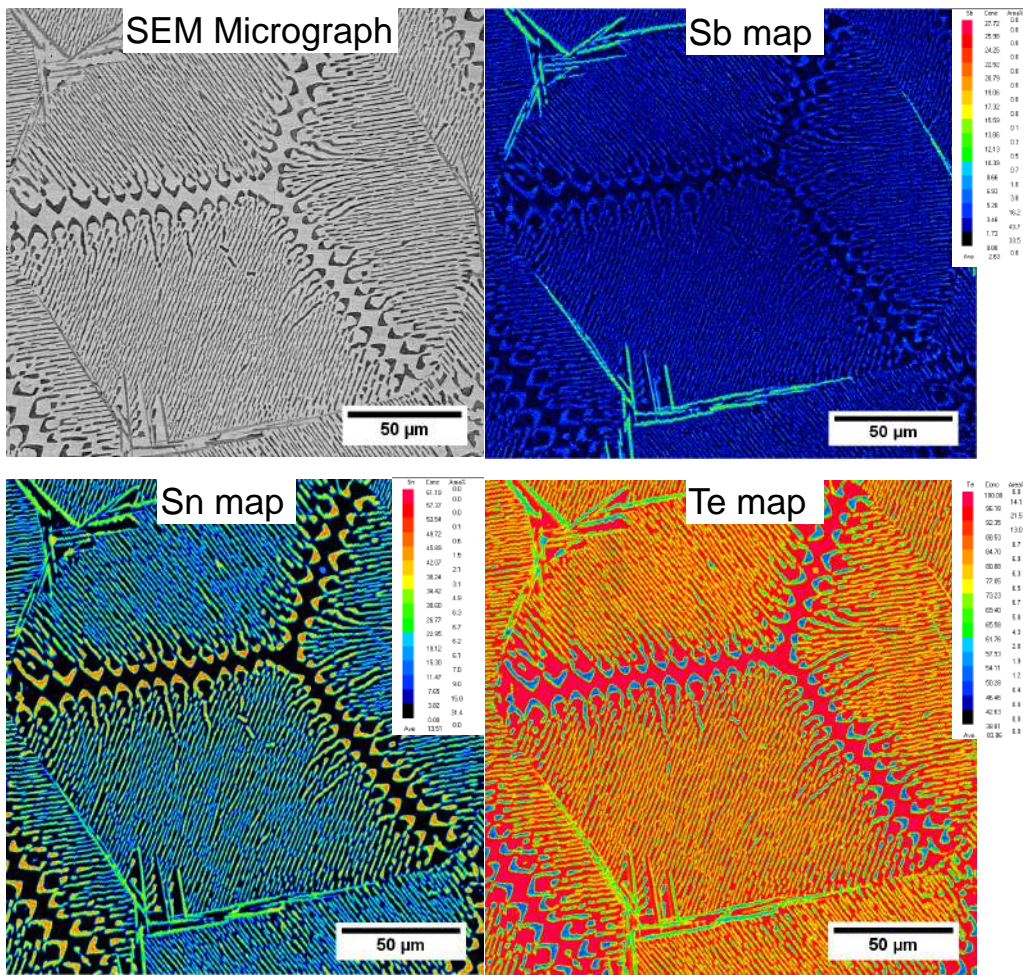
(b) Eutectic colony due to Cu-addition.



(c) Eutectic colony due to Ge-addition.



(d) Eutectic colony due to In-addition.



(e) Eutectic colony due to Sb-addition.

Figure 5.11: Composition distribution maps obtained for each of the element using electron probe microanalyzer shows segregation of impurities in the inter-colony regions.

The composition distribution maps are presented in Fig. 5.11 which reveal that the segregation of impurities in the inter-colony regions, owing to higher compositions in the SnTe-phase in the inter-colony regions. The other observation is that the impurity has solubility majorly in the SnTe phase but not in (Te) phase, which could be due to the presence of inherent Sn vacancies in the SnTe phase and almost no solubility of the elements in (Te) as depicted in the ternary phase diagrams. Due to the segregation of Sb (refer Fig. 5.11e), the composition of the liquid in the segregated part shifts to an invariant three-phase eutectic composition leading to the formation of a third phase in the segregated regions (refer Fig. 5.12b).

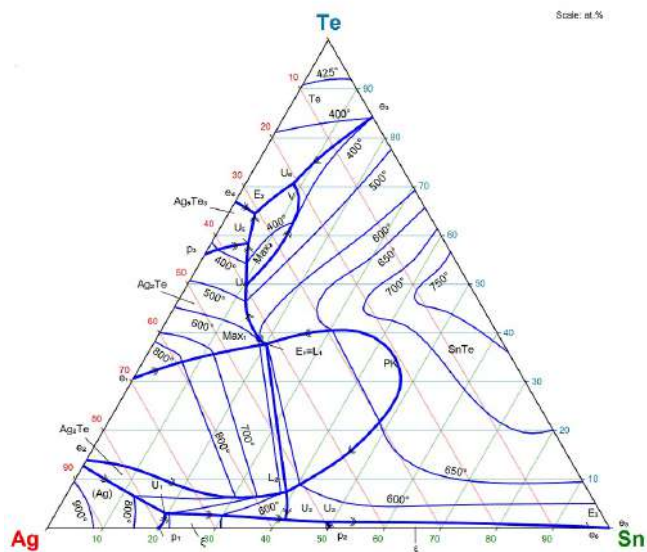
Because Ag, Cu, Ge, and In addition to the Sn-Te eutectic system leads to similar structures, we have limited our investigations to Ag and Sb addition. Fig. 5.12a and 5.12b are the ternary liquidus projections corresponding to Ag-Sn-Te, Sb-Sn-Te systems, respectively, which helps to decide the univariant two-phase eutectic compositions.

### 5.2.2.2 Ag addition to Sn-Te eutectic

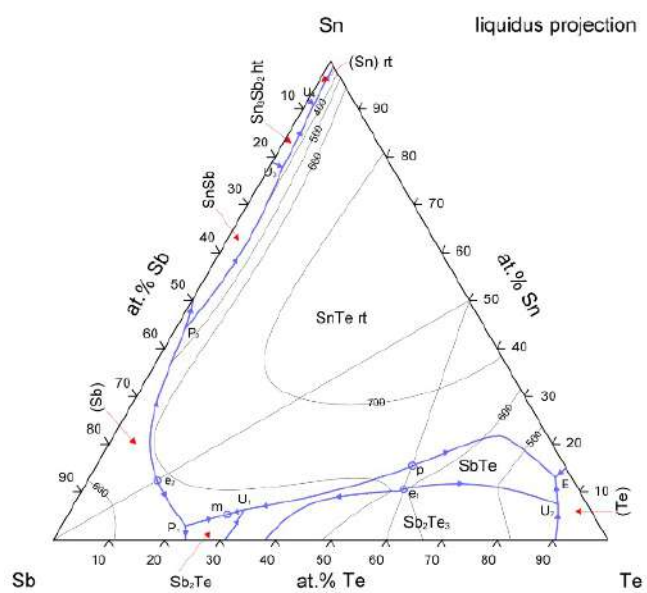
We begin with the morphological characterization of the samples with Ag-impurity addition that lead to colony formation. A typical colony microstructure is depicted in Figures 5.13a and 5.13b, that shows the transverse and longitudinal sections respectively of a directionally solidified sample for an imposed solidification velocity of  $21\mu\text{m}/\text{s}$  with an impurity addition of 0.5% Ag following the mono-variant line in the Ag-Sn-Te ternary phase diagram (refer Fig. 5.12a). We observed a colony structure with an inherent three-fold symmetry in the internal morphology, while the intrinsic eutectic structure remains rod-like or connected rod-like (strings of rods). The longitudinal sections reveal that the individual eutectics grow in a branched fashion, assuming an angle of approximately  $54^\circ$  to the central colony axes.

#### Critical velocity for colony formation

In order to determine the critical velocities beyond which instabilities occur, we have conducted experiments at different velocities for a given Ag composition. In addition, we have also performed experiments for varying impurity compositions and determined the critical velocities for each system. Fig. 5.15 shows the critical velocity for different percentages of Ag, while the microstructures are plotted in Fig. 5.14. We see that with the addition of Ag, the critical velocity decreases, which is also in agreement with the Mullins-Sekerka type mechanism for the destabilization of the interface, where the thermal length scales with the solute

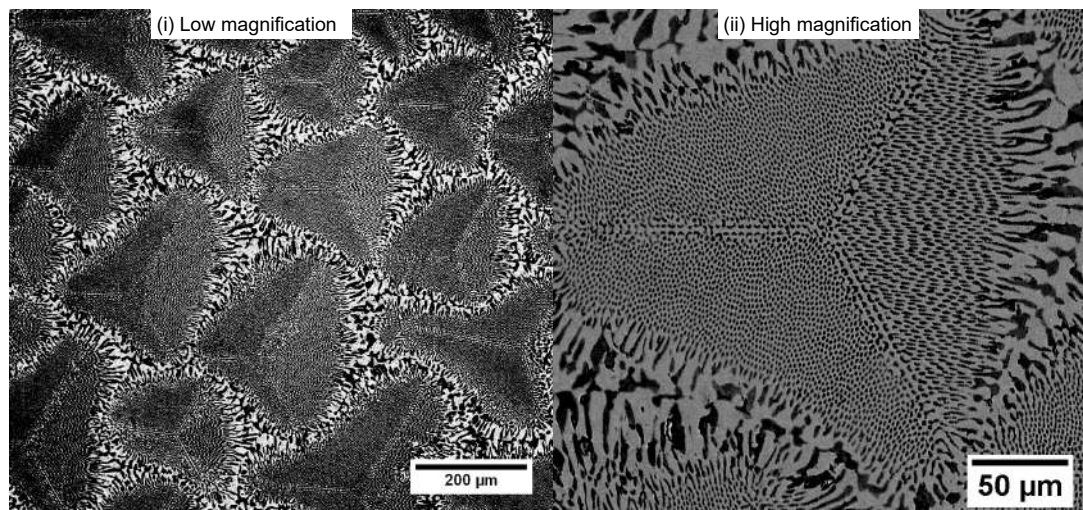


(a) Ag-Sn-Te ternary Phase Diagram [192].

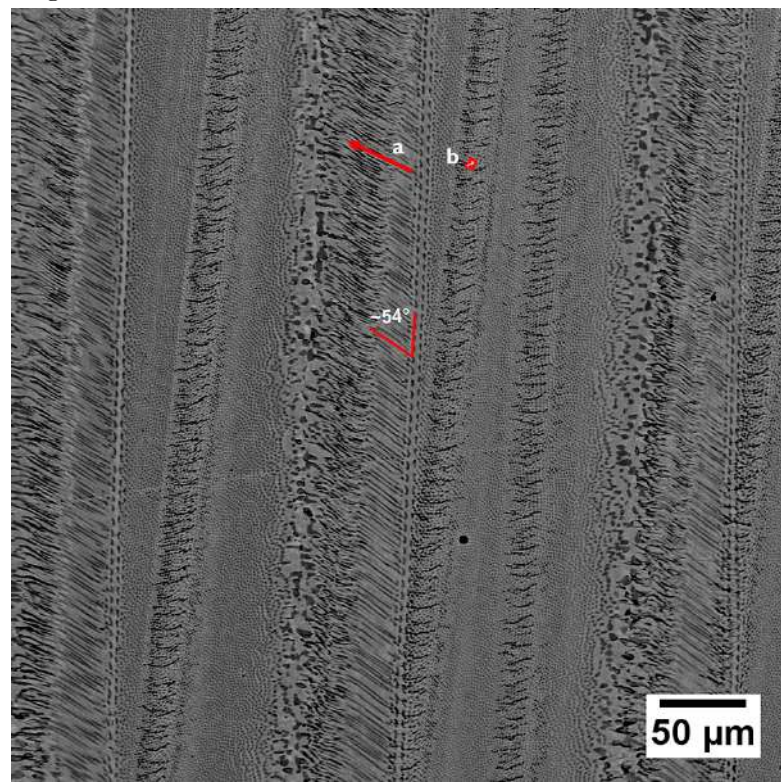


(b) Sb-Sn-Te ternary Phase Diagram [193].

Figure 5.12: Liquidus Projection of Ternary Phase Diagrams.



(a) Transverse sections of the colonies where (i) is low magnification image and (ii) is high magnification image



(b) Longitudinal section of the colonies, growth direction is from bottom to top

Figure 5.13: Typical colony microstructure observed due to addition of Ag as an impurity, where transverse section shows inherent three-fold symmetry in the internal morphology and longitudinal section shows tilted growth of eutectic in **a**, **b** directions as highlighted in the image where tilt angle is close to  $54^\circ$  from the central axis.

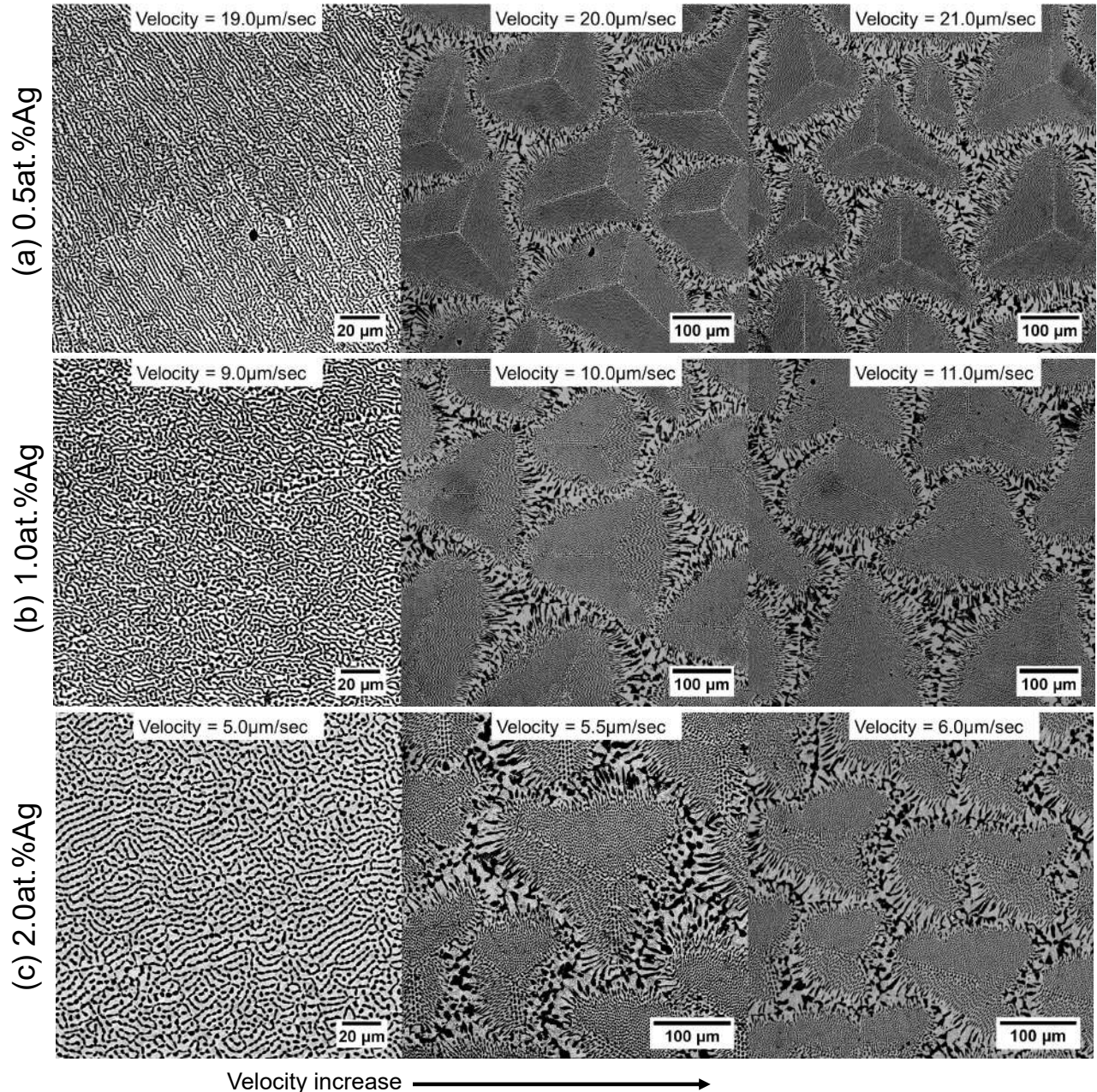


Figure 5.14: Microstructures captured from transverse sections of samples solidified with different percentage of Ag (increases from top to down) at different velocities (increases from left to right).

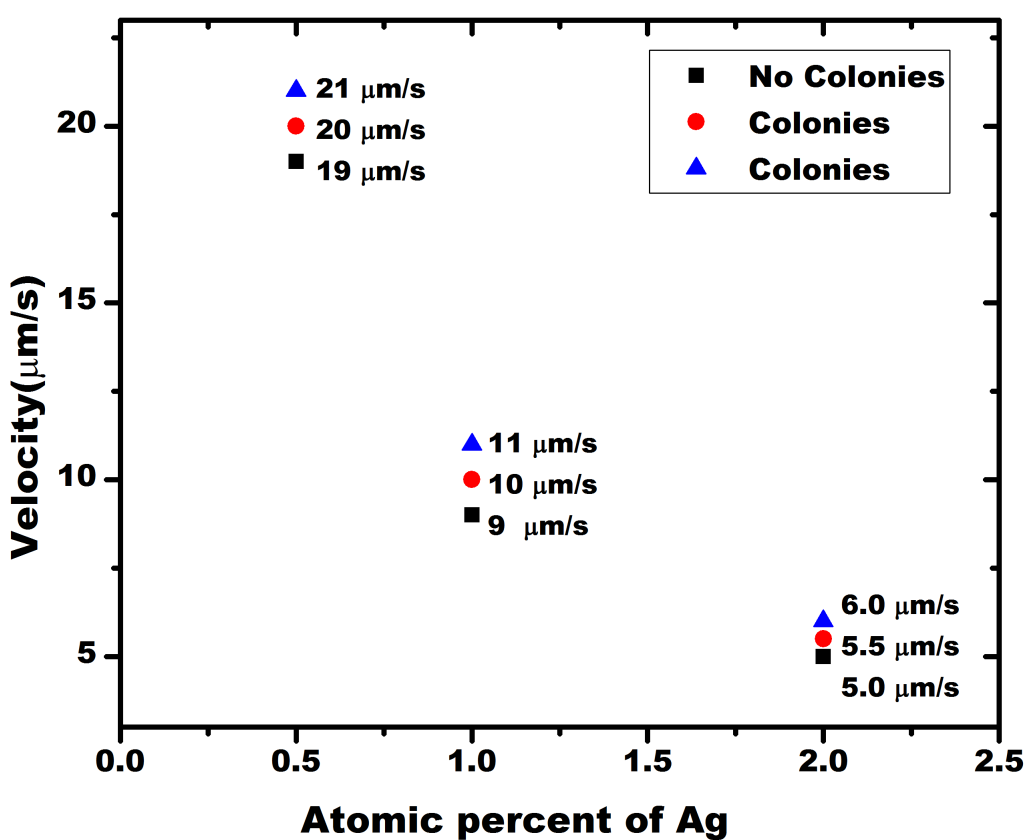


Figure 5.15: Plot showing the morphology observed for three different percentages of Ag at different velocities thereby revealing the critical velocity beyond which the instability occurs.

content and thereby, with the increase in Ag, the interface would become increasingly unstable to perturbations. In other words, the formation of instability occurs when  $G/V \leq m\Delta c/D$ . For constant temperature gradient ( $G$ ), liquid diffusivity ( $D$ ), and slope of liquidus curve ( $m$ ); critical velocity for the initiation of instability is inversely proportional to the amount of impurity added. Hence, the critical velocity beyond which instabilities amplify decreases with an increase in impurity content. While from the relation, one expects the variation of the critical velocity with impurity composition to be linear, however, this also depends on the variation of the liquidus slope  $m$  with composition in the liquid. Comparing the microstructures before the interface becomes unstable; we see that as the critical velocity increases, the microstructure of the stable eutectic front that destabilizes becomes finer following the  $\lambda^2 V$  scaling for eutectics, where the scaling constant also shows variation with the amount of impurity content. Whereas the eutectic spacing becomes finer as the critical speed increases, the colony spacing, on the other hand, is approximately the same just around the critical point, which is expected from a Mullins-Sekerka type of instability. This offers an interesting paradigm of microstructural engineering, wherein multiple scales that are representative of the microstructure may be modified upon the addition of an impurity. Further, we also see that the internal structure of the colonies has a three-fold symmetry for the Ag additions of 1 at% and 0.5 at%, whereas it is absent for the case of 2 at%. This is most likely caused by the nucleation of a separate eutectic grain having a different growth orientation where the colony axis is tilted with respect to the growth direction.

**Structure of the colonies: Crystallography and morphology** In this section, we perform a combination of crystallographic and morphological characterization of the colonies in order to delineate their structure during growth. Electron backscatter diffraction (EBSD) has been carried out to identify the orientation relationships between the phases (refer Section 5.2.1.2 for crystal structures), during the growth of the colonies. Pole figures obtained from the EBSD are shown in Fig. 5.16. Pole figures reveal that the entire colony is a single eutectic grain. We find that the orientation relationship between the phases remains the same as the orientation relationship observed in the binary eutectic, i.e., the (111) plane of SnTe crystal is parallel to the (0001) plane of (Te) crystal and (10 $\bar{1}$ ) plane of SnTe is parallel to (11 $\bar{2}$ 0) plane of (Te).

By comparing the colony structure shown in Fig. 5.16e and Fig. 5.13b with the corresponding pole figures shown in Fig. 5.16a, 5.16b, we find that the colony axes is aligned with the  $\langle 0001 \rangle$

direction of (Te) and corresponding  $\langle 111 \rangle$  direction of SnTe which is shown schematically in Fig. 5.16f. In order to further reveal the structure of the colony and the structure of the solid-liquid

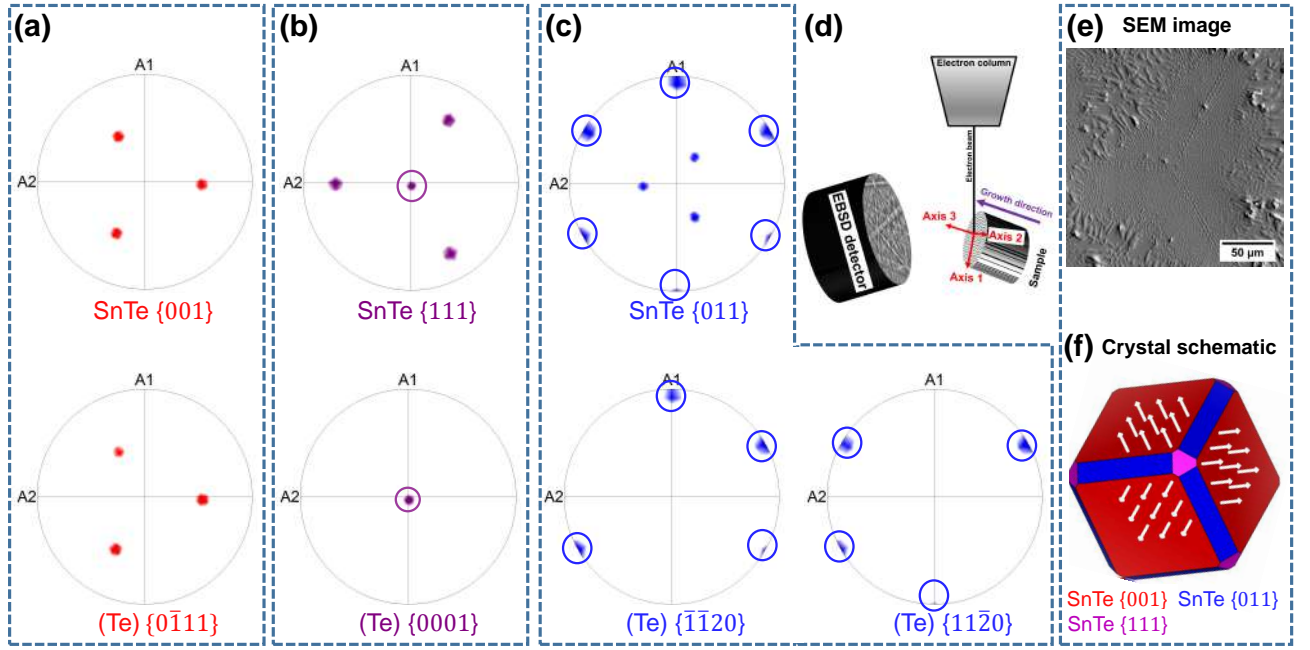


Figure 5.16: Pole figures of SnTe and (Te) obtained from EBSD data of eutectic colony obtained due to Ag addition (SEM image is shown in (e)) for the sample solidified at  $21.0\mu\text{m}/\text{s}$  with sample orientation as shown in schematic (d) are plotted in (a), (b), (c). Orientation relationships are the same as the relations observed in the case of binary eutectic, i.e.,  $(111)_{\text{SnTe}} // (0001)_{(\text{Te})}$  and  $(10\bar{1})_{\text{SnTe}} // (11\bar{2}0)_{(\text{Te})}$ . Crystallographic planes in connection to morphology of the colony shown in (e) are highlighted using VESTA [13] in crystal schematic (f).

interface, we have quenched the solidification front and is as shown in Fig. 5.17. The quenched interface shows that the solid-liquid interface is pyramidal. Based on our previous EBSD results, and the quenched interface structure, we can infer that the colonies grow along  $\langle 0001 \rangle$  direction of (Te) ( $\langle 111 \rangle$  direction of SnTe) with the eutectic having the same crystallographic orientation relationship while branching from central colony axes. A schematic depicting the possible shape of the solid-liquid interface of the colonies is presented in Fig. 5.17c. Further, we have utilized FEI Helios(G4) dual-beam microscope to dissect the colony using gallium ions at appropriate locations and angles to confirm the internal colony structure. Fig. 5.18 shows the images captured using the SEM after sectioning the sample as depicted in the corresponding schematic in the inset. The images are captured at an angle with respect to the growth direction that is around  $52^\circ$ . From Fig. 5.18a, it is clear that the image captured is close to a true transverse section, wherein the rods are growing perpendicularly outwards from the plane

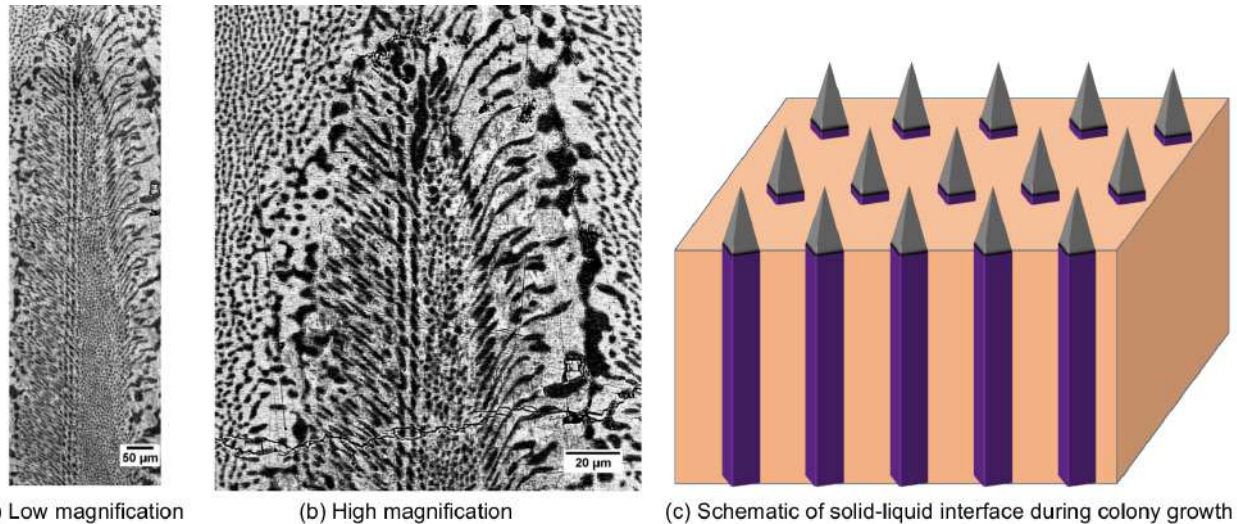


Figure 5.17: Morphology of the quenched solid-liquid interface of the colony, while the schematic shows the shape of the colonies across the solid-liquid interface.

of the paper. This is also conformant with the growth directions (a, b) of the eutectic that are highlighted in Fig. 5.13b that also reveals that eutectic is growing at an angle close to  $54.73^\circ$  which is the angle between [001] and [111] of the SnTe phase. Combining with the pole figures depicted in Fig. 5.16 we derive that the growth of the (Te)-phase is approximately normal to the  $\{0\bar{1}11\}$  planes and the SnTe crystals grow approximately normal to the  $\{001\}$  planes that are tilted with respect to the colony axes. Surprisingly, these are also the growth directions observed in stable binary eutectic growth of the SnTe-Te eutectic. Similarly, Fig. 5.18b, 5.18c shows how the eutectic emerges from the central longitudinal section. Based on these results, we can confirm that the solidification interface is probably faceted with the eutectic growing in a branched manner from the central colony axes. With this discussion, it is also clear that the experiments in Fig. 5.14c correspond to tilted colonies as revealed by EBSD.

### 5.2.2.3 Sb addition to Sn-Te eutectic

A typical colony microstructure due to the addition of Sb as an impurity is shown in Fig. 5.19, which shows the transverse section of a directionally solidified sample for an imposed solidification velocity of  $15\mu\text{m}/\text{s}$  with an impurity addition of 1.0% Sb. We observe that the structure is similar to colonies obtained with Ag addition exhibiting a similar inherent three-fold symmetry in the internal morphology, however, there is an important difference where a lamellar morphology instead of rod-like morphology occupies the internal structure of the

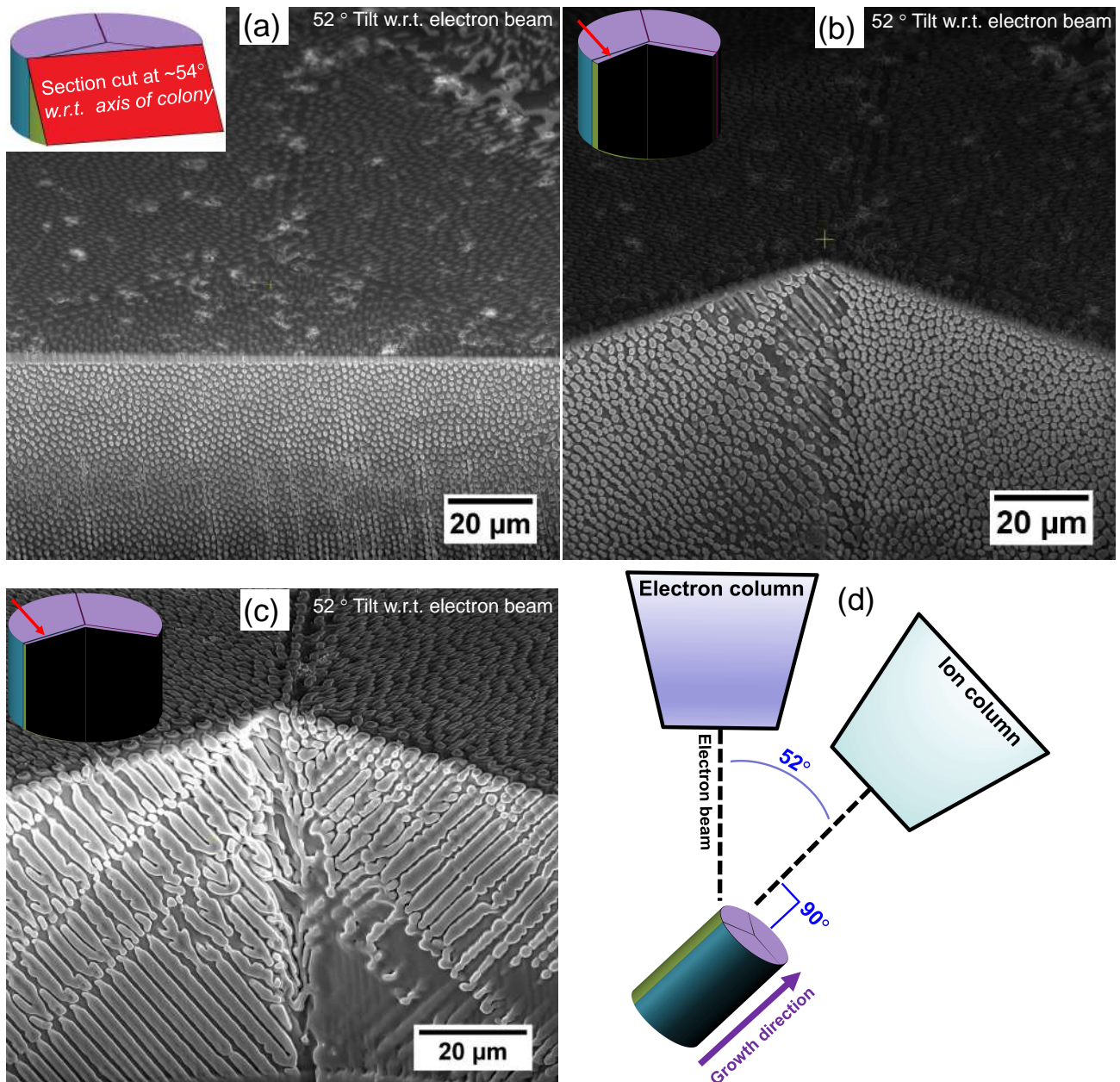


Figure 5.18: Internal structure of the colony captured using SEM when the sample is tilted at an angle  $52^\circ$  (refer schematic (d)). Image (a) is captured when the colony was cut at an angle  $54^\circ$  as highlighted in the inset schematic. Image (b), (c) are captured after dissecting one of the three parts of the colony close to the central longitudinal axis as highlighted in their respective inset schematics to show eutectic emerging from the central longitudinal section with rod morphology.

colony. The reasons for such a phenomenon could be due to a change in the volume fraction of the SnTe phase upon addition of Sb (refer phase diagram [194]) but more importantly, it appears that the solid-solid interfaces are probably anisotropic that lead to the formation of well-aligned lamellae in the internal structure of the colony. This modification to the eutectic structure for velocities lesser than the critical velocity is also clear in Fig. 5.20 where a mixture of rods and broken-lamellar fragments (refer Fig. 5.20(b)) form in contrast to the mixture of rod and labyrinth structures for Ag-addition (refer Fig. 5.20(a)). While the reasons for this transition in the nature of the solid-solid interface is presently unclear to us, the probable reasons for the anisotropy might be due to change in the nature of bonding in the SnTe phase due to the addition of Sb. However, a thorough investigation is required, which we intend to pursue in the future.

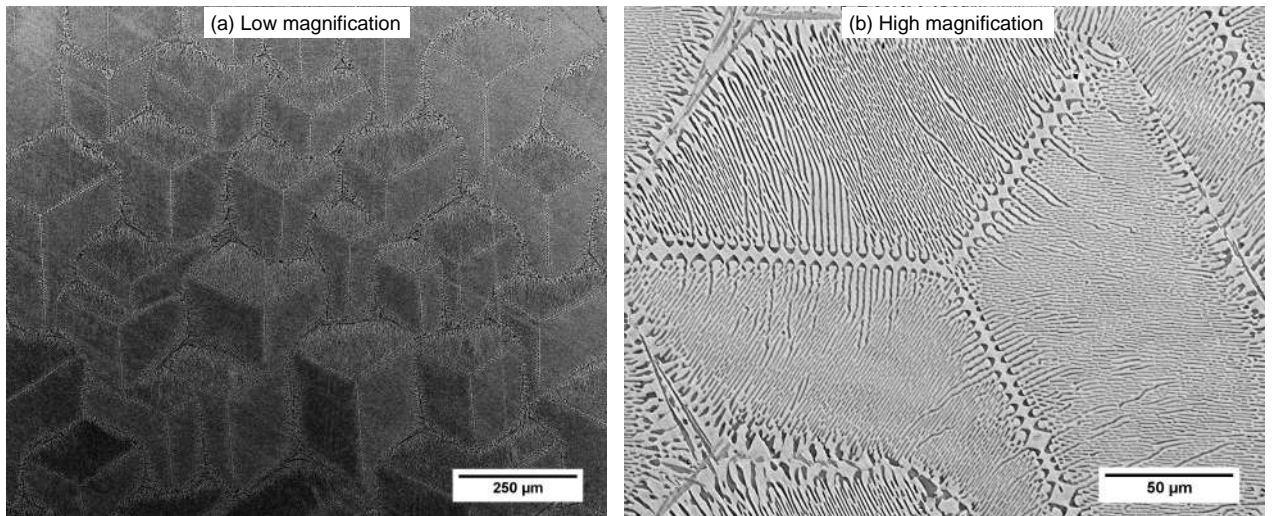


Figure 5.19: Typical colony microstructure observed due to addition of Sb as an impurity, where (a) is low magnification and (b) is high magnification transverse section images showing inherent three-fold symmetry in the internal morphology, while the eutectic structure is modified to a lamellar type.

In order to further portray the differences between the colony structures, we perform FIB. Under constant exposure of the sample surface consisting of both phases, the milling rate of Tellurium is much higher than that of SnTe that allows us to selectively mill out (Te), giving us a limited three-dimensional perspective of the growth microstructure. Fig. 5.21 highlights the difference between both colonies where the internal structure of the colony is rod-like for the case of Ag-addition, while it is lamellar for the Sb-addition.

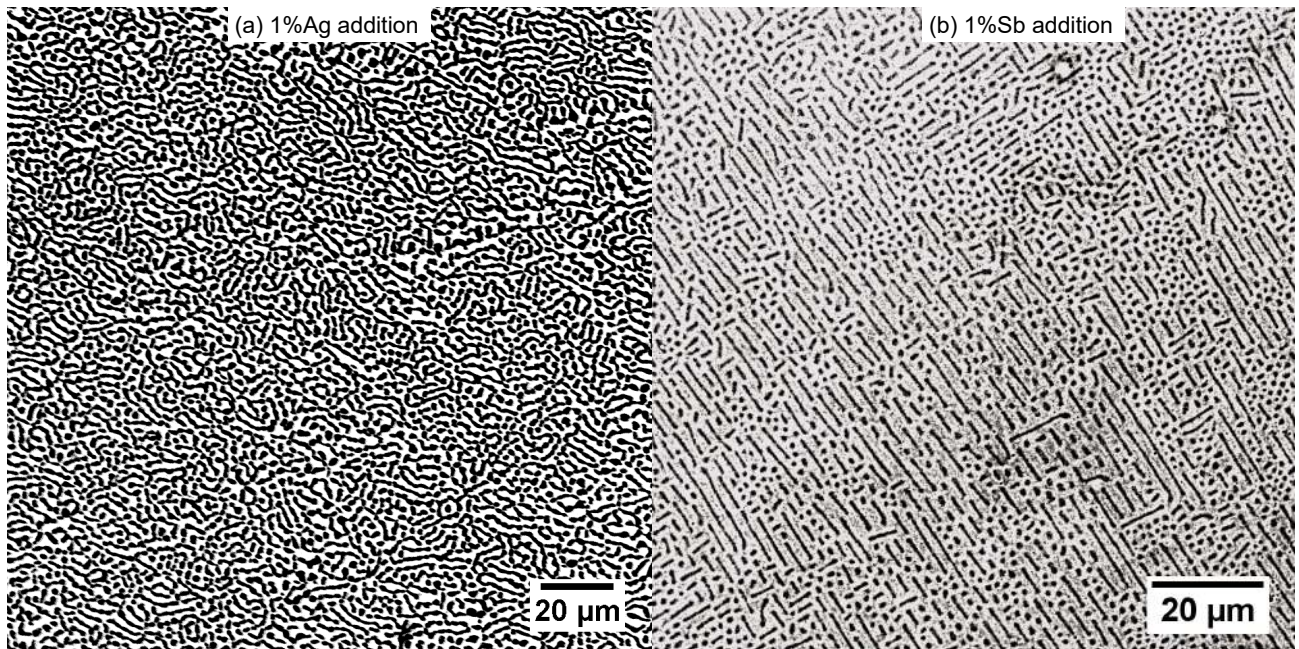


Figure 5.20: Morphology of eutectic structure in the presence of Ag/Sb as an impurity below critical velocity. Ag addition results in mixture of rod/labyrinth structures while Sb addition results in mixture of rod and well-aligned lamellar structures.

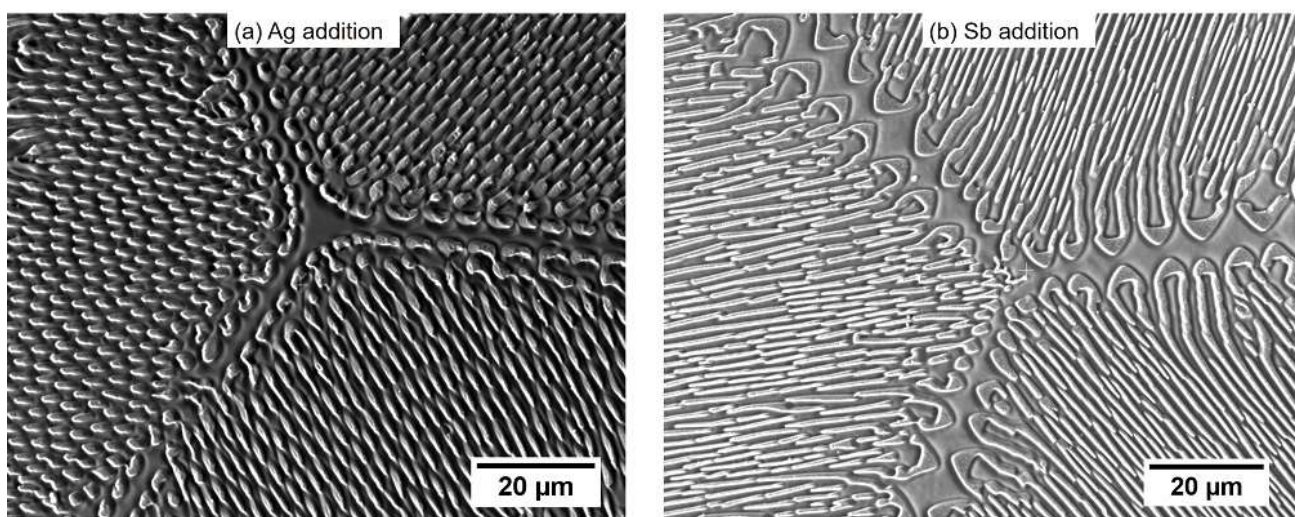


Figure 5.21: Morphology of colony structure in presence of Ag/Sb as an impurity, where the (Te) phase is removed. Images show lamellar structure for Sb-addition whereas rod-structure for Ag-addition.

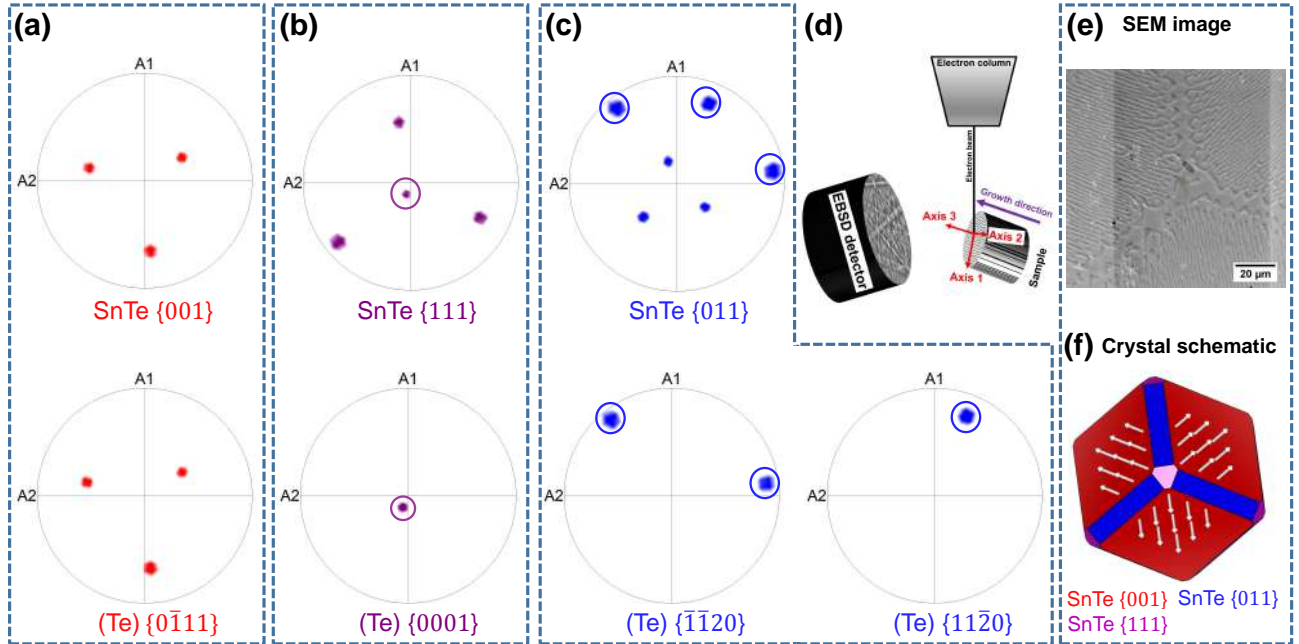


Figure 5.22: Pole figures of SnTe and (Te) obtained from EBSD data of eutectic colony obtained due to Sb addition (SEM image is shown in (e)) for the sample solidified at  $15.0 \mu\text{m}/\text{s}$  with sample orientation as shown in schematic (d) are plotted in (a), (b), (c). Orientation relationships are same as the relations observed in the case of binary eutectic and Ag added colonies, i.e.,  $(111)_{\text{SnTe}} // (0001)_{(\text{Te})}$  and  $(10\bar{1})_{\text{SnTe}} // (11\bar{2}0)_{(\text{Te})}$ . Crystallographic planes in connection to the morphology of the colony shown in (e) are highlighted using VESTA [13] in crystal schematic (f).

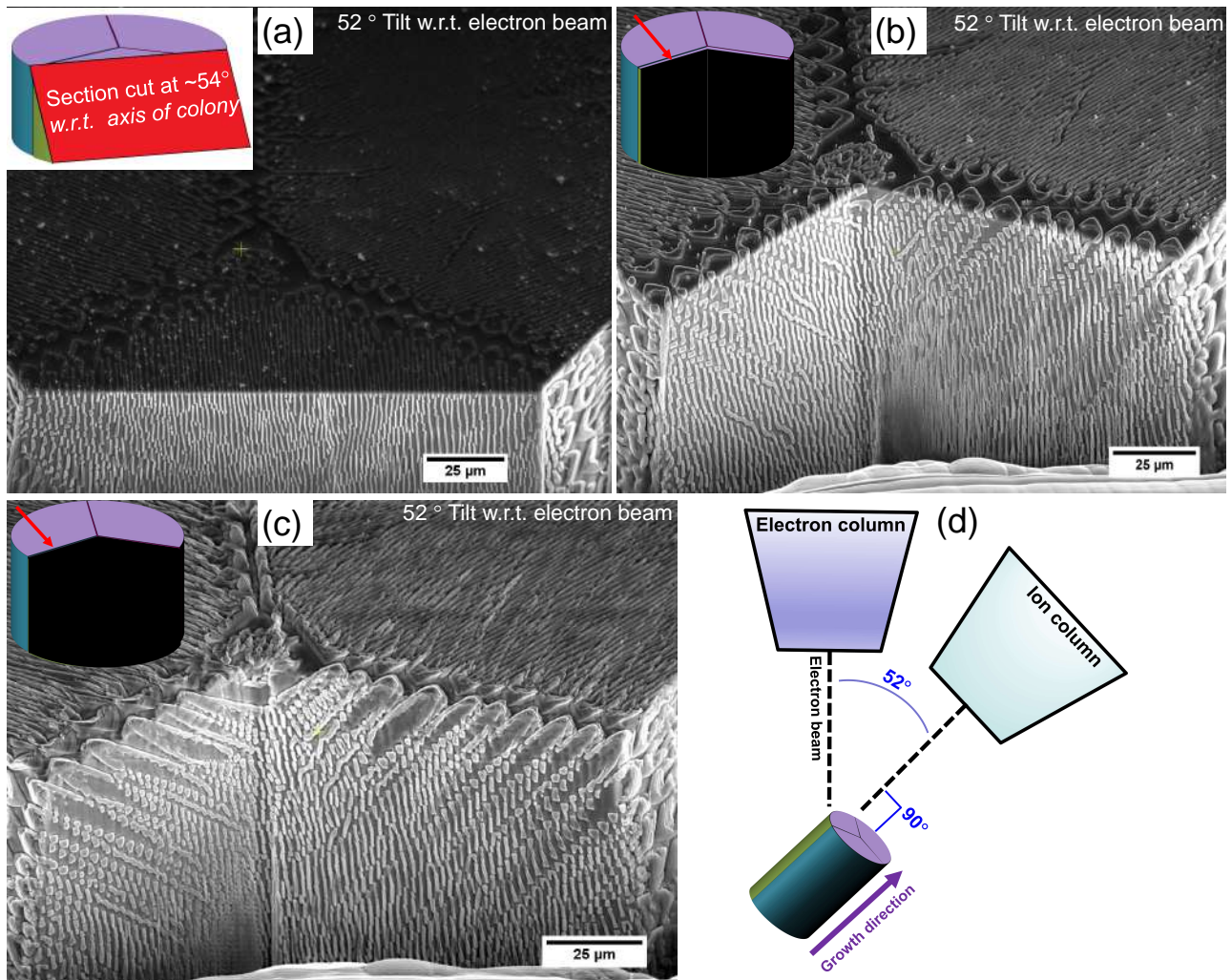


Figure 5.23: Internal structure of the colony captured using SEM when the sample is tilted at an angle  $52^\circ$  (refer schematic (d)). Image (a) is captured when the colony was cut at an angle  $54^\circ$  as highlighted in the inset schematic. Image (b), (c) are captured after dissecting one of the three parts of the colony close to the central longitudinal axis as highlighted in their respective inset schematics to show eutectic emerging from the central longitudinal section with lamellar morphology.

### Structure of the colonies: Crystallography and morphology

As we have seen in the previous sections, the orientation relationships between the phases in the binary SnTe-Te eutectic system are not affected due to the formation of colonies. However, the internal structure of the colony obtained due to Ag and Sb additions are different, so it is important to determine and compare the orientation relationship between the phases. We performed EBSD of the colony structures in order to obtain the pole figures as depicted in Fig. 5.22. We find that the orientation relationships between the phases remain the same as that observed in the binary eutectic and colonies observed due to Ag addition, i.e., (111) plane of the SnTe crystal is parallel to the (0001) plane of (Te) crystal and (10 $\bar{1}$ ) plane of SnTe is parallel to (11 $\bar{2}$ 0) plane of (Te).

Here again, we dissect the colony using gallium ions at appropriate locations and angles to confirm the internal colony structure. From Fig. 5.23a, it is clear that the image captured is close to a true transverse section, wherein the lamellae are growing perpendicularly outwards from the plane of the paper. By comparing the colony structure shown in Figures 5.22e and 5.23, with the corresponding pole figures shown in Fig. 5.22a, 5.22b and schematic shown in Fig. 5.22f, we find that this colony growth is very similar to those observed with Ag addition except that morphology of the eutectic is modified. Similarly, Fig. 5.23b, 5.23c shows how the lamellar eutectic emerges from the central longitudinal section. Based on these results, we can confirm that the solidification interface is probably faceted with lamellar eutectic growing from the central colony axes.

## 5.3 Summary

In this chapter, we have experimentally investigated microstructural formation both during stable invariant two-phase growth and during colony formation upon addition of impurities, in the SnTe-(Te) based alloy system. For stable two-phase growth in the binary SnTe-(Te) we observe microstructures with morphologies distributed between connected rod-like (weakly aligned strings of rods) and rod-like ( random distribution of rods or rod-strings). We have obtained the eutectic scaling constant  $\lambda^2 V$  as  $40.32 \mu\text{m}^3/\text{sec}$  for the binary SnTe-(Te) eutectic system where the solid phases also share an orientation relationship between the (Te) and SnTe phases, i.e., (111) plane of the SnTe crystal is parallel to the (0001) plane of (Te) crystal and (10 $\bar{1}$ ) plane of SnTe is parallel to (11 $\bar{2}$ 0) plane of (Te). Upon addition of a third component

to the eutectic leads to a diffusive instability (similar to a Mullins-Sekerka instability) leading to the formation of two-phase colonies which arise beyond a critical velocity depending on the impurity composition. In our experiments, we find that the colony exhibits an internal structure that appears to arise because of the solid-liquid interface being strongly anisotropic. Critical velocities beyond which these instabilities form are determined for each of the impurity levels, from which we confirm that the instability is similar to a Mullins-Sekerka like instability as the critical velocity reduces with an increase in the impurity content, that is further substantiated by the composition maps, which show that the impurity additions are segregated in the inter-colony regions. Here, while the colonies obtained by adding either Ag or Sb as an impurity show inherent three-fold symmetry in the morphology, but the eutectic is rod-like for Ag-addition, while for Sb-addition, the morphology of the eutectic is lamellar. We expect this change to be due to the modifications of the volume fraction of the SnTe- phase as well as the nature of the solid-solid interface, where we suspect that the interfacial free-energy becomes a function of the orientation. While we presently are unsure about the origin of this anisotropy, we expect the underlying reason to be a change in the nature of bonding in the SnTe-phase upon addition of Sb. Additionally, we observe that the orientation relations observed between SnTe and (Te) remains the same even after the formation of colonies for both the impurity additions. We find that the colony axis is aligned with the  $\langle 0001 \rangle$  direction of (Te) and  $\langle 111 \rangle$  direction of SnTe, while the eutectic phases grow in a branched manner from the central colony axes, with three-fold symmetry. Here, we find that the (Te) crystals grow approximately normal to the  $\{0\bar{1}11\}$  planes and the SnTe crystals grow approximately normal to the  $\{001\}$  planes which is the same set of directions as in the binary eutectic.

# Chapter 6

## Exotic three-phase microstructures in the ternary Ag-Cu-Sb eutectic system

*"It seems as if the evasive atoms still hide from the curious eye of the casual sightseer and reveal themselves rewardingly only to the serious researcher." –Erwin Müller*

In the previous chapters, we have investigated the formation of a broken-lamellar morphology in the binary Sn-Zn system and exotic colony formation in the ternary Sn-Te system. In this chapter, we investigate the formation of ternary eutectic microstructures. Eutectic solidification in ternary systems is a complex process involving the interaction of several material and process parameters resulting in intriguing patterns. Therefore, in this chapter, we explore the formation of microstructures in the invariant three-phase eutectic alloy and compositions that permit a univariant reaction where the initial liquid undergoes a two-phase eutectic reaction, and the last liquid undergoes a three-phase eutectic reaction as shown in Fig. 6.1.

### 6.1 Results and discussions

#### 6.1.1 Phase selection

Ag-Cu-Sb ternary system possesses a three-phase eutectic reaction at Ag-21.6 at.%Cu-36 at.%Sb, 426 °C, during which the liquid transforms into two intermetallic compounds, i.e., silver antimonide -  $\text{Ag}_3\text{Sb}$  (dyscrasite), copper antimonide -  $\text{Cu}_2\text{Sb}$  (cuprostibite), and an antimony rich solid-solution (Sb)[198, 199, 200, 201]. The crystal structures of the  $\text{Ag}_3\text{Sb}$ ,  $\text{Cu}_2\text{Sb}$ , and Sb-rich phase are confirmed as given in table 6.1 using selected area electron diffraction (SAED)

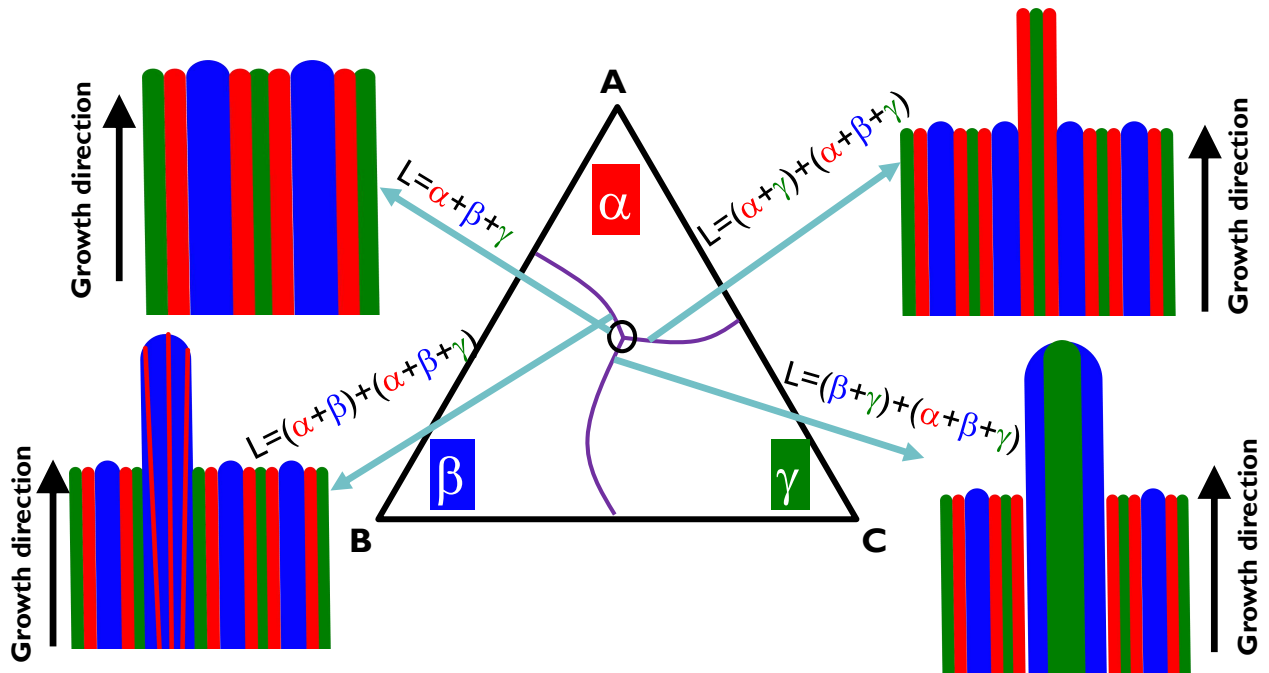


Figure 6.1: Schematic of a liquidus projection, and the microstructure involving two-phase eutectic colonies along with a three-phase eutectic reaction in the final liquid and an invariant three-phase eutectic.

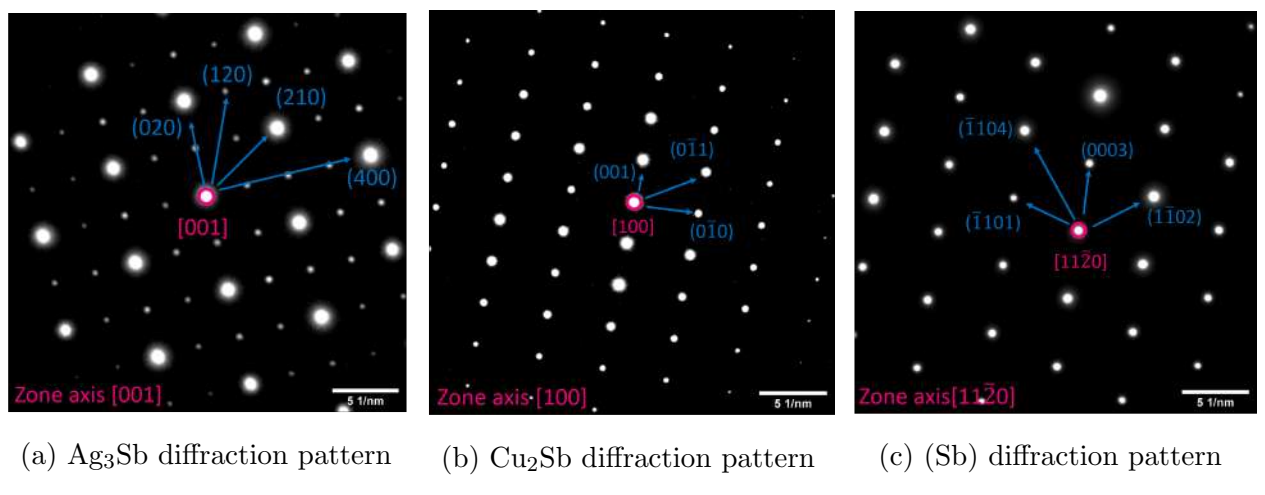


Figure 6.2: ((a), (b), (c)) are the selected area electron diffraction (SAED) pattern from silver antimonide-Ag<sub>3</sub>Sb, copper antimonide-Cu<sub>2</sub>Sb, and antimony rich solid-solution (Sb) taken in such a way that the zone axis matches with the direction of the imposed temperature gradient obtained from site-specific TEM lamella prepared from a region near the blocky (Sb) phase that consists of all three phases. Results correspond to the eutectic alloy solidified at 0.5  $\mu\text{m}/\text{s}$ .

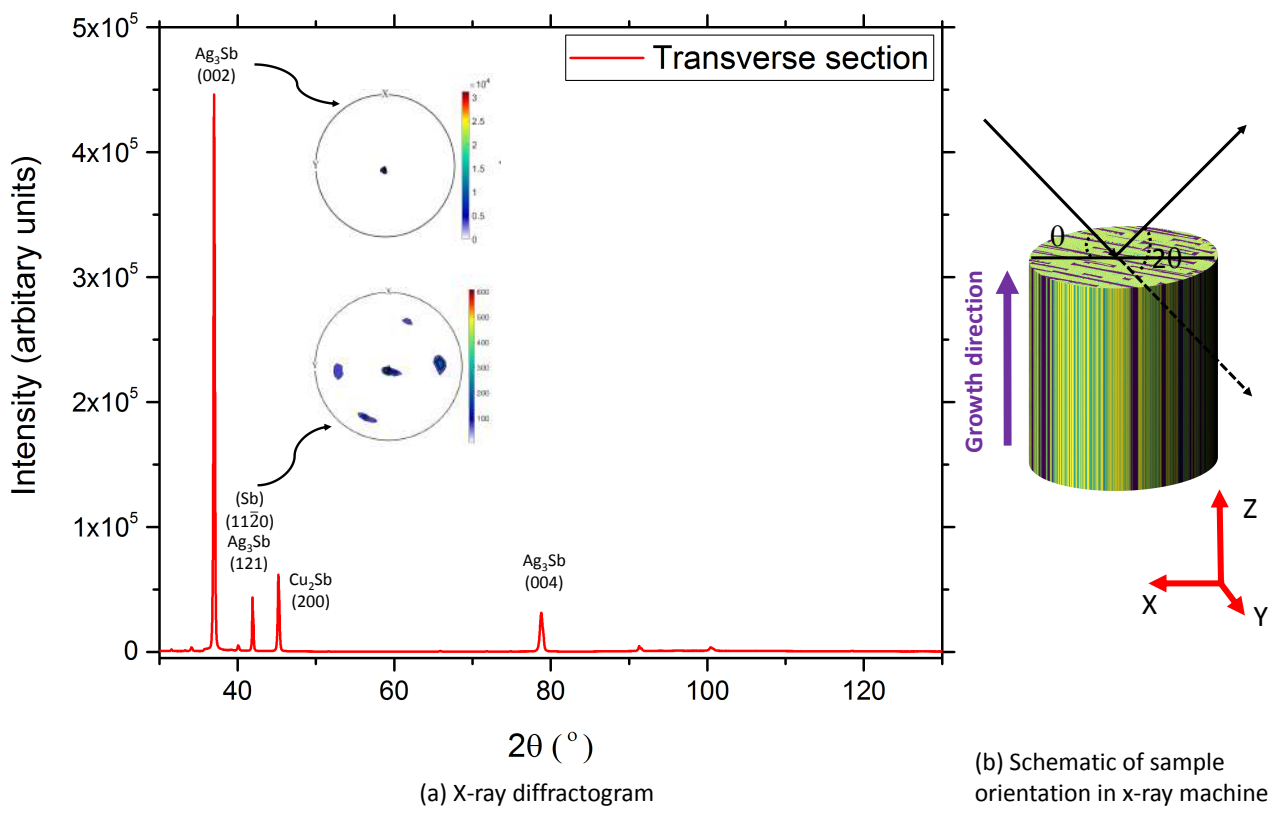


Figure 6.3: (a) is the x-ray diffractogram corresponding to the eutectic sample (solidified at  $0.5 \mu\text{m/s}$ ) obtained by conducting x-ray diffraction on the transverse section (section perpendicular to imposed temperature gradient) as shown in the schematic (b). The inset of (a) has x-ray pole figures corresponding to the  $\text{Ag}_3\text{Sb}$  and (Sb) diffraction peaks.SAED pattern shown in Fig. 6.2 corresponds to the same sample.

Phase	Crystal system	Space group	Pearson symbol	lattice parameters (nm)
Ag <sub>3</sub> Sb	Orthorhombic[195]	Pmnm	oP8	a=0.611; b=0.536; c=0.485
Cu <sub>2</sub> Sb	Tetragonal[196]	P4/nmm	tP6	a=b=0.408; c=0.620
(Sb)	Rhombohedral[197]	R̄3m	hR6	a=0.43*; c=1.146*

Table 6.1: Crystal structure of the phases present in the system (\*hexagonal cell).

spots obtained in transmission electron microscope (TEM) and X-ray diffraction pattern as shown in Fig.6.2.

## 6.1.2 Morphological selection

### 6.1.2.1 Ternary eutectic composition

Fig. 6.4 shows the microstructures of the eutectic composition (Ag<sub>42.4</sub>Cu<sub>21.6</sub>Sb<sub>36</sub>) captured in transverse sections obtained at different velocities. The bright phase is Ag<sub>3</sub>Sb, the gray phase is Cu<sub>2</sub>Sb, and the dark phase is (Sb). Although the element Sb is the heavier among the chosen elements; due to etching, it appears as the darkest phase in most of the experiments except at 0.5  $\mu\text{m}/\text{s}$  where the Sb pit is much larger and backscatter electron signal from the pit leads to a bright contrast as shown in Fig. 6.5.

Transverse sections in Fig. 6.4 depicts that the morphology of the (Sb) phase is fibrous at high velocities ( $V = 8.0, 16.0, 32.0 \mu\text{m}/\text{s}$ ) while the morphology becomes blocky at low velocity ( $V = 0.5 \mu\text{m}/\text{s}$ ) with a length scale much larger than that of morphologies observed at higher velocities (refer Fig. 6.7b). The exciting features of the morphology are shown using an arrow in the SEM image of Fig. 6.4a, where the blocky (Sb) structures seem to surround the other two solid phases during growth as also revealed in Fig. 6.8b,c. The morphologies seem to be influenced by the presence of strong solid-liquid anisotropy either in the interfacial energy or in the attachment kinetics. These microstructures are unique in eutectic systems occurring in only limited systems in nature. In the discussion section 6.1.2.3, using the results obtained from SEM, X-ray tomography, and EBSD, we propose a growth mechanism leading to the formation of such structures. Further, the morphology of (Sb) observed at a velocity of 1.0  $\mu\text{m}/\text{s}$  exhibits structures resembling elongated plates aligned in fixed orientations. The morphology of the gray phase, i.e., Cu<sub>2</sub>Sb is predominantly rod/broken-lamellar exhibiting a regular structure in all experiments and we will discuss its features in the following sections. The Ag<sub>3</sub>Sb phase

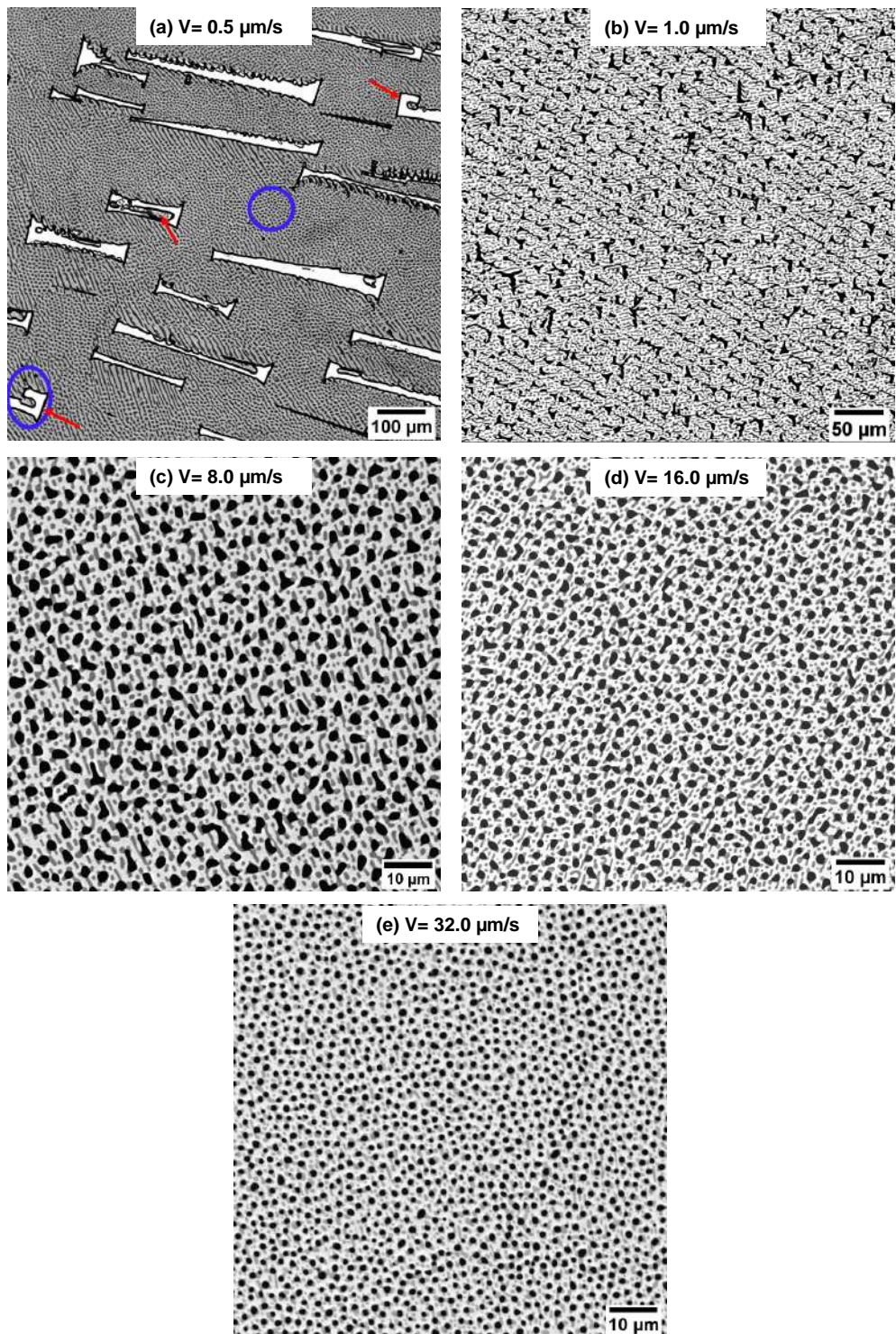


Figure 6.4: (a)-(e) are the SEM images captured in the transverse section of directionally solidified ternary Ag-Cu-Sb eutectic (at.-%: Ag<sub>42.4</sub>Cu<sub>21.6</sub>Sb<sub>36</sub>) alloys obtained at different velocities i.e., 0.5, 1.0, 8.0, 16.0, 32.0  $\mu\text{m/s}$  respectively. Images reveal that with decreasing solidification velocity, the (Sb) transforms from a fibrous to bulky structure, whereas Cu<sub>2</sub>Sb is predominantly a mixture of rod/broken-lamellar type morphology.

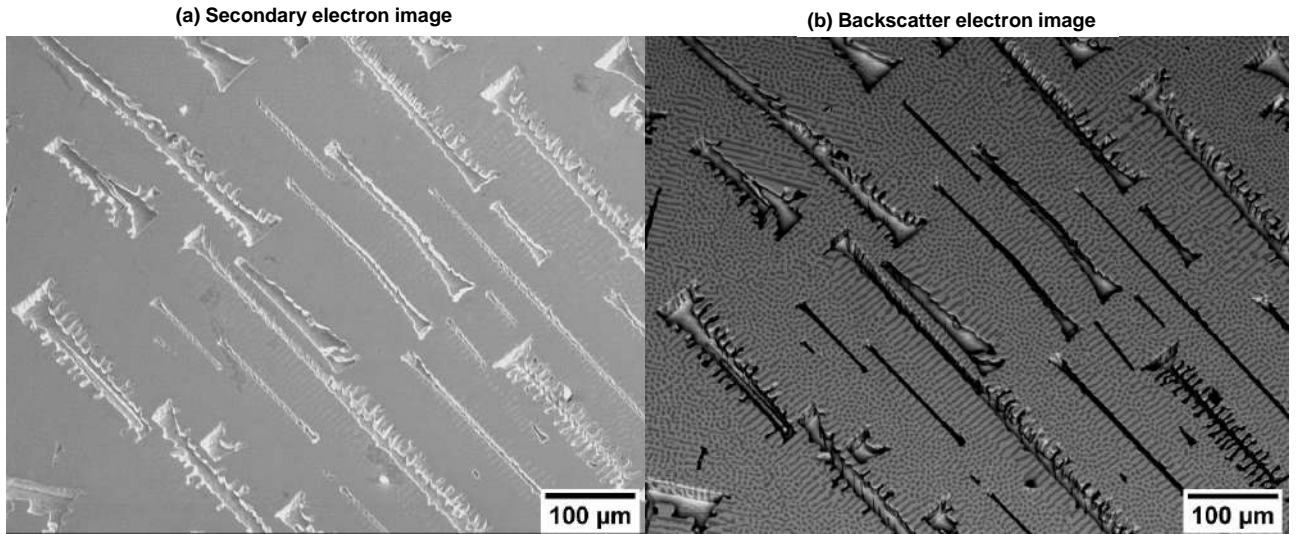


Figure 6.5: (a) is Secondary electron image, while (b) is Backscatter electron image from same location. The contrast of the (Sb) phase (bright or dark) depends on the width of the pit. Size of pit influences the BSE signal from (Sb) phase. Hence some of the (Sb) regions appear dark while others appear bright.

forms a continuous morphology in these experimental micrographs.

#### 6.1.2.2 Ternary off-eutectic composition- $\text{Ag}_{35}\text{Cu}_{25}\text{Sb}_{40}$ )

A composition, i.e.,  $\text{Ag}_{35}\text{Cu}_{25}\text{Sb}_{40}$  close to the ternary eutectic composition, has been chosen to study the influence of composition on three-phase growth. This composition leads to an increase in  $\text{Cu}_2\text{Sb}$  and (Sb) phase percentages. The alloys of the selected composition are directionally solidified at different velocities, and the transverse section images of the samples are as shown in Fig. 6.6. Images reveal that the directionally solidified samples do not exhibit any primary phase(s) formation, which could be due to the composition selected lying in the three-phase coupled zone which depends on the material properties (liquidus slopes in phase diagram/solutal diffusivities etc.) and processing conditions (temperature gradient and velocity). The (Sb) phase's morphology is mostly a dog bone type structure; however, the feature becomes blocky at low velocity ( $V = 0.5 \mu\text{m/s}$ ) with similar features (shown with an arrow) as observed in the eutectic sample solidified at  $0.5 \mu\text{m/s}$ . The mechanisms behind the evolution of such microstructures is similar and is discussed in the section 6.1.2.3. Further, at these off-eutectic compositions, the (Sb) phase at higher velocities exhibits a dog-bone type structure with a increased volume percentage of (Sb), in contrast to the fibrous structure at

the eutectic composition. Even with the change in the far-field liquid composition, the Cu<sub>2</sub>Sb phase morphology is very similar to that observed at the three-phase eutectic composition.

As grayscale images obtained from SEM are difficult to quantify, the images are firstly segmented using three-level thresholding [173], and thereafter spatial relationships between the phases are deduced by computing the 2-point spatial correlations [170, 171, 172]. The reduced vector space map contains all radial vectors and their probabilities of occurrence becomes a strong basis for analysis of the microstructures. Additionally, the spatial correlations are utilized for determining the spacings in microstructures obtained for both compositions solidified at different velocities, and the results are shown in Fig. 6.7, where the error bars in the plot are the standard deviation in the eutectic spacing data. We linearly fit the observed  $\lambda$  versus  $V^{-0.5}$  ( $\lambda$  is spacing, V is the velocity) for both the phases in the two compositions as shown in Fig. 6.7. The square of the slope obtained from the linear fitting reveals the eutectic scaling constant, i.e.,  $\lambda^2V$  that is approximately 10.24  $\mu\text{m}^3/\text{sec}$  for the Cu<sub>2</sub>Sb phase and 89.54  $\mu\text{m}^3/\text{sec}$  for (Sb) phase for the ternary eutectic composition, while for the alloy Ag<sub>35</sub>Cu<sub>25</sub>Sb<sub>40</sub>,  $\lambda^2V$  is approximately 12.96  $\mu\text{m}^3/\text{sec}$  for the Cu<sub>2</sub>Sb phase and 105.36  $\mu\text{m}^3/\text{sec}$  for the (Sb) phase. The differences in the scaling could have arisen due to variation in morphology as well as the crystallographic orientations between the samples. Further, a considerable deviation from the eutectic scaling is observed at the lower velocity of 0.5  $\mu\text{m}/\text{s}$ . The underlying reason for the  $\lambda^2V = \text{constant}$  scaling relation is due to a coupled influence of diffusion and capillarity [2]. The deviations from the eutectic scaling can be attributed to a shift towards an interface limited growth at lower velocities for the (Sb) crystal.

### 6.1.2.3 Discussions

We have already seen that the morphology of the Sb-rich phase is different in the lower velocity experiments, both in terms of morphology and length scale associated with it. In order to understand the growth behavior at  $V=0.5 \mu\text{m}/\text{s}$ , we have utilized the non-destructive X-ray tomography technique. Further, we have correlated the pole figures obtained from X-ray measurements (refer Fig. 6.2) and electron backscatter diffraction (EBSD) (refer Fig. 6.10a) results with the morphology in order to identify the growth mechanism.

From the results obtained from the X-ray tomography, we have selected one such interesting feature of the (Sb) phase in the microstructure and reconstructed it in 3D to show its evolution at different growth stages as sub-figures (i-v) of Fig. 6.8a by making the other phases transparent

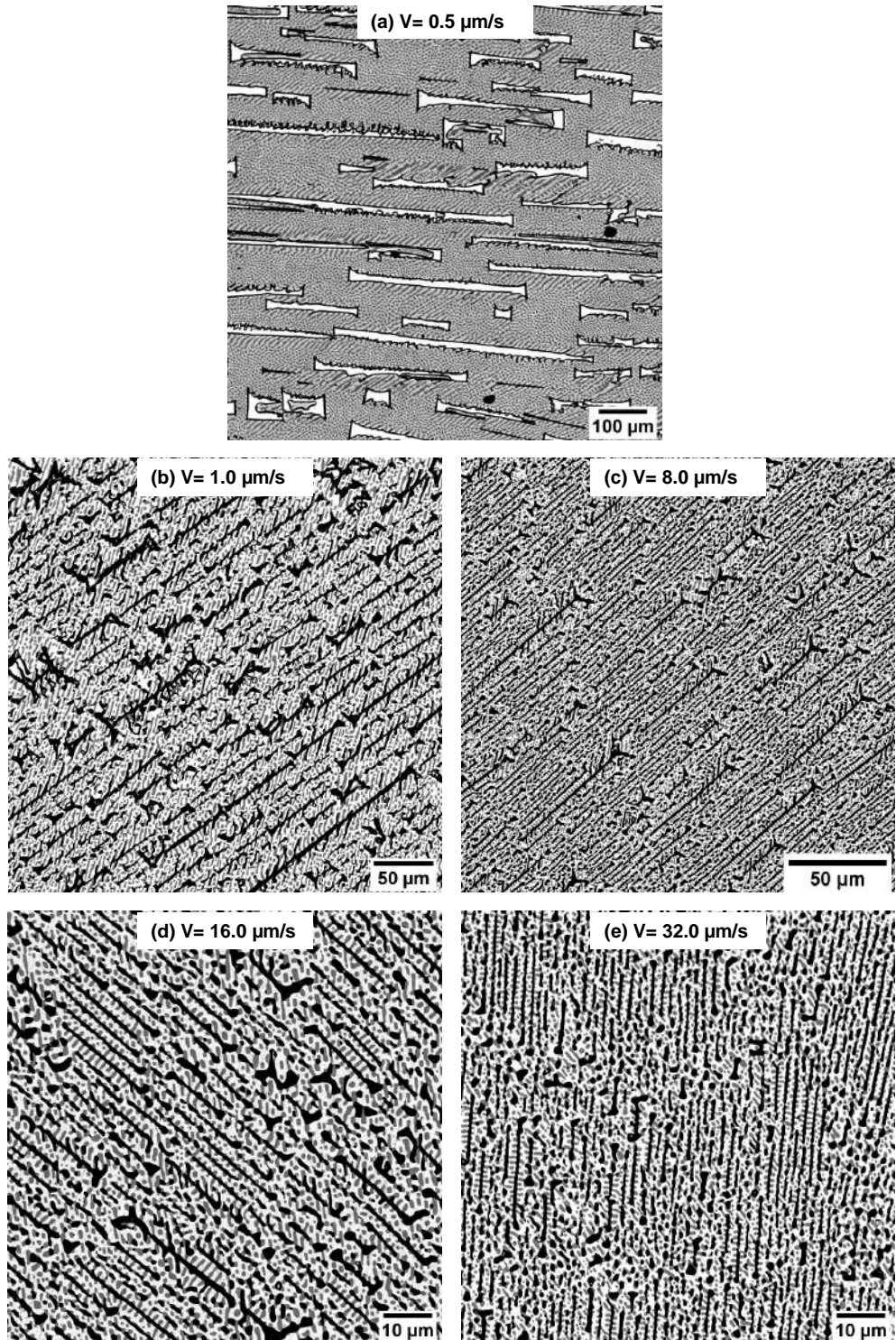
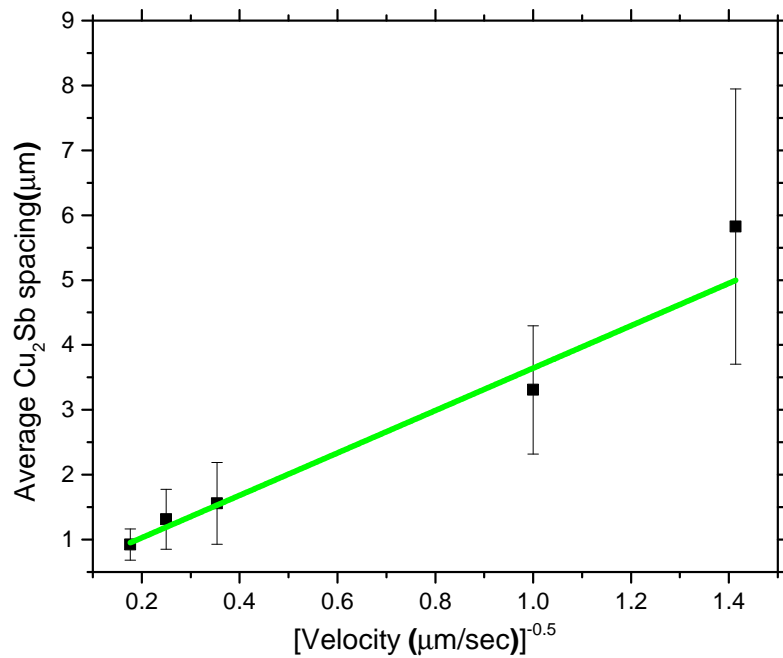
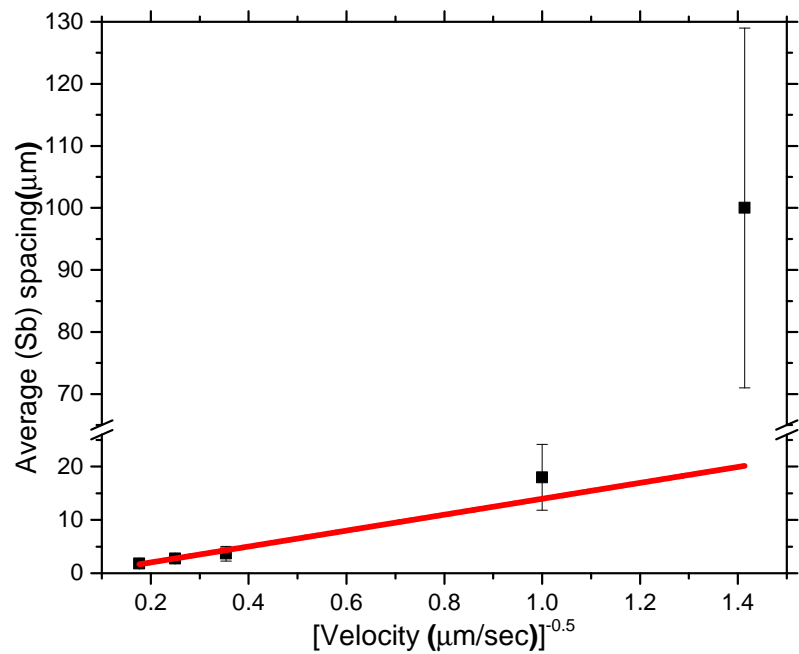


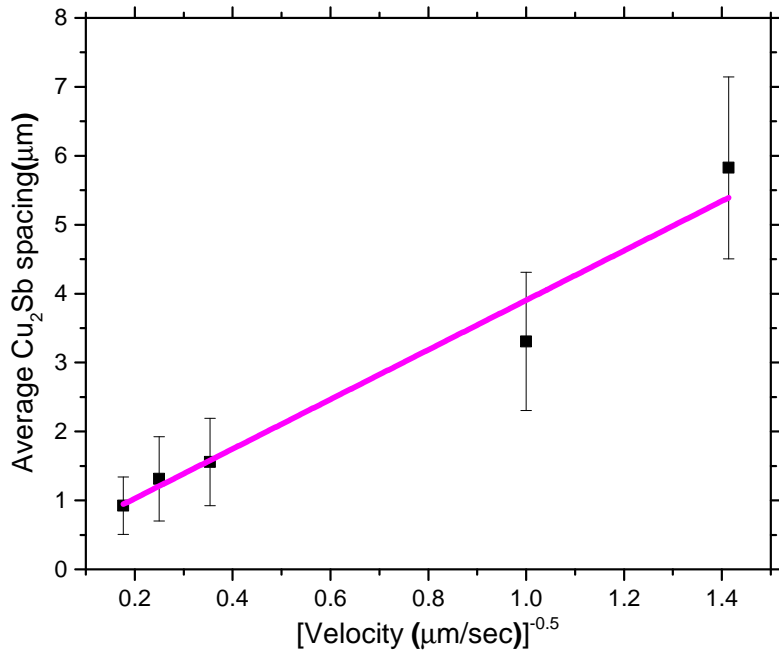
Figure 6.6: (a)-(e) are the SEM images captured in the transverse section of directionally solidified alloys of  $\text{Ag}_{35}\text{Cu}_{25}\text{Sb}_{40}$  (at.%) composition obtained at different velocities, i.e., 0.5, 1.0, 8.0, 16.0, 32.0  $\mu\text{m/s}$  respectively. Images show that the (Sb) phase exhibits dog bone type morphology at higher velocities and bulky structure at 0.5  $\mu\text{m/s}$ , whereas  $\text{Cu}_2\text{Sb}$  phase exhibits predominantly rod/broken-lamellar type morphologies.



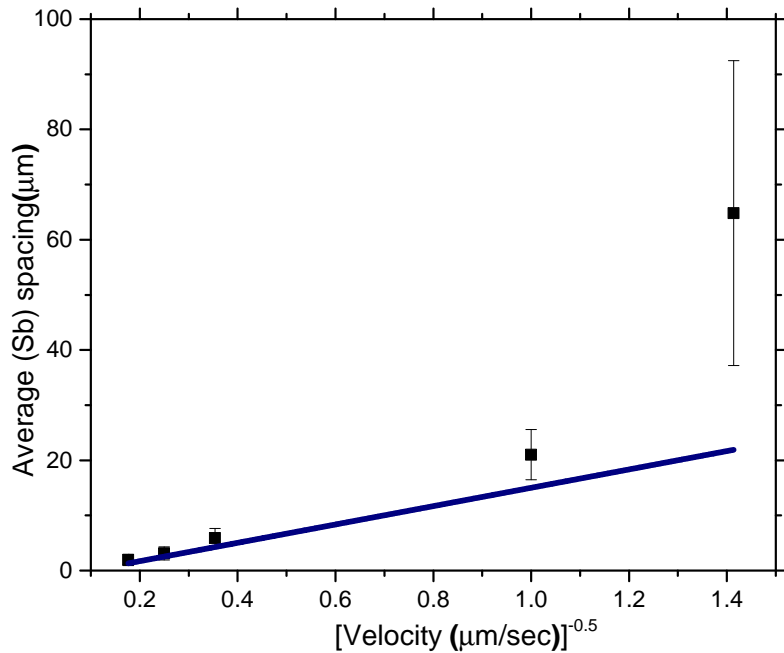
(a)  $\text{Cu}_2\text{Sb}$  spacing in the eutectic alloy.



(b) (Sb) spacing in the eutectic alloy.

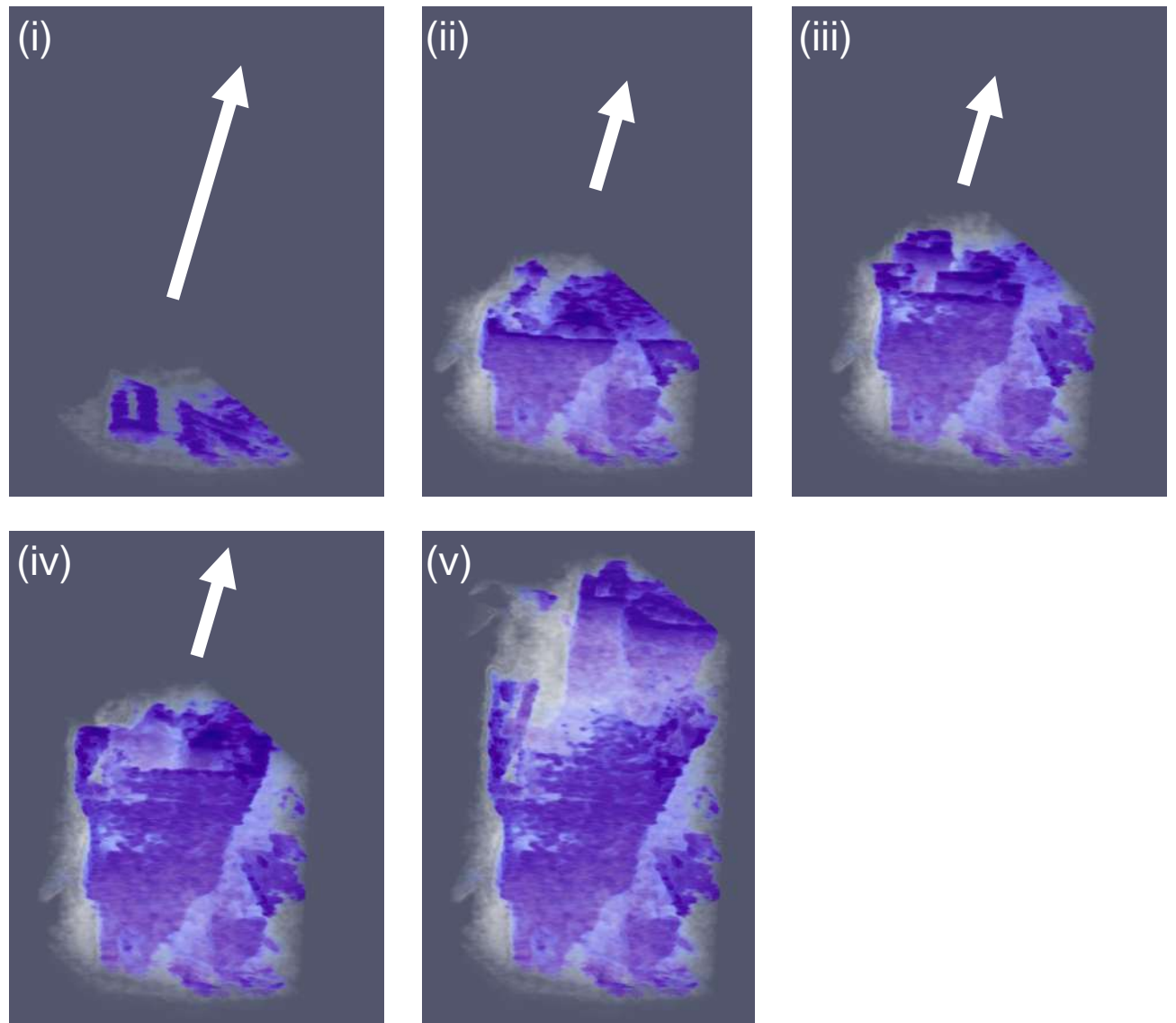


(c)  $\text{Cu}_2\text{Sb}$  spacing in  $\text{Ag}_{35}\text{Cu}_{25}\text{Sb}_{40}$  alloy.



(d) (Sb) spacing in  $\text{Ag}_{35}\text{Cu}_{25}\text{Sb}_{40}$  alloy.

Figure 6.7: Average eutectic spacing variation with velocity.



(a) (i)-(v) are the images of the (Sb) phase (blue region) obtained by reconstructing the x-ray tomography dataset to illustrate its morphology at different stages during the growth. The other phases present in the sample are made transparent.

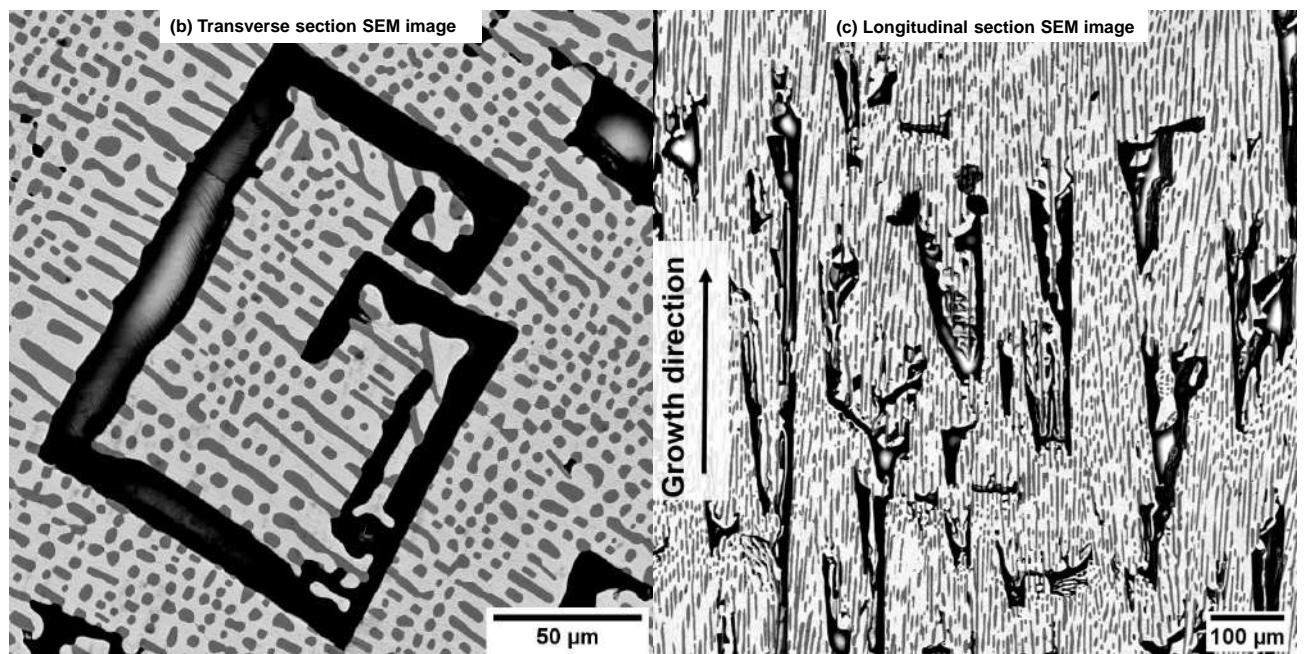
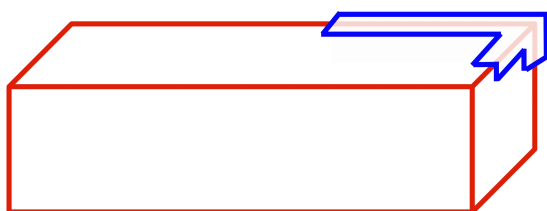


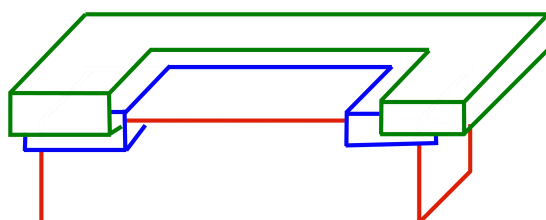
Figure 6.8: (a) is the collage of (Sb) phase during evolution obtained using an x-ray tomography dataset, whereas (b), (c) are three-phase microstructures captured using SEM in the transverse and longitudinal sections, respectively. Images correspond to the sample solidified at the velocity of  $0.5 \mu\text{m/s}$ . Images reveal the formation of hollow space inside the blocky phase morphology, which gradually widens as it evolves.



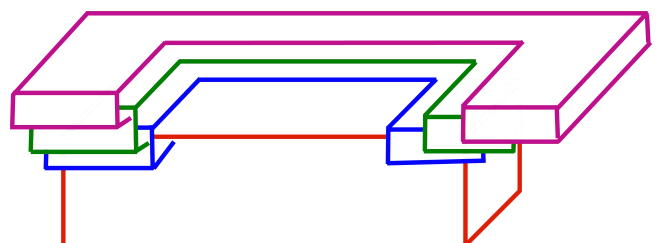
(a)



(b)



(c)



(d)

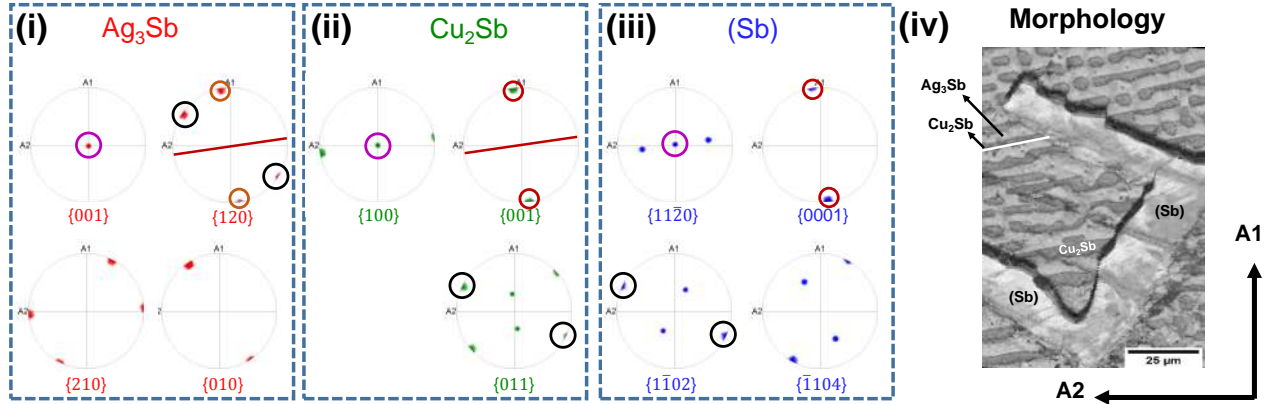
Figure 6.9: (a)-(d) are the schematics to elucidate the mechanism at different stages during the growth of the (Sb) phase.

in the images. The transverse and longitudinal section images of such a (Sb) feature are shown in Fig. 6.8b,c respectively. The 3D volume rendering images, SEM images of Fig. 6.8 reveal the evolution of (Sb) phase in 3D, wherein we can see the possible formation of a hollow space inside the blocky phase morphology, which gradually widens as it evolves. Further, the results obtained from the diffraction experiments (refer Fig. 6.2,6.10b,6.10c), reveal that one of the  $\{11\bar{2}0\}$  family planes is exposed to the liquid during the growth. These planes might be the thermodynamically low energy solid-liquid interface planes. Based on the observations, we propose the following mechanism for the evolution of such eutectic structures using the schematics as shown in Fig. 6.9.

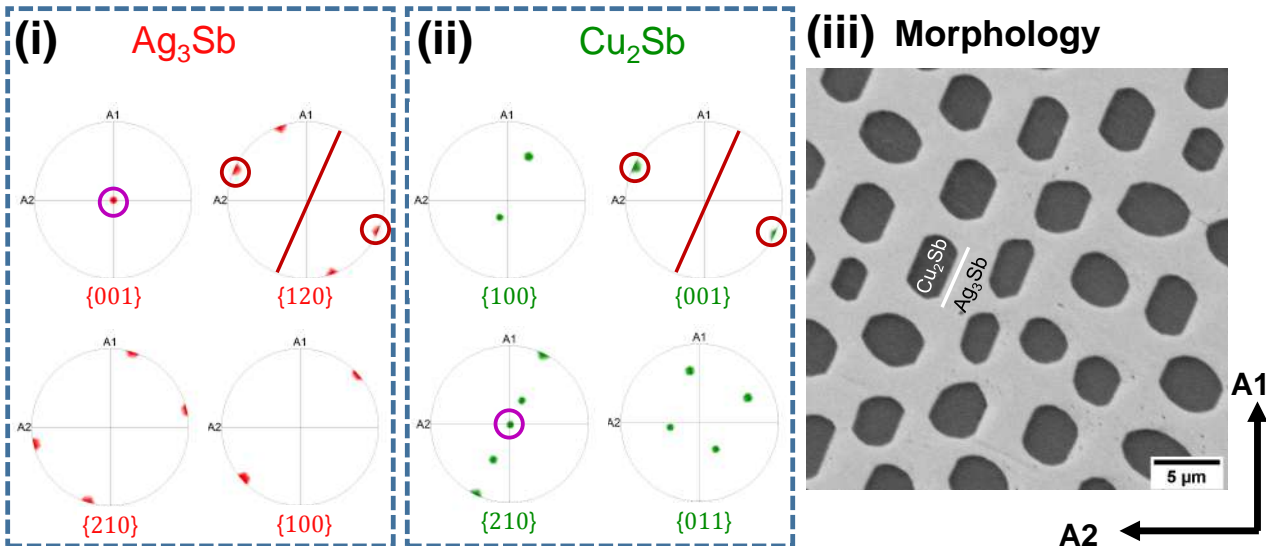
Let us consider a crystal (shown as red in the schematic (a)) that has flat interfaces with liquid. We suspect that the  $\{11\bar{2}0\}$ (see Sec. 6.1.3) family planes of the Sb crystal that are facing the liquid for this growth condition are atomistically smooth, thereby the growth occurs by the formation and propagation of ledges. As seen in the schematic, the ledges occur at corners/edges in the morphology, and growth propagates laterally where the atomic attachment occurs most readily. As the temperature gradient translates vertically, ledge formation initiates again on the solidified corners and edges and the process continues. The completion of the lateral growth depends on the speed of transverse and may lead to the formation of 'G' or 'C' shapes if the growth occurs with multiple edges, while dog bone or 'L' shape appears if the growth happens with only one edge. The coexistence of all these morphologies in the same microstructure can also be observed. A natural consequence of the mechanism is that we have a morphology where the enclosed space widens with solidification time (refer to Fig.6.8), where the liquid is rich in Ag/Cu that allows the coupled growth of the other solid phases  $\text{Ag}_3\text{Sb}$  and  $\text{Cu}_2\text{Sb}$ . Such morphologies have been reported in many crystal growth processes [202, 203, 204, 205, 206], however, the formation of such morphologies in the case of melt growth is rare in the literature [207, 208].

Further, in the eutectic samples solidified at velocities 8.0, 16.0, 32.0  $\mu\text{m}/\text{s}$ , (Sb) exhibits a fibrous morphology, whereas in the off-eutectic ( $\text{Ag}_{35}\text{Cu}_{25}\text{Sb}_{40}$ ), (Sb) exhibits a dog bone type microstructure. As we see later in the section on crystallographic orientation selection, this is related to the change in the growth directions, where the dog bone features are a result of the same mechanism that leads to the formation of blocky C, G and L type morphologies, while the fibrous morphologies clearly indicate a transformation in the growth mechanism to possibly a diffusion controlled evolution.

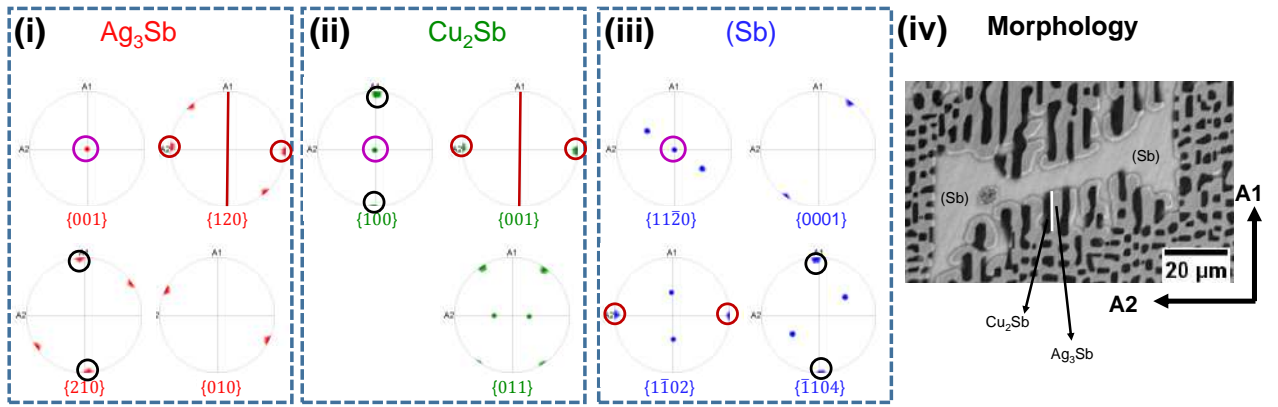
### 6.1.3 Crystallographic orientation selection



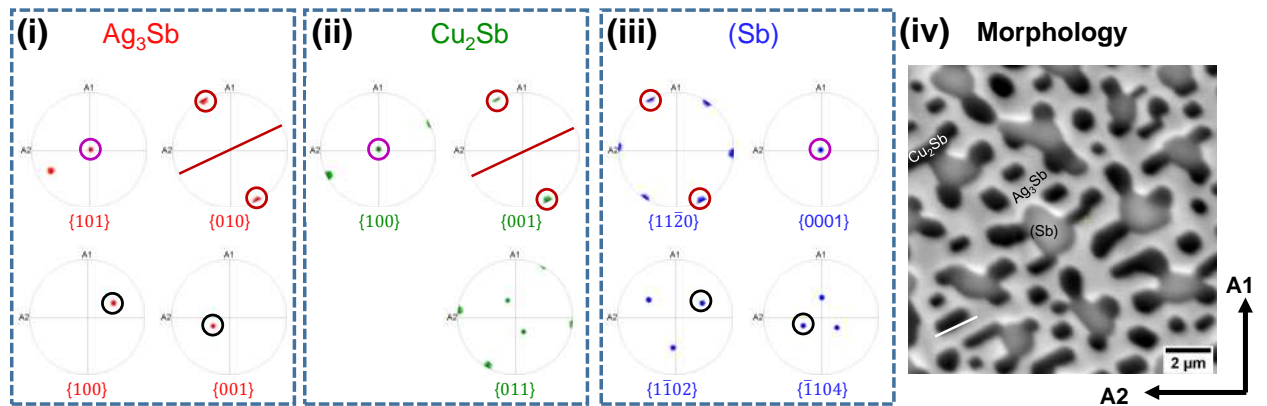
(a) (i), (ii), (iii) are the pole figures of  $\text{Ag}_3\text{Sb}$ ,  $\text{Cu}_2\text{Sb}$ , and Sb-rich phases obtained from ternary eutectic sample solidified at  $0.5 \mu\text{m/s}$  near to the bulky (Sb) consisting of three-phase microstructure as shown in (iv) exhibiting orientation relationships i.e. one of the  $\{001\}_{\text{Ag}_3\text{Sb}} \parallel$  one of the  $\{100\}_{\text{Cu}_2\text{Sb}} \parallel$  one of  $\{11\bar{2}0\}_{(\text{Sb})}$ , and  $\{120\}_{\text{Ag}_3\text{Sb}} \parallel \{001\}_{\text{Cu}_2\text{Sb}} \parallel \{0001\}_{(\text{Sb})}$ .



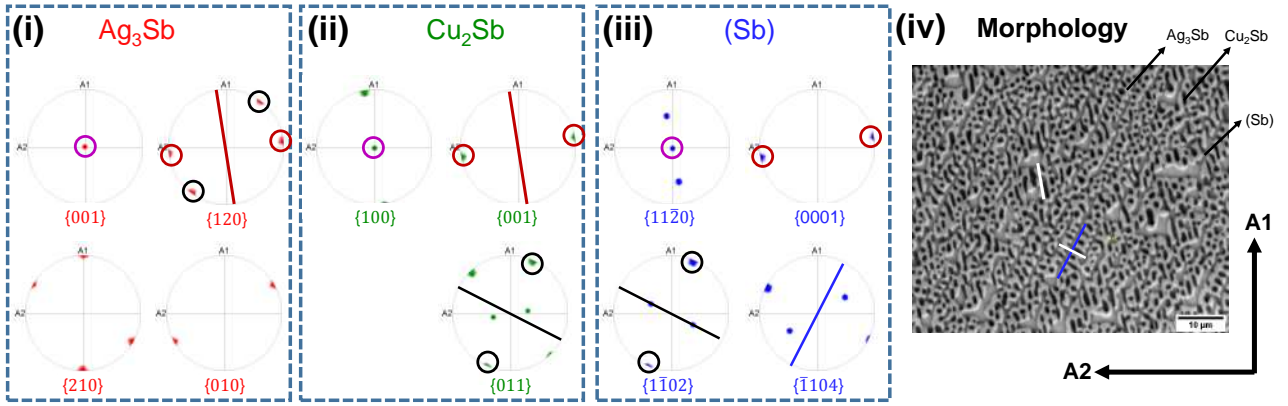
(b) (i), (ii) are the pole figures of  $\text{Ag}_3\text{Sb}$ ,  $\text{Cu}_2\text{Sb}$  phases obtained from ternary eutectic sample solidified at  $0.5 \mu\text{m/s}$ , little distance away from the bulky (Sb) consisting of relatively randomly  $\text{Cu}_2\text{Sb}$  phase as shown in (iii) exhibiting orientations as one of the  $\{001\}_{\text{Ag}_3\text{Sb}} \parallel$  one of the  $\{210\}_{\text{Cu}_2\text{Sb}}$ , and  $\{120\}_{\text{Ag}_3\text{Sb}} \parallel \{001\}_{\text{Cu}_2\text{Sb}}$ .



(c) (i), (ii), (iii) are the pole figures of  $\text{Ag}_3\text{Sb}$ ,  $\text{Cu}_2\text{Sb}$ , and Sb-rich phases obtained from ternary eutectic sample solidified at  $0.5 \mu\text{m}/\text{s}$  where  $\text{Cu}_2\text{Sb}$  features appear approximately perpendicular to the bulky (Sb) consisting of three-phase microstructure as shown in (iv) exhibiting orientations as one of the  $\{001\}_{\text{Ag}_3\text{Sb}}||$  one of the  $\{100\}_{\text{Cu}_2\text{Sb}}||$  one of  $\{11\bar{2}0\}_{(\text{Sb})}$ , and  $(\bar{1}20)_{\text{Ag}_3\text{Sb}}|| (001)_{\text{Cu}_2\text{Sb}}||$  one of  $(\bar{1}\bar{1}02)_{(\text{Sb})}$ .



(d) (i), (ii), (iii) are the pole figures of  $\text{Ag}_3\text{Sb}$ ,  $\text{Cu}_2\text{Sb}$ , and Sb-rich phases obtained from ternary eutectic sample solidified at  $32.0 \mu\text{m}/\text{s}$  consisting of three-phase microstructure as shown in (iv) exhibiting orientation relationships i.e. one of the  $\{101\}_{\text{Ag}_3\text{Sb}}||$  one of the  $\{100\}_{\text{Cu}_2\text{Sb}}|| (0001)_{(\text{Sb})}$ , and  $(010)_{\text{Ag}_3\text{Sb}}|| (001)_{\text{Cu}_2\text{Sb}}||$  one of  $\{11\bar{2}0\}_{(\text{Sb})}$ .



(e) (i), (ii), (iii) are the pole figures of  $\text{Ag}_3\text{Sb}$ ,  $\text{Cu}_2\text{Sb}$ , and Sb-rich phases obtained from  $\text{Ag}_{35}\text{Cu}_{25}\text{Sb}_{40}$  alloy solidified at  $16.0 \mu\text{m/s}$  consisting of three-phase microstructure as shown in (iv) exhibiting orientation relationships i.e. one of the  $\{001\}_{\text{Ag}_3\text{Sb}} \parallel$  one of the  $\{100\}_{\text{Cu}_2\text{Sb}} \parallel$  one of  $\{11\bar{2}0\}_{(\text{Sb})}$ , and  $(120)_{\text{Ag}_3\text{Sb}} \parallel (001)_{\text{Cu}_2\text{Sb}} \parallel (0001)_{(\text{Sb})}$ . The trace of dog-bone (Sb) is highlighted using a blue line.

Figure 6.10: Pole figures obtained from EBSD data of different microstructures. EBSD is performed on transverse sections with A1, A2 directions as shown in the corresponding morphology. Planes lying in the center of the pole figure correspond to the planes facing the liquid. The solid-solid interface trace between  $\text{Ag}_3\text{Sb}$  and  $\text{Cu}_2\text{Sb}$  is highlighted on the morphology as well as the pole figures.

EBSD was conducted on transverse sections for the samples that capture the range of morphologies observed in our experiments. Pole figures obtained for different microstructures are shown in Fig. 6.10 (For unit cell settings, refer to table 6.1). Following inferences can be drawn by comparing the location of poles to the corresponding morphology (A1, A2 directions are as shown in the image (iv)).

### The samples exhibiting the blocky morphology

We begin with the samples solidified at a velocity  $V=0.5\mu\text{m/s}$  where we get three different types of microstructures in the experiments. While the (Sb) phase in all the experiments at this velocity has a blocky morphology that is either 'G', 'C', 'L' or dog-bone shaped, we observe different microstructures for the  $\text{Cu}_2\text{Sb}$  phase distributed in the  $\text{Ag}_3\text{Sb}$  matrix phase. In Fig. 6.4a, we see that  $\text{Cu}_2\text{Sb}$  phase that shares an interface with the (Sb) has an orientation of the solid-solid interface that is at a fixed inclination with the (Sb) phase whereas at a short distance away from the (Sb) phase a more random distribution of rods of  $\text{Cu}_2\text{Sb}$  is observed. Crystallographically, the  $\text{Cu}_2\text{Sb}$  in both the locations are different as depicted in Figs. 6.10a, 6.10b.

This observation of different crystals hints at the possibility of nucleation events occurring at separate times during the solidification, wherein, one of the orientations of the Cu<sub>2</sub>Sb phase has nucleated with the (Sb)-phase as a surface and the second orientation occurs through independent nucleation in the liquid and in relation to the Ag<sub>3</sub>Sb phase. Crystallographic relations between the three phases is evident, wherein we find for the three-phase microstructure near to the blocky (Sb) phase as highlighted in Fig.6.10a(iv), the following relations hold: one of the {001} poles of Ag<sub>3</sub>Sb || one of the {100} poles of Cu<sub>2</sub>Sb || one of {11̄20} poles of (Sb) along with (120) pole of Ag<sub>3</sub>Sb || {001} poles Cu<sub>2</sub>Sb || {0001} poles of (Sb). TEM diffraction patterns obtained from three-phase microstructures near the blocky (Sb) phase confirms the same orientation relationship for the sample solidified at 0.5  $\mu\text{m}/\text{s}$  as shown in Fig. 6.2.

In addition, we observe a preferential set of (Sb) planes facing the liquid, which hints at the possible presence of solid-liquid interfacial energy anisotropy. Furthermore, one of the {1̄104} and one of the {11̄02} planes are perpendicular to the trace of 'C' morphology in the section in Fig.6.10a(iv). These planes could play a role in the mechanism discussed in the previous section (see Sec.6.1.2.3), where attachment of atoms occur on these planes. For the Cu<sub>2</sub>Sb phases that are distributed relatively randomly a little distance away from the (Sb)-phase in Fig.6.4a, the crystallographic relations with the Ag<sub>3</sub>Sb phases are depicted in Fig.6.10b. Here, we see that the (1̄20) pole of Ag<sub>3</sub>Sb phase, instead of the (120) pole of Ag<sub>3</sub>Sb, is parallel to the {001} pole of the Cu<sub>2</sub>Sb phase which indicates that there is a rotation of the Cu<sub>2</sub>Sb crystal orientation with respect to the other two phases, which results in the {001} pole of Ag<sub>3</sub>Sb now becoming parallel to the one of {210} poles of Cu<sub>2</sub>Sb. We also note from the high resolution image of the morphology in Fig.6.10b that the solid-solid interface has a shape that resembles a truncated ellipse, where the truncating planes are parallel to the (1̄20) planes of Ag<sub>3</sub>Sb as well as the {001} planes of Cu<sub>2</sub>Sb as derived by comparing the straight edges of the morphology in Fig.6.10b(iv) with the respective pole figures. The morphology of the Cu<sub>2</sub>Sb phase has signatures of the presence of solid-solid interfacial energy anisotropy where the straight edges in the morphology in Fig.6.10b(iv) correspond to low energy directions/planes of the  $\gamma - \text{plot}$  of the interface separating the Ag<sub>3</sub>Sb and Cu<sub>2</sub>Sb phases. This is also true for the lamellar features near the (Sb) blocky morphology where the interface between the the Ag<sub>3</sub>Sb and Cu<sub>2</sub>Sb is parallel to (120) plane of Ag<sub>3</sub>Sb and (001) pole of Cu<sub>2</sub>Sb.

Apart from these, a third morphology is also observed as shown in Fig.6.10c(iv) where, in contrast to the morphology in Fig.6.10a(iv), the Cu<sub>2</sub>Sb features appear to be perpendicular to

the blocky (Sb) morphology instead of being inclined in Fig.6.10a(iv). This difference in the microstructure also has its basis in the crystallography, where in the orientation relationships, instead of the relation (120) pole of  $\text{Ag}_3\text{Sb} \parallel \{001\}$  poles  $\text{Cu}_2\text{Sb} \parallel \{0001\}$  poles of (Sb), in Fig.6.10a, we have ( $\bar{1}20$ ) pole of  $\text{Ag}_3\text{Sb} \parallel \{001\}$  poles  $\text{Cu}_2\text{Sb} \parallel$  one of the  $\{1\bar{1}02\}$  poles of (Sb). While this is a small change, it is important to mention that, from the previous relation where the (120) pole of  $\text{Ag}_3\text{Sb} \parallel \{001\}$  poles  $\text{Cu}_2\text{Sb} \parallel \{0001\}$  poles of (Sb), it follows that the ( $\bar{1}20$ ) pole of  $\text{Ag}_3\text{Sb}$  is nearly parallel to one of  $\{1\bar{1}02\}$  poles of (Sb), while in the crystallographic relations displayed in Fig.6.10c, it is clear that the basal planes of (Sb) are no longer parallel to any of the  $\{120\}$  poles of  $\text{Ag}_3\text{Sb}$ . We believe it is this difference that leads to the modified microstructure in Fig.6.10c with respect to Fig.6.10b.

### **The samples exhibiting the regular ternary eutectic**

EBSD of the ternary alloy solidified at  $32.0 \mu\text{m/s}$  is shown in Fig. 6.10d. It reveals that the growth behavior of the  $\text{Ag}_3\text{Sb}$  and (Sb) phases is different in comparison to samples solidified at  $0.5 \mu\text{m/s}$  as well as the samples that are richer in Sb. Here, the  $\text{Ag}_3\text{Sb} \{101\}$ , (Sb)  $\{0001\}$  and the  $\text{Cu}_2\text{Sb} \{100\}$  planes face the liquid. This corresponds to an approximately  $90^\circ$  rotation of the (Sb) phase in terms of its orientation with the temperature gradient in comparison with the previous morphologies obtained for solidification at lower velocities. The change in the orientation of the (Sb) phase probably brings about a change in the growth mechanism as revealed by a more uniform distribution of the fibrous (Sb) phase along with the other solid phases in contrast to the blocky structures discussed in the preceding section. Here, the  $\text{Cu}_2\text{Sb}$  interface shapes have a similarity with the morphologies observed in Fig.6.10b(iii) that resemble a truncated ellipse. However, here the straight edges in the  $\text{Cu}_2\text{Sb}$  morphology are parallel to the  $\{010\}$  planes of  $\text{Ag}_3\text{Sb}$  as shown in Fig.6.10d(i) instead of the  $\{120\}$  planes in Fig.6.10b(i), while they continue to be parallel to the  $\{100\}$  planes of  $\text{Cu}_2\text{Sb}$  as shown in Fig.6.10d(ii). The orientation relationship obtained in this microstructure having the fibrous morphology is  $\text{Ag}_3\text{Sb}\{101\} \parallel \text{Cu}_2\text{Sb}\{100\} \parallel (\text{Sb})\{0001\}$  and  $\text{Ag}_3\text{Sb}\{010\} \parallel \text{Cu}_2\text{Sb}\{001\} \parallel (\text{Sb})\{11\bar{2}0\}$ .

### **The samples exhibiting the dog bone morphology of $\text{Ag}_{35}\text{Cu}_{25}\text{Sb}_{40}$ alloy**

EBSD of the  $\text{Ag}_{35}\text{Cu}_{25}\text{Sb}_{40}$  alloy solidified at  $16.0 \mu\text{m/s}$  is shown in Fig. 6.10e. Pole figures reveal that  $\{001\}$  planes of  $\text{Ag}_3\text{Sb}$ ,  $\{100\}$  planes of  $\text{Cu}_2\text{Sb}$  and  $\{11\bar{2}0\}$  planes of (Sb) face the

liquid which are the same as the planes observed in the sample solidified at  $0.5 \mu\text{m}/\text{s}$  (refer Fig. 6.10a). Further,  $\text{Ag}_3\text{Sb}$  and  $\text{Cu}_2\text{Sb}$  exhibit the same orientation relationship that is observed in sample solidified at  $0.5 \mu\text{m}/\text{s}$  (see Fig. 6.10b), i.e.,  $\text{Ag}_3\text{Sb}\{001\} \parallel \text{Cu}_2\text{Sb}\{100\} \parallel (\text{Sb})11\bar{2}0$  and  $\text{Ag}_3\text{Sb}(120) \parallel \text{Cu}_2\text{Sb}\{001\} \parallel (\text{Sb})(0001)$ . As in the case of the morphologies at the lower velocity  $V=0.5\mu\text{m}/\text{s}$ , we find that for this set of crystal orientation relations we have as a corollary that  $\text{Ag}_3\text{Sb}(\bar{1}20)$  planes are nearly parallel to the  $1\bar{1}02$  planes of (Sb) and similarly the (011) planes of  $\text{Cu}_2\text{Sb}$  are parallel to the  $1\bar{1}02$  planes of (Sb). In terms of the differences in the morphology in comparison to the observations in Fig. 6.10a(iv), here we observe two orientations for the  $\text{Ag}_3\text{Sb}-\text{Cu}_2\text{Sb}$  solid interface; one of them is the same as that observed in Fig. 6.10b where the  $\text{Ag}_3\text{Sb}-\text{Cu}_2\text{Sb}$  interface is parallel to the (120) planes of  $\text{Ag}_3\text{Sb}$  as well as the (001) planes of  $\text{Cu}_2\text{Sb}$ ; and a second orientation that is approximately parallel to the  $(\bar{1}20)$  planes of  $\text{Ag}_3\text{Sb}$  as well as the (011) planes of  $\text{Cu}_2\text{Sb}$ . This hints at the possibility that for this orientation relationship, there are at least two facet planes in the corresponding Wulff-shape of the solid-solid interface which are highlighted in the SEM images as shown in Fig. 6.10e(iv). Furthermore, one of the  $\{\bar{1}104\}$  family of planes are parallel to the trace of dog bone morphology of (Sb).

#### 6.1.4 Two-phase colonies with three phase eutectic

In the previous section we have presented the morphologies that form during three-phase growth in the Ag-Cu-Sb eutectic system. In this section, we present microstructure formation involving two-phase eutectic colonies along with a three-phase eutectic reaction in the final liquid.

##### 6.1.4.1 $\text{Ag}_3\text{Sb}$ -(Sb) eutectic colonies

An off ternary eutectic composition, i.e.,  $\text{Ag}_{47}\text{Cu}_{15}\text{Sb}_{38}$ , has been chosen close to the two-phase eutectic line in the vicinity of the ternary eutectic composition. Transverse section images of the alloy solidified at different velocities are as shown in Fig. 6.11. Microstructures reveal the formation of hierarchical structures having two-phase colonies and three-phase eutectic morphologies.

We observe that the  $\text{Ag}_3\text{Sb}$  and (Sb) eutectic colonies exhibit complex structures with an inherent 3-fold symmetry that probably originates from the rhombohedral crystal symmetry of the (Sb) phase, as its dendrites exhibit a similar morphology and crystallography as shown in Fig. 6.18ii. The structure of the colony is different from that of exotic colonies observed in the previous chapter 5 and other eutectics, i.e.,  $\text{Al}_2\text{O}_3$ -  $\text{ZrO}_2$  ( $\text{Y}_2\text{O}_3$ ) [190],  $\text{MnSb}$ -(Sb)-X [191],

however, similarity can be found with the colonies reported in Ref. [153, 154, 209, 210]. In order to reveal the complex structure of the colony, we have milled the colony using gallium ions parallel to the two plates of the colony and the image is captured with the sample orientation as shown in the schematic of Fig. 6.12e, and the morphology captured is shown in Fig. 6.12d which is cut close to the vanes in the direction parallel to the plate morphology. The results observed are correlated with the crystallographic results obtained using EBSD. Poles obtained for  $\text{Ag}_3\text{Sb}$  and (Sb) are shown in Fig. 6.13 along with the corresponding SEM image. Pole figures (a), (d) in Fig. 6.13, reveals that the colony axis is aligned perpendicular to the {001} plane of  $\text{Ag}_3\text{Sb}$  and {0001} plane of (Sb). Further, poles shown in (b), (c), (e) of Fig. 6.13, reveals that the {11̄20} family of (Sb) being parallel to {010}, {210} family of  $\text{Ag}_3\text{Sb}$  which are highlighted in the crystal schematic of Fig. 6.13i,j. As the morphology shares features of the rhombohedral (Sb) crystal, the correlation between the morphology and crystallographic planes is made in terms of (Sb) planes, however, one can find corresponding  $\text{Ag}_3\text{Sb}$  planes using the relation ( $\{11\bar{2}0\}_{(Sb)} \parallel \{010\}_{\text{Ag}_3\text{Sb}}$ ,  $\{210\}_{\text{Ag}_3\text{Sb}}$  and  $\{0001\}_{(Sb)} \parallel \{001\}_{\text{Ag}_3\text{Sb}}$ ).

The three-fold symmetric complex fish skeleton is firstly composed of the {11̄20} family of planes of (Sb) that form the plates meeting at a central spine. This can be derived by comparing the pole figures (e) in Fig. 6.13 with the corresponding SEM image (h) in Fig. 6.13. Further, the colony structure exhibits branching from the central axes as shown in the longitudinal section image (see Fig. 6.12(a)) in combination with the three-dimensional perspective derived from dissecting the colony using gallium ions, highlighted in Fig. 6.12 d. These branches emanating from the central spine and which are perpendicular to the {11̄20} family of planes are at angle to the central spine. The angle that the trace of the branches on the {11̄20} plane makes with the central spine is approximately  $37^\circ$  as shown in Fig. 6.12d and consequently the plate normals make an angle of around  $53^\circ$  with the basal plane of (Sb). Correlating this information with the crystallography (see Fig. 6.13d,e,g) we find that the {1̄102} family of planes are the closest low-indexed candidates for the branches that emanate from the central axes which are perpendicular to the {11̄20} family of planes. Concurrently, the trace of the {1̄102} branches on the {11̄20} plane denote the approximate growth direction of the plates which is again derived from the crystallographic analysis as being parallel to the (1̄104) plane normal (approximately, see Fig. 6.13 d, f). For an illustration of the complex structure, a schematic of the colony is shown in Fig. 6.12b and a crystal schematic in Fig. 6.12c with the planes are discussed.

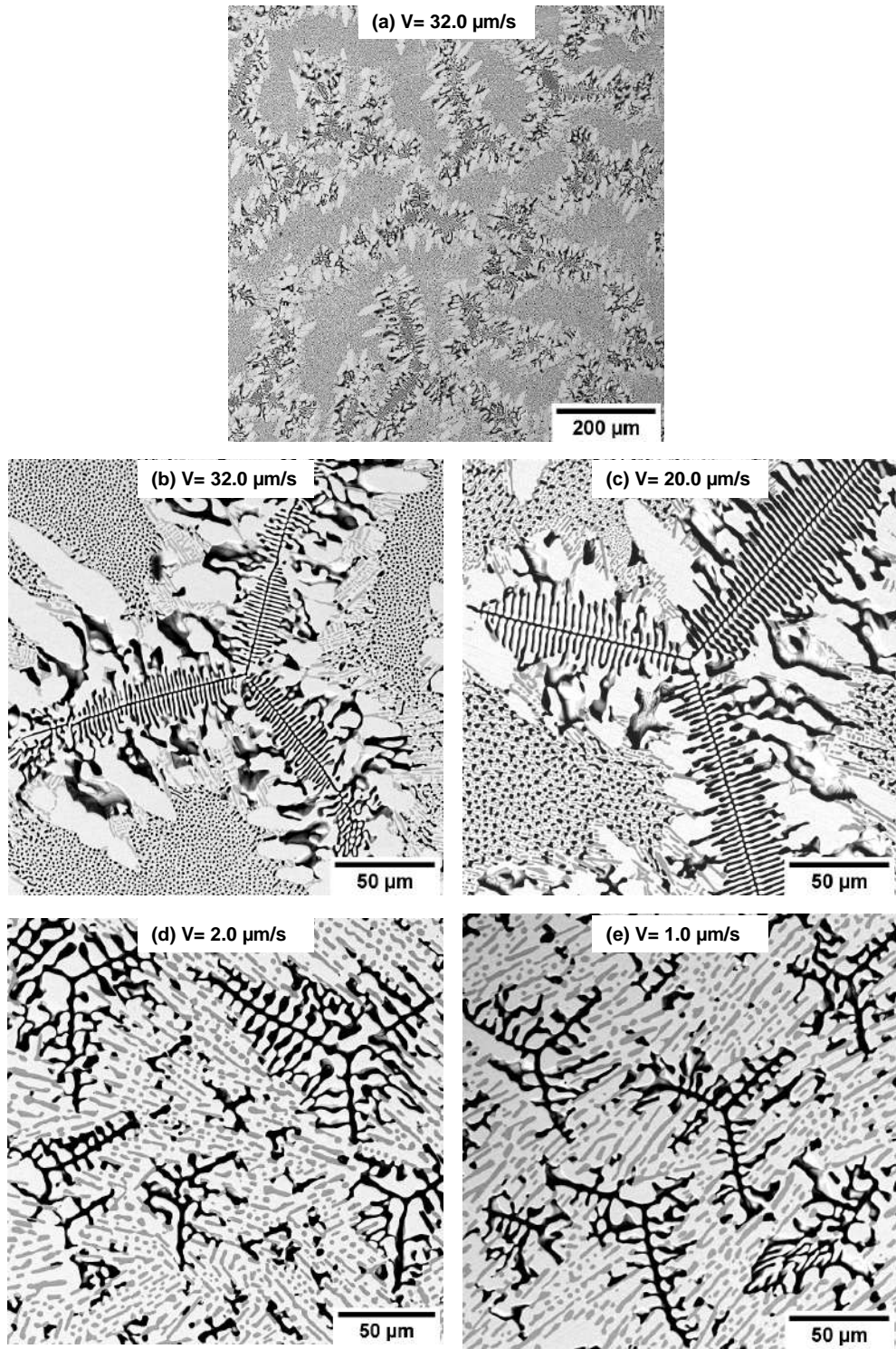


Figure 6.11: (a) is low magnification SEM image captured in transverse section of  $\text{Ag}_{47}\text{Cu}_{15}\text{Sb}_{38}$  (at.%) alloy solidified at  $V = 32.0 \mu\text{m/s}$  which shows two-phase and three-phase structures. (b)-(e) are the images captured in transverse sections of the alloy solidified at different velocities, i.e., 32.0, 20.0, 2.0, 1.0  $\mu\text{m/s}$ , respectively. Colonies exhibit complex internal morphology with inherent three-fold symmetry.

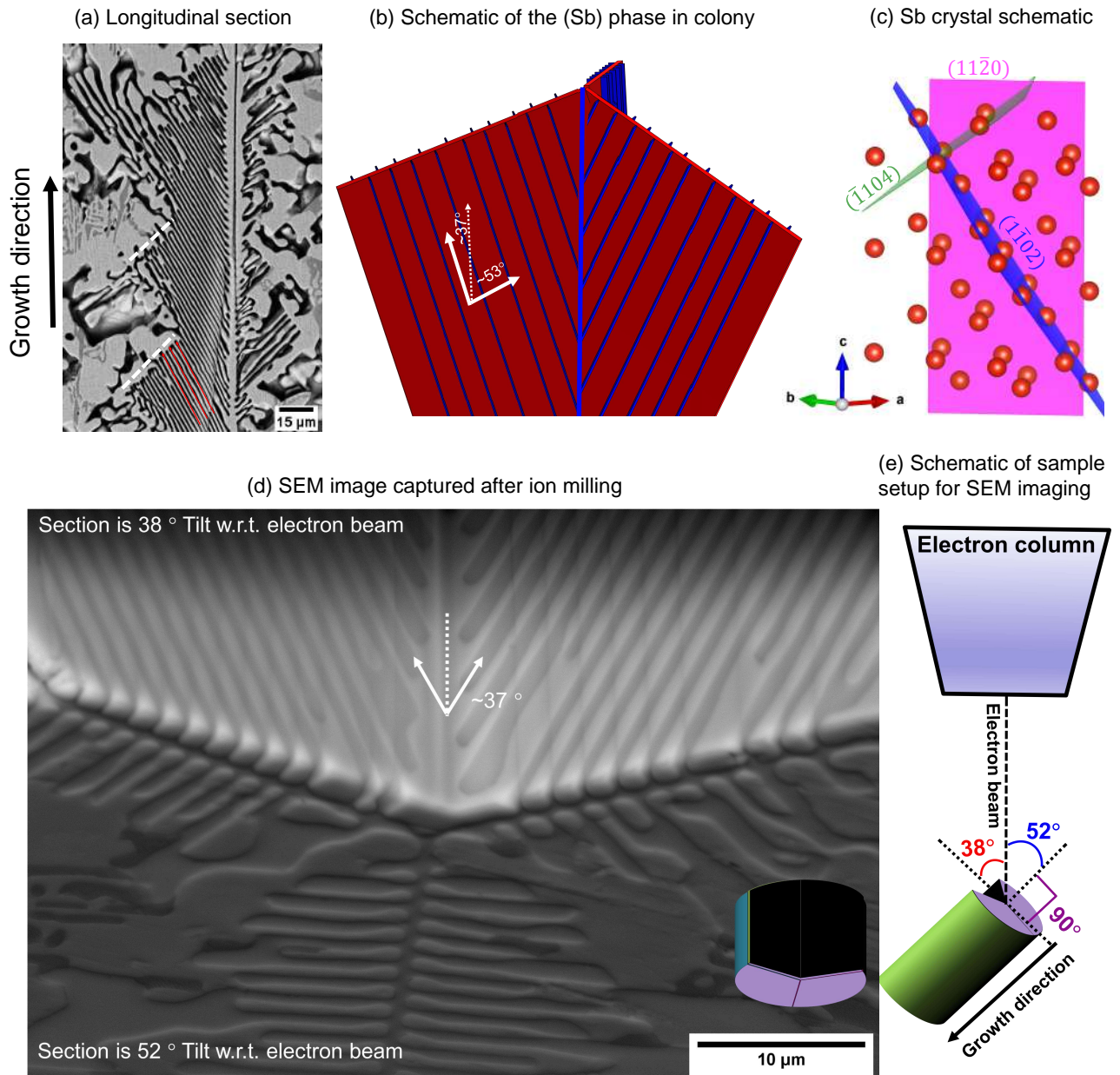


Figure 6.12: (a) is a longitudinal section of the colony. (b) is a schematic of the Sb-rich phase in the colony. (c) is (Sb) crystal schematic with planes  $(11\bar{2}0)$ ,  $(\bar{1}102)$ ,  $(\bar{1}104)$  highlighted using VESTA [13]. Image (d) is the sectional view of the colony after dissecting as shown in the inset schematic, which is captured when the sample is tilted as shown in the schematic (e) at an angle 52° and 38° with respective to transverse and longitudinal sections, respectively.

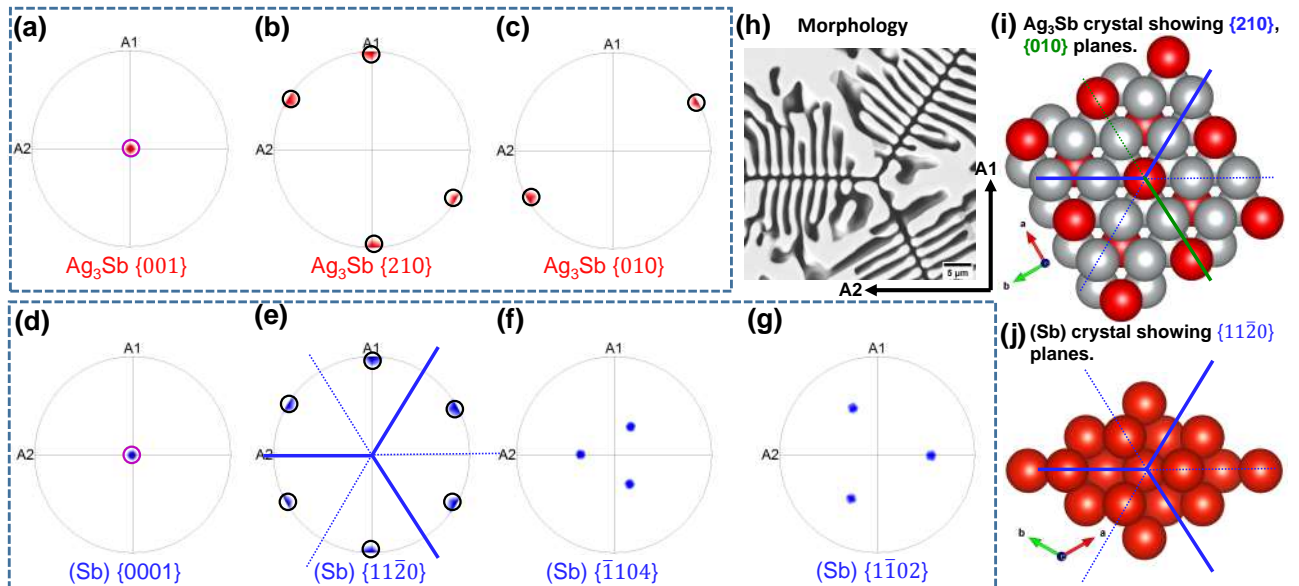


Figure 6.13: Pole figures of  $\text{Ag}_3\text{Sb}$  phase and  $(\text{Sb})$  phase plotted using EBSD data for the two-phase eutectic colony solidified at  $32.0 \mu\text{m/s}$  with the corresponding image as shown in (h) where growth direction is out of view. The three vanes have plate morphology in the colony corresponding to  $\{11\bar{2}0\}_{(\text{Sb})}$ , which are highlighted in the pole figure as well as in crystal schematics (j) using VESTA [13]. The  $(1\bar{1}02)_{(\text{Sb})}$ ,  $(\bar{1}104)_{(\text{Sb})}$ ) poles lie at an angle  $36.9^\circ$ ,  $56.4^\circ$  from the central axis respectively, and are perpendicular to  $(11\bar{2}0)_{(\text{Sb})}$ .

#### 6.1.4.2 Ag<sub>3</sub>Sb-Cu<sub>2</sub>Sb eutectic colonies

A composition, i.e., Ag<sub>43.4</sub>Cu<sub>21.6</sub>Sb<sub>35</sub> has been chosen for the investigation of Ag<sub>3</sub>Sb-Cu<sub>2</sub>Sb two-phase eutectic colony close to the ternary eutectic point. The alloy is solidified at different velocities and the microstructures obtained, are shown in Fig. 6.14. Similar to the previous composition (discussed in section 6.1.4.1) that leads to Ag<sub>3</sub>Sb-(Sb) colonies and three-phase eutectic microstructures, the selected composition exhibits Ag<sub>3</sub>Sb-Cu<sub>2</sub>Sb colonies surrounded by three-phase microstructures in the samples solidified at velocities 8.0, 16.0, 64.0  $\mu\text{m}/\text{s}$ . However, samples solidified at 1.0, 4.0  $\mu\text{m}/\text{s}$  do not exhibit the formation of colonies. The reason for such microstructures can be explained based on constitutional-supercooling concepts ( $G/V \leq m\Delta c/D$ ) [69], i.e., for constant material parameters (solutal diffusivity ( $D$ ), fixed composition ( $\Delta c$ ), liquidus slope ( $m$ )), and temperature gradient ( $G$ ), the formation of instability depends on velocity, i.e., below the critical velocity instabilities can disappear. The microstructure of the three-phase eutectic structures observed for this composition at 1.0, 4.0  $\mu\text{m}/\text{s}$  consists of an irregular (Sb) phase and a Cu<sub>2</sub>Sb morphology, which is distinct from the microstructures observed at the ternary eutectic composition. This change could be attributed to a shift in the volume percentage of the phases due to a different alloy composition and crystallography.

EBSD has been performed on the transverse section of the sample obtained at 1.0  $\mu\text{m}/\text{s}$  in order to understand the crystallographic basis behind the formation of the different three-phase eutectic microstructures. The position of the poles in Fig. 6.15, reveals that the planes facing the liquid are the same as in the case of the invariant three-phase eutectic composition that is solidified at 0.5  $\mu\text{m}/\text{s}$ , i.e., the {001} plane normal of Ag<sub>3</sub>Sb, {100} plane normal of Cu<sub>2</sub>Sb and the {11̄20} plane normal of (Sb) are all parallel to the growth direction. However, the microstructures derived at the invariant ternary eutectic composition at lower velocities are either blocky or dog-bone type. The change in the morphology of the (Sb) phase is probably due to the reduced volume fraction, where signatures of the elongated dog-bone structure is visible in the microstructure of Fig. 6.14e.

The second feature in the microstructure is the difference in the Ag<sub>3</sub>Sb and Cu<sub>2</sub>Sb morphologies in the three-phase eutectic microstructures that are below the velocity threshold of the instability. Here we derive from the crystallographic relationships between the Ag<sub>3</sub>Sb and the Cu<sub>2</sub>Sb (see Fig. 6.15) that while the growth directions remain the same as the experiments at the ternary eutectic composition at  $V=0.5\mu\text{m}/\text{s}$  (see Fig. 6.10a), the second set of relations that define the orientation relationship i.e Ag<sub>3</sub>Sb{100}|| Cu<sub>2</sub>Sb{001} are different from both the pos-

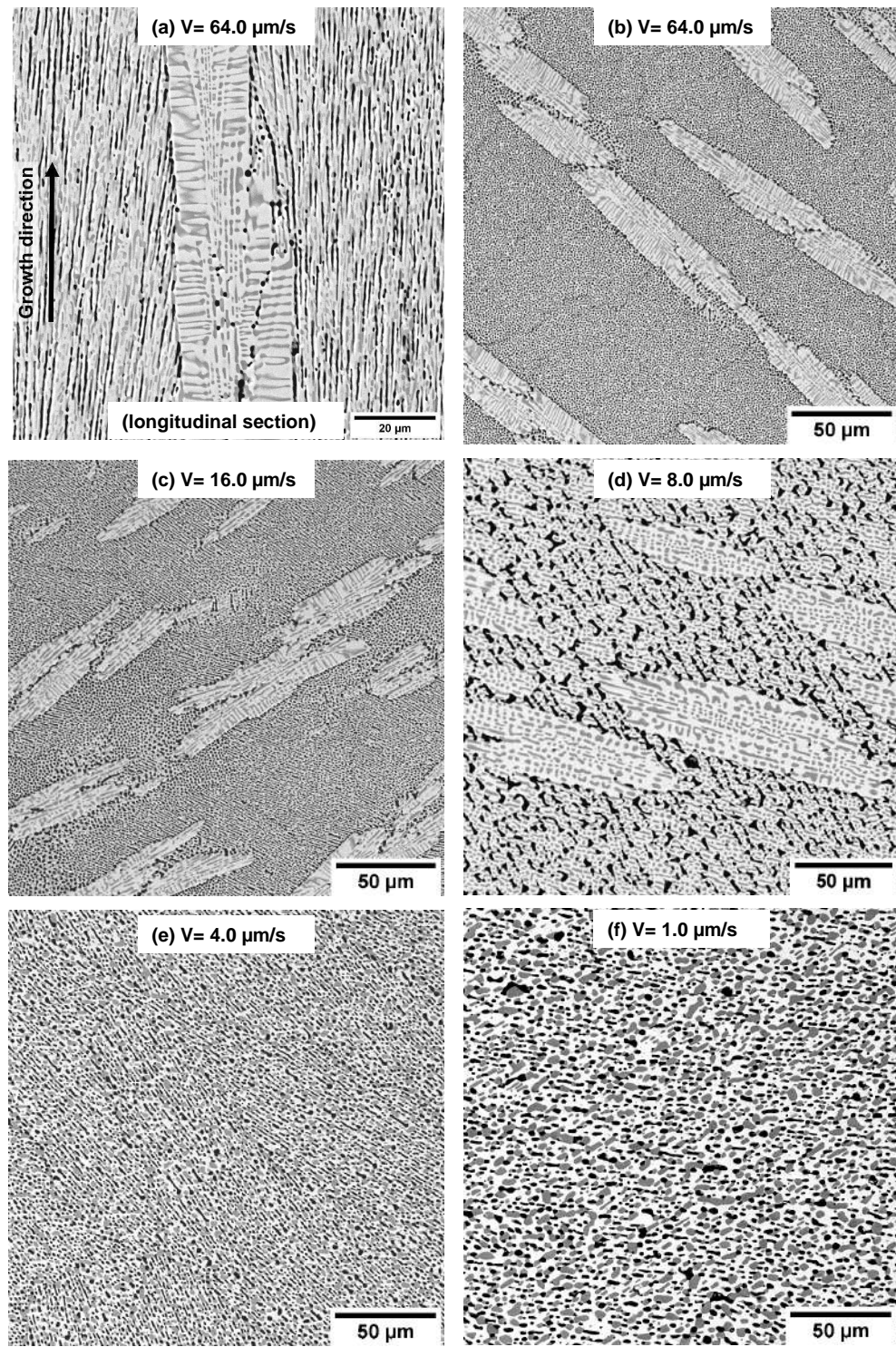


Figure 6.14: (a) and (b) are the SEM images captured in the longitudinal and transverse section of  $\text{Ag}_{43.4}\text{Cu}_{21.6}\text{Sb}_{35}$  (at.%) alloy directionally solidified at  $64.0 \mu\text{m/s}$ , while (c)-(f) are transverse section images obtained at different velocities, i.e.,  $16.0, 8.0, 4.0, 1.0 \mu\text{m/s}$  respectively. Samples solidified at  $4.0, 1.0 \mu\text{m/s}$  do not exhibit the formation of two-phase colonies, while the samples solidified at  $64.0, 16.0, 8.0 \mu\text{m/s}$  show two-phase colonies and three-phase eutectic. Two-phase colonies exhibit plate-type morphology.

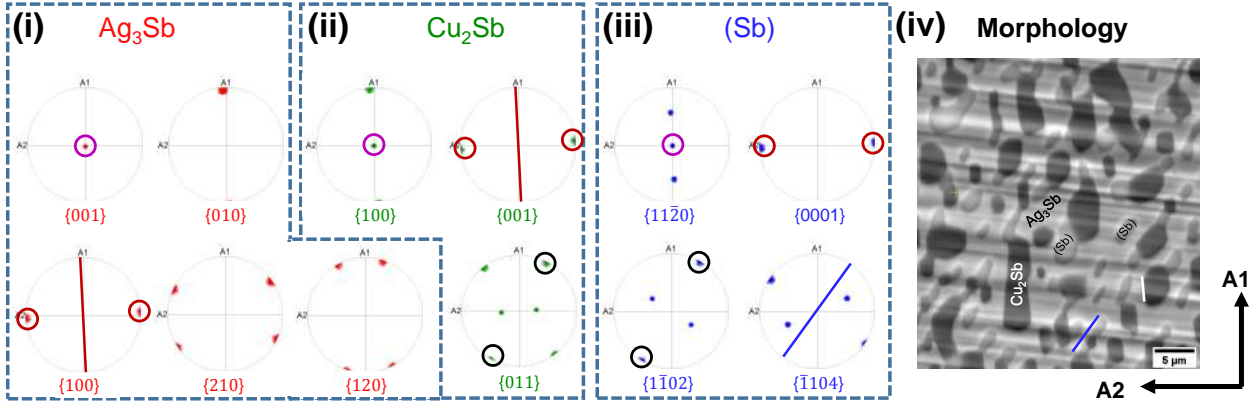


Figure 6.15: (i), (ii), (iii) are the pole figures of  $\text{Ag}_3\text{Sb}$ ,  $\text{Cu}_2\text{Sb}$ , and Sb-rich phases obtained from  $\text{Ag}_{43.4}\text{Cu}_{21.6}\text{Sb}_{35}$  (at.%) alloy directionally solidified at  $1.0 \mu\text{m/s}$ , where EBSD is performed on transverse sections with A1, A2 directions as shown in the corresponding morphology (iv). Orientation relations are one of the  $\{001\}_{\text{Ag}_3\text{Sb}}||$  one of the  $\{100\}_{\text{Cu}_2\text{Sb}}||$  one of  $\{11\bar{2}0\}_{(\text{Sb})}$ , and  $(100)_{\text{Ag}_3\text{Sb}}|| (001)_{\text{Cu}_2\text{Sb}}||(0001)_{(\text{Sb})}$ .

sibilities at the ternary eutectic composition observed at lower and higher velocities (Fig. 6.10a, Fig. 6.10b, Fig. 6.10c, Fig. 6.10d, Fig. 6.10e). This change in the crystallographic relationship between the two crystals, probably leads to an interface with reduced solid-solid interfacial energy anisotropy resulting in a more random distribution of the  $\text{Cu}_2\text{Sb}$  phases in Fig. 6.14e,f than in the morphologies obtained at the ternary eutectic composition. Thus, the overall change in the microstructure may be attributed to changes in the composition and therefore volume fractions as well as the crystallographic relations between the  $\text{Ag}_3\text{Sb}$  and the  $\text{Cu}_2\text{Sb}$  phases.

Furthermore, for the experiments leading to instabilities, we can see the  $\text{Ag}_3\text{Sb}-\text{Cu}_2\text{Sb}$  colonies exhibit a complex plate-type morphology as shown in longitudinal and transverse sections of Fig. 6.14a,b. Previously, we have observed that the origin of the complex morphology in the case of  $\text{Ag}_3\text{Sb}-(\text{Sb})$  colonies is related to the symmetry of the (Sb) phase. Similarly, the complex morphology of the  $\text{Ag}_3\text{Sb}-\text{Cu}_2\text{Sb}$  colonies are related to the properties of the  $\text{Cu}_2\text{Sb}$  phase as well as the anisotropic nature of the  $\text{Ag}_3\text{Sb}-\text{Cu}_2\text{Sb}$  solid-solid interface. This observation is supported by separate experiments on the Cu-rich side of the phase diagram that reveals a plate type morphology of the  $\text{Cu}_2\text{Sb}$  phase co-existing with the three-phase eutectic morphologies as shown in Fig. 6.18i), where the  $\text{Cu}_2\text{Sb}$  and the  $\text{Ag}_3\text{Sb}$  planes that are parallel to the lamellar interface are the same as in the invariant three-phase eutectic reactions.

Additionally, crystallographic characterization of the colony exhibiting the plate morphology shown in Fig. 6.16 reveals that the orientation relationship between the two phases in the colony

is very similar to the crystallographic relations found between the phases in the experiments at the ternary eutectic composition, i.e., the growth direction is normal to  $\{001\}$  planes of  $\text{Ag}_3\text{Sb}$  and  $\{100\}$  planes of  $\text{Cu}_2\text{Sb}$  while the second set of planes corresponding to the orientation relationship are  $\text{Ag}_3\text{Sb}\{120\} \parallel \text{Cu}_2\text{Sb}\{001\}$ . Given the symmetry of the  $\text{Ag}_3\text{Sb}$  crystal the relation  $\text{Ag}_3\text{Sb}\{210\} \parallel \text{Cu}_2\text{Sb}\{100\}$  also follows as revealed in Fig. 6.16 for this orientation relationship. Comparing the SEM image in Fig. 6.16 with the corresponding poles of  $\text{Ag}_3\text{Sb}$  and  $\text{Cu}_2\text{Sb}$  phases, we find that for the two plate orientations observed in the colony structure, the lamellar traces are either parallel to the set ( $\text{Ag}_3\text{Sb}\{120\}$ ,  $\text{Cu}_2\text{Sb}\{001\}$ ) or ( $\text{Ag}_3\text{Sb}\{210\}$ ,  $\text{Cu}_2\text{Sb}\{100\}$ ). The schematic representation of these planes are highlighted in Fig. 6.16g,h.

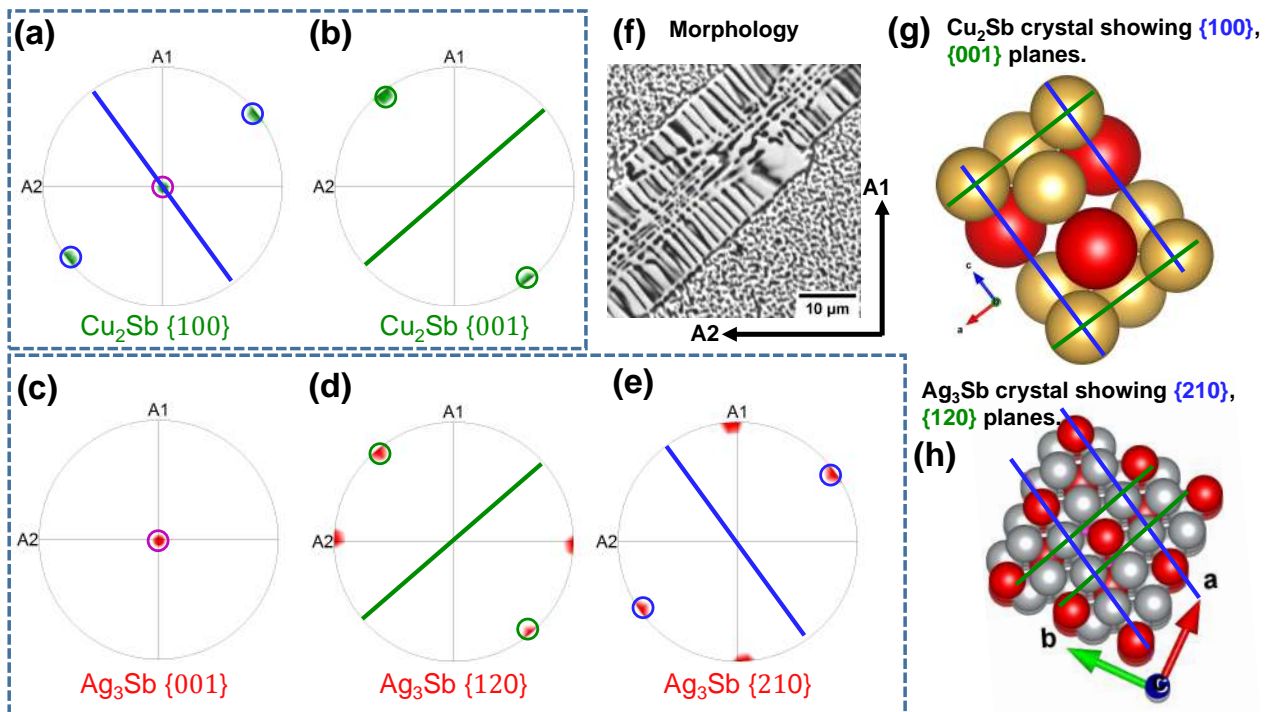


Figure 6.16: (a), (b) are the pole figures of  $\text{Ag}_3\text{Sb}$ , while (c), (d), and (e) are the pole figures of  $\text{Cu}_2\text{Sb}$  obtained from two-phase eutectic colony solidified at  $64.0 \mu\text{m/s}$  consisting of plate morphology as shown in (f). EBSD is performed on transverse section with A1, A2 axis as shown in (f). Orientation relationships obtained are one of the  $\{001\}_{\text{Ag}_3\text{Sb}} \parallel$  one of the  $\{100\}_{\text{Cu}_2\text{Sb}}$ , and  $(120)_{\text{Ag}_3\text{Sb}} \parallel (001)_{\text{Cu}_2\text{Sb}}$ . The solid-solid interface traces are highlighted on the corresponding pole figures, and crystal schematics (g) and (h) using VESTA [13].

With regards to the three-phase eutectic structures that form along with the colonies in Figs. 6.14b,c,d, we find the morphologies are similar to those observed at the ternary eutectic composition, where features similar to the dog-bone structure for the (Sb) phase are observed

for  $V=8.0 \mu\text{m/s}$  (see Fig.6.14d), while those at higher velocities are much finer, exhibiting similarities with the lamellar part of the dog-bone structure for the (Sb) phase. However, smaller regions exhibiting a fibrous structure for the (Sb) phase are also visible in Fig.6.14c which is probably due to a (Sb) phase with a different orientation in the sample. Thus the morphology of the (Sb) phase and the growth mechanism is dependent on the orientation of the solid-liquid interface as observed previously for the experiments at the ternary eutectic composition. Similarly, the  $\text{Ag}_3\text{Sb}$  and the  $\text{Cu}_2\text{Sb}$  in the three-phase eutectic structure have the same orientation relationship observed in the experiments at the higher velocities performed for the pure ternary eutectic composition (see Fig.6.10e).

#### 6.1.4.3 $\text{Cu}_2\text{Sb}$ -(Sb) two-phase structures

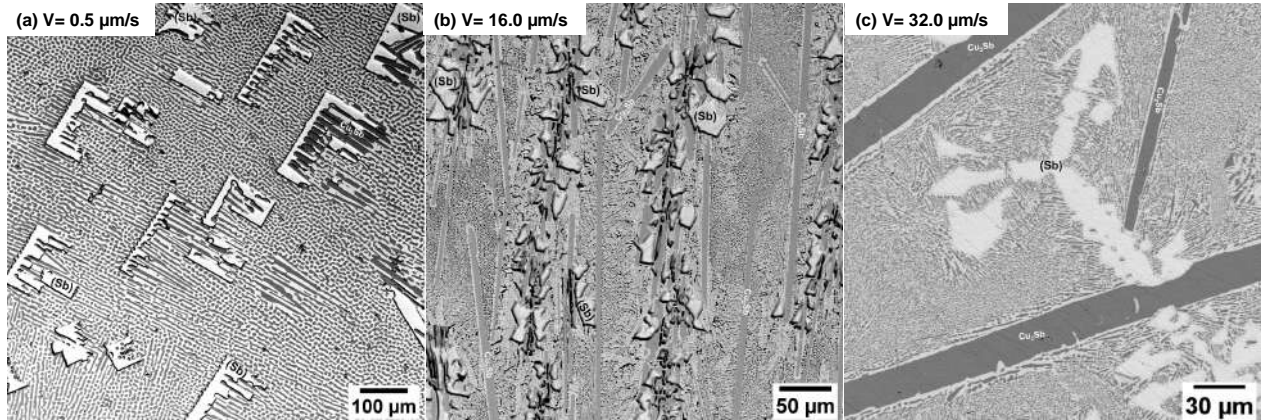


Figure 6.17: (a), (b), (c) are the SEM images taken in the transverse section of  $\text{Ag}_{23}\text{Cu}_{27}\text{Sb}_{50}$  (at.%) alloy directionally solidified at  $0.5$ ,  $16.0$ ,  $32.0 \mu\text{m/s}$  velocities respectively. The morphology observed in the sample solidified at  $0.5 \mu\text{m/s}$  is similar to the ternary eutectic having the bulky structure of (Sb), while at higher solidification velocities ( $16.0$ ,  $32.0 \mu\text{m/s}$ ), two phases exhibit uncoupled growth behavior.

We have already seen the fascinating morphologies of the  $\text{Ag}_3\text{Sb}$ -(Sb) and  $\text{Ag}_3\text{Sb}-\text{Cu}_2\text{Sb}$  two-phase colonies, which are primarily due to the (Sb) and  $\text{Cu}_2\text{Sb}$  phases present in the colonies. As these phases provided exciting structures, in this section, we attempted to study the morphology of two-phase colonies that consist of the  $\text{Cu}_2\text{Sb}$  and (Sb) phases; hence a composition  $\text{Ag}_{23}\text{Cu}_{27}\text{Sb}_{50}$  that leads to the formation of  $\text{Cu}_2\text{Sb}$  and (Sb) two-phase eutectic and ternary three-phase eutectic microstructures is chosen. The alloy is solidified at three different velocities, and the transverse section images are shown in Fig. 6.17. Microstructure observed

in the sample solidified at  $0.5 \mu\text{m}/\text{s}$  exhibits three-phase eutectic morphologies very similar to that observed at the ternary eutectic composition. At higher velocities, three-phase growth front is destabilized, and the morphologies are as shown in Fig. 6.17b,c. These structures are different from that of the regular two-phase eutectic colonies, which can be due to the growth behavior of the  $\text{Cu}_2\text{Sb}$  and  $(\text{Sb})$  phases being largely uncoupled because of the vastly different crystal structures which is similar to the mechanism proposed by [198], where the authors also claim that  $\text{Cu}_2\text{Sb}$  nucleates and grows as a plate independently without coupling with  $(\text{Sb})$ . The morphology of  $(\text{Sb})$  observed for a velocity of  $32.0 \mu\text{m}/\text{s}$  sample is very similar to the  $\text{Ag}_3\text{Sb}-(\text{Sb})$  colony structure exhibiting three-fold symmetry while  $\text{Cu}_2\text{Sb}$  morphology is a plate-like structure that is similar to that observed in the  $\text{Ag}_3\text{Sb}-\text{Cu}_2\text{Sb}$  colony structure. Further, EBSD results (refer Fig. 6.18) reveal that the  $\text{Cu}_2\text{Sb}$  plates are formed with  $\{001\}$  family of planes that share the same crystallographic relation with the  $\text{Ag}_3\text{Sb}$  phase as in the  $\text{Ag}_3\text{Sb}-\text{Cu}_2\text{Sb}$  colony structure, while the pole figures of  $(\text{Sb})$  reveal the existence of the same orientation of crystallographic planes as observed in the case of the  $\text{Ag}_3\text{Sb}-(\text{Sb})$  colony, i.e., the axis of dendrite being the  $[0001]$  direction of  $(\text{Sb})$  and the  $\{11\bar{2}0\}$  family forming the three vanes. Thus the morphological instabilities for this particular composition lead to  $\text{Cu}_2\text{Sb}$  and  $(\text{Sb})$  microstructures that appear to evolve largely uncoupled, where the  $(\text{Sb})$  phase exhibits its inherent crystallographic symmetry, while the  $\text{Cu}_2\text{Sb}$  takes a form that is largely dictated by the anisotropic nature of the  $\text{Ag}_3\text{Sb}-\text{Cu}_2\text{Sb}$  interface.

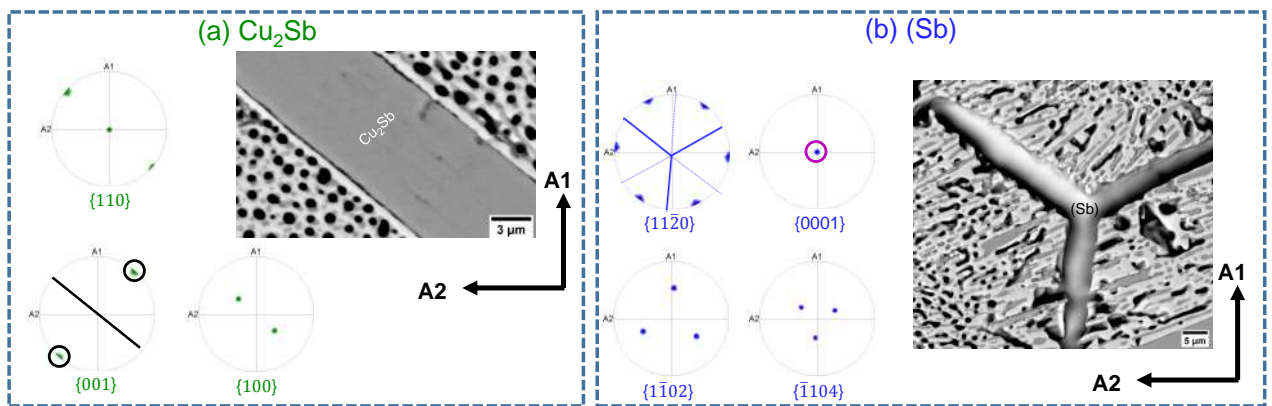


Figure 6.18: EBSD is conducted for both the  $\text{Cu}_2\text{Sb}$  plate and  $(\text{Sb})$  dendritic phases, observed in the  $\text{Ag}_{23}\text{Cu}_{27}\text{Sb}_{50}$  alloy solidified at  $32.0 \mu\text{m}/\text{s}$  on transverse sections with A1, A2 directions as shown in the respective images. (a) consists of  $\text{Cu}_2\text{Sb}$  pole figures corresponding to plate morphology, while (b) consists of  $(\text{Sb})$  pole figures corresponding to its dendritic morphology. The solid traces are highlighted on the corresponding pole figures.

## 6.2 Summary

In this chapter, we have experimentally investigated the formation of three-phase microstructures in the Ag-Cu-Sb eutectic system that contains two intermetallic compounds, i.e., silver antimonide- $\text{Ag}_3\text{Sb}$ , copper antimonide- $\text{Cu}_2\text{Sb}$ , and an antimony rich solid-solution (Sb). Diverse morphologies are observed in this system that includes both invariant reactions giving rise to three-phase microstructures as well as univariant reactions leading to the formation of hierarchical microstructures involving two-phase colonies along with three-phase eutectic microstructures. For the invariant reaction, we find that the (Sb) phase exhibits different growth mechanisms depending on the crystallographic orientation, wherein for the cases where the  $\{1\bar{1}20\}$  planes face the liquid, we observe a ledge growth type mechanism that leads to the formation of blocky and dog-bone structures at lower speeds and a largely plate-like structure at larger speeds. Conversely, for the cases where the growth of the (Sb) phase occurs perpendicular to the basal plane, we have a more fibrous morphology. This indicates the presence of solid-liquid interfacial/kinetic anisotropy for the phase, which influences the morphology as well as the growth mechanism depending on the orientation of the crystal. Along with this, we find different orientation relationships between the three phases that influence the relative orientations of  $\text{Ag}_3\text{Sb}/\text{Cu}_2\text{Sb}$  interfaces with the (Sb) interface, their form as well their distribution. Here, we observe that in cases where the  $\{120\}$  or the  $\{010\}$  family of planes in the  $\text{Ag}_3\text{Sb}$  are parallel to the  $\{100\}$  planes of  $\text{Cu}_2\text{Sb}$  the resulting interface between the phases indicates co-incidence with the respective parallel planes on either side demonstrating the presence of strong solid-solid anisotropy for these orientation relationships between the crystals.

For the case of univariant reactions, we have performed experiments for compositions that lead to the formation of different combinations of two-phase eutectic colonies, namely ( $\text{Ag}_3\text{Sb}$ -(Sb)), ( $\text{Ag}_3\text{Sb}-\text{Cu}_2\text{Sb}$ ) while it was not possible to derive coupled growth of the  $\text{Cu}_2\text{Sb}$ -(Sb) phases. The microstructures involving the two-phase colonies highlight geometrical and structural hierarchy. Specifically, the  $\text{Ag}_3\text{Sb}$ -(Sb) two-phase colonies exhibit a complex structure with inherent 3-fold symmetry, which is reminiscent of the (Sb) crystal. We observe a skeletal structure whose spine is formed by three  $\{11\bar{2}0\}$  planes of (Sb), whereas the branches are formed by the  $\{1\bar{1}02\}$  (Sb) planes that emanate out from the central colony axes. The growth direction of the colony is specified along the  $\{001\}$  and  $\{0001\}$  plane normals of the  $\text{Ag}_3\text{Sb}$  and (Sb) phases, respectively. Similarly, the  $\text{Ag}_3\text{Sb}-\text{Cu}_2\text{Sb}$  two-phase colonies exhibit a plate-type morphology with inherent 2-fold symmetry. The orientation relation observed between the

$\text{Ag}_3\text{Sb}$  and  $\text{Cu}_2\text{Sb}$  phases in the colony, is the same as that observed in three-phase eutectic microstructures observed in the invariant reactions. Finally, while we do not observe  $\text{Cu}_2\text{Sb}-(\text{Sb})$  colonies, the experimental microstructures highlight uncoupled growth of both phases where the morphology of the phases inherit their intrinsic crystal symmetries.

In summary, from the perspective of structure formation in three-phase eutectics, the results presented in this chapter indicate that the presence of strong anisotropy in the solid-solid or the solid-liquid interfacial energies exerts a direct influence on the resulting morphologies that exhibit features having a clear relation to the symmetry groups of the growing crystals. In particular, orientation relationships with a well-defined solid-solid interfacial energy anisotropy along with the underlying crystal symmetries of the phases influence the morphologies of the growing phases as well as the growth directions. Similarly, the crystalline symmetry influences the growth mechanisms depending upon the nature of the solid-liquid interfaces, which in turn may lead to the formation of varied microstructures. Given this underlying crystallographic basis, it may be possible to anticipate possible orientation relationships as well as growth mechanisms in other eutectic systems based on just the symmetry groups of the evolving phases, and future work may be directed towards the formulation of unified rules of structure formation, particularly in strongly anisotropic systems.

# Chapter 7

## Conclusions and future prospects

*"All knowledge is connected to all other knowledge. The fun is in making the connections."* —**Arthur C. Aufderheide**

### 7.1 Conclusions

This thesis reveals the formation of exotic eutectic microstructures in three different systems utilizing the homemade directional solidification apparatus and advanced characterization techniques. The investigation has started with a simple binary two-phase Sn-Zn eutectic in chapter 4 that consists of (Sn) and (Zn) phases. Then, complexity has been increased in the microstructure by introducing impurities to the SnTe-(Te) eutectic in chapter 5 where we first observe the evolution of complex structures. Finally, in chapter 6 complex three-phase microstructures are investigated that occur in the ternary Ag-Cu-Sb system, which contains two intermetallic compounds, i.e., silver antimonide- $\text{Ag}_3\text{Sb}$ , copper antimonide- $\text{Cu}_2\text{Sb}$ , and an antimony rich solid-solution (Sb). The three-phase microstructures include structures that form during invariant three-phase growth and complex hierarchical structures consisting of two-phase eutectic colonies along with three-phase eutectic morphologies.

The other exciting feature of the study is that while in the first system, the anisotropic phase, i.e., (Zn), has a deficient volume percentage, while in the second system, the anisotropic phase, i.e., (Te), is the major phase and forms a continuous matrix and further in the third system, (Sb) is neither minority phase nor majority phase. Therefore, the study reveals the formation of very diverse microstructures. The principal findings of the thesis are as follows:

1. We provide experimental evidence of solid-solid interfacial energy anisotropy in the case of the binary Sn-Zn eutectic system utilizing different techniques.
2. Results in the chapter 4 on the Sn-Zn eutectic reveal that interfacial energy anisotropy in the solid-solid interfaces can stabilize lamellar morphologies in contrast to rod morphologies even in systems that consist of a low-percent minority phase.
3. We find basal planes of (Zn) forming lamellar interface in the Sn-Zn eutectic system; similarly, we can suspect similar reasons for the formation of broken-lamellar morphology of (Zn) in Bi-Zn and In-Zn eutectic systems.
4. In the case of binary SnTe-(Te) eutectic, we observe microstructures that consist of connected rod-type (weakly aligned strings of rods) at lower velocities ( $V=0.5, 1.0, 2.0, 4.0 \mu\text{m/s}$ , while with an increase in velocity, we observe the random distribution of rods.
5. In the case of ternary SnTe-Te eutectic, i.e., with the addition of a third component to eutectic, we observe a diffusive instability (similar to a Mullins-Sekerka instability) causing the formation of two-phase eutectic colonies which appear beyond a critical velocity depending on the impurity composition.
6. The colonies observed in SnTe-(Te) eutectic system have a complex internal structure that displays a three-fold symmetry reminiscent of the trigonal symmetry of the (Te) crystal, arising probably because of strong anisotropy in the solid-liquid interfacial energy or the growth kinetics. The complex structure of the colonies is very similar to the colonies observed in  $\text{Al}_2\text{O}_3$ -  $\text{ZrO}_2$  ( $\text{Y}_2\text{O}_3$ ) [188, 189, 190], MnSb-(Sb,Bi) and MnSb-(Sb,Sn) [191] systems. All the morphologies that exhibit similar colony structures reported in the literature have inherent rod eutectic morphologies, however, we report the formation of such colonies with a lamellar morphology as well.
7. The morphological rod to lamellar transition due to addition an impurity is rare. We find evidence of such a phenomenon in the SnTe-(Te) eutectic system due to the addition of Sb.
8. For the invariant reaction in the Ag-Cu-Sb system, we find that the  $\text{Ag}_3\text{Sb}$  forms a continuous matrix that contains (Sb) and  $\text{Cu}_2\text{Sb}$  phase; (Sb) phase exhibits different growth mechanisms depending on the crystallographic orientation leading to the formation

of distinct morphologies, while Cu<sub>2</sub>Sb is predominantly rod/broken-lamellar exhibiting a regular structure.

9. The formation of hollow morphologies during eutectic growth is rare. We provided experimental evidence of hollow crystal formation during eutectic solidification.
10. For the case of univariant reactions in the Ag-Cu-Sb system, we have performed experiments for compositions that lead to the formation of different combinations of two-phase eutectic colonies, namely (Ag<sub>3</sub>Sb-(Sb)), (Ag<sub>3</sub>Sb-Cu<sub>2</sub>Sb) while it was not possible to derive coupled growth of the Cu<sub>2</sub>Sb-(Sb) phases.
11. The microstructures of the Ag-Cu-Sb system involving the two-phase colonies and three-phase eutectic highlight geometrical and structural hierarchy.
12. The two-phase Ag<sub>3</sub>Sb-(Sb) colonies exhibit a complex internal structure that displays a three-fold symmetry reminiscent of the rhombohedral symmetry of the (Sb) crystal.
13. The two-phase Ag<sub>3</sub>Sb-Cu<sub>2</sub>Sb colonies exhibit a plate-type morphology with inherent 2-fold symmetry.
14. We find a unique orientation relationship between eutectic phases in the case of the SnTe-Te system. In contrast, we find more than one orientation relationship between the eutectic phases in the case of the Sn-Zn eutectic and ternary Ag-Cu-Sb system.
15. Among the phases present in the three chapters, we find similarity between (Zn) phase in Sn-Zn eutectic and Cu<sub>2</sub>Sb phase in ternary Ag-Cu-Sb system, i.e., both exhibit typical broken-lamellar type structures and lamellar interfaces being formed by {0001}<sub>(Zn)</sub>, {001}<sub>Cu<sub>2</sub>Sb</sub>. Further, we find similarity between (Te) in SnTe-(Te) and (Sb) in the Ag-Cu-Sb system that makes colonies with 3-fold symmetry where {0001}<sub>(Te)</sub> and {0001}<sub>(Sb)</sub> forms the axis of the colonies. In essence, {0001}<sub>(Zn)</sub>, {0001}<sub>(Te)</sub>, {0001}<sub>(Sb)</sub>, and {001}<sub>Cu<sub>2</sub>Sb</sub> plays a vital role in formation of microstructures.

## 7.2 Future prospects

This thesis ends by highlighting some of the fundamental unanswered questions related to eutectic solidification.

1. **Nucleation and initial transient dynamics:** Although the growth of eutectics<sup>1</sup> is relatively well understood, the nucleation and initial transient dynamics are not fully understood. Furthermore, how do the starting microstructure or initial-stage dynamics affect the final steady-state microstructure quantitatively?
2. **Quantification of solid-solid interfacial energy anisotropy:** To obtain quantitative knowledge on the strength and form of the solid-solid interfacial free energy anisotropy in systems that have a low volume percentage of the minority phase which exhibits broken lamellar morphology (an example is Sn-Zn eutectic) using specialized equipment like the rotational directional solidification setup or solidification along complicated paths like in spirals that can reveal the strength and form of the anisotropy of the solid-solid interface in three dimensions.
3. **Lamellar faults:** Formation mechanism and growth dynamics of lamellar faults, particularly in systems with strong solid-solid interfacial energy.
4. **Presence of impurities:** As evidenced in our experiments of (Sb) addition to the SnTe-Te eutectic system, further studies on morphological transitions (for example, rod to lamellar) due to the presence of impurities are required through the modification of solid-liquid and solid-solid interfacial energies. Moreover, the stability of the solid-liquid interface is also a function of the amount and properties of the impurities. How are mechanisms responsible for two-phase instabilities during univariant eutectics (as eutectics possess non-linear dynamics) different from the mechanisms occurring during single-phase instabilities?
5. **Solidification in higher multi-component systems:** Growth dynamics of multi-component eutectic phases, for example, high entropy eutectics require further investigation. Further, while we have studied the evolution of two-phase colonies, the question remains whether three-phase colonies can occur? The studies promise to be enriching

---

<sup>1</sup>in regular non-faceted binary systems

particularly when the influence of the anisotropic nature of the interfaces and multiple components are superimposed.

6. **Solidification in anisotropic systems:** The formation of complex microstructures in highly anisotropic systems remains to be explored in detail. This is particularly valid for the investigation of interface growth concerning the faceted phase in eutectics, which requires further understanding. In-situ characterization is necessary for unraveling certain growth mechanisms, such as the formation of eutectic colonies in highly anisotropic eutectic systems.

# List of Publications and Conferences

## Journal publications

1. **Shanmukha Kiran Aramanda**, Salapaka Sai Kiran, Sumeet Khanna, Kamanio Chattopadhyay, Abhik Choudhury, "Exotic colony formation in Sn-Te eutectic system", **Acta-materialia**, Volume 197, 2020, pp. 108-121.
2. **Shanmukha Kiran Aramanda**, Sumeet Khanna, Salapaka Sai Kiran, Kamanio Chattopadhyay, Abhik Choudhury, "Crystallographic and morphological evidence of solid-solid interfacial energy anisotropy in the Sn-Zn eutectic system", **Metallurgical and Materials Transactions -A** 51, 6387–6405 (2020).
3. Sumeet Khanna, **Shanmukha Kiran Aramanda**, Abhik Choudhury, "Role of anisotropy in the formation of broken-lamellar structures in eutectic systems", **Metallurgical and Materials Transactions -A** 51, 6327–6345 (2020).
4. **Shanmukha Kiran Aramanda**, Kamanio Chattopadhyay, Abhik Choudhury, "Exotic three-phase microstructures in the ternary Ag-Cu-Sb eutectic system" (under review, **Acta-materialia**).  
.

## Conferences

1. **Shanmukha Kiran Aramanda**, Salapaka Sai Kiran, Sumeet Khanna, Kamanio Chattopadhyay, Abhik Choudhury, “Experimental investigation of the eutectic morphology in Sn-Zn eutectic system” **Seventh International Conference on Solidification Science and Processing** (ICSSP-2018). November 19-22, 2018. Trivandrum, Kerala, India (**Best poster award\***).
2. **Shanmukha Kiran Aramanda**, Salapaka Sai Kiran, Kamanio Chattopadhyay, Abhik Choudhury, “Coupled growth of tin-zinc eutectic crystals during directional solidification and influence of solid-solid interface anisotropy in morphological evolution” **International Symposium on Modeling of Crystal Growth Processes and Devices**, 26 - 28 February 2019. Chennai, Tamil Nadu, India (**Best paper award\***).
3. **Shanmukha Kiran Aramanda**, Salapaka Sai Kiran, Kamanio Chattopadhyay, Abhik Choudhury, “Role of solid-solid and solid-liquid anisotropies in eutectic colony structure formation” **5th International Conference on Advances in Solidification Processes** (ICASP-5) **5th International Symposium on Cutting Edge of Computer Simulation of Solidification, Casting and Refining** (CSSCR-5) June 17-21 2019. Salzburg, Austria.
4. **Shanmukha Kiran Aramanda**, Salapaka Sai Kiran, Kamanio Chattopadhyay, Abhik Choudhury, “Formation of self-organized SnTe-Te eutectic colonies” **12th Asia-Pacific Microscopy Conference** (APMC-2020). 3 - 7 February 2020, Hyderabad, India (**Best metallography award\***).

\*Best poster/paper awards in solidification conference, best metallography award in microscopy conference.

# References

- [1] JD Hunt and KA Jackson. Binary eutectic solidification. *Trans. Metall. Soc. AIME*, 236(6):843–852, 1966. [xiv](#), [xv](#), [xvi](#), [2](#), [4](#), [5](#), [11](#), [18](#), [20](#), [29](#), [30](#), [32](#)
- [2] K A Jackson and J D Hunt. Lamellar and rod eutectic growth. *Transactions of The Metallurgical Society of AIME*, 236:1129–1142, 1966. [xiv](#), [7](#), [8](#), [9](#), [10](#), [21](#), [29](#), [63](#), [97](#), [128](#)
- [3] DJ Fisher and W Kurz. A theory of branching limited growth of irregular eutectics. *Acta Metallurgica*, 28(6):777–794, 1980. [xv](#), [12](#)
- [4] DG McCartney, JD Hunt, and RM Jordan. The structures expected in a simple ternary eutectic system: Part 1. theory. *Metallurgical Transactions A*, 11(8):1243–1249, 1980. [xv](#), [16](#), [17](#)
- [5] Daniel Lewis, Sarah Allen, Michael Notis, and Adam Scotch. Determination of the eutectic structure in the ag-cu-sn system. *Journal of electronic materials*, 31(2):161–167, 2002. [xv](#), [21](#), [22](#)
- [6] MA Ruggiero and JW Rutter. Origin of microstructure in the 332 k eutectic of the bi-in-sn system. *Materials science and technology*, 13(1):5–11, 1997. [xv](#), [21](#), [22](#)
- [7] Anne Dennstedt, A Choudhury, Lorenz Ratke, and B Nestler. Microstructures in a ternary eutectic alloy: devising metrics based on neighbourhood relationships. In *IOP Conference Series: Materials Science and Engineering*, volume 117, page 012025. IOP Publishing, 2016. [xvi](#), [21](#), [23](#), [25](#)
- [8] RJ Contieri, CT Rios, M Zanotello, and R Caram. Growth and three-dimensional analysis of a nb-al-ni ternary eutectic. *Materials characterization*, 59(6):693–699, 2008. [xvi](#), [21](#), [23](#)

## REFERENCES

- [9] S Liu, JH Lee, and R Trivedi. Dynamic effects in the lamellar–rod eutectic transition. *Acta Materialia*, 59(8):3102–3115, 2011. [xvi](#), [26](#), [27](#)
- [10] Andrea Parisi and Mathis Plapp. Defects and multistability in eutectic solidification patterns. *EPL (Europhysics Letters)*, 90(2):26010, 2010. [xvi](#), [26](#), [28](#)
- [11] Abhik Choudhury. Pattern-formation during self-organization in three-phase eutectic solidification. *Transactions of the Indian Institute of Metals*, 68(6):1137–1143, 2015. [xvi](#), [26](#), [28](#)
- [12] Sn-zn binary phase diagram 0-100 at.% zn: Datasheet from “pauling file multi-naries edition – 2012” in springermaterials ([https://materials.springer.com/isp/phase-diagram/docs/c\\_0902137](https://materials.springer.com/isp/phase-diagram/docs/c_0902137)). Copyright 2016 Springer-Verlag Berlin Heidelberg & Material Phases Data System (MPDS), Switzerland & National Institute for Materials Science (NIMS), Japan. [xviii](#), [58](#)
- [13] Koichi Momma and Fujio Izumi. Vesta 3 for three-dimensional visualization of crystal, volumetric and morphology data. *Journal of applied crystallography*, 44(6):1272–1276, 2011. [xx](#), [xxii](#), [xxiii](#), [xxiv](#), [xxvi](#), [xxvii](#), [76](#), [97](#), [113](#), [118](#), [144](#), [145](#), [149](#)
- [14] Sn-te binary phase diagram 0-100 at.% te: Datasheet from “pauling file multi-naries edition – 2012” in springermaterials ([https://materials.springer.com/isp/phase-diagram/docs/c\\_0903205](https://materials.springer.com/isp/phase-diagram/docs/c_0903205)). Copyright 2016 Springer-Verlag Berlin Heidelberg & Material Phases Data System (MPDS), Switzerland & National Institute for Materials Science (NIMS), Japan. [xxi](#), [88](#)
- [15] Philip Ball. Nature’s patterns: a tapestry in three parts. *Nature’s Patterns: A Tapestry in Three Parts by Philip Ball*. Oxford University Press, July 2009., 2009. [1](#)
- [16] Philip Ball. *Patterns in nature: why the natural world looks the way it does*. University of Chicago Press, 2016. [1](#)
- [17] Klaus Kassner. *Pattern formation in diffusion-limited crystal growth*. World Scientific, 1996. [1](#)
- [18] Ichiro Sunagawa. *Crystals: growth, morphology, & perfection*. Cambridge University Press, 2007. [1](#)

## REFERENCES

- [19] JD Hunt. Pattern formation in solidification. *Science and Technology of Advanced Materials*, 2(1):147–155, 2001. [1](#)
- [20] Bruce Chalmers. Principles of solidification. In *Applied solid state physics*, pages 161–170. Springer, 1970. [1](#)
- [21] Wilfried Kurz and David J Fisher. *Fundamentals of solidification*, volume 1. trans tech publications Aedermannsdorf, Switzerland, 1986. [1](#)
- [22] Jonathan A Dantzig and Michel Rappaz. *Solidification*. EPFL press, 2009. [1](#)
- [23] M Asta, C Beckermann, A Karma, W Kurz, R Napolitano, M Plapp, G Purdy, M Rappaz, and R Trivedi. Solidification microstructures and solid-state parallels: Recent developments, future directions. *Acta Materialia*, 57(4):941–971, 2009. [1](#), [16](#)
- [24] U Hecht, L Gránásy, T Pusztai, B Böttger, M Apel, V Witusiewicz, L Ratke, Jimmy De Wilde, Ludo Froyen, D Camel, et al. Multiphase solidification in multicomponent alloys. *Materials Science and Engineering: R: Reports*, 46(1-2):1–49, 2004. [2](#), [16](#)
- [25] Johannes Hoetzer, Michael Kellner, Philipp Steinmetz, and Britta Nestler. Applications of the phase-field method for the solidification of microstructures in multi-component systems. *J. Indian Inst. Sci.*, 96(3):235–256, 2016. [2](#), [16](#)
- [26] Geoffrey Allan Chadwick. Eutectic alloy solidification. *Progress in materials science*, 12:99–182, 1963. [2](#), [29](#)
- [27] Roy Elliott. *Eutectic solidification processing: crystalline and glassy alloys*. Elsevier, 2013. [2](#), [31](#), [33](#)
- [28] Alain Karma and Mathis Plapp. New insights into the morphological stability of eutectic and peritectic coupled growth. *JOM*, 56(4):28–32, 2004. [2](#)
- [29] Seong Gyoon Kim, Won Tae Kim, Toshio Suzuki, and Machiko Ode. Phase-field modeling of eutectic solidification. *Journal of crystal growth*, 261(1):135–158, 2004. [2](#)
- [30] Silvère Akamatsu and Mathis Plapp. Eutectic and peritectic solidification patterns. *Current Opinion in Solid State and Materials Science*, 20(1):46–54, 2016. [2](#), [29](#)

## REFERENCES

- [31] László Rátkai, Gyula I Tóth, László Környei, Tamás Pusztai, and László Gránásy. Phase-field modeling of eutectic structures on the nanoscale: the effect of anisotropy. *Journal of materials science*, 52(10):5544–5558, 2017. [2](#) [18](#)
- [32] FS Galasso. Unidirectionally solidified eutectics for optical, electronic, and magnetic applications. *JOM*, 19(6):17–21, 1967. [2](#)
- [33] FS Galasso, FC Douglas, and JA Batt. Recent studies of eutectics for nonstructural applications. *JOM*, 22(6):40–44, 1970. [2](#)
- [34] H Weiss. Electromagnetic properties of eutectic composites (a critical review). *Metallurgical Transactions*, 2(6):1513–1521, 1971. [2](#)
- [35] JD Parsons and AS Yue. Growth of fiber optic eutectics and their applications. *Journal of Crystal Growth*, 55(3):470–476, 1981. [2](#)
- [36] GA Chadwick. Structure and properties of eutectic alloys. *Metal Science*, 9(1):300–304, 1975. [2](#)
- [37] Barnasree Chanda, Gaurav Potnis, Parijat P Jana, and Jayanta Das. A review on nano-/ultrafine advanced eutectic alloys. *Journal of Alloys and Compounds*, 827:154226, 2020. [2](#)
- [38] Chandra Sekhar Tiwary, Prafull Pandey, Suman Sarkar, Rakesh Das, Sumanta Samal, Krishanu Biswas, and Kamanio Chattopadhyay. Five decades of research on the development of eutectic as engineering materials. *Progress in Materials Science*, page 100793, 2021. [2](#)
- [39] Isaac Chang and Qing Cai. From simple binary to complex multicomponent eutectic alloys. *Progress in Materials Science*, page 100779, 2021. [2](#)
- [40] RI Merino, MF Acosta, and VM Orera. New polaritonic materials in the thz range made of directionally solidified halide eutectics. *Journal of the European Ceramic Society*, 34(9):2061–2069, 2014. [2](#)
- [41] Shunsuke Kurosawa, Akihiro Yamaji, Yuui Yokota, Yoshisuke Futami, Kei Nishimoto, Noriaki Kawaguchi, Kentaro Fukuda, and Akira Yoshikawa. Growth and optical properties

## REFERENCES

- of lif/laf<sub>3</sub> eutectic crystals. *Journal of the European Ceramic Society*, 34(9):2111–2115, 2014. [2](#)
- [42] Dorota A Pawlak. Metamaterials and photonic crystals—potential applications for self-organized eutectic micro-and nanostructures. *Scientia Plena*, 4(1), 2008. [2](#)
- [43] Dorota A Pawlak, Sebastian Turczynski, Marcin Gajc, Katarzyna Kolodziejek, Ryszard Diduszko, Krzysztof Rozniatowski, Julita Smalc, and Irina Vendik. How far are we from making metamaterials by self-organization? the microstructure of highly anisotropic particles with an srr-like geometry. *Advanced Functional Materials*, 20(7):1116–1124, 2010. [2](#)
- [44] Paweł Osewski, Alessandro Belardini, Marco Centini, Constantinos Valagianopoulos, Grigore Leahu, Roberto Li Voti, Monika Tomczyk, Andrea Alù, Dorota A Pawlak, and Concita Sibilia. New self-organization route to tunable narrowband optical filters and polarizers demonstrated with zno–znwo<sub>4</sub> eutectic composite. *Advanced Optical Materials*, 8(7):1901617, 2020. [2](#)
- [45] W Kurz and DJ Fisher. Dendrite growth in eutectic alloys: the coupled zone. *International Metals Reviews*, 24(1):177–204, 1979. [3](#)
- [46] C Lemaignan. Initial stages of eutectic solidification. *Acta Metallurgica*, 29(8):1379–1384, 1981. [3](#)
- [47] Silvère Akamatsu, Gabriel Faivre, and Sébastien Moulinet. The formation of lamellar-eutectic grains in thin samples. *Metallurgical and Materials Transactions A*, 32(8):2039–2048, 2001. [3](#)
- [48] Mingfang Zhu, Lei Zhang, Honglei Zhao, and Doru M Stefanescu. Modeling of microstructural evolution during divorced eutectic solidification of spheroidal graphite irons. *Acta Materialia*, 84:413–425, 2015. [7](#)
- [49] W.A. Tiller. Polyphase solidification. *Liquid metals and solidification, Seminar 39th National Metal Congress, Chicago*, pages 276–318, 1958. [9](#)
- [50] RM Jordan and JD Hunt. Interface undercoolings during the growth of pb-sn eutectics. *Metallurgical Transactions*, 3(6):1385–1390, 1972. [9, 24](#)

## REFERENCES

- [51] HE Cline, JL Walter, E Lifshin, and RR Russell. Structures, faults, and the rod-plate transition in eutectics. *Metallurgical Transactions*, 2(1):189–194, 1971. [10](#)
- [52] S Strässler and WR Schneider. Stability of lamellar eutectics. In *Physics of condensed matter*, pages 153–178. Springer, 1974. [10](#)
- [53] JS Langer. Eutectic solidification and marginal stability. *Physical Review Letters*, 44(15):1023, 1980. [10](#)
- [54] Wiktor Eckhaus. *Studies in non-linear stability theory*, volume 6. Springer Science & Business Media, 1965. [10](#)
- [55] S Akamatsu, G Faivre, M Plapp, and A Karma. Overstability of lamellar eutectic growth below the minimum-undercooling spacing. *Metallurgical and Materials Transactions A*, 35(6):1815–1828, 2004. [12](#)
- [56] S Akamatsu, M Plapp, G Faivre, and A Karma. Pattern stability and trijunction motion in eutectic solidification. *Physical review E*, 66(3):030501, 2002. [12](#)
- [57] G Faivre and J Mergy. Tilt bifurcation and dynamical selection by tilt domains in thin-film lamellar eutectic growth: Experimental evidence of a tilt bifurcation. *Physical Review A*, 45(10):7320, 1992. [12](#)
- [58] Gabriel Faivre. Morphological instabilities of lamellar eutectic growth fronts: a survey of recent experimental and numerical results. *Journal of Crystal growth*, 166(1-4):29–39, 1996. [12](#)
- [59] Alain Karma and Armand Sarkissian. Morphological instabilities of lamellar eutectics. *Metallurgical and Materials Transactions A*, 27(3):635–656, 1996. [12](#)
- [60] Marie Ginibre, Silvère Akamatsu, and Gabriel Faivre. Experimental determination of the stability diagram of a lamellar eutectic growth front. *Physical Review E*, 56(1):780, 1997. [12](#)
- [61] Roger Folch and Mathis Plapp. Phase-field modeling of eutectic solidification: From oscillations to invasion. In *Interface and Transport Dynamics*, pages 182–189. Springer, 2003. [12](#)

## REFERENCES

- [62] Silvère Akamatsu, Sabine Bottin-Rousseau, and Gabriel Faivre. Experimental evidence for a zigzag bifurcation in bulk lamellar eutectic growth. *Physical review letters*, 93(17):175701, 2004. [12](#)
- [63] Silvère Akamatsu, Sabine Bottin-Rousseau, and Gabriel Faivre. Stability of lamellar eutectic growth in thick samples. *Philosophical Magazine*, 86(24):3703–3715, 2006. [12, 24](#)
- [64] AJ McLeod, LM Hogan, C McL Adam, and DC Jenkinson. Growth mode of the aluminum phase in al-si and al-al<sub>3</sub>fe eutectics. *Journal of Crystal Growth*, 19(4):301–309, 1973. [13](#)
- [65] KF Kobayashi and LM Hogan. The crystal growth of silicon in al-si alloys. *Journal of Materials Science*, 20(6):1961–1975, 1985. [13](#)
- [66] M Shamsuzzoha and LM Hogan. Crystal morphology of unmodified aluminium-silicon eutectic microstructures. *Journal of crystal growth*, 76(2):429–439, 1986. [13](#)
- [67] LM Hogan and H Song. Aluminium grain structures in al-si eutectic alloys. *Acta Metallurgica*, 35(3):677–680, 1987. [13](#)
- [68] WA Tiller, KA Jackson, JW Rutter, and B Chalmers. The redistribution of solute atoms during the solidification of metals. *Acta metallurgica*, 1(4):428–437, 1953. [15](#)
- [69] William W Mullins and RF Sekerka. Stability of a planar interface during solidification of a dilute binary alloy. *Journal of applied physics*, 35(2):444–451, 1964. [15, 18, 43, 146](#)
- [70] Blas Echebarria, Roger Folch, Alain Karma, and Mathis Plapp. Quantitative phase-field model of alloy solidification. *Physical Review E*, 70(6):061604, 2004. [16](#)
- [71] DG McCartney, RM Jordan, and JD Hunt. The structures expected in a simple ternary eutectic system: Part ii. the al-ag-cu ternary system. *Metallurgical Transactions A*, 11(8):1251–1257, 1980. [18](#)
- [72] MD Rinaldi, RM Sharp, and MC Flemings. Growth of ternary composites from the melt: Part ii. *Metallurgical Transactions*, 3(12):3139–3148, 1972. [18](#)
- [73] WM Rumball. Cellular growth in eutectic systems. *Metallurgia*, 78(468):141–145, 1968. [18](#)

## REFERENCES

- [74] PK Rohatgi and CMJR Adams. Colony and dendritic structures produced on solidification of eutectic aluminum copper alloy. *TRANS MET SOC AIME*, 245(7):1609–1613, 1969. [18](#)
- [75] Silvère Akamatsu and Gabriel Faivre. Traveling waves, two-phase fingers, and eutectic colonies in thin-sample directional solidification of a ternary eutectic alloy. *Physical Review E*, 61(4):3757, 2000. [18](#)
- [76] Silvère Akamatsu, Mikael Perrut, Sabine Bottin-Rousseau, and Gabriel Faivre. Spiral two-phase dendrites. *Physical review letters*, 104(5):056101, 2010. [18, 21](#)
- [77] Yeqing Wang, Jianrong Gao, Paul Chao, Nancy S Muyanja, Ragnvald H Mathiesen, and Ashwin J Shahani. In-situ evidence for impurity-induced formation of eutectic colonies in an interdendritic liquid. *Materials Letters*, page 129637, 2021. [18](#)
- [78] Mathis Plapp and Alain Karma. Eutectic colony formation: A phase-field study. *Physical Review E*, 66(6):061608, 2002. [18, 31](#)
- [79] Arka Lahiri, Chandrashekhar Tiwary, Kamanio Chattopadhyay, and Abhik Choudhury. Eutectic colony formation in systems with interfacial energy anisotropy: A phase field study. *Computational Materials Science*, 130:109–120, 2017. [18, 21](#)
- [80] Mathis Plapp and Alain Karma. Eutectic colony formation: A stability analysis. *Physical Review E*, 60(6):6865, 1999. [18, 31](#)
- [81] Tamás Pusztai, László Rátkai, Attila Szállás, and László Gránásy. Spiraling eutectic dendrites. *Physical Review E*, 87(3):032401, 2013. [21](#)
- [82] Silvère Akamatsu, Sabine Bottin-Rousseau, Gabriel Faivre, and Efim A Brener. Scaling theory of two-phase dendritic growth in undercooled ternary melts. *Physical review letters*, 112(10):105502, 2014. [21](#)
- [83] Toshiaki Himemiya and Takateru Umeda. Three-phase planar eutectic growth models for a ternary eutectic system. *Materials Transactions, JIM*, 40(7):665–674, 1999. [21](#)
- [84] Abhik Choudhury, Mathis Plapp, and Britta Nestler. Theoretical and numerical study of lamellar eutectic three-phase growth in ternary alloys. *Physical Review E*, 83(5):051608, 2011. [21](#)

## REFERENCES

- [85] Arka Lahiri and Abhik Choudhury. Revisiting jackson-hunt calculations: Unified theoretical analysis for generic multi-phase growth in a multi-component system. *Acta Materialia*, 133:316–332, 2017. [21](#)
- [86] Philipp Steinmetz, Michael Kellner, Johannes Hötzer, and Britta Nestler. Quantitative comparison of ternary eutectic phase-field simulations with analytical 3d jackson–hunt approaches. *Metallurgical and Materials Transactions B*, 49(1):213–224, 2018. [21](#)
- [87] U Büyük, Necmettin Maraşlı, HASAN Kaya, Emin Çadırlı, and K Keşlioğlu. Directional solidification of al–cu–ag alloy. *Applied Physics A*, 95(3):923–932, 2009. [21](#)
- [88] Anne Dennstedt and Lorenz Ratke. Microstructures of directionally solidified al–ag–cu ternary eutectics. *Transactions of the Indian Institute of Metals*, 65(6):777–782, 2012. [21](#)
- [89] Johannes Hötzer, Philipp Steinmetz, Anne Dennstedt, Amber Genau, Michael Kellner, Irmak Sargin, and Britta Nestler. Influence of growth velocity variations on the pattern formation during the directional solidification of ternary eutectic al-ag-cu. *Acta Materialia*, 136:335–346, 2017. [21](#)
- [90] Philipp Steinmetz, Anne Dennstedt, Melis Şerefoğlu, Irmak Sargin, Amber Genau, and Ulrike Hecht. Crystal orientation relationships in ternary eutectic al-al<sub>2</sub>cu-ag<sub>2</sub>al. *Acta Materialia*, 157:96–105, 2018. [21](#)
- [91] Carlos Triveño Rios, Srdjan Milenkovic, Sergio Gama, and Rubens Caram. Influence of the growth rate on the microstructure of a nb–al–ni ternary eutectic. *Journal of crystal growth*, 237:90–94, 2002. [21](#)
- [92] Carlos Triveno Rios, Srdjan Milenkovic, and Rubens Caram. A novel ternary eutectic in the nb–al–ni system. *Scripta materialia*, 48(10):1495–1500, 2003. [21](#)
- [93] C Triveño Rios, MF Oliveira, R Caram, C Bolfarini, CS Kiminami, et al. Directional and rapid solidification of al–nb–ni ternary eutectic alloy. *Materials Science and Engineering: A*, 375:565–570, 2004. [21](#)
- [94] L Snugovsky, DD Perovic, and JW Rutter. Solidification of ternary eutectic and near eutectic alloys in the ag–cu–sn system. *Materials science and technology*, 20(11):1403–1413, 2004. [21](#)

## REFERENCES

- [95] U Böyük and N Maraşlı. The microstructure parameters and microhardness of directionally solidified sn–ag–cu eutectic alloy. *Journal of alloys and compounds*, 485(1-2):264–269, 2009. [21](#)
- [96] H Kaya, U Böyük, E Çadırli, Y Ocak, S Akbulut, K Keşlioğlu, and N Maraşlı. Dependency of microstructural parameters and microindentation hardness on the temperature gradient in the in- bi- sn ternary alloy with a low melting point. *Metals and Materials International*, 14(5):575–582, 2008. [21](#)
- [97] Samira Mohagheghi and Melis Şerefoglu. Quasi-isotropic and locked grain growth dynamics in a three-phase eutectic system. *Acta Materialia*, 151:432–442, 2018. [21](#)
- [98] VT Witusiewicz, U Hecht, S Rex, and M Apel. In situ observation of microstructure evolution in low-melting bi–in–sn alloys by light microscopy. *Acta materialia*, 53(13):3663–3669, 2005. [21](#)
- [99] S Mohagheghi, U Hecht, S Bottin-Rousseau, Silvère Akamatsu, G Faivre, and M Şerefoglu. Effects of interphase boundary anisotropy on the three-phase growth dynamics in the  $\beta$  (in)–in<sub>2</sub>bi– $\gamma$  (sn) ternary-eutectic system. In *IOP Conference Series: Materials Science and Engineering*, volume 529, page 012010. IOP Publishing, 2019. [21](#), [31](#)
- [100] Samira Mohagheghi and Melis Şerefoglu. Dynamics of spacing adjustment and recovery mechanisms of abac-type growth pattern in ternary eutectic systems. *Journal of Crystal Growth*, 470:66–74, 2017. [21](#)
- [101] H Kabassis, JW Rutter, and WC Winegard. Microstructure of one of the ternary eutectic alloys in the bi-in-sn system. *Metallurgical and Materials Transactions A*, 15(8):1515–1517, 1984. [21](#)
- [102] MA Ruggiero and JW Rutter. Origin of microstructure in 350 k eutectic of bi–in–sn ternary system. *Materials science and technology*, 11(2):136–142, 1995. [21](#)
- [103] S Rex, B Böttger, V Witusiewicz, and U Hecht. Transient eutectic solidification in in–bi–sn: two-dimensional experiments and numerical simulation. *Materials Science and Engineering: A*, 413:249–254, 2005. [21](#)

## REFERENCES

- [104] Sabine Bottin-Rousseau, Melis Şerefoglu, Sinan Yüçetürk, Gabriel Faivre, and Silvère Akamatsu. Stability of three-phase ternary-eutectic growth patterns in thin sample. *Acta Materialia*, 109:259–266, 2016. [21](#)
- [105] Kaveh Dargahi Noubary, Michael Kellner, Philipp Steinmetz, Johannes Hoetzer, and Britta Nestler. Phase-field study on the effects of process and material parameters on the tilt angle during directional solidification of ternary eutectics. *Computational Materials Science*, 138:403–411, 2017. [21](#)
- [106] Philipp Steinmetz, Johannes Hötzer, Michael Kellner, Amber Genau, and Britta Nestler. Study of pattern selection in 3d phase-field simulations during the directional solidification of ternary eutectic al-ag-cu. *Computational Materials Science*, 148:131–140, 2018. [21](#)
- [107] Badrinarayan P Athreya, Jonathan A Dantzig, Shan Liu, and Rohit Trivedi. On the role of confinement on solidification in pure materials and binary alloys. *Philosophical Magazine*, 86(24):3739–3756, 2006. [24](#)
- [108] LM Fabietti and JA Sekhar. Quantitative microstructure maps for restrained directional growth. *Journal of materials science*, 29(2):473–477, 1994. [24](#)
- [109] Melis Serefoglu and RE Napolitano. On the selection of rod-type eutectic morphologies: Geometrical constraint and array orientation. *Acta Materialia*, 56(15):3862–3873, 2008. [24](#)
- [110] Melis Şerefoglu, Ralph E Napolitano, and Mathis Plapp. Phase-field investigation of rod eutectic morphologies under geometrical confinement. *Physical Review E*, 84(1):011614, 2011. [24](#)
- [111] Melis Şerefoglu, S Bottin-Rousseau, S Akamatsu, and G Faivre. Dynamics of rod eutectic growth patterns in confined geometry. *IOP Conference Series: Materials Science and Engineering*, 27:012030, jan 2012. [24](#)
- [112] Mikael Perrut, Andrea Parisi, Silvère Akamatsu, Sabine Bottin-Rousseau, Gabriel Faivre, and Mathis Plapp. Role of transverse temperature gradients in the generation of lamellar eutectic solidification patterns. *Acta Materialia*, 58(5):1761–1769, 2010. [24](#)

## REFERENCES

- [113] A Zhang, Z Guo, and S-M Xiong. Eutectic pattern transition under different temperature gradients: A phase field study coupled with the parallel adaptive-mesh-refinement algorithm. *Journal of Applied Physics*, 121(12):125101, 2017. [24](#)
- [114] A Hellawell. The growth and structure of eutectics with silicon and germanium. *Progress in Materials Science*, 15(1):3–78, 1970. [24](#), [31](#), [33](#)
- [115] DJS Cooksey, D Munson, MP Wilkinson, and A Hellawell. The freezing of some continuous binary eutectic mixtures. *Philosophical Magazine*, 10(107):745–769, 1964. [26](#)
- [116] Daniel Lewis, James Warren, William Boettinger, Tamás Pusztai, and László Gránásy. Phase-field models for eutectic solidification. *Jom*, 56(4):34–39, 2004. [26](#)
- [117] Philipp Steinmetz, Michael Kellner, Johannes Hötzter, Anne Dennstedt, and Britta Nestler. Phase-field study of the pattern formation in al-ag-cu under the influence of the melt concentration. *Computational Materials Science*, 121:6–13, 2016. [29](#)
- [118] G Wulff. On the question of speed of growth and dissolution of crystal surfaces. *Z. Kristallogr*, 34(5/6):449, 1901. [29](#)
- [119] JA Dantzig. Equilibrium shapes for crystalline solids. [29](#)
- [120] MR Taylor, RS Fidler, and RW Smith. Broken lamellar eutectic growth; structure of the silver-bismuth eutectic. *Journal of Crystal Growth*, 3:666–673, 1968. [29](#)
- [121] TG Digges and RN Tauber. Characterization of the morphology of the bi- ag eutectic by electrical analogs. *Metallurgical Transactions*, 2(6):1683–1689, 1971. [29](#)
- [122] HW Kerr and MH Lewis. Crystallographic relationships and morphologies of the bi-zn and bi-ag eutectic alloys. *Journal of Crystal Growth*, 15(2):117–125, 1972. [29](#), [89](#)
- [123] TG Digges Jr and RN Tauber. Structure of bi-ag eutectic alloy. *Journal of Crystal Growth*, 8(1):132–134, 1971. [29](#)
- [124] MA Savas, L Clapham, and RW Smith. The effect of growth rate and morphological transitions on interphase spacings of bi-ag, pb-ag and bi-mnbi eutectics. *Journal of Materials Science*, 25(2):909–913, 1990. [29](#)

## REFERENCES

- [125] HW Kerr and WC Winegard. The structure of some eutectics with high ratios of the volume fractions. *Canadian Metallurgical Quarterly*, 6(1):67–70, 1967. [29](#)
- [126] MR Taylor, RS Fidler, and RW Smith. The classification of binary eutectics. *Metallurgical Transactions*, 2(7):1793–1798, 1971. [29, 89](#)
- [127] Mevlüt Şahin and Emin Çadırli. The effects of temperature gradient and growth rate on the microstructure of directionally solidified sn–3.5 ag eutectic solder. *Journal of Materials Science: Materials in Electronics*, 23(2):484–492, 2012. [29](#)
- [128] JF Bromley, F Vnuk, and RW Smith. Mechanical properties of sn-ag 3 sn alloys. *Journal of materials science*, 18(10):3143–3153, 1983. [29](#)
- [129] G Piatti and G Pellegrini. The structure of the unidirectionally solidified al-al 2 au eutectic. *Journal of Materials Science*, 11(5):913–924, 1976. [29](#)
- [130] G Beghi, G Piatti, and KN Street. The structure of the unidirectionally solidified al-alsb binary eutectic. *Journal of Materials Science*, 6(2):118–125, 1971. [29](#)
- [131] MN Croker, RS Fidler, and RW Smith. The characterization of eutectic structures. *Proceedings of the Royal Society of London. A. Mathematical and Physical Sciences*, 335(1600):15–37, 1973. [29, 57](#)
- [132] M Notis, D Shah, S Young, and C Graham. Structure and magnetic properties of directionally solidified bi-mnbi eutectic alloys. *IEEE Transactions on Magnetics*, 15(2):957–966, 1979. [29](#)
- [133] M Sahoo, GW Delamore, and RW Smith. Mechanical properties characterization of the broken-lamellar eutectic composite cd-ge. *Journal of Materials Science*, 15(5):1097–1103, 1980. [29](#)
- [134] GS Nishimura, RS Fidler, MR Taylor, and RW Smith. The classification of the indium-zinc eutectic. *Canadian Metallurgical Quarterly*, 8(4):319–322, 1969. [29](#)
- [135] PJ Taylor, HW Kerr, and WC Winegard. Structure of the sn-zn eutectic. *Canadian Metallurgical Quarterly*, 3(3):235–237, 1964. [29, 57, 59](#)

## REFERENCES

- [136] D Jaffrey and GA Chadwick. The nucleation, growth morphology, and thermal stability of sn- zn and al- al 3 ni eutectic alloys. *Metallurgical Transactions*, 1(12):3389–3396, 1970. 29, 57, 59, 72, 74, 77, 79
- [137] F Vnuk, M Sahoo, D Baragar, and RW Smith. Mechanical properties of the sn-zn eutectic alloys. *Journal of Materials Science*, 15(10):2573–2583, 1980. 29, 57, 59, 72
- [138] H Kaya, M Gündüz, E Çadırlı, and O Uzun. Effect of growth rate and lamellar spacing on microhardness in the directionally solidified pb-cd, sn-zn and bi-cd eutectic alloys. *Journal of Materials Science*, 39(21):6571–6576, 2004. 29, 57, 59
- [139] H Kaya, E Çadırlı, and M Gündüz. Effect of growth rates and temperature gradients on the spacing and undercooling in the broken-lamellar eutectic growth (sn-zn eutectic system). *Journal of materials engineering and performance*, 12(4):456–469, 2003. 29, 43, 57, 59, 89
- [140] Yasuto Goto, Masao Kurosaki, and Hisao Esaka. The characterization of structure in tin-zinc binary eutectic alloys using unidirectional solidification. *Journal of the Japan Institute of Metals*, 75(7):392–397, 2011. 29, 57, 59
- [141] Mevlüt Şahin and Fatih Karakurt. The effect of the solidification rate on the physical properties of the sn-zn eutectic alloy. *Physica B: Condensed Matter*, 545:48–54, 2018. 29, 57, 59
- [142] KP Sharma and RN Rai. Synthesis and characterization of novel binary organic monotectic and eutectic alloys. *Thermochimica acta*, 535:66–70, 2012. 29
- [143] B Caroli, C Caroli, G Faivre, and J Mergy. Lamellar eutectic growth of cbr4-c2cl6: effect of crystal anisotropy on lamellar orientations and wavelength dispersion. *Journal of crystal growth*, 118, 1992. 29
- [144] A Valance, C Misbah, D Temkin, and K Kassner. Analytic theory for parity breaking in lamellar eutectic growth. *Physical Review E*, 48, 1993. 29
- [145] S Bottin-Rousseau, M Şerefoğlu, Silvère Akamatsu, and G Faivre. The surface tension force of anisotropic interphase boundaries is perpendicular to the solidification front during eutectic growth. 27(1):012088, 2012. 29, 31

## REFERENCES

- [146] S Akamatsu, S Bottin-Rousseau, M Şerefoğlu, and G Faivre. A theory of thin lamellar eutectic growth with anisotropic interphase boundaries. *Acta Materialia*, 60(6-7):3199–3205, 2012. [29](#), [31](#)
- [147] S Akamatsu, S Bottin-Rousseau, M Şerefoğlu, and G Faivre. Lamellar eutectic growth with anisotropic interphase boundaries: Experimental study using the rotating directional solidification method. *Acta Materialia*, 60(6-7):3206–3214, 2012. [29](#), [31](#), [83](#)
- [148] Supriyo Ghosh, Abhik Choudhury, Mathis Plapp, Sabine Bottin-Rousseau, Gabriel Faivre, and Silvère Akamatsu. Interphase anisotropy effects on lamellar eutectics: A numerical study. *Physical Review E*, 91(2):022407, 2015. [29](#), [31](#)
- [149] Sabine Bottin-Rousseau, Mehdi Medjkoune, Oriane Senninger, Laurent Carroz, Richard Soucek, Ulrike Hecht, and Silvère Akamatsu. Locked-lamellar eutectic growth in thin al-al<sub>2</sub>cu samples: in situ directional solidification and crystal orientation analysis. *Journal of Crystal Growth*, page 126203, 2021. [29](#)
- [150] Supriyo Ghosh and Mathis Plapp. Influence of interphase boundary anisotropy on bulk eutectic solidification microstructures. *Acta Materialia*, 140:140–148, 2017. [31](#)
- [151] Ulrike Hecht, Janin Eiken, Silvère Akamatsu, and Sabine Bottin-Rousseau. Phase boundary anisotropy and its effects on the maze-to-lamellar transition in a directionally solidified al-al<sub>2</sub>cu eutectic. *Acta Materialia*, 170:268–277, 2019. [31](#)
- [152] Sabine Bottin-Rousseau, Oriane Senninger, Gabriel Faivre, and Silvère Akamatsu. Special interphase orientation relationships and locked lamellar growth in thin in-in<sub>2</sub>bi eutectics. *Acta Materialia*, 150:16–24, 2018. [31](#)
- [153] MN Croker, RS Fidler, and RW Smith. The cellular growth of bi-pb<sub>2</sub>bi eutectic. *Journal of Crystal Growth*, 11(2):121–130, 1971. [31](#), [142](#)
- [154] SD Bagheri and JW Rutter. Origin of microstructure in bi–pb and bi–sn binary eutectics. *Materials science and technology*, 13(7):541–550, 1997. [31](#), [32](#), [142](#)
- [155] P Magnin, JT Mason, and R Trivedi. Growth of irregular eutectics and the alsi system. *Acta metallurgica et materialia*, 39(4):469–480, 1991. [31](#), [33](#)

## REFERENCES

- [156] Ashwin J Shahani, Xianghui Xiao, and Peter W Voorhees. The mechanism of eutectic growth in highly anisotropic materials. *Nature communications*, 7:12953, 2016. [31](#), [33](#), [59](#)
- [157] RL Fullman and DL Wood. Origin of spiral eutectic structures. *Acta Metallurgica*, 2(2):188–193, 1954. [32](#)
- [158] HY Liu and H Jones. Solidification microstructure selection and characteristics in the zinc-based zn-mg system. *Acta metallurgica et materialia*, 40(2):229–239, 1992. [32](#)
- [159] Saman Moniri, Hrishikesh Bale, Tobias Volkenandt, Yeqing Wang, Jianrong Gao, Tianxiang Lu, Kai Sun, Robert O Ritchie, and Ashwin J Shahani. Multi-step crystallization of self-organized spiral eutectics. *Small*, page 1906146, 2020. [32](#)
- [160] Percy W Bridgman. Certain physical properties of single crystals of tungsten, antimony, bismuth, tellurium, cadmium, zinc, and tin. In *Collected Experimental Papers, Volume III*, pages 1851–1932. Harvard University Press, 2013. [35](#)
- [161] Donald C Stockbarger. The production of large single crystals of lithium fluoride. *Review of Scientific Instruments*, 7(3):133–136, 1936. [35](#)
- [162] Donald C Stockbarger. The production of large artificial fluorite crystals. *Discussions of the Faraday Society*, 5:294–299, 1949. [35](#)
- [163] Ta-Wei Fu and William R Wilcox. Influence of insulation on stability of interface shape and position in the vertical bridgman-stockbarger technique. *Journal of Crystal Growth*, 48(3):416–424, 1980. [35](#)
- [164] EM Monberg, WA Gault, F Simchock, and F Dominguez. Vertical gradient freeze growth of large diameter, low defect density indium phosphide. *Journal of Crystal Growth*, 83(2):174–183, 1987. [35](#)
- [165] EM Monberg, H Brown, and CE Bonner. The dynamic gradient freeze growth of inp. *Journal of crystal growth*, 94(1):109–114, 1989. [35](#)
- [166] Dieter Hofmann, Thomas Jung, and Georg Müller. Growth of 2 inch ge: Ga crystals by the dynamical vertical gradient freeze process and its numerical modelling including transient segregation. *Journal of crystal growth*, 128(1-4):213–218, 1993. [35](#)

## REFERENCES

- [167] Henry G Weller, Gavin Tabor, Hrvoje Jasak, and Christer Fureby. A tensorial approach to computational continuum mechanics using object-oriented techniques. *Computers in physics*, 12(6):620–631, 1998. [42](#)
- [168] Z Moser, J Dutkiewicz, W Gasior, and J Salawa. The sn-zn (tin-zinc) system. *Journal of Phase Equilibria*, 6(4):330–334, 1985. [43](#), [57](#), [72](#)
- [169] To Jasinski and AoFo Witt. On control of the crystal-melt interface shape during growth in a vertical bridgman configuration. *Journal of Crystal Growth*, 71(2):295–304, 1985. [47](#)
- [170] D Wheeler, D Brough, T Fast, S Kalidindi, and A Reid. Pymks: materials knowledge system in python, 2014. [53](#), [89](#), [128](#)
- [171] Surya R Kalidindi. *Hierarchical materials informatics: novel analytics for materials data*. Elsevier, 2015. [53](#), [89](#), [128](#)
- [172] David B Brough, Daniel Wheeler, and Surya R Kalidindi. Materials knowledge systems in python—a data science framework for accelerated development of hierarchical materials. *Integrating materials and manufacturing innovation*, 6(1):36–53, 2017. [53](#), [89](#), [128](#)
- [173] Ping-Sung Liao, Tse-Sheng Chen, Pau-Choo Chung, et al. A fast algorithm for multilevel thresholding. *J. Inf. Sci. Eng.*, 17(5):713–727, 2001. [53](#), [128](#)
- [174] F Bachmann, Ralf Hielscher, and Helmut Schaeben. Texture analysis with mTEX—free and open source software toolbox. In *Solid State Phenomena*, volume 160, pages 63–68. Trans Tech Publ, 2010. [56](#)
- [175] R Elliot and A Moore. The undercooling at the solid-liquid interface of the tin-zinc eutectic. *Scripta Metallurgica*, 3(4):249–251, 1969. [57](#)
- [176] P Pandey, CS Tiwary, and K Chattopadhyay. Effects of minute addition of ni on microstructure and mechanical properties of sn-zn eutectic alloy. *Journal of Electronic Materials*, 45(10):5468–5477, 2016. [57](#)
- [177] P Pandey, CS Tiwary, and K Chattopadhyay. Effects of cu and in trace elements on microstructure and thermal and mechanical properties of sn-zn eutectic alloy. *Journal of Electronic Materials*, 48(5):2660–2669, 2019. [57](#)

## REFERENCES

- [178] M Straumanis and N Brakes. The morphology of bi-cd, sn-zn, sn-cd, and al-si eutectics. *Z. Physik. Chem. B*, 38, 1937. [57](#), [72](#), [74](#), [76](#)
- [179] Herbert Herman. *Advances in materials research*, volume 4. Wiley-Interscience, 1970. [57](#), [72](#)
- [180] B Cantor and GA Chadwick. Eutectic crystallography by x-ray texture diffractometry. *Journal of Crystal Growth*, 30(1):109–112, 1975. [57](#), [72](#), [74](#), [76](#)
- [181] Adam J Schwartz, Mukul Kumar, Brent L Adams, and David P Field. *Electron backscatter diffraction in materials science*. Springer, 2000. [72](#)
- [182] David B Williams and C Barry Carter. *The transmission electron microscope*. Springer, 1996. [72](#)
- [183] Logan G Ware, Daniel H Suzuki, and Zachary C Cordero. Thermodynamic stability and kinematic accessibility of curved grain boundaries in directionally solidified bicrystals. *Journal of Materials Science*, 55:1–12, 2020. [77](#)
- [184] A Passerone and N Eustathopoulos. Equilibrium structural transitions of solid-liquid interfaces in zinc based alloys. *Acta Metallurgica*, 30(7):1349–1356, 1982. [83](#)
- [185] RC Sharma and YA Chang. The sn- te (tin-tellurium) system. *Bulletin of Alloy Phase Diagrams*, 7(1):72–80, 1986. [87](#)
- [186] B Predel. Sn-te (tin-tellurium). In *Pu-Re-Zn-Zr*, pages 1–5. Springer, 1998. [87](#)
- [187] Andrea Parisi and Mathis Plapp. Defects and multistability in eutectic solidification patterns. *EPL (Europhysics Letters)*, 90(2):26010, 2010. [95](#)
- [188] Christopher Boldt. Directional solidification of the alumina-zirconia ceramic eutectic system. 1994. [102](#), [155](#)
- [189] JH Lee, A Yoshikawa, H Kaiden, K Lebbou, T Fukuda, DH Yoon, and Y Waku. Microstructure of y<sub>2</sub>o<sub>3</sub> doped al<sub>2</sub>o<sub>3</sub>/zro<sub>2</sub> eutectic fibers grown by the micro-pulling-down method. *Journal of Crystal Growth*, 231(1-2):179–185, 2001. [102](#), [155](#)

## REFERENCES

- [190] Lian-sheng Fu, Guo-qing Chen, Xue-song Fu, and Wen-long Zhou. Insights into the ternary eutectic microstructure formed in intercolony regions in al<sub>2</sub>o<sub>3</sub>–zro<sub>2</sub> (y<sub>2</sub>o<sub>3</sub>) system. *Journal of the American Ceramic Society*, 102(1):498–507, 2019. [102](#), [141](#), [155](#)
- [191] M Durand-Charre and F Durand. Effects of growth rate on the morphology of monovariant eutectics: Mn<sub>sb</sub>-(sb, bi) and mnsb-(sb, sn). *Journal of Crystal Growth*, 13:747–750, 1972. [102](#), [141](#), [155](#)
- [192] Günter Effenberg, Bernd Grieb, and Materials Science International Team, MSIT®. Ag-sn-te ternary phase diagram evaluation · phase diagrams, crystallographic and thermodynamic data: Datasheet from msi eureka in springermaterials ([https://materials.springer.com/msi/docs/sm\\_msi\\_r\\_10\\_017334\\_01](https://materials.springer.com/msi/docs/sm_msi_r_10_017334_01)). Copyright 1988 MSI Materials Science International Services GmbH. [108](#)
- [193] Sb-sn-te liquidus projection of ternary phase diagram: Datasheet from “pauling file multinary edition – 2012” in springermaterials ([https://materials.springer.com/isp/phase-diagram/docs/c\\_0952750](https://materials.springer.com/isp/phase-diagram/docs/c_0952750)). Copyright 2016 Springer-Verlag Berlin Heidelberg & Material Phases Data System (MPDS), Switzerland & National Institute for Materials Science (NIMS), Japan. [108](#)
- [194] Sb-sn-te isothermal section of ternary phase diagram: Datasheet from “pauling file multinary edition – 2012” in springermaterials ([https://materials.springer.com/isp/phase-diagram/docs/c\\_0952756](https://materials.springer.com/isp/phase-diagram/docs/c_0952756)). Copyright 2016 Springer-Verlag Berlin Heidelberg & Material Phases Data System (MPDS), Switzerland & National Institute for Materials Science (NIMS), Japan. [116](#)
- [195] Walter Burkhardt and Konrad Schubert. About brass-like phases with a3-related structure. *Zeitschrift Fur Metallkunde*, 50(8):442–452, 1959. [125](#)
- [196] Majken Elander, Gunnar Hägg, and Arne Westgren. *The crystal structure of Cu<sub>2</sub>Sb and Fe<sub>2</sub>As*. Almqvist & Wiksell, 1935. [125](#)
- [197] CS Barrett, P Cucka, and K Haefner. The crystal structure of antimony at 4.2, 78 and 298 k. *Acta Crystallographica*, 16(6):451–453, 1963. [125](#)
- [198] Ying Ruan and BingBo Wei. Dendritic and eutectic growth in sb 60 ag 20 cu 20 ternary

## REFERENCES

- alloy. *Science in China Series G: Physics, Mechanics and Astronomy*, 50(5):563–571, 2007. [122](#), [151](#)
- [199] Ying Ruan, Chongde Cao, and Bingbo Wei. Rapid growth of ternary eutectic under high undercooling conditions. *Science in China Series G: Physics, Mechanics and Astronomy*, 47(6):717–728, 2004. [122](#)
- [200] Ruan Ying, Wang Nan, Cao Chong-De, and Wei Bing-Bo. Ternary eutectic growth in a highly undercooled liquid alloy. *Chinese Physics Letters*, 21(8):1590, 2004. [122](#)
- [201] Wei Zhai, Baojian Wang, Liang Hu, and Bingbo Wei. Ternary eutectic growth during directional solidification of ag–cu–sb alloy. *Philosophical Magazine Letters*, 95(4):187–193, 2015. [122](#)
- [202] Christo N Nanev. Instability of faceted crystal shapes and their transformation into skeletons during growth under diffusion control. *Crystallography reviews*, 4(1):3–71, 1994. [135](#)
- [203] Christo N Nanev. Polyhedral instability-skeletal and dendritic growth. *Progress in crystal growth and characterization of materials*, 35(1):1–26, 1997. [135](#)
- [204] Ji-Ping Zhu, Shu-Hong Yu, Zhu-Bing He, Jun Jiang, Ke Chen, and Xiao-Yuan Zhou. Complex pbte hopper (skeletal) crystals with high hierarchy. *Chemical communications*, (46):5802–5804, 2005. [135](#)
- [205] Jiping Zhu, Wensheng Duan, and Yangping Sheng. Uniform pbs hopper (skeletal) crystals grown by a solution approach. *Journal of crystal growth*, 311(2):355–357, 2009. [135](#)
- [206] Zeda Yang, Jingyi Zhang, Lifu Zhang, Benwei Fu, Peng Tao, Chengyi Song, Wen Shang, and Tao Deng. Self-assembly in hopper-shaped crystals. *Advanced Functional Materials*, 30(26):1908108, 2020. [135](#)
- [207] I Minkoff and B Lux. Instability criteria for growth of a hopper crystal related to spiral eutectic morphology. *Journal of Crystal Growth*, 22(2):163–165, 1974. [135](#)
- [208] Gianna Alemaén Milaén, Brian Millier, Andrew Ritchie, Craig Bryan, Sarah Vinette, Bjorn Wielens, and Mary Anne White. Bismuth crystals: Preparation and measurement

## REFERENCES

- of thermal and electrical properties. *Journal of Chemical Education*, 90(12):1675–1680, 2013. [135](#)
- [209] DL Baragar, M Sahoo, and RW Smith. The structural modification of the complex-regular eutectics of bismuth-lead, bismuth-tin and bismuth-thallium. *Journal of Crystal Growth*, 41(2):278–286, 1977. [142](#)
- [210] Hsuan-Han Lai, Chih-Chun Hsieh, Chi-Ming Lin, and Weite Wu. Characteristics of eutectic  $\alpha$  (cr, fe)-(cr, fe) 23 c 6 in the eutectic fe-cr-c hardfacing alloy. *Metallurgical and materials transactions a*, 48(1):493–500, 2017. [142](#)